Monitoring, modelling and simulation of spiral concentrators

by

Ernst Carel Nienaber

Dissertation presented for the Degree

of

DOCTOR OF ENGINEERING

(EXTRACTIVE METALLURGICAL ENGINEERING)

in the Faculty of Engineering

at Stellenbosch University

Supervisor

Dr. Lidia Auret

December 2018

The financial assistance from Glencore and technical assistance from Multotec towards this research is hereby acknowledged. Opinions expressed and conclusions arrived at are those of the author and are not necessarily attributed to Glencore or Multotec.

Stellenbosch University https://scholar.sun.ac.za

DECLARATION

By submitting this thesis electronically, I declare that the entirety of the work contained therein is my own, original work, that I am the sole author thereof (save to the extent explicitly otherwise stated), that reproduction and publication thereof by Stellenbosch University will not infringe any third party rights and that I have not previously in its entirety or in part submitted it for obtaining any qualification.

This dissertation includes *2* original papers published in peer-reviewed journals or books and *2* unpublished publications. The development and writing of the papers (published and unpublished) were the principal responsibility of myself and, for each of the cases where this is not the case, a declaration is included in the dissertation indicating the nature and extent of the contributions of co-authors.

Date: *December 2018*

Copyright © 2018 Stellenbosch University

All rights reserved

Stellenbosch University https://scholar.sun.ac.za

ABSTRACT

Spiral concentrators are robust gravity separation devices often compactly implemented in industry with large amounts of spirals per plant – organized in banks. Current automated monitoring strategies at spiral concentrator plants involve quantifying overall feed and product stream states. However, spiral unit monitoring is performed by manual operator inspection and control is mainly achieved by operators manually changing splitter settings of spirals across a plant. In large spiral plants, containing thousands of individual spiral concentrators, changing splitters can become tedious or is sometimes neglected. Automated monitoring and control of spirals can aid spiral plant operators in achieving optimal spiral plant performance.

Computer vision orientated mineral interface detection have been proposed, in past studies, as a method to monitor spiral concentrators. This is due to the formation of different mineral bands within spiral troughs during heavy mineral separation. Particles differentiate based on density and size differences usually creating three, visually discernible, mineral bands (flowing down the spiral trough). These streams are known as the concentrate, middling and tailings streams. The concentrate band is often visually darker than the streams containing gangue and the mineral interfaces can serve as a useful cue for setting splitters. However, interface tracking on industrial slurries have not yet been demonstrated and due to the large number of spirals within spiral plants it is necessary to determine what sparse sensor implementation will look like (this is due to the lack of appropriate sensor placement algorithms for metallurgical plants).

This text follows a framework that spans from sensor development to sensor implementation strategy within spiral concentration plants – exploring possible stumbling blocks along the way. A spiral interface sensor is proposed, as a spiral monitoring tool, and demonstrated with experimental work during which spiral modelling was also performed. Two image processing algorithms, CVI (edge detection based) and CVII (logistic regression based), were prepared to detect spiral interfaces. Experimental modelling of a Multotec SC21 spiral concentrator was performed by formulating and comparing response surface methodology (RSM) with a proposed extended Holland-Batt model. Two sensor placement strategies, SPI (state estimation based) and SPII (metallurgical performance based), were prepared to help determine important monitoring positions based on steady state spiral plant simulations. Optimal monitoring locations minimize sensor network financial cost while maximizing some proxy for monitoring benefit. Spiral concentrator and spiral plant modelling (including optimal sensor placement) is based on the case study of the Glencore Rowland spiral plant which treats slurry containing UG2 ores to upgrade chromite content.

Algorithm CVII proved to be the superior interface detection approach and can identify chromite concentrate interfaces in slurry representative of industrial conditions. Spiral splitter control should be further investigated; however, spiral unit monitoring will still provide operators with useful information on process changes (should control be infeasible or unprofitable). RSM models were more precise than the extended Holland-Batt model; however, the latter showed superior extrapolation

Stellenbosch University https://scholar.sun.ac.za

and plant simulation ability (emphasizing the need that modelling should be done with plant simulation in mind). SPI and SPII were used to rank different sensor configurations. Optimal sensor configurations determined by SPI were ultimately controlled by sensor financial cost. SPII is accepted as a superior sensor placement algorithm since sensor cost and metallurgical performance benefit were weighted in a way similar to a return on investment problem (suggesting a new perspective for this inherent multi-objective problem).

Stellenbosch University https://scholar.sun.ac.za

OPSOMMING

Spiraalkonsentreerders is robuuste gravitasie skeidingsinstrumente wat dikwels in ‘n kompakte wyse geimplementeer word op aanlegte. Sensors word huidiglik net gebruik om hoof voer en produk strome se vloeitempos en digthede te benader. Monitering van spiraal eenhede word met die hand deur operateurs gedoen, en beheer word hoofsaaklik bewerkstellig deur operateurs wat met die hand die verdelerstellings van die spirale regoor die aanleg moet verander. In groot spiraalaanlegte, wat duisende individuele spiraalkonsentreerders bevat, kan die verstelling van verdelers vermoeiend raak of soms afgeskeep word. Geoutomatiseerde monitering en beheer van spirale kan spiraalaanlegoperateurs help om optimale werkverrigting van die spiraalaanleg te bereik.

Spiraal mineraalflodder-tussenvlak deteksie is al in die verlede aangewys as ‘n moontlike spiraal moniterings strategie. Dit is as gevolg van dat konsentrasiebande vorm tydens die skeiding van swaar minerale (deur middel van spirale). Partikels skei van mekaar as gevolg van verskille in digtheid en groottes en neig om drie visueel onderskeidelike konsentrasiebande te vorm. Operateurs wil ideaal hierdie strome op deel in konsentraat, tussenskot- en uitskotstrome. Die konsentraatband is baiemaal visueel donkerder as die strome wat gangerts bevat en die mineraaltussenvlak dien dikwels as ’n nuttige aanwysing om skeidingstoestelle te plaas.

Die teks stel ‘n raamwerk voor wat sensor ontwikkelling en die plasing van sensors, binne ‘n spiraalaanleg, insluit (struikel blokke met betrekking tot die projek se verskillende stappe word ook geidentifiseer). Die werking van spiraal tussenvlak sensors is gedemonstreer tydens eksperimentele werk wat ook gedien het vir spiraal modellering. Twee beeldverwerking algoritmes, genoem CVI (rand-deteksie gebaseer) en CVII (logistiese regressie gebaseer), is ontwikkel om spiraal tussenvlak deteksie te verrig. Eksperimentele modellering van ’n Multotec SC21 spiraalkonsentreerder is voltooi deur formulering en vergelyking van respons oppervlak (RSM) en voorgestelde uitgebreide Holland-Batt modelle. Ontwikkeling van twee sensor plasings algoritmes, SPI (toestand beraming gebaseer) en SPII (metallurgiese werkverrigting gebaseer), is ook voltooi sodat optimale plasing punte, gebaseer op sensor koste en metings of produksie werkverrigting benaderings, bepaal kon word. Spiraalkonsentreerder en spiraalaanleg modellering (insluitend optimale sensor plasing) is gebaseer op die gevallestudie van die Glencore Rowland spiraalaanleg wat UG2-erts bevattende flodder behandel om chromiet inhoud op te gradeer.

Algoritme CVII het beter tussenvlak deteksie gedemonstreer op mineraalflodder verteenwoordigend van industriële kondisies. Spiraal konsetreeder beheer moet verder ondersoek word, maar monitering sal steeds aanleg operateurs help om proses veranderinge op te spoor (sou dit wees dat spiraal beheer nie moontlik of winsgewend is nie). RSM spiraal modelle was meer presies met die opleidingdatastel; die uitgebreide Holland-Batt model wys beter bevestiging en aanleg simulasie uitslae (dit beklemtoon dat spiraal modellering gedoen moet word in ‘n mate wat daaropvolgende spiraalaanleg simulasie in ag neem). SPI en SPII was suksesvol gebruik om sensor plasing ranglyste te vorm. Optimale sensor plasing wat deur SPI gevind is, was hoofsaaklik gedryf deur sensor uitgawes. SPII is aanvaar as die

Stellenbosch University https://scholar.sun.ac.za

gepaste sensor plasings algoritme omdat optimale plasings besluite gebaseer is op ‘n verbeterde doel funksie wat plekhouers vir inkomestes (verbeterde metallurgiese werkverrigting) en uitgawes (sensor koste) vergelyk.

Stellenbosch University https://scholar.sun.ac.za

Acknowledgements

This project was made possible by the financial and technical support of Glencore. Glencore provided experimental equipment, spiral concentrator plant data (with flowsheets) and overall background to plant operations. Technical aid was also received from Multotec – regarding spiral concentrator specifications and experimental procedures.

Stellenbosch University https://scholar.sun.ac.za

Table of Contents

Chapter 1: Introduction 1
1.1. Spiral concentrators in gravity separation 1
1.2. Current monitoring and control of spiral concentrators 1
1.3. Sensor network design for metallurgical plants 2
1.4. Project objectives 3
1.5. Approach 3
1.6. Project scope 5
1.7. Thesis structure 6
Chapter 2: Background 8
2.1. Spiral concentrators 8
2.1.1. Significance within gravity separation 8
2.1.2. The spiral unit 9
2.1.3. Slurry flow and mineral separation characteristics of spiral concentrators 11
2.1.4. Spiral plants 14
2.2. Case study: Glencore Rowland site 16
2.2.1. Plant overview 16
2.2.2. Plant characteristics, variables and measurement 19
2.2.3. Spiral properties 20
2.2.4. Interface tracking and sensor placement consequences 21
2.3. Instrumentation network design for process plants 21
Chapter 3: Critical literature review 24
3.1. Modelling of spiral concentrators 24
3.1.1. CFD & DEM models 24
3.1.2. Mechanistic (semi-empirical) modelling 25
3.1.3. Spiral modelling using response surface methodology 26
3.1.4. Holland-Batt spline 27
3.1.5. Other empirical models 30
3.2. Spiral experiments 31
3.2.1. Previous methodologies 31
3.2.2. Previous experimental designs for spiral tests 31
3.2.3. Significant feed variables from previous spiral response surface methodology experiments 32
3.2.4. Effects of feed variables in mineral sands beneficiation 34
3.3. Spiral interface sensors 34
3.4. Spiral plant simulation 35
3.5. State estimation and sensor placement in metallurgical plants 38

Stellenbosch University https://scholar.sun.ac.za

Chapter 4: Methodology 41
4.1. Overview 41
4.2. Interface detection 42
4.2.1. Problem outline 42
4.2.2. Algorithm CVI: Edge detection approach 45
4.2.3. Algorithm CVII: Logistic regression approach 45
4.3. Spiral modelling 46
4.3.1. Process stream inference and response surface methodology execution 46
4.3.2. Extended Holland-Batt spline model 49
4.4. Spiral plant simulation 52
4.5. Interface sensor placement 56
4.5.1. Overview 56
4.5.2. Algorithm SPI: State estimation based placement 57
4.5.3. Algorithm SPII: Metallurgical performance based placement 58
Chapter 5: Results and discussion 62
5.1. Overview: Core results 62
5.2. Interface detection for chromite separation 64
5.2.1. Algorithm CVI (GA based) 64
5.2.2. Algorithm CVII (Logistic regression based) 67
5.3. Response surface methodology spiral models 73
5.3.1. Development of final tailings & interface response models 73
5.3.2. Development of spiral concentrate response models 79
5.3.3. Response models confirmation 81
5.4. Extended Holland-Batt spline model 82
5.4.1. Chromite data set 82
5.4.2. Hematite separation data set 86
5.5. Spiral plant simulation results 88
5.5.1. Response surface methodology models implementation case 88
5.5.2. Extended Holland-Batt model case 91
5.5.3. Simulating metallurgical performance 92
5.6. Optimal sensor placement 93
5.6.1. State estimation based approach 94
5.6.2. Metallurgical performance improvements 97
Chapter 6: Conclusion and recommendations 101
6.1. Contributions and novelty 101
6.2. Interface detection 102
6.2.1. Conclusions 102

Stellenbosch University https://scholar.sun.ac.za

6.2.2. Recommendations and future work 103
6.3. Spiral modelling & plant simulation 103
6.3.1. Conclusions 103
6.3.2. Recommendations and future work 105
6.4. Optimal sensor placement 105
6.4.1. Conclusions 105
6.4.2. Recommendations and future work 106
6.5. Published and submitted articles 107
7. References 109
8. Nomenclature 117
8.1. Image processing, genetic algorithms & logistic regression 117
8.2. Spiral modelling, simulation and sensor placement 119
9. Appendix A: Background 123
9.1. Image processing methods 123
9.1.1. Digital images & camera projection models 123
9.1.2. Contrast manipulation 125
9.1.3. Spatial filtering 126
9.1.4. Segmentation 129
9.1.5. Morphological image processing 134
9.2. Experimental design 135
9.2.1. Design categories 135
9.2.2. Screening experiments 135
9.2.3. Response surface methodology 136
9.2.4. Confirmation experiments 138
9.3. Data Reconciliation 138
9.3.1. State observers and estimation 138
9.3.2. Data processing, reconciliation and rectification 140
9.4. Genetic algorithms 142
9.5. Logistic regression 146
10. Appendix B: Literature 149
10.1. Tracer tests 149
10.2. Spiral circuit configuration, measurement and sampling in laboratory tests 149
11. Appendix C: Methodology 151
11.1. Interface detection 151
11.1.1. Algorithm CVI 151
11.1.2. Parameter optimization for Algorithm CVI 152
11.1.3. Algorithm CVII parameter optimization 155

Stellenbosch University https://scholar.sun.ac.za

11.1.4. Hardware used to train algorithms 157
11.1.5. Interface measurement 157
11.1.6. Calibration 158
11.2. Spiral experimentation: Equipment, feed preparation and experimental design 160
11.3. Interface sensor placement 160
11.3.1. Nonlinear data reconciliation 165
11.3.2. Sensor placement monitoring performance 167
11.3.3. Sensor variances, cost and product value 169
11.3.4. Monte Carlo simulations 170
12. Appendix D: Results 172
12.1. Interface detection for ilmenite separation 172
12.1.1. Algorithm CVI (GA based) 172
12.1.2. Algorithm CVII (Logistic regression based) 182
12.2. Experimental results and spiral modelling 187
12.2.1. Analysis of experimental design levels 187
12.2.2. Response surface methodology for spiral models (based on tailings stream responses) 191
12.2.3. Extended Holland-Batt model prediction interval estimation 194
12.3. Optimal sensor placement 195
12.3.1. Effect of plant feed conditions on Algorithm SPI 195
12.3.2. Effect of plant feed conditions on Algorithm SPII 197
12.3.3. Concentrate flow rate variance for two spiral bank case 199
13. Appendix E 201
13.1. Rowland plant description 201
13.2. Rowland plant PFD 202
14. Appendix F 203
15. Appendix G 205
15.1. Experimental test run order 205
15.2. Detailed experimental procedure 206
16. Appendix H 208
17. Appendix I 209
17.1. Ilmenite interface detection results 209
17.1.1. Algorithm CVI (GA-based) 209
17.1.2. Algorithm CVII (logistic regression based) cross-validation 210
17.1.3. Algorithm CVII (logistic regression based) interface detection 213
17.2. Chromite interface detection results 214
17.2.1. Algorithm CVII (logistic regression based) interface detection 214
17.2.2. Algorithm CVII interface detection examples from experimental runs 216

Stellenbosch University https://scholar.sun.ac.za

17.3. Interface detection pseudocode 218
17.3.1. Algorithm CVI training (GA based) 218
17.3.2. Algorithm CVII training (logistic regression based) 219
18. Appendix J 221
18.1. Feed grade and solids density calibration curve 221
18.2. Measured and reconciled experimental design levels 223
18.3. Camera calibration errors 228
19. Appendix K 230
19.1. Concentrate grade soft sensor variance 230
19.2. Data reconciliation and sensor network implementation cost MATLAB code 231

Stellenbosch University https://scholar.sun.ac.za

List of figures

Figure 1.1: Spiral monitoring project stages 5
Figure 1.2: Thesis layout (green: main content; white: supplementary text; grey: additional flowsheets, process descriptions and results) 7
Figure 2.1: Helicoid for spiral concentrator 10
Figure 2.2: Ilmenite (1st frame) and chromite (2nd frame) ore separation examples (gulleys and splitters are visible) 10
Figure 2.3: Primary (blue arrow) and secondary (red arrow) flow lines in a spiral concentrator 12
Figure 2.4: Simple slurry profile in a spiral concentrator (adapted from Holland-Batt, 1995: 1382) .. 13
Figure 2.5: Simplified and partial chromite spiral circuit piping and instrumentation diagram (adapted from Holland-Batt, 1982: 55) 15
Figure 2.6: Rowland feed grade for June 2015 17
Figure 2.7: Rowland concentrate grade for June 2015 17
Figure 2.8: Rowland feed cumulative particle size distribution (for May 2015) - compared with a reference UG2 cumulative particle size distribution 18
Figure 2.9: Effects of slimes on mineral separation ranging from a trough with banking to a cleaned spiral (a, b, c represent various slurry states that can be observed on a spiral plant). 18
Figure 3.1: Simple spiral separation curve for MOI recovery in concentrate stream (based on the Holland-Batt model) 28
Figure 3.2: Proportionality of separation efficiency example (adapted from Fourie, 2007) 29
Figure 3.3: Recovery curve after feed grade adjustment 30
Figure 3.4: Spiral mass-recovery curve (data obtained from Sadeghi, 2015) 36
Figure 3.5: Simple spiral plant (adapted from Wills & Napier-Munn, 2005: 75) 37
Figure 4.1: Methodology diagram (white blocks represent methodology sections in this chapter) 41
Figure 4.2: Ilmenite sands and UG2 ore slurries separating on spiral troughs (left: ilmenite, right: chromite) 42
Figure 4.3: Desired detection results (left: middling interface, right: concentrate interface) 43
Figure 4.4: Interface detection summary 44
Figure 4.5: Simplified interface detection algorithm CVI 45
Figure 4.6: Interface extractions 46
Figure 4.7: Calculation of R' at W' (the query feed slurry recovery) 50
Figure 4.8: Primary circuit PFD (obtained from Figure 16.1) 54
Figure 4.9: Methodology workflow diagram 56
Figure 4.10: Example of a simple grade recovery curve with the black arrow showing direction of metallurgical optimization (adapted from Wills & Napier-Munn, 2005) 60
Figure 5.1: Overall true and false positive Algorithm CVII concentrate interface detections on training (left) and testing (right) images (chromite case, using 35-by-35 pixel kernel) 62

Stellenbosch University https://scholar.sun.ac.za

Figure 5.2: Simulated metallurgical performance contours, at different feed conditions, for WPL primary circuit concentrate stream (left: RSM model points on contours; right: extended Holland-Batt spline) 63
Figure 5.3: $C*$ solutions of Equation 4.18 with $\alpha = 24$ h (Algorithm SPII; $C3$ is recleaner, $C8$ is cleaner-recleaner, $C11$ is rougher-cleaner-recleaner and $C15$ includes all spiral banks) 64
Figure 5.4: Algorithm CVI (GA-based) training results for concentrate interface detection (chromite case, error bars represent variation by $1 \times \sigma$ based on n = 50, 100, 150, 200, 250 and 300 samples) . 65
Figure 5.5: Examples of chromite concentrate interface responses that Algorithm CVI (GA-based) generates 66
Figure 5.6: Algorithm CVI (GA-based) testing results for concentrate interface detection (chromite case, error bars represent variation by $1 \times \sigma$ based on n = 600 samples) 66
Figure 5.7: Algorithm CVII (logistic regression based) training precision, recall and F values for chromite concentrate detection (using different neighbourhood widths; error bars represent variation by $1 \times \sigma$ based on n = 50, 100, 150, 200, 250 and 300 samples) 68
Figure 5.8: Training times for different kernel sizes (chromite case, Algorithm CVII) 69
Figure 5.9: Algorithm CVII (logistic regression based) testing precision, recall and F values for chromite concentrate detection (using different neighbourhood widths; error bars represent variation by $1 \times \sigma$ based on n = 600 samples) 70
Figure 5.10: Algorithm CVII (logistic regression based) concentrate interface detection on training (left) and testing (right) images (chromite case, using 35-by-35 pixel kernel; error bars represent variation by $1 \times \sigma$ based on n = 50, 100, 150, 200, 250 and 300 samples for training and n = 600 samples for testing) 71
Figure 5.11: Gulley-concentrate interface detection on training (left) and testing (right) images (chromite case, using 35-by-35 pixel kernel; error bars represent variation by $1 \times \sigma$ based on n = 50, 100, 150, 200, 250 and 300 samples for training and n = 600 samples for testing) 72
Figure 5.12: Overall true and false positive Algorithm CVII gulley-concentrate interface detections on training (left) and testing (right) images (chromite case, using 35-by-35 pixel kernel) 72
Figure 5.13: Standardised residuals for final flow ratio (left), grade (middle) and recovery (right) models 75
Figure 5.14: Reconciled tailings stream values vs predicted values for final spiral flow ratio (left), grade (middle) and recovery (right) models 76
Figure 5.15: Predicted concentrate interface vs. measured interface values (left: Algorithm CVII's results, right: label image results) 78
Figure 5.16: Standardised interface model residuals (left: Algorithm CVII's results, right: label image results) 78
Figure 5.17: Standardised concentrate HM grade (left) and HM recovery (right) model residuals after parameter selection 79

Stellenbosch University https://scholar.sun.ac.za

Figure 5.18: Reconciled concentrate stream response values vs. predicted concentrate HM grade (left) and HM recovery (right) responses after parameter selection 79
Figure 5.19: Prediction results on the confirmation run (left: flow ratio, centre left: tailings HM grade, centre right: tailings HM recovery, right: concentrate interface; error bars represent 95% prediction interval) 82
Figure 5.20: Concentrate solids (left) and HM recovery (right) standardised residuals (Holland-Batt spline case) 83
Figure 5.21: Reconciled concentrate recovery values vs. predicted concentrate solids (left) and HM recovery (right). Holland-Batt spline model case 84
Figure 5.22: Concentrate HM recovery prediction comparison at the confirmation run for the extended Holland-Batt spline model (left) and RSM (right) (error bars represent 95% prediction interval) 86
Figure 5.23: Concentrate solids (left) and $Fe2O3$ recovery (right) standardised residuals (Holland-Batt spline model case) 87
Figure 5.24: Reconciled concentrate $Fe2O3$ recovery values vs. predicted values (left: plot for test 7; right: plot for test 10). Holland-Batt spline model case 87
Figure 5.25: Primary circuit PFD (obtained from Figure 4.8) 89
Figure 5.26: Process stream flow rate (left), solids fraction (middle) and grade (right) variables (using RSM models to simulate spirals) 90
Figure 5.27: Process stream flow rate (left), solids fraction (middle) and grade (right) variables (using Holland-Batt spline mode to simulate spirals) 92
Figure 5.28: Simulated metallurgical performance, at different feed conditions, for WPL primary circuit concentrate stream (left: RSM models; right: extended Holland-Batt spline; obtained from Figure 5.2) 93
Figure 5.29: Sensor network implementation cost vs. the square root of JL in order of reducing redundancy (left: plot for the omission of 1 – 6 sensors; right: omission of 7 – 12 sensors; Algorithm SPI) 94
Figure 5.30: Plant feed HM grade for optimal sensor removal (1st sensor omission case; Algorithm SPI) 96
Figure 5.31: Improvement in JL (relative to starting conditions of each optimization run) vs. sensor configuration (see Table 7 for names) cost (Algorithm SPII) 97
Figure 5.32: Improvement in revenue produced vs. sensor configuration (see Table 7 for names) cost (Algorithm SPII) 98
Figure 5.33: Sensor configuration (see Table 4.3 for names) solutions vs. feed HM flow rates (Algorithm SPII; $\alpha = 24\ h$) 99
Figure 6.1: Summary of project steps and contribution(s) (green: research outputs; white: articles) 101
Figure 9.1: Example of an intensity matrix with the 8-bit image it represents 123
Figure 9.2: Relation between world, image and camera coordinates (Adapted from Salvi, Armangué and Batlle, 2002) 125

Stellenbosch University https://scholar.sun.ac.za

Figure 9.3: Histogram equalization example (red bars: before equalization; blue bars: after equalization) 126
Figure 9.4: Gaussian image smoothing. Filtering is performed first in the horizontal direction and then followed by filtering in the vertical direction ($\sigma G = 4$) 128
Figure 9.5: Comparison of smoothing filters (kernel sizes used are 32-by-32 pixels) 128
Figure 9.6: Thresholding at I(x,y) < 100 and I(x,y) > 100 130
Figure 9.7: Intensity image (left), its smoothed gradient (middle, exaggerated) and gradient (or edge) direction (right) maps 132
Figure 9.8: Edge thinning (left) and hysteresis thresholding (middle and right) 132
Figure 9.9: 8 (right) and 4 (left) connected components 134
Figure 9.10: State estimation example 141
Figure 9.11: Diagram of general GA implementation 145
Figure 9.12: Example of logistic classification 148
Figure 11.1: Interface detection Algorithm CVI with parameters shown 151
Figure 11.2: Orientation of a connected component 152
Figure 11.3: Training images (left) with labels (right) 155
Figure 11.4: Feature extraction, from slurry images, for pixel classification (3×3 kernel case) 156
Figure 11.5: Label images for Algorithm CVII 156
Figure 11.6: Tracking of interface pixels in binary interface map (red line extends from gulley; blue line extends from spiral trough periphery) 158
Figure 11.7: Detected checkerboard pattern corners (red circles) and re-projected corners (yellow crosses) 159
Figure 11.8: Experimental equipment diagram 161
Figure 11.9: Chromite ore quartering 162
Figure 11.10: Examples of slurry images that were captured (left: Milesight camera, right: GoPro camera) 164
Figure 11.11: Examples of calibration images (left: Milesight camera, right: GoPro camera) 164
Figure 11.12: 30 sampled feed conditions for Plant I (left: feed flow rate vs. feed solids content; right: feed flow rate vs. feed HM grade) 171
Figure 12.1: Performance function results during training of Algorithm CVI (GA based) on ilmenite image sets of different sizes (middling case; error bars represent variation by $1 \times \sigma$ based on n = 50, 100, 150, 200 and 300 samples) 173
Figure 12.2: Training on image sets of different sizes (ilmenite concentrate case; error bars represent variation by $1 \times \sigma$ based on n = 50, 100, 150, 200 and 300 samples) 174
Figure 12.3: Resulting edge detections for ilmenite concentrate interface detection (error bars represent variation by $1 \times \sigma$ based on n = 50, 100, 150, 200 and 300 samples) 174
Figure 12.4: Variations in trained parameters for the GA-based Algorithm CVI (ilmenite, middling case) 176

Stellenbosch University https://scholar.sun.ac.za

Figure 12.5: Variations in trained parameters for the GA-based Algorithm CVI (ilmenite, concentrate case) 177
Figure 12.6: Performance function results during testing of Algorithm CVI (GA-based) with optimal parameter sets (ilmenite, middling case; error bars represent variation by $1 \times \sigma$ based on n = 500 samples) 178
Figure 12.7: Performance function results during testing of Algorithm CVI (GA-based) with optimal parameter sets (ilmenite, concentrate case; error bars represent variation by $1 \times \sigma$ based on n = 500 samples) 179
Figure 12.8: Sensitive parameters for ilmenite middling interface detection (error bars represent variation by $1 \times \sigma$ based on n = 500 samples) 180
Figure 12.9: Change in ilmenite middling interface detection during sensitivity analysis 180
Figure 12.10: Sensitive parameters for ilmenite concentrate interface detection (error bars represent variation by $1 \times \sigma$ based on n = 500 samples) 181
Figure 12.11: Change in ilmenite concentrate interface detection during sensitivity analysis 182
Figure 12.12: Precision, recall and F-statistc for logistic classifier training, ilmenite middling case (error bars represent variation by $1 \times \sigma$ based on n = 50, 100, 150, 200 and 300 samples) 183
Figure 12.13: Left: optimal parameters from logistic regression for each training set, right: averaged optimal parameters (ilmenite case, error bars represent variation by $1 \times \sigma$ based on n = 5 replicates) 184
Figure 12.14: Convolution kernels for red, green and blue channels (obtained from mean parameter values plotted in Figure 12.13) 184
Figure 12.15: Logistic regression training times for ilmenite slurry detection case 185
Figure 12.16: Precision, recall and F-statistc for logistic classifier testing (ilmenite case, error bars represent variation by $1 \times \sigma$ based on n = 50, 100, 150, 200 and 300 samples) 185
Figure 12.17: Ilmenite middling interface detection results on training (left) and testing (right) sets (Algorithm CVII, error bars represent variation by $1 \times \sigma$ based on n = 50, 100, 150, 200 and 300 samples for training and n = 500 samples for testing) 186
Figure 12.18: Ilmenite concentrate interface detection results on training (left) and testing (right) sets (Algorithm CVII, error bars represent variation by $1 \times \sigma$ based on n = 50, 100, 150, 200 and 300 samples for training and n = 500 samples for testing) 186
Figure 12.19: Ilmenite slurry (middle), middling interface and concentrate interface (right) detection using Algorithm CVII ($\alpha = 0.99$) 187
Figure 12.20: Scaled deviation of measured and reconciled design levels (left: feed HM grade, middle: feed SG, right: feed volumetric flow rate) 188
Figure 12.21: Measured experimental levels and design levels (first two principal components from 4; 58.5 % variance captured by PC 1, 16.7 % variance captured by PC 2) 189
Figure 12.22: Reconciled experimental levels and design levels (first two principal components from 4; 62.8 % variance captured by PC 1, 16.6 % variance captured by PC 2) 190

Stellenbosch University https://scholar.sun.ac.za

Figure 12.23: Measured spiral tailings responses (left: flow ratio, middle: tailings HM grade, right: tailings HM recovery; error bars represent $1 \times \sigma$ based on n = 3 replicates) 190
Figure 12.24: Reconciled spiral tailings responses (left: flow ratio, middle: tailings HM grade, right: tailings HM recovery; error bars represent $1 \times \sigma$ based on n = 3 replicates) 191
Figure 12.25: Standardised residuals for flow ratio (left), tailings HM grade (middle) and tailings HM recovery (right) full quadratic models 192
Figure 12.26: Standardised residuals for flow ratio (left), tailings HM grade (middle) and tailings HM recovery (right) models after parameter selection 194
Figure 12.27: Reconciled tailings stream response values vs predicted values (left: flow ratio, middle: tailings HM grade, right: tailings HM recovery) 194
Figure 12.28: Feed flow rate vs. the square root of JL (left: plot for the omission of 1 – 6 sensors; right: omission of 7 – 12 sensors; Algorithm SPI) 195
Figure 12.29: Feed solids fraction (top) and HM grade (bottom) vs. the square root of JL (left: plot for the omission of 1 – 6 sensors; right: omission of 7 – 12 sensors; Algorithm SPI) 196
Figure 12.30: Reconciled revenue vs. the square root of JL (left: plot for the omission of 1 – 6 sensors; right: omission of 7 – 12 sensors; Algorithm SPI) 197
Figure 12.31: Improvement in revenue produced vs. feed flow rate at different sensor configurations (see Table 4.3 for configuration names; Algorithm SPII) 197
Figure 12.32: Improvement in revenue produced vs. feed solids fraction at different sensor configurations (see Table 4.3 for configuration names; Algorithm SPII) 198
Figure 12.33: Improvement in revenue produced vs. feed HM grade at different sensor configurations (see Table 4.3 for configuration names; Algorithm SPII) 198
Figure 16.1: Simplified PFD of primary and secondary spiral circuits 208
Figure 17.1: Cross-validation results for logistic regression training (ilmenite case with training 50 images; regularization parameter – λ – values are given on the y-axis) 210
Figure 17.2: Cross-validation results for logistic regression training (ilmenite case with training 100 images; regularization parameter – λ – values are given on the y-axis) 211
Figure 17.3: Cross-validation results for logistic regression training (ilmenite case with training 150 images; regularization parameter – λ – values are given on the y-axis) 211
Figure 17.4: Cross-validation results for logistic regression training (ilmenite case with training 200 images; regularization parameter – λ – values are given on the y-axis) 212
Figure 17.5: Cross-validation results for logistic regression training (ilmenite case with training 300 images; regularization parameter – λ – values are given on the y-axis) 212
Figure 17.6: Chromite slurry interface detection, using Algorithm CVII, in example images from experimental runs 1 to 12 (using 35-by-35 filter trained on 300 images; $h > 0.3$; interfaces are dilated by 5 pixels) 216

Stellenbosch University https://scholar.sun.ac.za

Figure 17.7: Chromite slurry interface detection, using Algorithm CVII, in example images from experimental runs 13 to 24 (using 35-by-35 filter trained on 300 images; $h > 0.3$; interfaces are dilated by 5 pixels) 217
Figure 17.8: Chromite slurry interface detection, using Algorithm CVII, in example images from experimental runs 25 to 27 (using 35-by-35 filter trained on 300 images; $h > 0.3$; interfaces are dilated by 5 pixels) 218
Figure 17.9: Chromite slurry interface detection, using Algorithm CVII, in an example image from experimental run 28 (using 35-by-35 filter trained on 300 images; $h > 0.3$; interfaces are dilated by 5 pixels) 218
Figure 18.1: XRF (left) and density analysis (right) of WPL ore samples after quartering 221
Figure 18.2: Image coordinate reprojection errors for each experimental run (error bars represent $1 \times \sigma$, based on n = 54 replicates) 229
Figure 18.3: World coordinate reprojection errors for each experimental run (error bars represent $1 \times \sigma$, based on n = 54 replicates) 229

Stellenbosch University https://scholar.sun.ac.za

List of tables

Table 2.1: Gravity concentration vs. flotation (table entries obtained from Burt, 1984: 4 & Mojela, 2015) 9
Table 2.2: General operating ranges for spiral concentrators 11
Table 2.3: SC 21 and HX 5 design (Mojela, 2015) 20
Table 2.4: SC 21 and HX 5 capacities (Mojela, 2015) 21
Table 3.1: Experimental parameters and settings in previous spiral experiments 32
Table 3.2: T-test p-values and significant variables (for full quadratic models) from previous RSM spiral experiments (interaction terms excluded) 33
Table 4.1: Feed stream conditions 55
Table 4.2: Plant I's process streams considered for sensor placement (as used by Algorithm SPI) 57
Table 4.3: Sensor placement configurations 59
Table 5.1: F-test and correlation coefficient results for final spiral response models 74
Table 5.2: Significant parameters for the final flow ratio, tailings grade and tailings recovery models ($x1$ – coded feed HM grade, $x2$ – coded feed SG, $x3$ – coded feed flow rate and $x4$ – coded splitter setting) 74
Table 5.3: $\mathcal{R}2$ and F-test results of the interface models after parameter selection 77
Table 5.4: Significant variables of the interface models after parameter selection ($x1$ – coded feed HM grade, $x2$ – coded feed SG, $x3$ – coded feed flow rate and $x4$ – coded splitter setting) 77
Table 5.5: $\mathcal{R}2$ and F-test results for concentrate response models after parameter selection 80
Table 5.6: Significant variables for concentrate stream response models ($x1$ – coded feed HM grade, $x2$ – coded feed SG, $x3$ – coded feed flow rate and $x4$ – coded splitter setting) 81
Table 5.7: Experimental levels for the confirmation run (run 29) 81
Table 5.8: Parameter solutions for the concentrate solids and HM recovery (Holland-Batt spline model case) 84
Table 5.9: $\mathcal{R}2$ and Akaike information criterion results concentrate solids and HM recovery models (Holland-batt spline model case) 85
Table 5.10: Confirmation point (run 29) results for concentrate stream recoveries 85
Table 5.11: Correlation coefficient and parameter results for the concentrate solids and $Fe2O3$ recovery (Holland-Batt spline model case) 88
Table 5.12: Process stream(s) results for the first feed condition set (using RSM models to simulate spirals) 90
Table 5.13: Process stream(s) results for the second feed condition set (using RSM models to simulate spirals) 90
Table 5.14: Process stream(s) results for the third feed condition set (using RSM models to simulate spirals) 91
Table 5.15: Total mass flow rate error and MOI recovery in overall concentrate stream (using RSM models to simulate spirals) 91

Stellenbosch University https://scholar.sun.ac.za

Table 5.16: Total mass flow rate error and MOI recovery in overall concentrate stream (using Holland-Batt spline model to simulate spirals) 92
Table 5.17: Locations of optimally removed sensors (by Algorithm SPI) in order of reducing redundancy (1 – 7 sensor omission cases) 95
Table 9.1: Simple 2^2screening experiment 135
Table 9.2: Three factor response surface designs 137
Table 9.3: Comparison of different 3 factor RSMs 137
Table 9.4: CCD and Box-Behnken test run amount vs. increment in number of factors (Adapted from Trutna et al., 2013: 5.3.3.6.3) 138
Table 11.1: Algorithm CVI parameters 152
Table 11.2: Boundary conditions 154
Table 11.3: MATLAB functions used for interface detection Algorithm CVI 155
Table 11.4: Design levels (details on level fixing during experimentation is provided in Appendix G) 163
Table 11.5: Primary circuit connectivity matrix 166
Table 11.6: Initial process stream variable variances 169
Table 11.7: Sensor price estimates 170
Table 11.8: Chromite market price estimates per ton of chromium/chromite 170
Table 12.1: GA training time (ilmenite, middlings case) 173
Table 12.2: GA training time (ilmenite, concentrate case) 175
Table 12.3: Number of middling interface detections (ilmenite case, GA-based Algorithm CVI testing) 179
Table 12.4: Estimated experimental design levels for model development (runs 2-28) 191
Table 12.5: F-test and correlation coefficient results for quadratic tailings models based on reconciled values 192
Table 12.6: F-test and correlation coefficient results after parameter selection 193
Table 12.7: Significant parameters for the flow ratio, tailings HM grade and tailings HM recovery models after parameter selection ($x1$ – coded feed HM grade, $x2$ – coded feed SG, $x3$ – coded feed flow rate and $x4$ – coded splitter setting) 193
Figure 13.1: Simplified PFD (stream and equipment tags omitted) 202
Table 15.1: Original 4 factor Box-Behnken design and blocked 4 factor Box-Behnken design 205
Table 15.2: Blocked 4 factor Box-Behnken design with within block randomization 206
Table 17.1: σ and mean results for $J1$ and $J2$ results for the ilmenite middling detection training case (GA-based Algorithm CVI) 209
Table 17.2: σ and mean results for $J1$ and $J2$ results for the ilmenite middling detection testing case (GA-based Algorithm CVI) 209
Table 17.3: σ and mean results for $J1$ and $J2$ results for the ilmenite concentrate detection training case (GA-based Algorithm CVI) 209

Stellenbosch University https://scholar.sun.ac.za

Table 17.4: σ and mean results for $J1$ and $J2$ results for the ilmenite concentrate detection testing case (GA-based Algorithm CVI) 210
Table 17.5: σ and mean results for $J1$ and $J2$ results for the ilmenite middling detection training case (logistic regression based Algorithm CVII) 213
Table 17.6: σ and mean results for $J1$ and $J2$ results for the ilmenite middling detection testing case (logistic regression based Algorithm CVII) 213
Table 17.7: σ and mean results for $J1$ and $J2$ results for the ilmenite concentrate detection training case (logistic regression based Algorithm CVII) 213
Table 17.8: σ and mean results for $J1$ and $J2$ results for the ilmenite concentrate detection testing case (logistic regression based Algorithm CVII) 214
Table 17.9: σ and mean results for $J1$ and $J2$ results for the chromite concentrate detection training case (logistic regression based Algorithm CVII using 35-by-35 filter) 214
Table 17.10: σ and mean results for $J1$ and $J2$ results for the chromite concentrate detection testing case (logistic regression based Algorithm CVII using 35-by-35 filter) 214
Table 17.11: σ and mean results for $J1$ and $J2$ results for the chromite gulley-concentrate detection training case (logistic regression based Algorithm CVII using 35-by-35 filter) 215
Table 17.12: σ and mean results for $J1$ and $J2$ results for the chromite gulley-concentrate detection testing case (logistic regression based Algorithm CVII using 35-by-35 filter) 215
Table 18.1: Measured and reconciled experimental design level means 223
Table 18.2: Measured and reconciled experimental design level variances 224
Table 18.3: Deviations of centered measured and centered reconciled feed conditions from the experimental design levels (centering performed with originally planned experimental levels) 225
Table 18.4: Measured and reconciled tailings response means 226
Table 18.5: Measured and reconciled tailings response variances 227
Table 18.6: Mean interface measurements per experimental run based on the results of Algorithm CVII and manually labelled images 228
Table 19.1: Parameter and t-test results for Equation 19.1 230

Stellenbosch University https://scholar.sun.ac.za

Chapter 1: Introduction

1.1. Spiral concentrators in gravity separation

Spiral concentrators have become common mineral separators since the creation of the Humphrey spiral in the 1940s. Originally used to concentrate chromite bearing sands it is now widely used to concentrate heavy mineral (HM) sands and fine coal. Spiral concentrators receive slurry at a feed box (mounted at the top) and product streams are divided using splitters. As minerals flow down the spiral different particles stratify due to combined factors such as centrifugal force, different settling regimes and interstitial trickling. Smaller, denser, particles tend to move to the centre of the spiral while less dense minerals move to the spiral trough periphery (Wills & Napier-Munn, 2005: 236).

The separation action of spirals generally creates three, visually discernible, concentration bands that are divided into streams by a primary splitter box. These streams are simply referred to as the concentrate, middling and tailings streams (in some cases multiple middling/tailings streams are considered). In the case of heavy mineral separation, the concentrate band is often visually darker than the streams containing gangue. This often serve as a useful cue for setting splitters (Vermaak, Visser, Bosman & Krebs, 2008: 148).

Spiral concentrators can be compactly installed in plants by fixing two to three spirals on single support columns. The compact implementation of spirals allow the scale-up of plant capacity to the extent where thousands of spirals are used. Thousands of tons per hour of feed can be treated by large spiral plants but this, however, incurs a significant problem. Spiral plant performance can be substantially influenced by variation in feed conditions such as flow rate, density, viscosity, grade and particle size distribution (PSD) generally resulting in recovery losses (Wills & Napier-Munn, 2005: 238; Steinmuller, 2005). For large flow rates this implies that thousands of tons per hour of material can report to tailings streams. Control of the factors influencing spiral plant performance is still a significant challenge with few options currently available to help alleviate operation problems (Vermaak et al., 2008: 148).

1.2. Current monitoring and control of spiral concentrators

Monitoring of spiral concentrators, within spiral plants, is limited to inspection of the plant by operators (Bredenhan, 2015). Control of plant concentrate grade and recovery losses, due to fluctuating feed, is achieved by operators adjusting splitters. Splitters are still changed by hand and in large plants, with thousands of spirals, this can become tedious or can even be neglected resulting in further performance losses (Dallaire, Laplante & Elbrond, 1978: 124; Steinmuller, 2005; Vermaak et al., 2008: 148).

An automated method is required to help alleviate the effect that fluctuating spiral plant feeds and inadequate splitters settings can have on performance. Since colour differences are visible between the different slurry bands that form on a spiral trough (during heavy mineral separation) it is possible to track mineral band interfaces to infer splitter settings or changes in feed conditions. A monitoring

Stellenbosch University https://scholar.sun.ac.za

system, accompanied by appropriate spiral models, is an ideal method by which operators can be alerted to short term variations in spiral operation. The tracking tool must be robust since the presence of slurry slimes can greatly complicate the visual inference problem (Vermaak et al., 2008: 153).

Introducing interface sensors to industrial applications will incur additional instrumentation installation and maintenance cost to current plant upkeep. Before the final benefit of interface sensors can be concluded it will be necessary to determine optimal sensor placement and its economic benefit. Sensor cost must be weighed against its impact on the revenue a plant produces. An optimal sensor implementation will minimise upgrade cost and improve plant state estimation (via data reconciliation of process variables) and/or plant production performance.

1.3. Sensor network design for metallurgical plants

Optimal sensor placement approaches for process plants typically rely on state estimation performance – possibly weighed against sensor cost (Bagajewicz, 2002: 3). Steady state data reconciliation, which is a state estimation approach for process plants, is used to find more likely process states given the process flowsheet, measurements and noise models (Romagnoli, & Sánchez, 2000: 77). Therefore, data reconciliation is useful, for sensor network performance formulation, when mass flow rate, density and concentration sensors (and their variances) are readily available. However, online concentration, density and flow rate sensors are expensive for mineral processing plants and – if used – will typically only be present at critical process streams (plant feed or concentrate).

Operators on mineral processing plants, like spiral plants, may not be interested in flow rate and density gauge placements or improvements in monitoring performance (especially when flowsheets are complex and sensor installation cost is high). In the case of spiral plants, operators will be more interested in having spiral splitters automated or at least know which splitters are the most important to control (Bredenhan, 2015). This can help alleviate the burden and uncertainty coupled with manual splitter adjustments. Thus, it is more relevant to find sensor placement algorithms that do not focus (or at least solely focus) on improving variable estimation but to determine how monitoring can potentially lead to better plant performance. This may also lead to more efficient use of plant labour.

Literature on optimal instrumentation placement in metallurgical plants is sparse and, sensor placement studies in general, do not consider many different plant steady states (which allows investigation of sensor placement robustness to feed condition changes). The intrinsic multi-objective problem, weighing monitoring performance with sensor cost, requires further investigation so that appropriate objective weighting strategies can be found. Optimal sensor placement, for metallurgical plants, will benefit from tying monitoring performance with plant production rate or metallurgical performance.

Stellenbosch University https://scholar.sun.ac.za

1.4. Project objectives

This project aims to find robust placements of spiral interface sensors (the proposed spiral monitoring tool) within a spiral plant. Sensor placement algorithms must be developed along with appropriate spiral models – following successful monitoring of spiral mineral interfaces – and then applied to a spiral plant flowsheet. Sensitivity analysis of optimal sensor placements, to spiral plant feed conditions, can be used to investigate sensor location robustness. However, before interface sensor placement can be considered it is first necessary to determine whether mineral interfaces can be successfully tracked in slurries representative of industrial conditions.

After literature study completion, this project aims to demonstrate interface monitoring algorithms capable of isolating different interfaces that may form in spiral slurries and measure the different concentration bands' widths. An interface sensor provides a new spiral concentrator response: concentrate interface width; which is influenced by feed conditions. Concentrate interface widths can be experimentally modelled similar to spiral product stream recoveries and grades to obtain models that can be used for spiral plant simulation and optimal interface sensor placement.

Installing interface monitoring equipment at many spirals in a spiral bank can easily become expensive implying that a methodology is required to determine optimal placement of interface sensors within a spiral plant. When spiral models are available the spiral circuit in question can be simulated and sensor placement can be determined either by investigating interface (or throughput and product quality) sensitivities or by finding sensor networks that minimize installation cost and maximizes plant monitoring or production performance.

The following objectives can be identified from the project aims:

1. Produce a critical literature study of spiral operation, spiral application in industry, machine vision and optimal sensor placement methodologies.
2. Demonstrate interface detection on slurries representative of industrial spiral conditions.
3. Prepare empirical models and identify the methods best suited for plant simulation.
4. Develop a metallurgical performance based sensor placement algorithm and compare with existing state estimation approaches.
5. Determine sensor placement robustness to changing feed conditions via Monte Carlo spiral plant simulations.

1.5. Approach

Algorithm development and experimentation are tantamount to achieving this study's objectives. The first stage of algorithm development is geared toward producing software that can detect mineral interfaces within spiral troughs as feed conditions vary. Firstly, acquisition of images showing slurry minerals separating on a spiral trough is required and must be captured during experimentation. Classical image processing functions or statistical classifiers can then be used to isolate any existing

Stellenbosch University https://scholar.sun.ac.za

mineral interfaces in the images and track them. Training and testing images, for interface detection, was obtained on mineral separation using industrial slurries (obtained via Glencore). Manually labelled, or ground truth, images, required to evaluate and validate detector performance, accompanies the image training/testing set. Finally, calibration is required to convert pixel measurements to metric based measurements.

Once slurry interfaces can be measured, modelling of spiral concentrator responses can be performed by varying feed conditions. Statistical spiral models (linear and nonlinear) can be searched via ordinary least squares followed by statistical parameter selection to determine all significant variables. Mass balances can be combined with spiral models to simulate steady-state spiral circuits for fixed feed conditions. Resulting spiral simulations give the initial values required for final sensor placement strategy.

Lastly, optimal sensor placement based on monitoring performance (obtained from state estimation) provides means to determine interface sensor placement if these sensors can be approximated as grade sensors. An alternative can also be tested to determine if sensor placement can be tied to potential improvements in metallurgical performance. Sensor placement robustness to different steady state conditions can also be investigated via Monte Carlo simulations. Comparison of both sensor placement solutions should give an indication of which solutions can lead to improved monitoring performance or metallurgical performance.

Figure 1.1 shows the different stages of this study starting with experimental equipment preparation and interface detector formulation. Development of interface sensor software extends into the experimental stage since slurry images are acquired during experimentation. Spiral modelling and model selection is performed after the conclusion of laboratory work. Final model selection is performed after spiral plant simulation to determine which models are better suited to circuit modelling. Optimal sensor placement can be conducted after adequate spiral models are identified and plant simulations are completed.

Stellenbosch University https://scholar.sun.ac.za

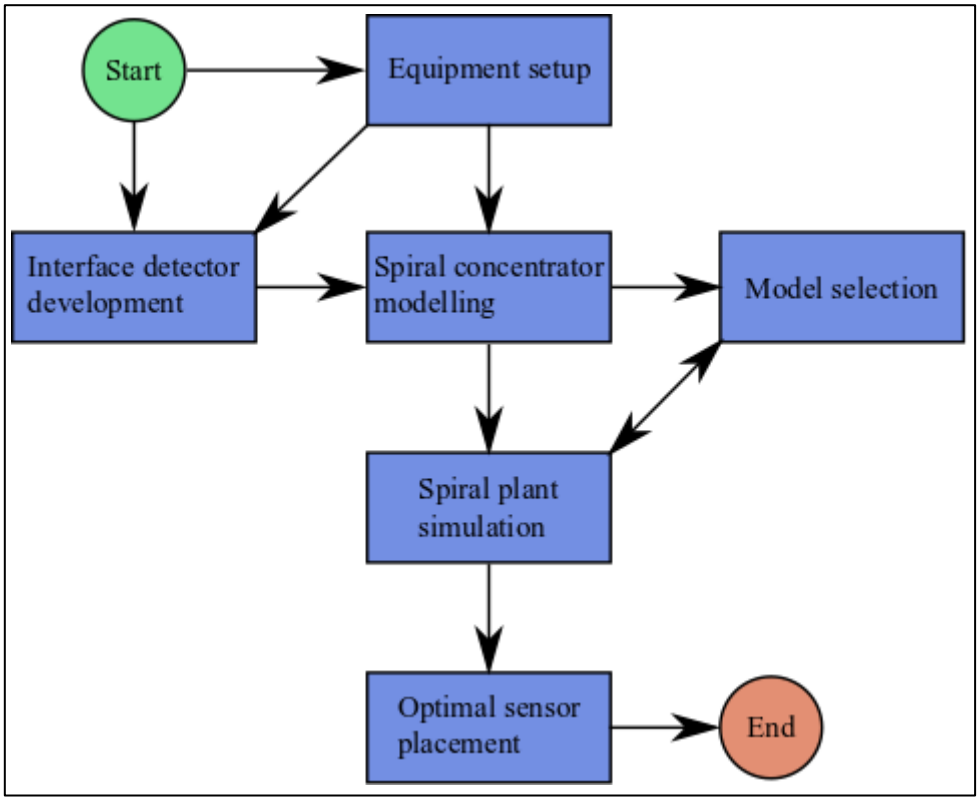

Figure 1.1: Spiral monitoring project stages

1.6. Project scope

This study and its objectives are focused on the case of HM concentration via spiral concentrators. Mineral interface detection is performed on images captured from ilmenite and chromite concentration experiments executed at the Department of Process Engineering at Stellenbosch University. Different mineral separation case studies provide means to determine how robust an interface tracking approach is. Two interface detection methodologies (the first uses conventional image processing functions and the second uses statistical learning) are prepared and applied to the different images to confirm a suitable method for future interface detection problems or sensor development. Most importantly interface detection for industrial slurries must be confirmed.

The remainder of the project is devoted to the case study of a spiral plant processing flotation tailings of treated Upper Group 2 (UG2) ores bearing Platinum Group Metals (PGM) rich chromite. The plant in question is the Rowland site spiral circuit of Glencore. Ore (that will serve as feed) and equipment for this study's experimental work were obtained from the Rowland site with the goal of simulating a section of the plant. Experiments will be devoted to finding how feed grade, density, flow rate and splitter settings of the spirals (the same spiral equipment model as used in the Rowland plant) affect spiral concentrator performance and concentrate interface measurements. Linear regression models and a new extended mass-yield model is prepared and compared to determine the best spiral model. The new mass-yield model will also be fitted to hematite separation data to partially validate parameter results.

Stellenbosch University https://scholar.sun.ac.za

Spiral models resulting from experimental work will be used to prepare a mass balance of a section of the Rowland spiral plant which will form a basis for interface sensor placement. Two methods, one using data reconciliation and the other optimizing metallurgical performance, are iterated over a number of Monte Carlo plant simulations to determine and compare optimal sensor solutions. At this stage Monte Carlo simulations only consider changing feed conditions. Additional information required to complete this analysis include sensor costs and variances – which is partially inferred from experimental work done at Stellenbosch University. Plant revenue is determining from chromite market prices. Variation of product price versus time and product grade is not considered.

1.7. Thesis structure

The main content of this document contains 6 chapters (illustrated in Figure 1.2) ranging from the necessary spiral background to literature, methodology, project results and overall conclusions. Chapter 2 provides general background of spiral concentrators (as a gravity separation unit), the spiral plant case study and instrumentation placement for process plants. Critical literature, required to accomplish Objectives 2, 3 & 5, is summarised in Chapter 3. Objective 1 is addressed by both Chapters 2 & 3. Chapter 4 contains the methodology and materials required to produce the results in Chapter 5. Interface detection results for the chromite ore case is presented along with spiral models for chromite concentration. The final results include spiral circuit steady-state mass balances obtained using the spiral models and optimal sensor placement solutions obtained by monitoring and metallurgical performance maximization.

Wide fields of knowledge are drawn upon to complete this project, including gravity separation, computer vision, statistical learning, experimental modelling, mathematical optimization and state estimation. Some of the literature, methodology and non-critical results are organized into Appendices A – D (see Figure 1.2) to ensure coherency and conciseness. Supplementary background information and literature (not directly relevant to spiral concentrators) is provided in Appendix A (which is an appendix to Chapter 2). The material in Appendix A cover image processing methods, different experimental designs, data reconciliation, genetic algorithms and logistic regression. Appendix B, the appendix to Chapter 3, contains a short literature review of previous spiral experimental methodology – as a supplement to Chapter 3's content. Details of image processing and statistical learning models and their optimization is contained in Appendix C along with the experimental methodology and additional information on optimal sensor placement (specifically the Monte Carlo simulations mentioned in Objective 4). Mineral sands interface detection, preliminary spiral model fitting and sensor placement sensitivity analysis is provided in Appendix D.

Stellenbosch University https://scholar.sun.ac.za

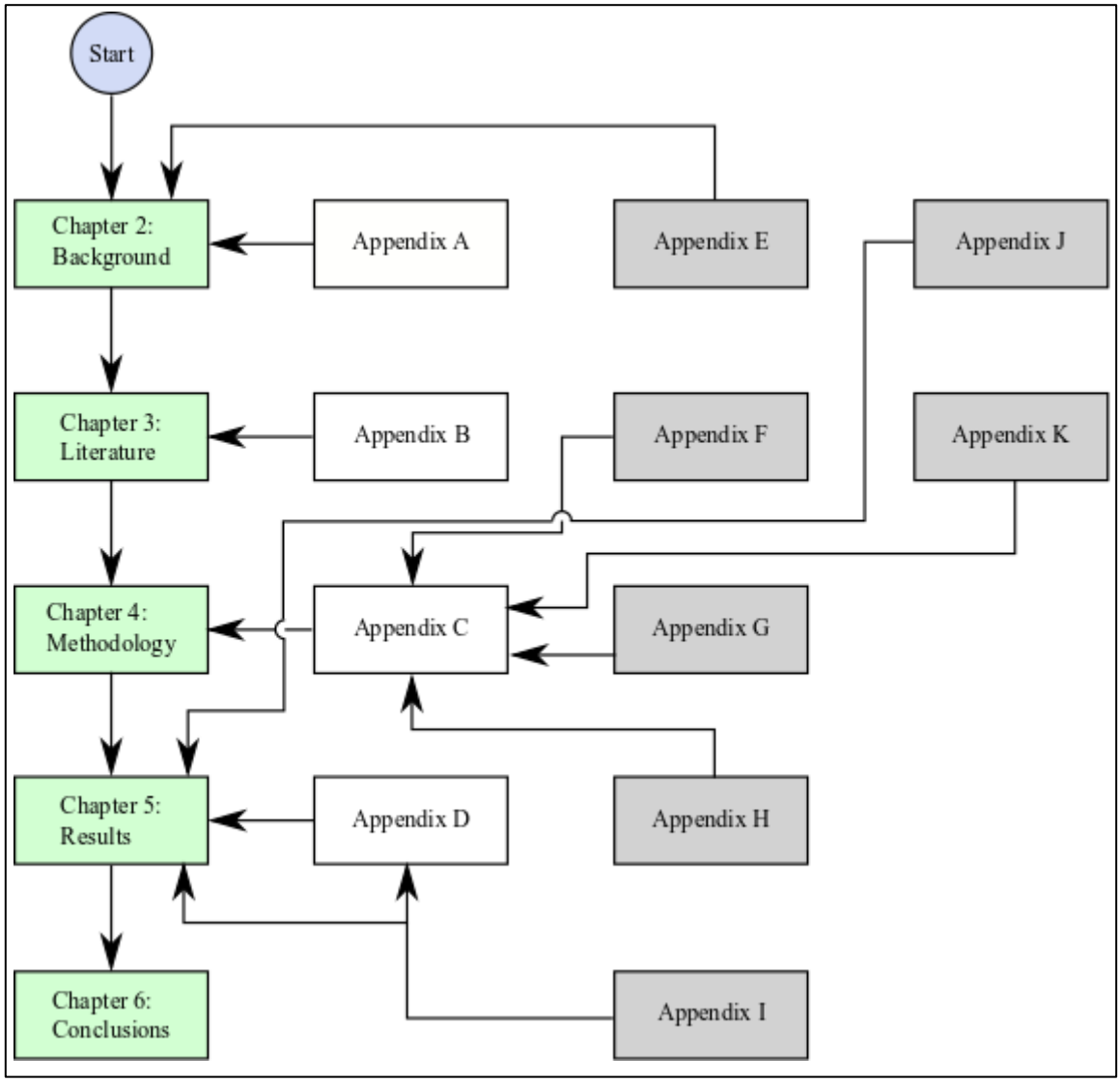

Figure 1.2: Thesis layout (green: main content; white: supplementary text; grey: additional flowsheets, process descriptions and results)

Appendices E – K contain additional methodology descriptions and results (such as detailed tables) required to complete the results presented in Chapter 5 and Appendix D. These sections are indicated by shaded blocks in Figure 1.2. Highlights of these appendices include complete spiral plant diagrams in Appendices E & H, the example images of interface detections in Appendix I and the sensor variances obtained from Appendices J & K.

Lastly, it should be noted that separate nomenclature for image processing and spiral modelling, plant simulation and sensor placement work is used. Section 8.1 lists the relevant symbols for computer vision algorithms and Section 8.2 lists symbols for the remainder of this project's work. Symbols such as x have different meanings for the computer vision and spiral modelling cases. However, much of the image processing methodology is contained in Appendix C to reduce confusion.

Stellenbosch University https://scholar.sun.ac.za

Chapter 2: Background

2.1. Spiral concentrators

2.1.1. Significance within gravity separation

Gravity concentrators seek to separate minerals based mostly on differences in specific gravities (SG). This can occur in a fluid whereby particles separate due to their relative movement under the influence of gravity and various other forces (such as the resistance to motion incurred from a viscous fluid) (Burt, 1984: 4). Another very important factor in gravity separation is the sizes of particles to be separated; this can greatly affect which forces become major factors during gravity separation (Wills & Napier-Munn, 2005: 225).

Various methods of gravity concentration have been developed and some of the different machines include: jigs, cones, spirals, shaking tables, centrifuges and some dense medium separator (DMS) machines (Wills & Napier-Munn, 2005: 225, 241 & 242). Despite the adaptation of gravity concentration (for different applications) it saw a dramatic decrease in importance in industry with the emergence of mineral separation via froth flotation. Fines, low grade and complex ores could now be treated (via flotation) where gravity separation methods have failed in the past (Wills & Napier-Munn, 2005: 225). Developments in magnetic separation and leaching also led to a decline of the significance of spiral concentration (Burt, 1984: 3).

Gravity concentration remained a vital separation step for iron, tungsten and tin ore processing and began to regain its popularity around the 1970's (Burt, 1984: 4). Costs associated with flotation comprise the use of reagents (usually in the form of organic compounds, acids and caustic), electrical power and labour (Burt, 1984: 4). Flotation circuits generally require expensive equipment and the waste that is produced can become a problem due to ecological concerns (Wills & Napier-Munn, 2005: 225). Spiral concentrators are relatively simple and cheap equipment to operate with much less harmful effluent streams and lower power consumption (Burt, 1984: 4). The contrasts between flotation and gravity concentration can be seen in Table 2.1.

Stellenbosch University https://scholar.sun.ac.za

Table 2.1: Gravity concentration vs. flotation (table entries obtained from Burt, 1984: 4 & Mojela, 2015)

	Gravity concentration	Flotation
Particle sizes that can be treated	Generally 3 mm to 45 µm	About 300 µm to 10 µm
Preferred type of ore	Rich ores with coarse liberation sizes	Rich to low grade, complex ores; only fine particle size is required
Reagents	Generally no reagents are present	Organic compounds, acids (H_2SO_4) and caustic
Installed cost/ton ore throughput	Low	High
Power requirement	Low	High
Difficulty of operation	Simple; becomes more complicated with large circuits	Can become complex with larger circuits and implementation of process control
Effluent	Mostly slimes	Slimes with organic compounds and, depending on the process, varying pH

Materials that can be treated by the gravity separation route include coals, mineral sands, metal oxides and precious metals (like ores containing native gold) (Burt, 1984: 5; Wills & Napier-Munn, 2005: 236; King, Juckes & Stirling, 1992: 51; Subasinghe & Kelly, 1991: 1). Fines (particles < 50 µm) have always been difficult to separate by gravity concentration but further developments have helped increase the ability of existing equipment to solve this problem (Tripathy & Murthy, 2012: 387). Spiral concentrators have been shown to be able to treat fine chromite (particle size < 75 µm) to help solve the ultra-fines problem in that industry (by Tripathy and Murthy in 2012).

2.1.2. The spiral unit

Spiral concentrators (or spirals to be concise) consist of a helical trough winding around a vertical support (see Figure 2.1 for the helicoid shape). Originally designed for pre-concentration of low value ores, spirals have many different applications now which impact their design and implementation (Burt, 1984: 261; Holland-Batt, 1995: 4). Analytically a spiral concentrator can be visualised as many non-intersecting helicoid curves which are adjacently located and extends along the radial direction. Figure 2.1 shows a mesh curve with important factors shown. Most spiral trough profiles will have the design showed in Figure 2.1 which is the form of a quarter ellipse (quarter-circular arc) (Kapur & Meloy, 1998: 16 & 17). H_s represents the total height of the spiral, u_s the pitch, θ_s a local slope on the trough and α_s equal to the arctangent of u_s over r_s (the trough radius).

Stellenbosch University https://scholar.sun.ac.za

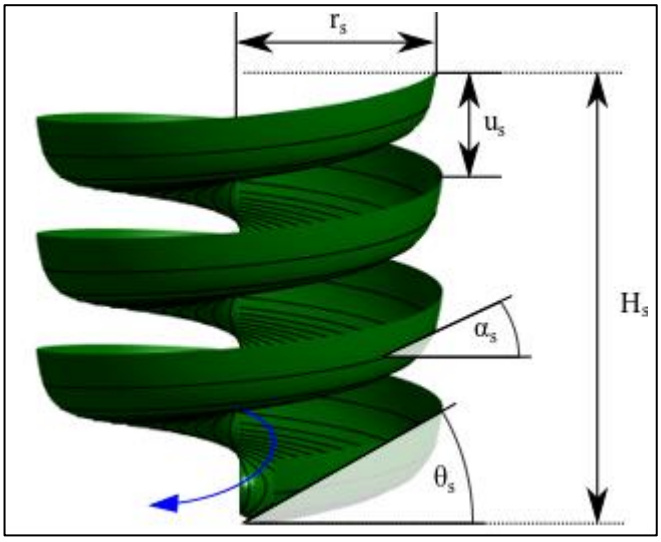

Figure 2.1: Helicoid for spiral concentrator

Spiral concentrators receive slurry feed from a feed box, placed at the top of the unit, which also serves to correct the slurry velocity, by forcing volumetric flow to enter the spiral through a different size area, ensuring a preferred pattern of flow (Burt, 1984: 263; Holland-Batt, 1995: 1389). Slurry enters the trough as a nearly homogenous mixture and as the slurry travels in the spiral particles from different minerals tend to stratify along the horizontal plane forming 2 or 3 distinct streams of concentrate, middlings and tailings or concentrate and tailings (Burt, 1984:263; Wills & Napier-Munn, 2005: 236). Figure 2.2 shows examples of two common types of ores, encountered in gravity separation, flowing as slurry down spiral troughs.

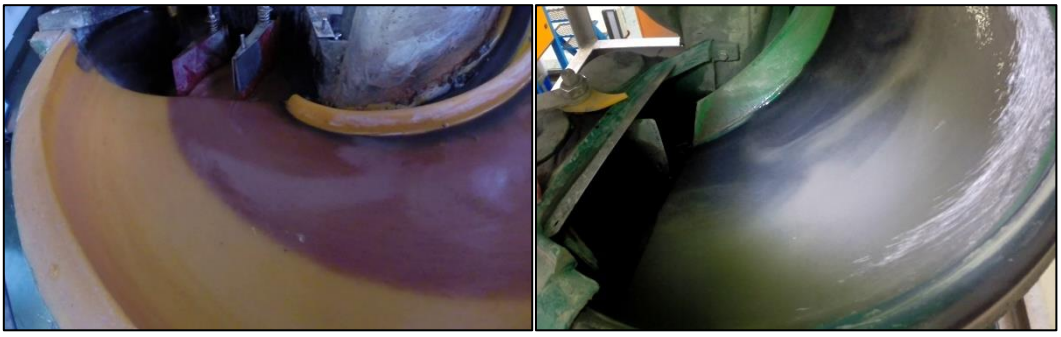

Figure 2.2: Ilmenite (1st frame) and chromite (2nd frame) ore separation examples (gulleys and splitters are visible)

Splitters are located at the bottom of the spiral which usually divides the slurry into the amounts of concentrate, middlings and tailings that operators wish to collect (Wills & Napier-Munn, 2005: 236). Spirals also contain several concentrate collector ports at the inner edge or the gulley spaced on vertical intervals along the spiral. These ports act as (auxiliary) splitters and are adjustable on some spiral designs. Re-pulpers can be added down the spiral trough after an auxiliary splitter to redistribute the slurry and allow further separation of valuable material near the periphery of the trough (Holland-Batt, 1995: 1389).

Stellenbosch University https://scholar.sun.ac.za

Some spiral designs include wash water ports to wash particles from the concentrate stream. Wash water ports are added at different vertical positions, near the inner edge or gulley, to improve the removal of light, usually entrained, particles from the stratified bed in the slurry (Burt, 1984: 264; Loveday, 1993: 2.2; Bazin, Sadeghi & Renaud, 2016: 75). During the early 1990s spirals typically did not include wash water systems since past experience have shown that they tend to become blocked. Adding wash water has the beneficial result of producing a cleaner concentrate and improving the flow of concentrate down the spiral (Loveday, 1993: 2.2).

Spiral concentrators can be installed in compact configurations to save additional floor space in mineral separation plants. Double or triple start spirals share a common support column and allow the placement of two or three spirals in the space of one (Wills & Napier-Munn, 2005: 238). This becomes an important design consideration for the design of spiral separation plants which can allow the placement of 2000 to 6000 units in a plant, greatly increasing the plant capacity (Dallaire et al., 1978: 128; Wills & Napier-Munn, 2005: 238).

2.1.3. Slurry flow and mineral separation characteristics of spiral concentrators

Spiral concentrators are robust units capable of operating under different permutations of the main operating variables: slurry flow rate, slurry solids content, splitter settings and solids particle size (Burt, 1984: 272). However, all these factors that influence spiral behaviour lead to complex flow patterns – which complicates splitter control and eventual slurry monitoring. Table 2.2 show the ranges between which mineral separation can be achieved with spirals over a broad series of different minerals (Wills & Napier-Munn, 2005: 236).

Table 2.2: General operating ranges for spiral concentrators

Variable	Typical range
Particle size	45 µm – 3000 µm
Slurry solids fraction	0.15 – 0.45
Slurry flow rate	1 – 3 t/h for low slope (per start). Steep slope spirals can operate up to 6 t/h throughput (per start).

Even though it is not shown in Table 2.2, feed grade also has a substantial effect on spiral efficiency (Dallaire et al, 1978: 124; Holland-Batt, 1995: 1385). Controlling feed grade as an input variable is more complicated and is not in direct control of the operators of a spiral concentration plant (Dallaire et al., 1978: 124). Changing feed grade and ore mineralogy is usually considered in design and modelling stages of a plant through pilot plant testing (Tripathy & Murthy, 2012; Vermaak et al., 2008).

Carrier liquid (in most cases water) density and viscosity also effect the separation obtained in a spiral concentrator (Vermaak, et al., 2008: 151; Matthews, Fletcher & Partridge, 1999: 215). Matthews et al.

Stellenbosch University https://scholar.sun.ac.za

(1999) performed numerical simulations of slurry flows in coal spirals and found that a denser carrier fluid could result in more definitive cuts (in the radial distance from the column) along the trough between coal and refuse products. Vermaak et al. (2008) showed that a higher slurry viscosity can visibly influence the shape of the concentrate band in heavy mineral separation spirals. Changing slurry viscosity can become an important consideration in spiral concentrator slurries if a high slimes content is present in the ore (larger fines content can alter slurry viscosity). Particle size range in spiral feeds affects efficiency depending on how wide or narrow the range is. Narrow particle size ranges tend to separate more efficiently in spirals (Loveday, 1993: 2.1). Richards, MacHunter, Gates & Palmer (2000: 69 - 73) performed tests on fine titanium (using FM1 spirals) and iron ore (using MG4C spiral) bearing sands and found that recovery drops when mean particles size (of the feed PSD) increases or decreases from approximately 100 µm.

Slurry flow and mineral separation profiles is usually considered to be fully developed after traveling the first 2 turns in the spiral (Holtham, 1991: 79; Boucher, Deng, Leadbeater, Langlois, Renaud & Waters, 2014: 127). Mineral separation in a spiral; however, will change along the trough when auxiliary splitters are implemented (Holland-Batt, 1995: 1385). Primary (via trough length) and secondary velocities are present in the developed flow as material move down the trough and across the trough; away from the gulley (see flow directions in Figure 2.3).

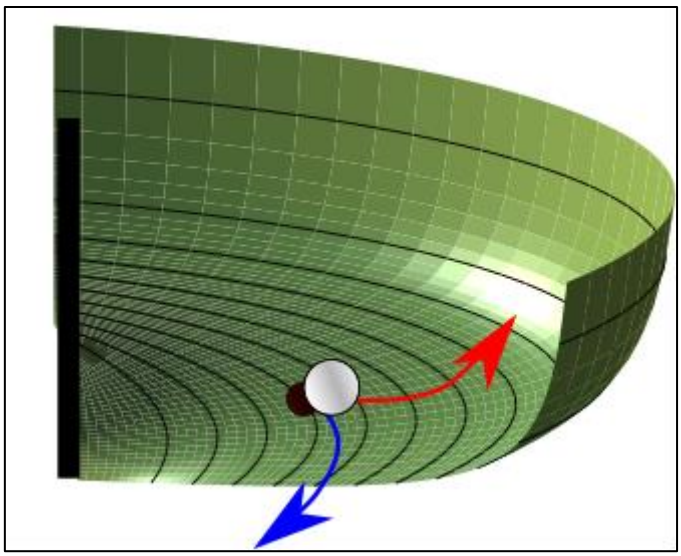

Figure 2.3: Primary (blue arrow) and secondary (red arrow) flow lines in a spiral concentrator

Primary flow down the trough can be seen as a result of the action of gravity on the slurry. Secondary fluid flow moves in a direction normal to the primary flow and is induced by the curvature of the spiral trough. It is due to the centrifugal force (which is at maximum at the free surface of the pulp) that water moves radially outward; away from the gulley (Matthews, Fletcher & Partridge, 1998: 973). Holtham (1991: 79) experimentally measured the secondary fluid flow on spiral concentrators empirically confirming its existence. Another important characteristic of the liquid flow on a spiral concentrator is the transition from laminar, to transitional, to turbulent flow regimes that can be

Stellenbosch University https://scholar.sun.ac.za

observed in the slurry as one moves away from the gulley in a radial direction across the trough (Matthews, Fletcher & Partridge, 1998: 973).

The separation of minerals (or stratification of minerals) in spiral concentrators is generally seen as being due to the combined effect of hindered settling and interstitial trickling (Burt, 1984: 263; Wills & Napier-Munn, 2005: 236). Gravitational and centrifugal forces (acting on each volume element of slurry) lead to the development of a flowing film velocity gradient (Figure 2.3) as well as a radial velocity gradient (Burt, 1984: 263; Doheim et al., 2013: 201). The result is that lighter suspended particles move to the trough periphery where centrifugal forces and gravitational forces reach equilibrium. Particle velocities decrease with increasing slurry depth (retarded by surface friction from the helicoid), thus experiencing less of the centrifugal force and follow the trough profile towards the inner edge. This is usually the route that heavier particles will follow when they concentrate in a spiral (Doheim et al., 2013: 202).

Particles that are larger than 3 mm (independent of particle density) and very fine heavy particles (< 75 µm) tend to move to the spiral trough periphery. Very large particles roll along the trough radius due to high overturning moments (inducing high velocities) and very fine material have very low settling velocities. This highlights the importance of screening spiral feeds to ensure particle sizes are within design ranges (Richards et al., 2000: 65 - 66). Figure 2.4 shows where particles with high or low density will concentrate across a spiral trough. Dark orbs represent more dense particles and light orbs represent less dense particles.

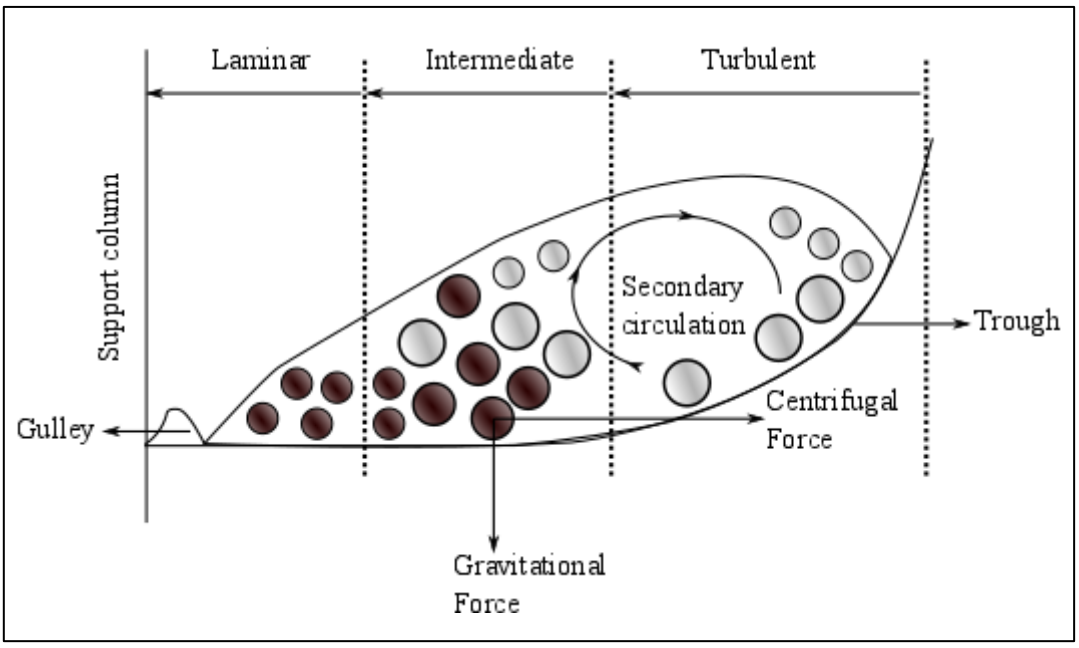

Figure 2.4: Simple slurry profile in a spiral concentrator (adapted from Holland-Batt, 1995: 1382)

Low density and large high density particles congregate in the middlings zone of the spiral and large low density particles will move to the outer extent of a spiral's trough (Loveday, 1993: 2.6). It is usually expected that particles of similar weight or hindered settling velocities will associate in the

Stellenbosch University https://scholar.sun.ac.za

same areas in the trough but this is not the case with spiral concentrators (implying the existence of other separating forces in the trough). In the case of separating chromite from silica particles, on spiral concentrators, large silica particles and small chromite particles will settle on opposite sides of the spiral trough (Loveday, 1993: 2.6). Loveday (1993) concluded that this separation result can be described by the existence of Bagnold (1954: 49) forces in regions of the slurry with high particle concentrations (Holtham, 1992: 220). Bagnold forces manifest as dispersive grain pressures that occur between particles in a linear flow region of a Newtonian fluid.

High shear rates in spiral troughs, due to the pulp volumetric flow rate, can increase the likelihood of the Bagnold force affecting mineral separation (Burt, 1984: 263). The Bagnold force will typically cause heavy particles to move to lower velocity zones in the vertical plane (toward the helicoid surface), while lighter minerals will move to higher velocity zones (Burt, 1984: 263).

Investigations performed by Holtham (1992), to determine the existence of the Bagnold effect in spiral slurries and to which extent it affected the slurry characteristics, concluded that Bagnold forces can occur in the particle bed that forms next to a spiral's gulley. Slurry with a density of about 15 % solids (in this case quartz) was fed to 2 different spiral concentrators at volumetric flow rates of 6 m^3/t and 4 m^3/t. Despite the overall slurry content which was lower than can be encountered in industry the solids content in the concentrate was about 50 % and could reach up to 73 %. The formation of bulges on the pulp surface was observed and was thought to be due to the Bagnold effect. Further calculations showed that the particle-inertia flow regime dominated in the inner edge of the spiral trough which is due to Bagnold forces at work (Holtham, 1992: 216).

The complex fluid flow patterns and particle interactions within spiral concentrators pose a significant problem for fundamental and even statistical spiral modelling (as is generally the case in mineral processing). This creates uncertainties, regarding to process optimization, during spiral operation and, naturally, translates to even greater ignorance of spiral bank performance during plant operation. Due to the uncertainty of how current spiral operation may influence product mineral grade and/or recovery it is necessary to improve monitoring of spirals.

2.1.4. Spiral plants

Spiral concentrator application in mineral beneficiation plants can be encountered in several phases: rougher, cleaner, re-cleaner and scavenger spirals (Davies, Goodman & Deschamps, 1991: 452; Holland-Batt, Balderson & Cross, 1982: 55). Each phase is basically a bank of spirals grouped together to achieve a common separation goal. Rougher spirals are usually implemented as the primary bank, typically treating larger particle sizes, and provide an initial separation into concentrate, middlings and tailings stream. Secondary spiral banks (such as cleaners) treat the low-grade primary concentrate while scavenger banks will typically treat fines and middling streams from other banks. Cleaner spirals treat finer and pre-concentrated material to produce a high-grade concentrate

Stellenbosch University https://scholar.sun.ac.za

(Holland-Batt et al., 1982: 55). Figure 2.5 provides a simplified diagram of spiral beneficiation plants in the chromite industry.

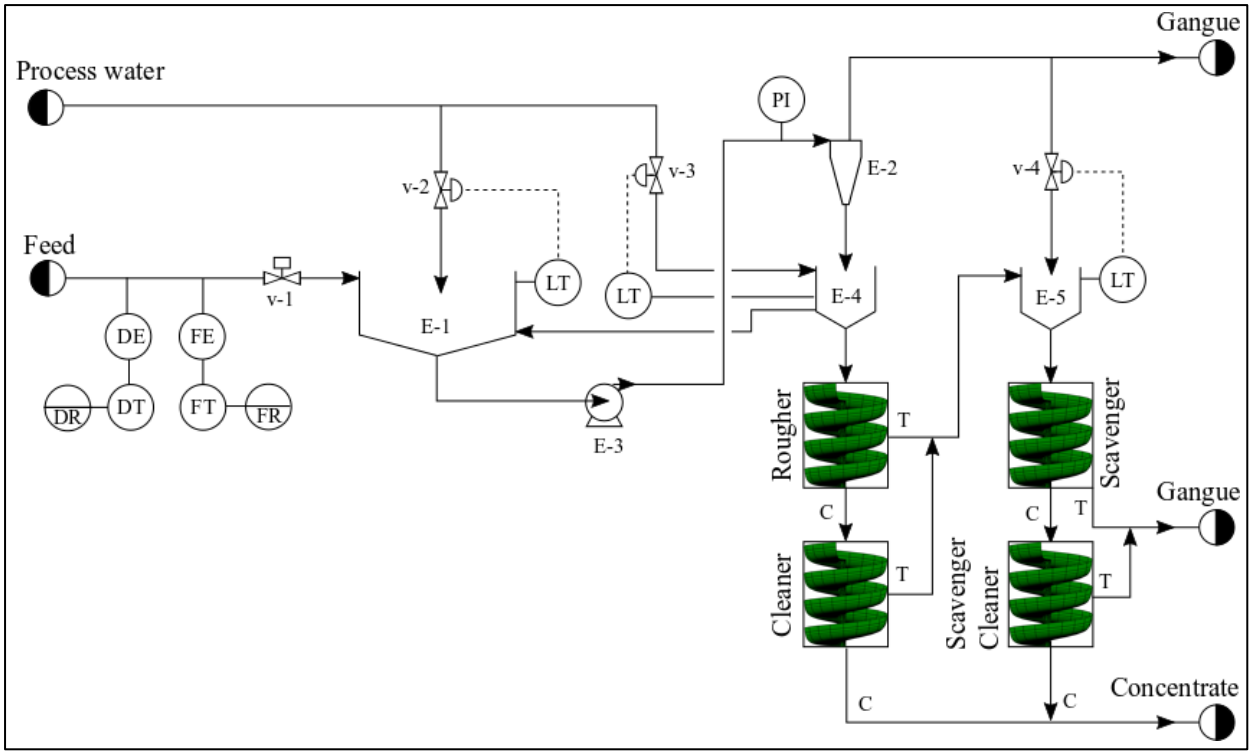

Figure 2.5: Simplified and partial chromite spiral circuit piping and instrumentation diagram (adapted from Holland-Batt, 1982: 55)

For the circuit spirals to operate properly it is imperative that the appropriate particle size ranges are fed to the spirals and that clean water is used as a carrier liquid. The minimum feed preparation required is that screens should be implemented before slurry reports to rougher or primary circuits to remove oversize and tramp (wood, plastic or metal chips) materials (Davies, Goodman & Deschamps, 1991: 452). Water feed should be screened with a 1 mm mesh to remove any solids that can cause blockages. Cyclone classifiers are also used in chromite circuits when a large quantity of slimes or fines are present (adapted from Holland-Batt, 1982: 55). Oversize particles can be crushed in a ball or rod mill and reintroduced to the spiral circuit for further beneficiation.

Spiral concentrators are common in chromite ore dressing plants since the 1980's and especially in South Africa (Burt, 1984: 433). Spirals have especially become useful in the processing of chromite tailings, resulting from platinum extraction, consisting of fines with particle sizes below 300 µm (Burt, 1984: 438; Dawson, 2010: 683). During the beneficiation of PGM's, collected from the UG2 reef ore, complete spiral plants will typically be placed downstream of flotation plants and treat the tailings produced there (Dawson, 2010: 683). Configuration of spiral units within chromite plants can vary greatly but will typically have a layout similar to Figure 2.5 (Burt, 1984: 433; Holland-Batt, 1982: 55). Plants treating UG2 ores will start with a rougher (primary) stage producing a concentrate

Stellenbosch University https://scholar.sun.ac.za

that will be cleaned by spiral cleaner (secondary) stages, and tailings (no middling produced) that will be scavenged by scavenger and scavenger cleaner stages.

Monitoring and control of the spirals within spiral plants are still conducted manually by operators. Some variables such as sump levels, process water additions and pump duties can be monitored or controlled online. Other variables that are typically monitored online is plant feed and product flowrates, and densities (Bredenhan, 2015). Online control of feed variables has not yet been developed for spiral plants and is dealt with manually by manipulating splitters, concentrate ports and even wash water distribution valves (Vermaak et al., 2008: 147; Bazin et al., 2015: 75). The development of spiral unit control systems first requires monitoring tools to be devised. Online spiral monitoring can help operators improve manual splitter placements and spiral cleaning campaigns (to remove build-up of slimes). Automatic manipulation of splitters will require vision based inferential sensors that determine the change in mineral concentrate bands within spiral slurries.

2.2. Case study: Glencore Rowland site

2.2.1. Plant overview

The Rowland site receives, from a nearby PGM concentration plant, a UG2 flotation tails stream which is treated – using a total of 192 triple start spirals (96 per module) - to produce chromite ($FeCr_2O_4$) concentrate. Two other resulting product streams include fine and coarse tails. The fine tails stream is produced by cyclone overflows and coarse tailings represent the final tailings produced by the spirals. Fine tails from the Rowland site report to flotation cells for further extraction of PGMs, coarse tails are disposed of in a tailings dam and plant concentrate is used as feed stock to chromite smelting operations. A description and simplified process flow diagram (PFD) of the chromite concentration process at the Rowland plant can be found in Appendix E (Section 13.2). The Rowland site is also called the Western Platinum plant or WPL (for brevity's sake) plant by Glencore.

Feed streams with average chromite grade of 25 % (with Cr/Fe ratio equal to 1.31) are upgraded to the concentrate target of 40 % which varies between 38 % and 42 % chromite (provided in Figures 2.6 & 2.7). UG2 ores typically contain V, Al_2O_3, MgO, CaO, SiO_2, Cr_2O_3 and FeO with a Cr/Fe ratio of 1.36 (Cramer, Basson & Nelson, 2004: 519); however, the Rowland site only analyses the feed (and tailings) composition in terms of Cr_2O_3. The concentrate Cr/Fe ratio typically varies between 1.26 and 1.37 for the Rowland site. Concentrate composition analysis is performed on-site to determine Cr_2O_3, FeO and SiO_2 content.

The minerals present in the Rowland site feed can also show variation; however, this is more important to downstream processes. Natural chromite can be described by $(Mg, Fe^{2+})O \cdot (Cr, Al, Fe^{3+})_2O_3$ which includes substitutions of Fe^{2+} by Mg and Cr by Al or Fe^{3+} (Sánchez-Ramos, Doménech-Carbó, Gimeno-Adelantado, Peris-Vicente, 2008). The concentrate product

Stellenbosch University https://scholar.sun.ac.za

typically produced falls below common metallurgical grade (Sánchez-Ramos et al., 2008) since the Cr_2O_3content is below 46 % and Cr/Fe is below 3.

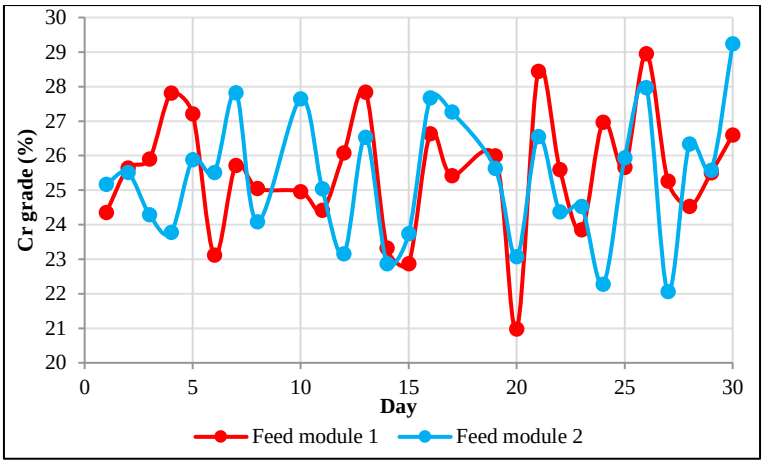

Figure 2.6: Rowland feed grade for June 2015

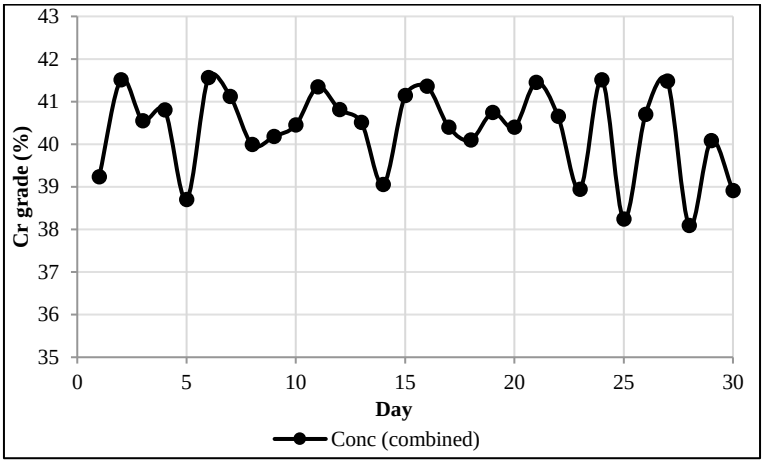

Figure 2.7: Rowland concentrate grade for June 2015

Average particle size in UG2 ore concentrates are 120 µm and maximum particle diameters do not usually exceed 800 µm. Sieve test will typically show that 99.9 % of UG2 concentrates passes 425 µm (Cramer, Basson & Nelson, 2004: 519). Figure 2.8 shows PSDs for the Rowland feed stream over May 2015. The majority of particles pass 300 microns which is in agreement with literature on UG2 concentrate's characteristics (Cramer, Basson & Nelson, 2004: 519; Dawson, 2010: 683). Figure 2.8 also shows that the majority (about 80 %) of particles fall below 100 microns in size which implies a high slimes content in the plant. Larger amounts of fines in plant feed emphasise the need for correct hydrocyclone sizing and operation (especially when considering maintenance).

Stellenbosch University https://scholar.sun.ac.za

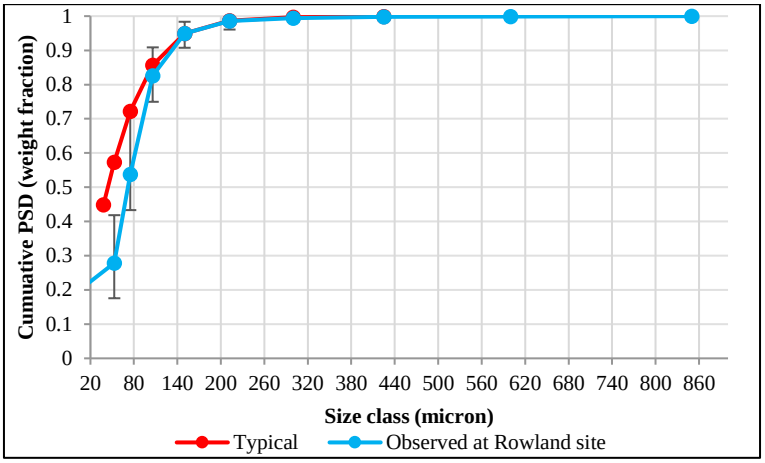

Figure 2.8: Rowland feed cumulative particle size distribution (for May 2015) - compared with a reference UG2 cumulative particle size distribution

Another important consideration in the Rowland plant feed is the residual flotation chemicals, wood chips and thin metal strips that it contains. Residual chemicals from the flotation process may contribute to the coagulation of slimes on the spirals which can block spiral gulleys or troughs. Wood and metal chips also present complications to plant operation since they can block spiral feed/product pipes and spiral gulleys. No vibrating screens are present at the Rowland site with the result that unwanted oversized material pass to the spirals. Figure 2.9 presents the extent of the slimes problem in a spiral trough and the effect on visually observable mineral separation – introducing the need for spiral cleaning (maintenance) every 2 days.

Slimes can lead to banking, particle entrainment and alteration of the slurry viscosity (Vermaak, Visser, Bosman & Krebs, 2008; Richards, MacHunter, Gates & Palmer, 2000) all of which reduces spiral performance. Figure 2.9b shows how the slurry particles are swept up by turbulent eddies, obscuring the mineral separation bands, making it difficult to visually observe any separation (except for the slurry in the concentrate gulley). Figure 2.9a shows the effects of banking in the spiral trough causing slurry to move through various unintended channels. Improved, or online, spiral monitoring can help plant operators to plan spiral cleaning regimes – based on the changing appearance of spiral slurries.

Figure 2.9: Effects of slimes on mineral separation ranging from a trough with banking to a cleaned spiral (a, b, c represent various slurry states that can be observed on a spiral plant).

Stellenbosch University https://scholar.sun.ac.za

Variability within the Rowland plant will ultimately depend on the variation in the flotation tailings received from the upstream PGM concentration plant. The feed received by the Rowland plant is not tailored to the optimal operation of spiral concentrators and will ultimately vary based on what the upstream flotation process requires to optimise PGM recovery.

The images and graphs presented here do not provide an exhaustive representation of the operation of the Rowland spiral plant modules and rather summarises some of the available plant information (and possible problems for spiral monitoring).

2.2.2. Plant characteristics, variables and measurement

Only Multotec spirals are implemented on the Rowland site with the majority being SC 21 and HX 5 models. HX 5's are used as the scavenger and scavenger cleaner spirals. Concentrate and middlings cuts from all spiral banks are grouped together in the same launders with tailings reporting to a different launder. Narrow middling cuts are usually implemented to allow the collection of a wider tailings band from the splitter box (Bredenhan, 2015). The only slimes pre-treatment at WPL is the hydrocyclones (used at the feed to the rougher and scavenger spirals) and no vibrating screens are implemented to remove tramp materials. There are no walls around the modules which exposes the spiral concentrators to the elements. Natural light entering the plant will complicate the use of an optical sensor on the spirals and the possibility of rain entering can also affect the spiral process as a whole.

The spiral modules are monitored from a control room placed in close proximity to the spiral modules where tank levels, pump speeds, flowrates, pressures and densities can be tracked. All variables monitored in the control room are not uploaded to a historian (hence no softcopy available on a server) but hardcopies of flowrates and densities are available (noted every day):

- Flowrates (in m^3/h) and densities (in SG) are measured at the plant feed (from the nearby PGM concentrator) and final coarse tails produced.
- Hydrocyclone pressure (in the feed line) at the rougher and scavenger spirals are monitored to ensure the gauge pressure remains at 140 kPa (pressure should not fall below this point).
- Chromite stacker (boom stacker) pressure is also monitored to ensure gauge pressure (in the feed to cyclones) do not fall below 50 kPa.

Slurry SG is measured at the overflow and underflow of each hydrocyclone bank to ensure that the correct separation of slimes is achieved. This measurement (done by weighing a 1 L hand drawn sample of slurry) is also performed to ensure overflow from the rougher cyclones has a higher density than the density of the overflow from the scavenger cyclone spirals.

Samples of the feed to the rougher cyclones, final concentrate and final coarse tailings are collected and analysed every day. PSD and compositional data are obtained to determine mineral grades in the different product streams and the partitioning of different particles sizes throughout the plant.

Stellenbosch University https://scholar.sun.ac.za

Compositional analysis is specifically performed to determine chromite grade within the concentrate which is one of the most significant performance variables. Plant inspection is executed once every 2 months to determine slurry flow rates and densities (using mobile mass flow meters) throughout the plant. This enables the calculation of mineral recovery within each of the products streams of the Rowland plant.

2.2.3. Spiral properties

The SC 21 and HX 5 spirals from Multotec form part of their range of mineral treating spirals. HX 5 spirals have a larger diameter and are designed to treat finer (low grade) minerals in scavenger sections of spiral plants. SC 21 usually treats higher grade slurries and is designed for cleaner/re-cleaner duties in a spiral plant; however, SC 21s are known to be used as roughers as well (Mojela, 2015).

SC 21 and HX 5 spirals differ significantly in trough radius but remain similar in other design aspects. Table 2.3 summarises the design differences of SC21 and HX 5 spiral as made by Multotec. Clearly HX 5 spiral will be able to treat larger slurry capacities (flow rates) making them ideal to scavenge tailing streams. More splitters are present in the SC 21, allowing more of the mineral of interest (MOI) to move toward the gulley – thereby increasing extraction of HM.

Table 2.3: SC 21 and HX 5 design (Mojela, 2015)

	Spiral model	
Element	SC 21	HX 5
Diameter (mm)	600	1000
u_s	21°	19°
Turns	3 or 5	3 or 5
Splitters	Sliding and auxiliary	Sliding

Differences in SC 21 and HX 5 capacities are summarised in Table 2.4. An increase in trough diameter significantly increases the amount of slurry that can be loaded onto a spiral and the HX 5 can treat more than double the amount of ore. SC 21 spirals are designed to treat larger particles making them more suitable for the production of HM concentrate.

Stellenbosch University https://scholar.sun.ac.za

Table 2.4: SC 21 and HX 5 capacities (Mojela, 2015)

	Spiral model	
Variable	SC 21	HX 5
Solid flow rate (t/h dry basis)	1.0-2.0	4.0-6.5
Volume flow rate (m^3/h)	3.4-5.3	7.6-13.5
PSD (µm)	45-1000	45-800
% solids	30-50	30-50

2.2.4. Interface tracking and sensor placement consequences

The spiral mineral interface tracking and plant sensor placement problem faces several significant challenges (when considering the Glencore plant in question). Interface detection is complicated by the slimes problem encountered with fine chromite processing. Tramp materials, present in the Rowland site slurries, also contribute to banking. Thus, it is imperative that robust interface trackers be developed – and that appropriate sensor placement is applied.

Sensor placement algorithms, that require plant simulation, is complicated by the lack of information on spiral bank operation. There are virtually no slurry measurements taken around individual spiral banks within the Rowland site. Validating spiral plant simulations will be difficult – since only plant feed and concentrate streams are investigated on site. The plant and spiral information presented in this section is still useful for experimental spiral modelling and initial plant flowsheet development.

2.3. Instrumentation network design for process plants

Instrumentation is the key to monitoring, modelling and control (and eventual automation) of chemical or metallurgical plants. Different sensors provide the data required to estimate the states of different process variables which is essential in product quality and yield accounting, fault detection and control, and ensuring overall operational safety (Bagajewicz, 2002: 3). In large process plants, with hundreds of different process streams and units, it becomes less obvious where instrumentation must be placed especially when this must be done sparingly. Quantitative approaches are required – methodologies that can be automated – to determine instrumentation placement strategies that are subject to monitoring performance or revenue production requirements.

Automated sensor network design is a knowledge field concerned with achieving theoretically optimal sensor placement in grass-root plant design or upgrading design scenarios. Common monitoring network design goals include (Bagajewicz, 2002: 3):

1. Estimability of specific or key variables.
2. Increased accuracy/precision of a certain set of variables.
3. Estimation robustness to gross errors and process faults.
4. Minimizing instrumentation cost.

Stellenbosch University https://scholar.sun.ac.za

The theory of optimal sensor placement focuses on the formulation of the above-mentioned goals into objective functions that can be optimized by appropriate algorithms. Estimability and estimation precision relates to monitoring performance and is considered from a data reconciliation perspective. Data rectification includes the reconciliation, bias and fault detection aspects (Bagajewicz, 2002: 5) but requires considerably more complicated analysis. Objective functions that combine robustness to gross errors with fault detection capability have not yet been fully established (Bagajewicz, 2002: 5). Maintenance cost can also be included in the sensor acquisition (or capital) costs (Lai, Chang, Ko & Chen, 2003: 4366; Bagajewicz, 2002: 5) but this remains an issue that requires further investigation.

A mathematical formulation of the optimal sensor placement problem can generally be expressed as Equation 2.1 (with constraints shown in Equations 2.2 to 2.4).

$$C^* = \underset{C}{\operatorname{argmin}}\, J_T \qquad \text{(Eq. 2.1)}$$

s.t.

$$C_{ij} \in \{0, 1\} \qquad \text{(Eq. 2.2)}$$

$$D_i \geq D_i^* \qquad \text{(Eq. 2.3)}$$

$$\sigma_i^2 \leq \left(\sigma_i^2\right)^* \qquad \text{(Eq. 2.4)}$$

Where:

- J_T represents total cost of sensor configuration C.
- C^* is the optimal sensor configuration. C_{ij} are i^{th} row and j^{th} column entries of C with i corresponding to sensor type and j corresponding to a plant variable (and therefore sensor location).
- D_i is the estimability of variable i and D_i^* is the minimum estimability.
- σ_i^2 represents standard deviation of variable estimation and $\left(\sigma_i^2\right)^*$ is the maximum variable variance.

Equation 2.1 represents a mixed integer combinatorial optimisation problem due to the discrete nature of C, D and the inclusion of continuous plant variables (such as flow rates) with precision σ. Mixed integer non-linear programming methods and tree searching methods (from graph theory) can be successfully applied to certain optimal sensor placement problems (Bagajewicz, 2002: 6). When larger plants with many variables and different sensor options are considered genetic algorithms (GAs) can be used to solve the optimisation problem (Bagajewicz, 2002: 12).

Designing or introducing new instrumentation to an existing metallurgical plant can be a challenging task. Even metallurgical accounting can become difficult since on-line flow measurements are rarely available (Tucker, 1985: 377); however, estimation of process variables is a must for future process

Stellenbosch University https://scholar.sun.ac.za

control and optimization (Mazzour, Hodouin & Makni, 2003: 186). Developing appropriate objective functions for instrument design, in metallurgical plants, is also challenging due to the lack of information on how sensor implementation costs, maintenance costs and monitoring performance vary at different locations in a plant.

Derivation of proper sensor placement algorithms for spiral plants first requires a detailed literature review – addressed in Chapter 3. The abundant literature on spiral unit operation is essential in preparing models for spiral plant simulation – which will allow sensor location investigations. A thorough review of sensor placement in metallurgical plants is required to find the remaining problems which complicate theoretical instrumentation designs.

Stellenbosch University https://scholar.sun.ac.za

Chapter 3: Critical literature review

3.1. Modelling of spiral concentrators

3.1.1. CFD & DEM models

In the past, the design of spiral concentrators was an iterative experimental process requiring laboratory and pilot-scale plant trials to determine optimal spiral designs and spiral bank configuration within plants (Matthews, Fletcher & Partridge, 1998: 966). As can be expected the experimental design procedure proved to be cumbersome and it became increasingly desirable to use fundamental models to simulate and design spiral concentrators. Advancement in computer hardware leading up to the 1990's made it possible to investigate fundamental models which can simulate slurry behaviour. It was intended that these models will help spiral manufacturers design optimized spiral units.

Matthews et al. (1998:966) used computational fluid dynamics (CFD) to model fluid flow and dilute slurry flow down an LD9 coal spiral. Fluid flow rates of 4, 6 and 8 m^3/h were investigated and agreed or was at least of the same order as measured data of slurry height and velocity profiles. Measured velocities at the outer periphery of the spiral was between 15 % and 20 % higher than predicted showing the significant effect that air entrainment has when pulp flow becomes turbulent. CFD modelling is also capable of capturing the secondary flow that exists in the spiral flow. Product particle distributions for dilute pulps were investigated and followed the classic distributions as observed in spirals. Finally, enough information was obtained from this study to suggest improvements to the LD9 spirals (Matthews et al., 1998: 978).

The CFD modelling performed by Matthews et al. (1998) showed that the carrier fluid behaviour could be captured and effectively modelled. The drawbacks were that turbulent flows could not yet be accurately modelled and that pulps with higher solids concentrations could not be investigated.

Doheim, Abdel Gawad, Mahran, Abu-Ali & Rizk (2013: 214) expanded upon the work done by Matthews et al. (1998) by simulating pulps with particle densities of 0.3 % and 3 %. Doheim et al. (2013: 214) also attempted to find the most effective turbulence model which can accurately describe spiral pulp at turbulent flow while minimizing the computational effort required. The obtained models produced velocity and velocity profile predictions that fell within the observed range and it was suggested by this study that the models could provide operators with a method to improve LD9 spiral operation.

Drawbacks from the Doheim et al. (2013) investigation are that the particles that were modelled in the study were silica spheres and the particle concentrations still fell well below the 15-40 % solids range. Future studies will have to investigate pulp flows with much higher solids content to produce models which can apply to how spirals are operated in practice.

Stellenbosch University https://scholar.sun.ac.za

Mishra & Tripathy (2010: 192) performed Discrete Element Method (DEM) simulations of a mixture of water and a batch of 12000 spheres (representing ore particles) as they travel down a spiral concentrator. A specific solids fraction was not reported. Use of DEM modelling was motivated due to the difficulty of solving mathematical models in CFD and the fact that empirical models (such as response surface methodology) only apply to certain types of spirals (Mishra & Tripathy, 2010: 192). It was found that primary splitters can maximize mineral recovery when placed at a certain turn (higher up than the standard bottom position) in the spiral. Preliminary model validation showed that DEM provides results in reasonable agreement with observation (average experimental and predicted concentrate grades were 56.67 % and 50.9 %; Mishra & Tripathy, 2010: 195). The limitations of DEM is similar to that of CFD modelling in that the solids concentration examined still falls significantly short of describing the true operation of a spiral concentrators.

3.1.2. Mechanistic (semi-empirical) modelling

Before CFD and DEM modelling of spirals, there has been many mechanistic based approaches to modelling spiral concentrators. These models are typically less cumbersome than the equations used in CFD analysis but usually rely heavily on empirical data (Matthews et al., 1998: 966). Reliance on empirical data creates the draw back that these models usually only apply to a certain spiral design and its application to a certain ore.

In 1989 Holland-Batt developed mechanistic models to describe the flow patterns within spiral pulps and the Subasinghe mechanistic model was aimed at predicting cut specific gravity on coal washing spirals (Loveday, 1993: 2.46 & 2.47; Subasinghe & Kelly, 1991: 1). The Holland-Batt model was capable of describing the slurry flow profiles and mineral distributions (at different particle sizes) across the spiral trough, but still requires empirical input and does not incorporate particle interactions. Holland-Batt's model is capable of describing the product recovery trend of a spiral operating at 15 % solids but it does not provide accurate results (Holland-Batt & Holtham, 1991). The major drawback with Subasinghe's model is that it is limited to the application of coal spirals (Subasinghe & Kelly, 1991: 1).

Loveday (1993: 5.3) investigated a chromite-silica pulp flow in a Multotec "21 degree" spiral and initially considered primary flow down the trough. Modelling of the primary spiral flow was performed in a way similar to Holland-Batt but also included Bagnold force and how it affects the primary fluid flow profile. It was found that laminar flow regimes (in the inner edge of the spiral trough) were the most accurately described type of flow and that intermediate and turbulent flow models did not correlate as well with experimental observation. Including the Bagnold effect helped to produce predictions in the order of what is observed but with a large degree of scatter (Loveday, 1993: 5.3).

Kapur & Meloy (1998: 15) attempted to model spiral pulp characteristics using force equilibrium models. The fluid behaviour was modelled based on Holland-Batt & Holtham's 1991 paper to obtain

Stellenbosch University https://scholar.sun.ac.za

methods of calculating volumetric flow rates and mean pulp velocities. Particle force balances include the major forces (gravity, centrifugal, lift, friction, drag forces) acting on particles and are simplified to obtain expressions describing the bulk flow of solids. Slurry flow down the trough is assumed to be in dynamic equilibrium and pulp flow in the secondary direction, along the trough profile, is assumed to be in static equilibrium. This means that particles move down the trough without an changing radial position on the trough (Kapur & Meloy, 1998: 23). Kapur & Meloy's (1998) model could replicate the trends observed in certain spiral pulps' solids density distribution along trough radial position. It was also noted that the force equilibrium model would require significant improvement before becoming useful for spiral design and optimisation.

Bazin et al. (2016: 75) modified Kapur & Meloy's (1998) model for a wash water spiral treating iron ore slurries. The spiral in question was divided into half turns (based on where water is injected or auxiliary splitters are located) with modelling performed on sequential sections of the spiral. Mass balances are performed for each half turn, to account for splitter cuts and wash water additions, followed by Kapur & Meloy's (1998) methodology to determine PSDs for different minerals. Spiral simulations were performed at feed conditions where the solids flow rate was 1.37 t/h and the Fe_2O_3 grade, of the particulate material, was 49 % (which is realistic operating conditions) and concentrate stream grade estimates where less than 2 % off from observed values (Bazin et al., 2016: 75). The Bazin et al. (2016) model was capable of capturing bulk spiral behaviour but this was only reported at 1 test point (in terms of feed conditions). It was also clear that the model can produce poor results for individual spiral bands and some mineral concentration trends can be completely misrepresented. Validation of Bazin's model required significant empirical data – especially if many feed conditions should be investigated (due to the number of parameters).

Similar to Kapur & Meloy's (1998) approach to modelling spirals, Das, Godiwalla, Panda, Bhattacharya, Singh & Mehrotra (2007) attempted to model a coal-washing spiral with a force equilibrium model. Das et al. (2007: 118) place much more emphasis on the effect Bagnold forces have on the spiral slurry. The radial distribution of slurry relative density (RD) for 1 mm and 1.5 mm particles were predicted and validated with results from literature. RD values for the slurry ranged between 3 and 2 which is similar to what can be observed in industry (Das et al., 2007: 128). Force equilibrium models rely heavily on empirical data and relations and, therefore, require further development but provide a much simpler first approximation method to modelling spirals than solving the Navier-Stokes equation as required by CFD (Das et al., 2007: 130).

3.1.3. Spiral modelling using response surface methodology

Development of CFD, DEM and mechanistic models of spirals have seen significant advancement and are capable of describing fluid flow and even dilute slurries (especially at laminar flow regimes). These models have already provided information on how existing coal and mineral spirals can be improved but still share a common drawback. Current CFD and DEM models do not yet model the slurry content range between 15 % and 45 % as implemented in industry, in its entirety. The models

Stellenbosch University https://scholar.sun.ac.za

of Kapur & Meloy (1998) and Das et al. (2007) model spiral slurries at higher density values, similar to what can be observed in industry, but both conclude these models require significant improvement.

Since the 2000s more advanced experimental design methods have been implemented in the testing of spiral concentrators to model and optimise these units. The types of experimental designs are also chosen in such a way so that the number of experiments (and associated cost) can be reduced, thereby performing more efficient experimentation. Some of the recent studies investigating spirals with optimising experimental design include Tripathy & Murthy's (2012) optimisation of spirals treating fine chromite; Honaker, Jain, Parekh & Saracoglu's (2007) work on ultrafine coal cleaning; and Dixit, Tiwari, Mukherjee & Banerjee's (2015) modelling of spirals separation of iron ore slimes. All these methods used the Box-Behnken experimental design to model and optimise the performance of a single laboratory spiral. Vermaak et al. (2008) also used an optimising experimental design but instead of implementing a Box-Behnken design they used a central composite design and three factor factorial design.

Experimental designs based on response surface methodology (RSM) are typically used to produce linear or quadratic empirical spiral models. These models are simple to analyse and implement in the optimisation of spirals. Through RSM a much more straight forward way to relate feed parameters to observed spiral product can be found – compared to involved fundamental and mechanistic approaches. Drawbacks of RSM modelling include:

- Models only apply to the spiral model in question.
- Important feed variables may be ignored (i.e. PSD).
- Responses only valid for specific feed conditions.
- Linear/quadratic trends may show poor extrapolation ability.

RSM methods were developed to optimize process responses and – at best – provide a Taylor series approximation of true process behaviour (Montgomery, 2001: 427). Previous studies of Tripathy & Murthy (2012), Honaker et al. (2007) and Dixit et al. (2015) used RSM to optimize spiral responses but also suggest the possible modelling of spiral units (using RSM) – which should be done with care.

3.1.4. Holland-Batt spline

Another empirical spiral modelling method is described by Holland-Batt (1990) based on common graphical methods for presentation of spiral separation results. This approach describes MOI recovery (versus feed slurry mass recovery) for a concentrate splitter cut that can – theoretically – span the entire trough. Figure 3.1 shows an example of the Holland-Batt spline.

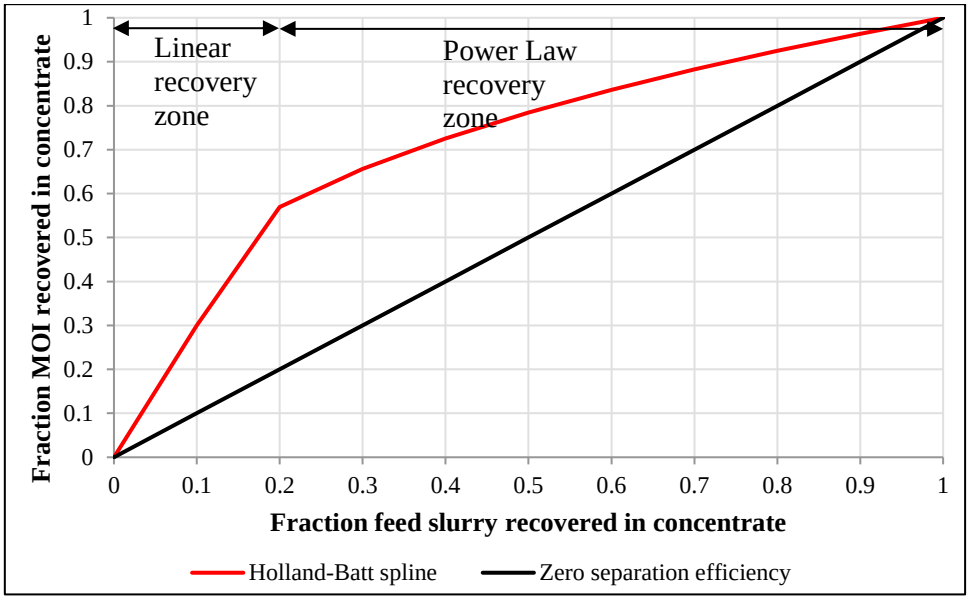

Figure 3.1: Simple spiral separation curve for MOI recovery in concentrate stream (based on the Holland-Batt model)

The Holland-batt spline has two recovery zones described by linear and power law functions. Equations 3.1 & 3.2 give the expressions for the two recovery zones. The measurement errors of R_1 and R_2 are assumed to be zero centered Gaussian noise. Transition of the piece-wise defined model (see Equation 3.3) occurs when the fraction feed slurry recovery W and the feed MOI grade f are equal (for ideal separation). Actual data will show a transition when $W > f$ (Holland-Batt, 1990: C13).

$$R_1 = a_1 W \qquad \text{(Eq. 3.1)}$$

$$R_2 = W^{a_2} \qquad \text{(Eq. 3.2)}$$

$$R = \begin{cases} R_1 + e, & W > f \\ R_2 + e, & W \leq f \end{cases} \qquad \text{(Eq. 3.3)}$$

Where:

- R_1 represents the linear recovery zone.
- R_2 represents the power law recovery zone.
- a_1 and a_2 are model parameters.
- $e \sim \mathcal{N}(0, \sigma^2)$. σ^2 is the model variance.

It has also been suggested that R should equal the minimum between R_1 and R_2 in lieu of finding a transition point (Grobler, Naudé & Zietsman, 2016: 190). Additional splines between R_1 and R_2 have also been proposed by Holland-Batt (1990: C14) and Grobler et al. (2016). The intention would be to smooth the transition between the linear and power law curves. This can be useful if separation data (after the initial recovery zone) do not show a clear power law trend.

Stellenbosch University https://scholar.sun.ac.za

The Holland-Batt spline was developed to explain separation efficiency for splitter cuts that span the entire spiral trough but the model lacks a vital aspect. Equation 3.3 was developed with the assumption that parameters are tuned to a particular steady state. Therefore, feed conditions must remain constant during experimentation, model fitting and model implementation (different feed conditions cannot be modelled by Equation 3.3). There is a provision available for changes in feed grade (Holland-Batt, 1990: C16). When separation efficiency between a reference curve (model based on experimental data) and a curve with perturbed feed grade remains proportional it becomes possible to perform extrapolation.

The feed correction method relies on spiral separation efficiency - defined by Equation 3.4 (Holland-Batt, 1990: C17; Fourie, 2007: 2).

$$E = \frac{R-W}{1-f} \qquad \text{(Eq. 3.4)}$$

Where:

- Spiral separation efficiency is denoted as E.

Figure 3.2 shows an example separation efficiency curve adjustment based on the efficiency proportionality principle. The original efficiency curve (the E values) can be obtained by applying Equation 3.4 to a Holland-Batt spline (similar to Figure 3.1). E' efficiency values were obtained via feed grade extrapolation based on the congruent triangles in Figure 3.2.

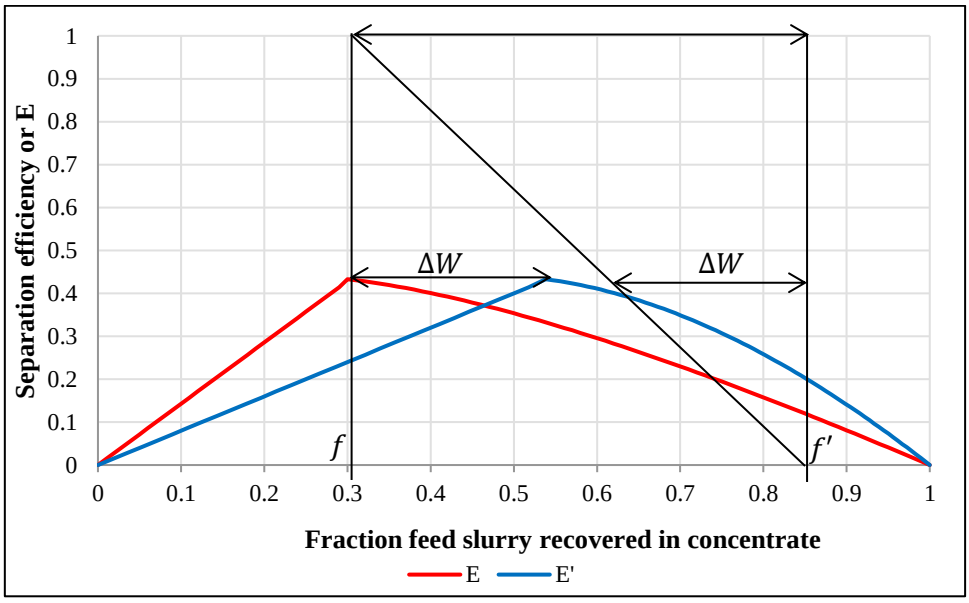

Figure 3.2: Proportionality of separation efficiency example (adapted from Fourie, 2007)

Taking that $\Delta E = E(R, W, f) - E(R', W', f') = 0$ (required by the proportionality assumption), and including triangle congruency, leads to: $1/\Delta f = E/\Delta W$. Thus, Equation 3.5 can be obtained – which allows us to shift W values proportionally to scaled feed grade differences.

Stellenbosch University https://scholar.sun.ac.za

$$W' = W + E(f' - f) \qquad \text{(Eq. 3.5)}$$

Once W' values have been calculated, new Holland-Batt splines can be obtained as in Figure 3.3. Increases in feed grade (with all other feed conditions constant) will shift the Holland-Batt spline closer to the zero separation efficiency line (or the $R = W$ line). A decrease in feed grade will have the opposite effect – moving the spline to the left of the $R = W$ line. The R' values at W' are equal to R values at W (thus R' at W is not equal to R at W').

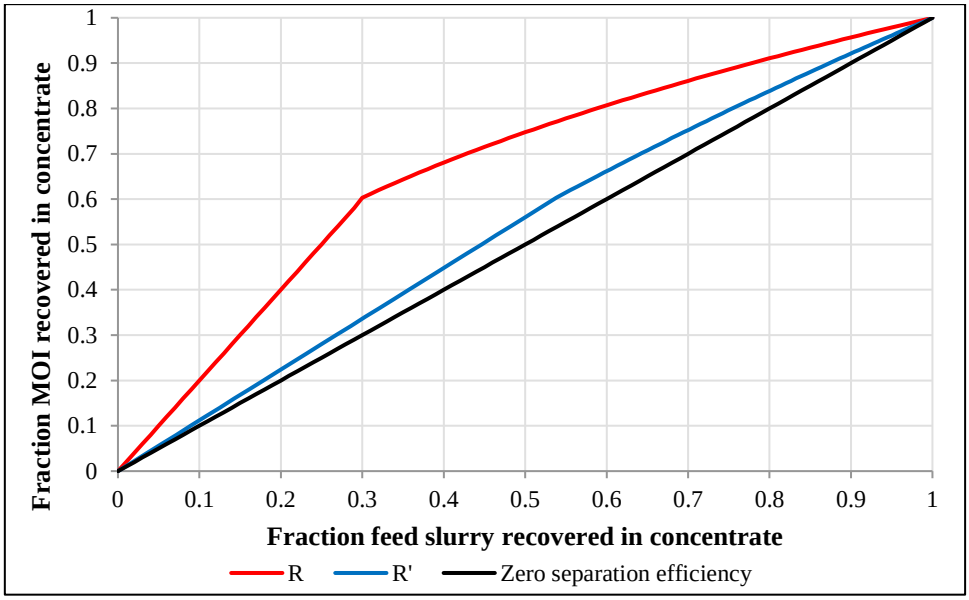

Figure 3.3: Recovery curve after feed grade adjustment

In general extrapolation is not recommended; however, spline extrapolation to higher feed grades are usually more accurate than extrapolation to lower grades (Holland-Batt, 1990: C17). Additional work is required to generalise the Holland-Batt (1990) model so that variations in feed slurry flow rate and density are appropriately included. It will also be necessary to investigate the feed grade extrapolation method at extremely high or low feed grade adjustments.

3.1.5. Other empirical models

Empirical models are based on experimental observations and are usually limited to certain spiral geometries separating a specific ore. Despite its limitations, empirical models are much simpler to perform calculations with and, using appropriate experimental designs, can potentially be expanded to other spiral applications (Loveday, 1993: 2.39).

Two examples of empirical models developed for spirals include the Tucker mineral ore and King et al. (1992) coal model. Both models describe the particle distribution obtained from product streams of spiral concentrators (Loveday, 1993: 2.39, 2.40 & 2.41; King, Juckes & Stirling, 1992: 51). The King et al. (1992) model described how the clean coal partition factor varies and particle density varied with splitter settings and particle size intervals. Partitioning of water flow rate was also modelled to

Stellenbosch University https://scholar.sun.ac.za

provide a more complete model of the spiral unit that is also more conducive for the modelling of spiral plants.

3.2. Spiral experiments

3.2.1. Previous methodologies

Many different experimental methodologies have been previously prepared to test spiral separators for various responses and characteristics. This is due in part to the fact that experimental investigation still remains the preferred way to model spirals at their typical operating conditions. Some well recorded methodologies can be recovered from Loveday (1993), Holland-Batt & Holtham (1991), Holtham (1991), Guest & Dunne (1985) and Sadeghi (2015). The appendix to this study's literature (Appendix B) summarises the core details of experimental setup, typical sampling and measurements inferred from samples.

3.2.2. Previous experimental designs for spiral tests

Previous experimental designs that used RSM to model spiral concentrators all considered the following factors as independent variables: feed grade, slurry flow rate (mass or volumetric), splitter position, slurry density and viscosity. These RSM designs would typically consider a three factor permutation of the significant independent variables resulting in the experimental design of choice being a Box-Behnken design; however, full factorial and three variable central composite designs (CCD) have also been implemented (Tripathy & Murthy, 2012; Honaker et al., 2007; Dixit et al., 2015; Vermaak et al., 2008).

From literature it is apparent that the preferred independent factors for a three-level Box-Behnken design is the splitter position (usually measured in cm from the support column), slurry density (as a solids mass %, actual density or RD) and (volumetric or mass) slurry flow rate (Tripathy & Murthy, 2012; Honaker et al., 2007; Dixit et al., 2015). More than one response is typically measured and multiple response surfaces can be developed for the grade of MOI in one of the product streams as well as yield or recovery. Tripathy & Murthy (2012: 392) performed a Box-Behnken design on fine chromite ore to model concentrate grade and recovery of chromite. Dixit et al. (2015) modelled alumina (Al_2O_3) grade and yield in their spiral concentrate stream (for the case of iron slimes concentration).

Table 3.1 gives examples of slurry flow rates, density, splitter position, particle size ranges and feed grade used in previous response surface designs. The total variation in splitter setting ranges from 3 cm to 14 cm but this will be dependent on the spiral trough width. Similar slurry flow rate and density ranges are implemented in most spiral tests which provide sufficient basis for future designs to adhere to and expand upon. Particle size has not been varied in previous experiments and is usually kept to a narrow size range since it has been previously stated (Loveday, 1993) that narrow size ranges show greater separation efficiency. Only Vermaak et al. (2008) (in Table 3.1) varied the total HM in the

Stellenbosch University https://scholar.sun.ac.za

feed. For modelling applications it can be very useful to vary feed characteristics but it can be challenging to prepare suitable feed batches with significantly different compositions.

Table 3.1: Experimental parameters and settings in previous spiral experiments

	Variable				
	Slurry flow rate	Pulp density	Splitter setting	Feed grade	Particle size range used (in µm)
Tripathy & Murthy (2012)	1.2 – 3 m^3/h	10 – 30 % solids by mass	12 – 16 cm	42.66 mass % Cr_2O_3 and Fe	25 - 150
Vermaak et al. (2008)	2.2 – 5 m^3/h	10 – 50 % solids by mass	-	5 – 20% total HM	53 - 500
Honaker et al. (2007)	2.8 – 6.4 m^3/h (originally reported as 46 – 106 L/min)	6 – 18 % solids by mass	16 – 30 cm	Test based on coal cleaning with feed containing 49.87 % ash	45 – 210 (41.11 % solids were below 45 micron)
Dixit et al. (2015)	2.1 – 4.3 m^3/h	10 – 20 % solids by mass	3 – 6 cm	63.26 % Fe by mass	25 – 150 (50% of solids were below 25 micron)

Many different variable levels are presented in Table 3.1 but this is due to separation on different ores and spirals. Despite the different reported operation conditions Table 3.1 provides a reference point from which to start designing experiments.

3.2.3. Significant feed variables from previous spiral response surface methodology experiments

Previous RSM based spiral experiments by Dixit et al. (2015) and Tripathy & Murthy (2012), who used heavy mineral slurries, provide a useful reference for feed variables that affect mineral separation significantly. Table 3.2 provides a summary of the significance of linear and quadratic terms in terms of coefficient t-test p-values. None of the interaction terms (for both cases) were significant when applying a full quadratic model (when considering p-values below 0.05 to be significant).

Stellenbosch University https://scholar.sun.ac.za

Table 3.2: T-test p-values and significant variables (for full quadratic models) from previous RSM spiral experiments (interaction terms excluded)

		Tripathy & Murthy (2012)		Dixit et al. (2015)	
		t-test p-values			
Model terms	Feed variables	Cr_2O_3 grade	Cr_2O_3 recovery	Al_2O_3 grade	Al_2O_3 yield
Linear	Density	0.39	0.01	0.00	0.01
	Volumetric flow rate	0.04	0.03	0.00	0.00
	Splitter setting	0.00	0.00	0.00	0.26
Quadratic	Density	0.11	0.18	0.05	0.39
	Volumetric flow rate	0.40	0.08	0.15	0.00
	Splitter setting	0.01	0.22	0.91	0.18

In the study of Tripathy & Murthy (2012) they found that feed flow rate, splitter setting and the square of the splitter setting had significant influence on the chromite concentrate grade. Increasing feed flow and splitter settings decreased the chromite grade in the concentrate. This result is logically sound since a wider splitter setting will allow more gangue to the concentrate stream and higher feed flow rates increase centrifugal force acting on slurry particles moving valuable particles away from the concentrate mineral band.

The chromite recovery model of Tripathy & Murthy (2012) had 3 significant variables which consists of all linear terms. Increasing feed density and flow rate decreases chromite recovery, however, increasing the splitter setting increases chromite recovery. An increased splitter setting allows more of the slurry material to enter the concentrate stream, thereby increasing recovery but with the trade-off of decreasing grade. Higher feed rates again increases centrifugal force on slurry particles and reduces particle residence time leading to the transport of valuable minerals to tailings. According to Tripathy & Murthy (2012), increased slurry density reduces recovery due to the presence of fine particles which increases slurry viscosity – leading to a reduced effect of density on mineral recovery.

In the study of Dixit et al. (2015) they found that all linear effects and the squared feed density term have a significant effect on alumina grade. Increasing all significant terms of the alumina grade model lead to decreases in alumina grade (except the splitter setting which increases grade) in the concentrate. Feed density, volumetric flow rate and squared volumetric flow rate had a significant effect on alumina yield. Increasing flow rate reduces yield but increasing feed density increases yield. Future spiral experiments focused on the separation of fine chromite can be compared to Tripathy & Murthy's (2012) study to validate results. For coarser chromite separation problems the study of Loveday (1993) should be used.

Stellenbosch University https://scholar.sun.ac.za

3.2.4. Effects of feed variables in mineral sands beneficiation

Richards et al. (2000: 68) investigated spiral separation trends for mineral sands (where TiO_2 beneficiation is relevant) at PSDs with the range 300 µm – 20 µm. It was found that increased feed flow rates generally reduces TiO_2 concentrate recovery and that feed SG variation leads to a quadratic trend (there exists an optimal feed SG and variation from this point reduces TiO_2 recovery). PSD was also a significant feed variable and it was found that optimal particle sizes exist and variation from these points generally reduce TiO_2 recovery in concentrate streams.

The study of Richards et al. (2000) did not use RSM to establish trends (as in the case of Section 3.2.3) – and also did not focus on chromite – but it does emphasize certain spiral feed variable trends (which can be useful for future spiral model comparison and parameter selection). From Section 3.2.3 and the work of Richards et al. (2000) it is clear that increased feed flow rates tend to linearly decrease concentrate MOI recovery. Feed density show similar linear trends but Richards et al. (2000) suggest that quadratic trends will also be significant (with clear optimal feed SG evident).

3.3. Spiral interface sensors

The focus of spiral research has almost always been on the mineral grade and recoveries obtained in concentrate streams. Analysis techniques like X-ray fluorescence (XRF) is usually the method by which MOI is quantified in spiral products but this can be expensive and time consuming. The current mineral quantification techniques also complicate future spiral design considerations such as splitter automation. Because mineral interfaces (Figure 2.2) are a common sight on spiral plants it has been suggested (Vermaak et al., 2008) to use interface measurements for MOI grade inferential sensors – or as an indicator for primary splitter settings.

In spiral literature there are three cases, before 2009, where some form of interface sensing has been considered. Vermaak et al. (2008: 148), Gold (1991: 8.1), and Mohanty, Zhang, Wang, Mahajan, Akbari, Bashir, Ramamoorthy and Hirschi (2014: 157) have all considered monitoring of spiral slurry and how it could be linked to control of primary splitters. Vermaak et al. (2008: 148) and Gold (1991: 8.1) focused on visual measurement of interfaces that form in mineral sands applications. Mohanty et al. (2014: 157) considered the monitoring and control problem in the case of coal cleaning.

Gold (1991: 8.1) developed the first machine vision framework capable of detecting concentrate interfaces in a binary ore which could be implemented, in the future, to control a spiral primary concentrate splitter via an actuator (future control implementation is mentioned as a recommendation). A colour camera was connected to a black-and-white frame grabber which sent digitized video recordings to a desktop computer. Interfaces where detected using a difference of averages edge detector that determines a final edge value from intensity values of two segmented regions. Segmentation can be achieved using LoG or Canny edge detectors (Gold, 1991: 8.1). Edge measurements were updated every 0.16 s and rapid fluctuations were smoothed using an averaging

Stellenbosch University https://scholar.sun.ac.za

filter. Gold's (1991) edge tracking software used an area of interest (AOI) window which a user could set within the camera image frame where the edge detection algorithm should be implemented.

Vermaak et al. (2008: 148) measured concentrate interfaces in a spiral slurry consisting of an ilmenite-silica ore. Seven high resolution images were obtained in quick succession after steady-state was reached and the ilmenite-silica interface was determined by measuring intensity changes along the direction of the trough. The interface location, in pixels, was converted to a metric distance (in mm) between the interface and the support column and the average between all seven measurements were calculated. Adding interface position as a spiral concentrator response variable provides a means to estimate feed mineral grade when the pulp density and flow rate is known (Vermaak et al., 2008: 148). Vermaak et al. (2008) prepared statistical models of ilmenite concentrate interfaces and found that interface width increases proportionally with feed density, grade and flow rate. Interface width was found to be inversely proportional to feed slurry viscosity. Feed grade and density were the most significant variables and feed flow rate was the least significant. Unfortunately, Vermaak et al. (2008) were unable to detect concentrate interfaces in slurries representative of industrial conditions. More robust sensors will be required to implement interface tracking in practice.

Vermaak et al. (2008) and Gold (1991) both showed that spirals can be monitored by optical measurements of slurry interfaces and that spiral performance can be estimated from the output of the inferential sensor. Interface tracking for industrial slurries remained an unsolved problem and it was unclear whether conventional image processing methods were suitable. Gold (1991) and Vemaak et al. (2008) did not implement any control but rather suggested controlling primary splitters of spiral concentrators. Vemaak et al. (2008) proposed that a feed-forward controller should be combined with an interface monitoring system to control concentrate product.

Lastly, during the cleaning of fine coals (with spirals) it is not possible to clearly see coal-gangue separation interfaces and so cut-points (or splitter positions) should be inferred using non-visual cues (Mohanty et al., 2014: 160). Mohanty et al. (2014: 164) used conductivity measurements of slurries and supernatants (in this case simply the water that aids in slurry transportation) to infer splitter cut-points and developed a system that could calculate a new splitter position in about 315s when implemented. Two tests were performed to achieve a SG cut set at 1.65 on a 1.28 SG slurry with the resulting SG cuts being 1.64 and 1.73 (Mohanty et al. 2014: 170).

3.4. Spiral plant simulation

The literature on spiral plant simulation and design is not as voluminous as the research on modelling spiral concentrators themselves. Difficulty in theoretical modelling of spiral concentrators greatly limit simulating sufficiently complicated plant models. Modelling entirely based on empirical models also introduces difficulty since intricate models could require significant experimental effort to account for different plant conditions. Spiral (or gravity concentration) plants are typically simulated via a combination of expert systems (knowledge-based systems supplementing simulations with

Stellenbosch University https://scholar.sun.ac.za

heuristics or databases) and experimental models in an attempt to replace theoretical modelling (Anthony, Van Deventer & Reuter, 1991). It is important to note here that only steady state simulation is considered for spiral plant modelling due to extra complexity incurred with the transient behaviour of spiral concentrators.

Previous research which specifically addresses spiral plant simulation includes studies by Holland-Batt, Balderson & Cross (1984), Fourie (2007) and Steinmuller (2005). Spiral plant simulation, in the time of the Holland-Batt et al. (1984) paper, was performed mostly by using experimental data from pilot plants. Mass balances and simple regression models (describing mineral recovery) is used to find optimal conditions where at to operate a spiral plant. Holland-Batt (1990), Fourie (2007) and Steinmuller (2005) present simpler modelling approaches which rely on the use of mass-recovery curves (see Figure 3.1). Figure 3.4 shows an example mass-recovery curve, describing recovery of valuable minerals vs. total feed mass recovered, for certain feed and spiral conditions. Typical experimental data points are also provided in Figure 3.4 with the common curve shaped fitted to training sets.

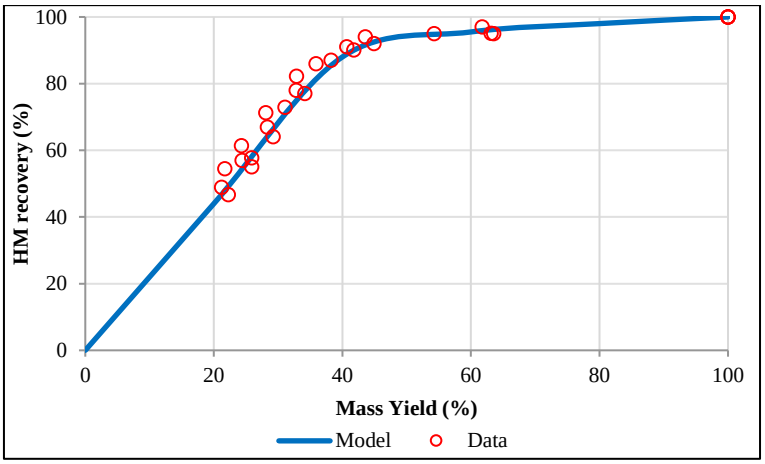

Figure 3.4: Spiral mass-recovery curve (data obtained from Sadeghi, 2015)

The mass-recovery curve in Figure 3.4 is valid for binary separation problems at specific conditions. Different feed conditions will change the curvature of the expected mass-recovery function. When multiple operating conditions and multicomponent separation is considered the curve in Figure 3.4 becomes a multidimensional manifold. For simple spiral simulation purposes (where binary separation of MOI and gangue can be assumed) mass-recovery curves can be used in combination with mass balances to investigate changing conditions in a spiral plant. To keep simulation simple, curves are usually prepared for rougher, cleaner and scavenger sections from pilot plant test work to eliminate exhaustive laboratory testing (Fourie, 2007). With simple spiral simulations, it is still important to note that great difficulty arises in extrapolating models to different feed conditions and resolving recycle streams (Steinmuller, 2005).

Stellenbosch University https://scholar.sun.ac.za

Even with simplified multi-component systems and spiral models, complex circuit designs can make metallurgical accounting tedious. Linear programming can be used to simplify mass balances on larger, more complicated spiral plants. The connection or adjacency matrix is used to represent the flow of process streams in a plant and to solve mass, material or species balances (Wills & Napier-Munn, 2005: 75; Romagnoli, & Sánchez, 2000: 13). Equation 3.6 is the simple definition of an adjacency matrix suitable for metallurgical processes.

$$M_{ij} = \begin{Bmatrix} +1 & stream\ entering\ node \\ 0 & stream\ not\ entering\ or\ leaving\ node \\ -1 & stream\ leaving\ node \end{Bmatrix} \qquad \text{(Eq. 3.6)}$$

Figure 3.5 shows a simple process to serve as an example of how a connection matrix can represent a process. Units such as the spirals are treated as graph nodes and process streams are treated as graph edges.

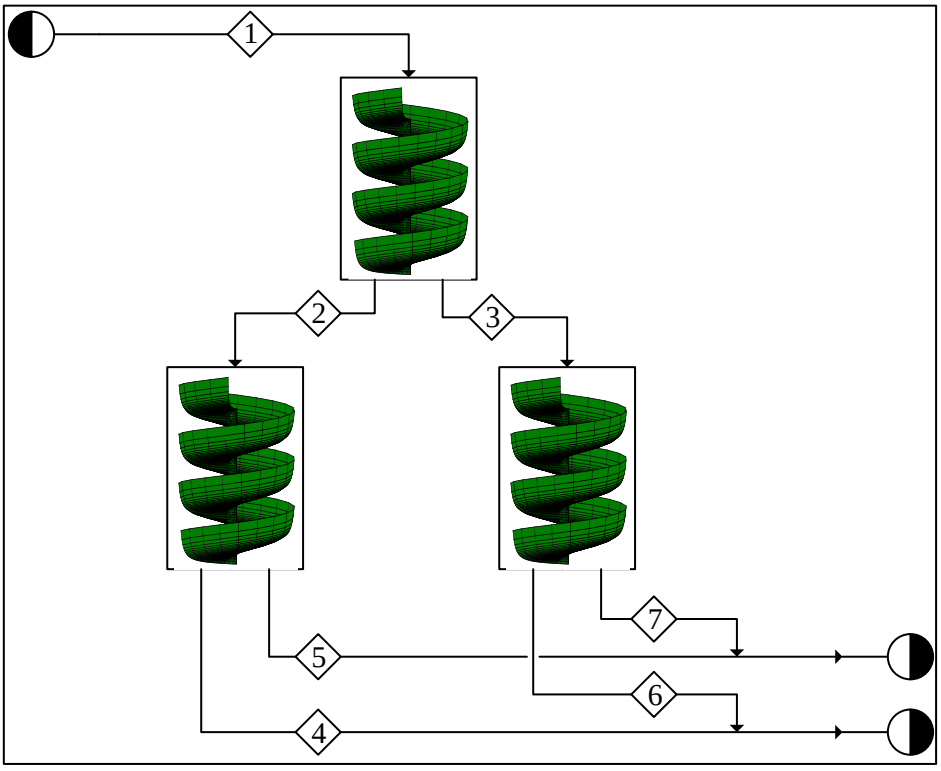

Figure 3.5: Simple spiral plant (adapted from Wills & Napier-Munn, 2005: 75)

The connection matrix that represents the process in Figure 3.5 is shown below. There are 3 rows that correspond to the number of unit processes and 7 columns that correspond to the total number of streams.

$$M = \begin{bmatrix} 1 & -1 & -1 & 0 & 0 & 0 & 0 \\ 0 & 1 & 0 & -1 & -1 & 0 & 0 \\ 0 & 0 & 1 & 0 & 0 & -1 & -1 \end{bmatrix}$$

Connection matrices can compactly aid in representing the total mass, material and species balances of a metallurgical system. Equation 3.7 is an adequate expression for a total mass balance of a process

Stellenbosch University https://scholar.sun.ac.za

and can be obtained via conservation of mass. Equation 3.8 represents a total mass, material and species balance which can be derived in a similar way to Equation 3.7 (Wills & Napier-Munn, 2005: 76; Romagnoli, & Sánchez, 2000: 78).

$$MX = 0 \qquad \text{(Eq. 3.7)}$$

$$\begin{bmatrix} M & 0 & 0 \\ 0 & M & 0 \\ 0 & 0 & M \end{bmatrix} \cdot \begin{bmatrix} X_1 \\ X_1 \odot X_2 \\ X_1 \odot X_2 \odot X_3 \end{bmatrix} = 0 \qquad \text{(Eq. 3.8)}$$

- Where $\odot$ refers to element wise multiplication or the Hadamard product.
- X_1 represents total mass flow rates.
- X_2 represents solids fractions.
- X_3 is the species of interest fractions of the solids.

Initial modelling of a spiral plant can be done by evaluating given empirical models for certain feed conditions. After spiral concentrator models have been used to solve non-redundant process stream flow rates and compositions Equation 3.8 can be used to resolve the remaining process stream properties. Formulation of a process via Equation 3.8 is also useful when doing sensitivity analysis and data reconciliation when redundant data is available (Wills & Napier-Munn, 2005: 76).

3.5. State estimation and sensor placement in metallurgical plants

With new instrumentation design for monitoring purposes the goal becomes to keep cost (initial investment) to a minimum while increasing the number of variables to be measured and the confidence in these measurements. In other words, instrumentation design is done to improve plant performance, by decreasing measured variable variance, at the lowest cost possible (Mazzour et al., 2003: 186; Hodouin, 2010: 16).

Data reconciliation is combined with combinatorial (or exhaustive) optimal sensor placement to provide measures of increased confidence – and reduced variation - in process variables. The system process model and process measurement model (for steady-state) equations can be compactly summarised in Equations 3.9 & 3.10 (Mazzour et al., 2003: 186; Romagnoli, & Sánchez, 2000: 77). Model errors are typically assumed to be normally distributed unless process model errors are assumed to be $\epsilon = 0$ (which is typically the case).

$$z(X) = \epsilon; \epsilon \sim \mathcal{N}(0, V_\epsilon) \qquad \text{(Eq. 3.9)}$$

$$Y = C(q(X) + e); e \sim \mathcal{N}(0, V_e) \qquad \text{(Eq. 3.10)}$$

Where:

- X is a vector of system variables.
- $z(X)$ is the process model.

Stellenbosch University https://scholar.sun.ac.za

- $q(X)$ contains the measurement model.
- Y is a vector of measurements and e is the measurement random error.
- V_e is the measurement variance matrix, and positive definite with $\mathrm{E}\left(e_i e_j^T\right) = 0$ when $i \neq j$.

The measurement matrix C (in Equation 3.10) has the same number of columns as the number of variables in X and its number of rows coincides with the number of sensors to be considered for reconciliation. Every row of C can only have one entry with a value of 1. If flow rate sensors are considered for the process in Figure 3.5 and flow rate sensors at streams 2, 3 and 4 are present then C becomes:

$$C = \begin{bmatrix} 0 & 1 & 0 & 0 & 0 & 0 & 0 \\ 0 & 0 & 1 & 0 & 0 & 0 & 0 \\ 0 & 0 & 0 & 1 & 0 & 0 & 0 \end{bmatrix}$$

If an additional flow rate sensor is added to stream 2 then a row, identical to C's first row, must be vertically concatenated with C.

All the process variables are contained in X and the process mass balance ($z(X)$) or system of measurements ($q(X)$) can be linear or non-linear functions of X. e is the error accompanying $q(X)$ which models the process measurements Y. Reconciliation of process variables is done via least squares minimization to find the most likely process states $\hat{X}$ of a plant. Weighted least squares can be used since it is unlikely that the absolute error of Y is not proportional to the measurement variable analysis methods (Wills & Napier-Munn, 2005: 85). Equation 3.11 gives the data reconciliation objective function when measurements are captured by Equation 3.10.

$$J = (Y - Cq(X))^T (CV_e C^T)^{-1} (Y - Cq(X)) \qquad \text{(Eq. 3.11)}$$

s.t.

$$z(X) = 0$$

The process constraint on Equation 3.11 is obtained by adapting Equation 3.9 so that conservation of mass applies. The concept of Lagrange multipliers is used to find the X that minimizes Equation 3.11 (Wills & Napier-Munn, 2005: 85). Minimizing Equation 3.12 shows how instrument design C improves process monitoring. When $z(X)$ and $q(X)$ is linear, Equation 3.12 has an analytical solution in the form of Equation 3.13.

$$J = (Y - Cq(X))^T (CV_e C^T)^{-1} (Y - q(X)) + \lambda z(X) \qquad \text{(Eq. 3.12)}$$

$$\hat{X} = P_1 Y + P_2 \qquad \text{(Eq. 3.13)}$$

Where:

- λ is a vector of Lagrange multipliers.

Stellenbosch University https://scholar.sun.ac.za

- P_1 and P_2 are matrices of constants.

The improved estimates of the variance of Y can be calculated using variance expectation $\hat{V} = Var(\hat{X})$. Simplification results in Equation 3.14 – giving improved estimates of variable measurement error for the linear process and measurement model case.

$$\hat{V} = P_1 V P_1^T \qquad \text{(Eq. 3.14)}$$

The updated metallurgical plant variables' states and precisions (obtained by using equations 3.13 and 3.14) is used in the objective functions that determine the optimality of a sensor configuration. Instrumentation design goals for metallurgical plants usually consist of sensor cost and monitoring performance objectives - for certain degrees of estimability. Equation 3.15 calculates the squared cost of the sensor placement strategy, using a vector of sensor prices P_s (Mazzour et al., 2003: 189). Equation 3.16 calculates the monitoring efficiency loss for sensor configuration C by weighting the coefficients L by the estimate variances.

$$J_C = P_s^T C^T C P_s \qquad \text{(Eq. 3.15)}$$

$$J_L = \frac{1}{2} trace(L\hat{V}L^T) \qquad \text{(Eq. 3.16)}$$

The coefficient matrix L must be derived from a process performance function. A function describing net revenue or some loss in revenue is ideal; however, no specific methodology exists for determining the appropriate process performance function. When such a function is available then L is obtained as the deviation of the Hessian of the process performance function (from its optima) with regard to X (Mazzour et al., 2003: 189; Forbes & Marlin, 1996: 720). After adapting Equation 2.1 the optimal sensor configuration can be found by solving Equation 3.17.

$$C^* = \underset{C \in \mathcal{D}}{\operatorname{argmin}}(J_C + \alpha \cdot J_L) \qquad \text{(Eq. 3.17)}$$

Where:

- $\mathcal{D}$ is the set of allowable possible sensor configurations.
- α alters the scale of J_L.

In previous optimal sensor design studies (Bagajewicz, 2002) Equation 3.17 only considers sensor cost at specific degrees of estimability (thus J_L is excluded). Some studies include a J_L term in Equation 3.17 but due to lack of information J_L was approximated as a sum - of σ_i's of the variables being monitored (Bagajewicz, 2002; Mazzour et al., 2003). Clear guidelines for the complete formulation of Equation 3.17 (when multiple objectives are considered) must be investigated, especially the factors affecting the scaling factor.

Stellenbosch University https://scholar.sun.ac.za

Chapter 4: Methodology

4.1. Overview

The main goals of this project were to develop software for a more robust spiral interface detector and then to investigate where such sensors should be placed within a spiral plant. Before sensor placement could be investigated it was necessary to determine whether interfaces in industrial slurries can be tracked and then estimate the uncertainty of mineral interface width measurements. Optimal sensor placement also requires a plant simulation which, in turn, needs process unit models. The process by which these tasks were completed follows the diagram in Figure 4.1.

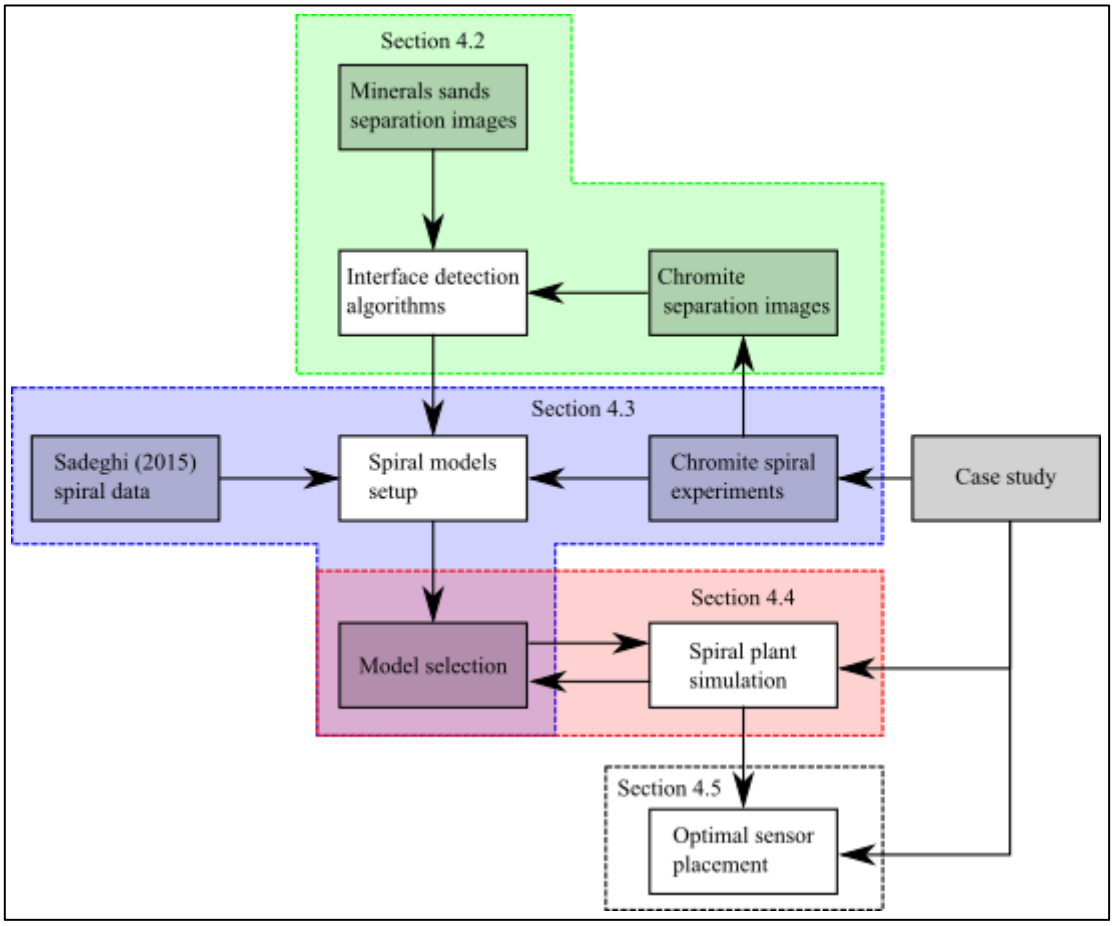

Figure 4.1: Methodology diagram (white blocks represent methodology sections in this chapter)

The image processing algorithms (see Section 4.2) that were developed were applied to mineral sands and chromite spiral separation images. Two detection algorithms were developed: one based on conventional image processing functions (Appendix A, Section 9.1) and the other based on a statistical learning approach (Appendix A, Section 9.5). The mineral sands images were the first available dataset and was used as an initial test of both algorithms. Chromite separation images became available during spiral experimentation and algorithm testing occurred in tandem with the experiments. The methodology in Section 4.2, and the final results obtained, is the more complete

Stellenbosch University https://scholar.sun.ac.za

account of work presented by Nienaber & Auret (2016) and Nienaber, McCoy & Auret (2017) which stemmed from the methodology and results in this project.

Experimental modelling was performed with a spiral (same equipment used at Glencore's Rowland plant) to investigate chromite separation – which is relevant to the case study. The superior interface detection algorithm was used to approximate mineral interface width measurements. Two spiral modelling methodologies, RSM and extended Holland-Batt models (Section 4.3), were prepared based on the experimental chromite separation data. Because the extended Holland-Batt model is a new concept, additional separation data (based on hematite beneficiation) from Sadeghi (2015) was used as preliminary validation of model parameters. Linear regression was used to approximate interface variance from experimental data – to be used for optimal sensor placement. Spiral model preparation was followed by model selection based on statistical analysis and plant simulation behaviour. The spiral plant simulation (Section 4.4) is based on the Rowland site's flowsheet.

The selected spiral model was used to perform Monte Carlo spiral plant simulations for use in the optimal sensor placement algorithms. Two sensor placement algorithms were prepared: the first is a state estimation approach and the second is based on metallurgical performance. Both methods provide means to rank optimal sensor placements based on different levels of sensor omission.

4.2. Interface detection

4.2.1. Problem outline

The preparation of interface detection software begins with the acquisition of images that shows the separation of minerals on a spiral trough. Figure 4.2 gives examples of what can be seen during spiral mineral separation and the images that can be captured. Separation is clearly visible but there are also several features that obscure viewing of mineral interfaces. Physical obstructions, reflections and shadows will all complicate interface detection. More detail on how images were acquired, during experimental work, is given in Appendix G and Appendix C.

Figure 4.2: Ilmenite sands and UG2 ore slurries separating on spiral troughs (left: ilmenite, right: chromite)

The interface detection algorithm must be able to differentiate between mineral bands and place a marker where it perceives composition change in the slurry. Desired detection examples are shown in

Stellenbosch University https://scholar.sun.ac.za

Figure 4.3 as a green arc overlay on the original image. Positions of the detected interface along with either the splitter, gulley or support column must be tracked to give a useful relative position of the interface and the state of mineral separation.

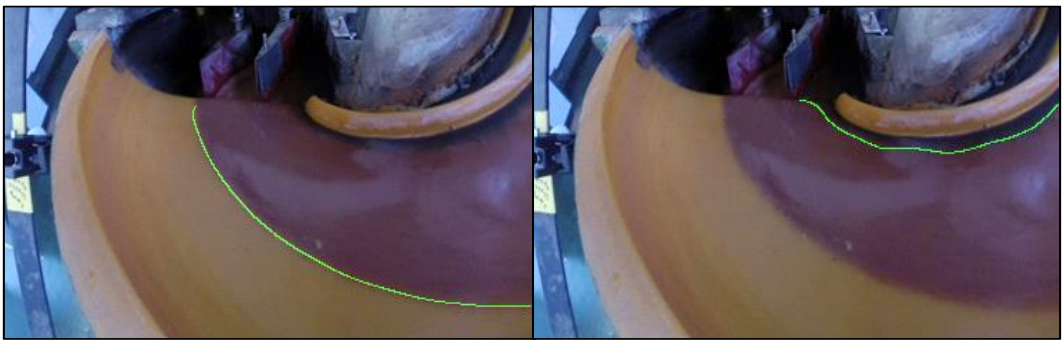

Figure 4.3: Desired detection results (left: middling interface, right: concentrate interface)

Red-green-blue (RGB) channel images, of spiral slurry separation, will serve as the input to the image processing algorithm which should finally produce binary images of the detected interface arc(s). Properties of the input images can be summarised as:

- $M \times N \times C$ size matrix.
- Pixels have 8-bit unsigned integer values.

Desired output image properties can be summarised as:

- $M_{out} \times N_{out}$ size matrix.
- Binary.
- 1 connected component per interface.
- Only true positive/negative detections.
- Localized detections.

Figure 4.4 visually compares input and output images and the possible error sources of interface detection. The calculation sequence of image processing results also roughly follows Figure 4.4. Input images are subjected to prepared/trained algorithms to produce output images which is compared to ground truths. Algorithm performance is given by measures which quantify the deviations of algorithm outputs to ground truth. Ground truth images were obtained via manual labelling of concentrate/middling interfaces (see Appendix C). Labelled images are essential in determining an interface detection algorithm's performance.

Stellenbosch University https://scholar.sun.ac.za

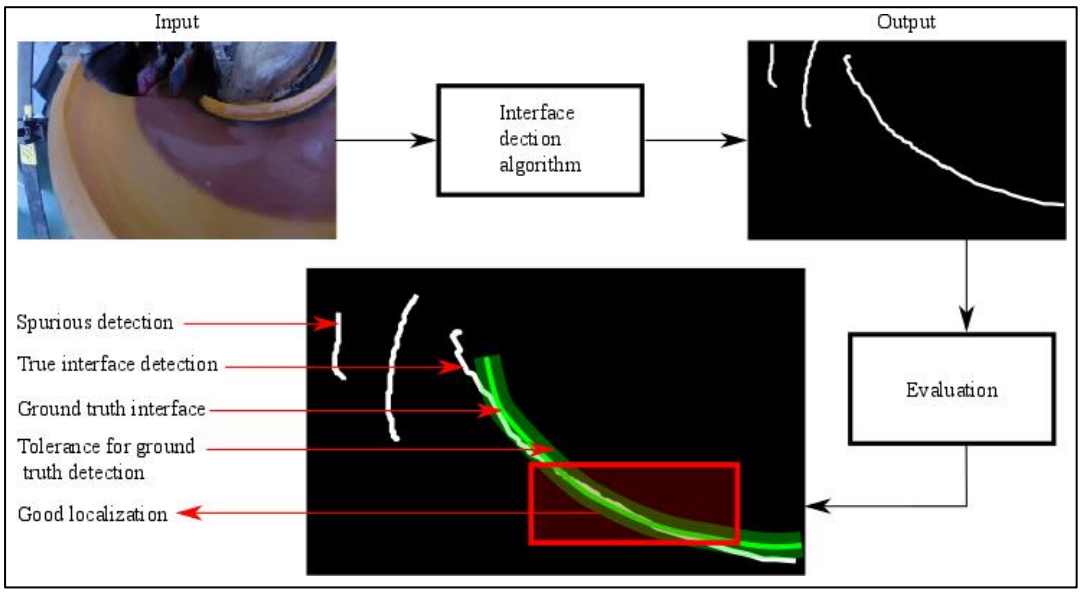

Figure 4.4: Interface detection summary

Due to the emergence of spurious detections (as seen in Figure 4.4) it is necessary to quantify image processing algorithms' training and testing performance – in order to discern which algorithm is superior. Therefore, overall objective functions, that compare algorithm outputs with labelled images, are required. Mean square error (MSE - Equation 4.1) between the algorithm output (I_{out}) and the interface ground truth (I_{label}) gives a simple similarity measure defining average deviation of the interface detection algorithm.

$$J_1 = \sum \frac{\left(I_{out,ij} - I_{label,ij}\right)^2}{M \times N} \rightarrow MSE \qquad \text{(Eq. 4.1)}$$

Better performance measures can be obtained by looking at how detections from I_{label} and I_{out} overlap. True positive interface detections are quantified using $t_p = I_{label} \cap I_{out}$, false positive detections with $f_p = \sim I_{label} \cap I_{out}$, false negatives with $f_n = \sim I_{out} \cap I_{label}$ and true negatives using $t_n = \sim I_{out} \cap \sim I_{label}$. Equations 9.11 – 9.13 from Section 9 become relevant here and help to statistically determine how well an interface algorithm performs. Averaging the true and false positive detections and then subtracting (as in Equation 4.2) them gives a performance measure that penalizes desired detection results with mistakes made by an interface detection algorithm.

$$J_2 = \sum \frac{t_{p,ij} - f_{p,ij}}{M \times N} \qquad \text{(Eq. 4.2)}$$

The range of J_1 in Equation 4.1 is $[0, \infty)$ and is essentially a crude absolute similarity measure – making no distinction between different detection types. J_2 has the range $[\frac{t_p}{M \times N}, -\infty)$ with positive and negative values clearly reflecting true and false positive detection rates. Lower values of J_1 will correspond to better interface detection while higher J_2 values indicate better t_p detections.

Stellenbosch University https://scholar.sun.ac.za

Two approaches were used to address the interface detection problem and both receive the same inputs and are finally evaluated according to Equations 4.1 and 4.2. Both methods constitute supervised learning problems yet train fundamentally different functions. The first approach (Algorithm CVI – computer vision algorithm I) uses a combination of established image processing functions to essentially reduce the interface detection problem to an edge detection problem. The second approach (Algorithm CVII – computer vision algorithm II) uses statistical learning to prepare functions that classify pixels based on pixels in its surrounding neighbourhood.

4.2.2. Algorithm CVI: Edge detection approach

The first interface detection algorithm uses median filtering, histogram equalization, Canny edge detection and morphological operations – organized in sequence to generate binary images from RGB input images (see Appendix C for details). Figure 4.5 presents the potential interface detection algorithm. RGB channels of incoming spiral slurry images are scaled, added, equalized and filtered before edge detection and morphological filtering steps.

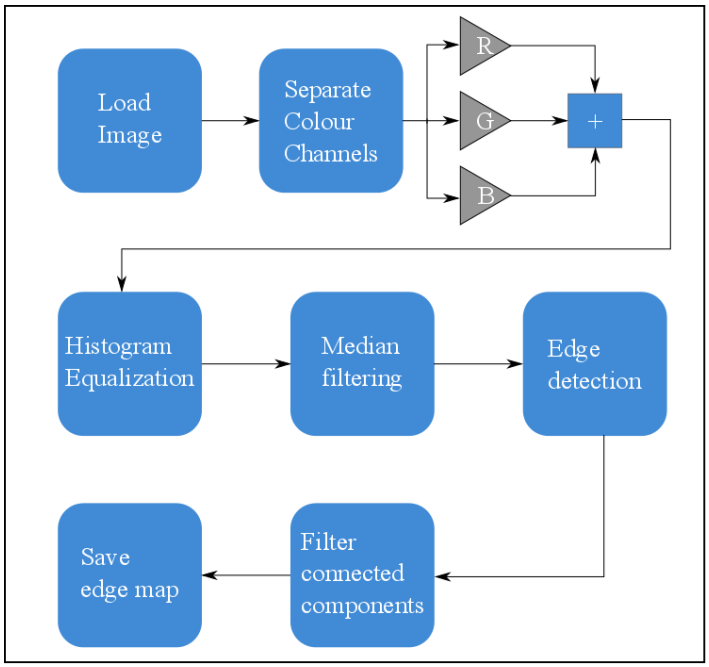

Figure 4.5: Simplified interface detection algorithm CVI

The image processing steps mentioned in Figure 4.5 introduces 13 parameters which are shown with their respective functions in Section 11.1. Parameters are optimised, on training images sets, using a genetic algorithm (GA). Optimised parameters, obtained on different training sets, are tested against a testing image set.

4.2.3. Algorithm CVII: Logistic regression approach

Algorithm CVII finds interfaces by first classifying pixels which belong to background, concentrate or middlings regions in an image of spiral slurry. After the classification of a slurry region as concentrate, an interface is found by isolating certain edges as summarised in Figure 4.6.

Stellenbosch University https://scholar.sun.ac.za

Morphological operations are used to find perimeters of the segmented slurry region(s) (obtained from logistic classification) and then specific pixels, of an interface, are identified via polar coordinates (see details of Algorithm CVII in Appendix C).

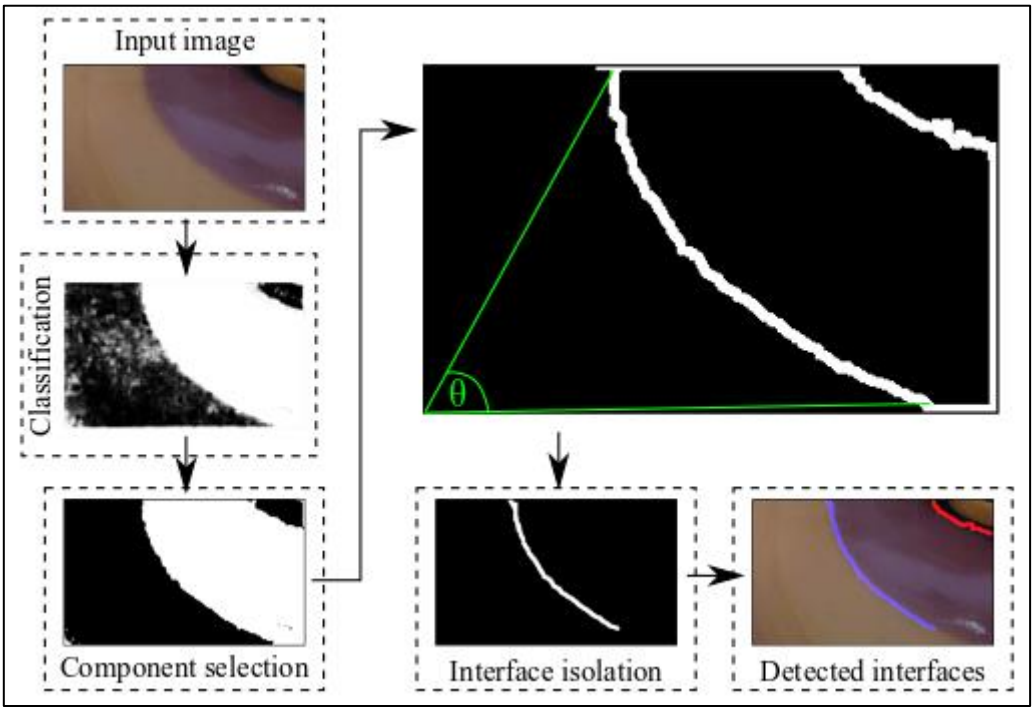

Figure 4.6: Interface extractions

Feature extraction is done using pixels of $m \times n$ neighbourhoods from each colour channel and classification is done by training a logistic regression function. Pixel labels, used for classifier training, are obtained by manual labelling of slurry images – similar to the case of Algorithm CVI. However, the labels for the logistic regression training case was the slurry instead of interface lines (used for training of Algorithm CVI). Training of logistic regression classifiers were done using unconstrained conjugate gradient search. Testing results for Algorithm CVII were prepared for the slurry and interface detection cases.

4.3. Spiral modelling

4.3.1. Process stream inference and response surface methodology execution

A detailed account of the experimental procedure is provided in Section 11.2 (of Appendix C). The experimental design used was a 4-factor Box-Behnken design to determine concentrate and tailings stream responses as feed grade (x_1), feed SG (x_2), feed flow rate (x_3) and primary splitter settings (x_4) change. Measured responses include concentrate and tailings flow rates and densities obtained during sampling. The remainder of this section discusses the inference used to determine grade(s) and recovery(s) – to be used in regression modelling.

Solids densities and solids composition must be determined from total mass flowrates, solids mass flow rates, volumetric flowrates and density measurements that were collected, from feed and product

Stellenbosch University https://scholar.sun.ac.za

streams, after experimentation. Equation 4.3 can be used to determine the solids density of feed or product streams (incompressibility of liquid and solids phases is assumed).

$$\frac{1}{p_{slurry}} = \frac{X_2}{p_{solids}} + \frac{1-X_2}{p_w} \qquad \text{(Eq. 4.3)}$$

Where:

- Slurry density is p_{slurry}.
- Water density p_w is equal to 0.99 g/cm^3.
- X_2 represents solids mass fraction.
- Solids density is p_{solids}.

A rough estimation of solids composition can be obtained by setting up a calibration curve between solids density and the concentration of a MOI. The chromite separation problem is simplified by considering the feed slurry as a combination of HM and light mineral (LM) species which is separated in the spiral product streams. Using this simplification, the MOI of this problem becomes the HM and the spiral concentration problem becomes concerned with HM recovery and grade in the concentrate stream (stream 7 in Figure 11.8). The shape of the calibration curve is given by Equation 4.4.

$$p_{solids} = b_1 + b_2 X_3 \qquad \text{(Eq. 4.4)}$$

Where:

- b_1 and b_2 are regression parameters.
- X_3 is the HM grade (as mass fraction).

The regression parameters of Equation 4.4 can be solved by using the solids density and composition analysis results from the representative samples obtained from homogenised ore to be used as spiral feed during the experimental tests. HM serves as a good indicator of Cr_2O_3 and Fe_2O_3 content and LM is an indicator of SiO_2 and Al_2O_3 content.

If XRF analysis of all experimental samples are available then Cr_2O_3 grade and recovery can be directly computed, however, obtaining true p_{solids} values can still be challenging. XRF provides major component composition analysis of solids but does not provide composition of different mineral phases (which in turn can be used to determine solids density precisely). Equation 4.3 is still required when all samples can be analysed via XRF which also implies that Equation 4.4 can be prepared to validate XRF results (for future composition analysis).

Because all stream measurements are repeated 3 times during experimentation it is possible to prepare rough estimates of all measurement expected values and variances. Once these values are available it is possible to perform reconciliation of the measurements using the spiral equipment mass balance and assuming all measurement distributions follow the Gaussian distribution. It is assumed that gross

Stellenbosch University https://scholar.sun.ac.za

errors are not present. It is also assumed that steady-state is achieved. Because every stream around the spiral concentrator, was observed, reconciliation implies that improved variable expected values and variances can be obtained.

The connectivity matrix M for the mass flow rates of the spiral in Figure 11.8 is $M = [1, -1, -1]$. Total mass flow rate, solids fractions and HM grades can be reconciled to give more precise expected values and variances for the measured variables. The reconciliation problem can be stated, using Equation 3.11 from Section 3.5, as Equation 4.5.

$$\min_{X} J = (Y - X)^T V^{-1} (Y - X) \qquad \text{(Eq. 4.5)}$$

s.t.

$$\begin{bmatrix} 1 & -1 & -1 & 0 & 0 & 0 & 0 & 0 & 0 \\ 0 & 0 & 0 & 1 & -1 & -1 & 0 & 0 & 0 \\ 0 & 0 & 0 & 0 & 0 & 0 & 1 & -1 & -1 \end{bmatrix} \begin{bmatrix} X_1 \\ X_1 \odot X_2 \\ X_1 \odot X_2 \odot X_3 \end{bmatrix} = z(X) = 0$$

Where:

- Y contains measured mass flow rate, solids fraction and HM grade averages of feed and product streams.
- V is the variance values flow rate, solids fraction and HM grade variables.
- $X = \begin{bmatrix} X_1 \\ X_2 \\ X_3 \end{bmatrix}$.

Equation 4.5 can be solved using successive linearization (see Section 11.3.1). The linearized constraints (with linearization performed around Y) are given by Equation 4.6. During successive linearization, constraints are linearized around the current iteration's $\hat{X}$ (after the initial iteration). Solutions of Equation 4.5 will have the same form as Equation 3.13. 5 Successive linearization steps were used to perform the data reconciliation of experimental data. Variance updates can be performed as show by Equation 3.14.

$$z(Y) + \begin{bmatrix} M & 0 & 0 \\ M \odot X_2^T & M \odot X_1^T & 0 \\ M \odot (X_1 \odot X_2)^T & M \odot (X_1 \odot X_2)^T & M \odot (X_1 \odot X_2)^T \end{bmatrix} (X - Y) = 0 \qquad \text{(Eq. 4.6)}$$

After spiral concentrator feed flow rates, solids fractions and grades (of the feed and product streams) have been reconciled, new estimates of spiral feed settings can be attained (giving precise estimates of the feed conditions obtained during experimentation – see Section 9.3.1). New feed HM grade estimates are directly obtained after reconciliation which, in turn, can be used to find feed p_{solids} according to Equation 4.4. Finally, feed slurry density can be calculated with Equation 4.3 which can be used to find the feed volumetric flow rate. The spiral output responses considered for modelling are tailings and concentrate HM grade, HM recovery and concentrate-tailings flow ratio (simply the mass

Stellenbosch University https://scholar.sun.ac.za

flow rate of concentrate divided by the mass flow rate of tailings). A flow ratio model gives a method with which to determine the overall mass balance around a spiral. Grade and recovery models allow calculation of solids and HM balances around a spiral. The same feature set is used to formulate all response models. Lastly, interface responses are also modelled to determine detection variance for sensor placement (see Sections 4.5 and 11.3).

Regression modelling of spiral responses were performed using MATLAB's fitlm() (for linear or full quadratic models) and stepwiselm() (for linear or full quadratic model parameter selection) functions from MATLAB's Statistics and Machine learning Toolbox. The function stepwiselm() reduces full quadratic models (see Equation 9.14 in Section 9.2) by keeping the significant parameters that minimize some model criterion. Default settings for stepwiselm() were used during spiral response model fitting which means that parameters are removed from the full quadratic model in a way that minimizes the regression model squared sum of errors. This will also tend to reduce F-test p-values resulting in models with improved statistical significance. Parameters are removed one by one based on their coefficient t-test p-values (Montgomery, 2001: 412). The parameter with the highest p-value is removed and then regression is repeated to find the new coefficient with the highest p-value. This process is repeated until none of the remaining coefficients have p-values higher than some threshold. Linear terms with p-values higher than the default threshold can still be included in the model if interaction or higher order terms of those linear terms are significant. The default coefficient p-value threshold, of stepwiselm() as implemented in MATLAB, is 0.1.

4.3.2. Extended Holland-Batt spline model

RSM spiral modelling was performed firstly because it was considered in recent literature (see Section 3.1) and secondly it allows inexpensive investigation of many experimental factors. This is especially useful to quickly model interface changes for the industrial slurry case. The cost benefits of RSM was particularly helpful in quickly acquiring models for spiral plant simulation. However, as mentioned in Section 3.1, RSM is not designed for metallurgical plant simulation. Therefore, an alternative, or in this case, an extended version of Holland-Batt's (1990) model is required to compare plant simulation ability.

Adding feed flow rate and slurry density terms to Equation 3.2 will help provide a more complete spiral concentrator model. Equation 3.2 can be extended to Equation 4.7 by adding two additional regression parameters.

$$R_2 = W^{a_2 + a_3 \Delta F + a_4 \Delta S} \qquad \text{(Eq. 4.7)}$$

Where:

- ΔF is a relative change in feed flow rate (t/h).
- ΔS is a relative change in feed slurry density (in SG).

Stellenbosch University https://scholar.sun.ac.za

Another critical component to fitting the Holland-Batt spline is finding the transition point between R_1 and R_2. The transition will occur when $R_1(T) = R_2(T)$; where $W = T$ is the transition point. Substituting Equations 3.1 and 4.7 leads to $a_1 T = T^{a_2 + a_3 \Delta F + a_4 \Delta S}$. Then the resulting equation is $R_1 = T^{a_2 - 1 + a_3 \Delta F + a_4 \Delta S} W$. Finally, Equation 3.1 can be rewritten as Equation 4.8. Equation 3.3 is left unchanged.

$$R_1 = a_1^{a_2 - 1 + a_3 \Delta F + a_4 \Delta S} W \qquad \text{(Eq. 4.8)}$$

Where:

- T is renamed a_1. The previous definition of a_1 is not necessary during optimization and, therefore, discarded (thereby reducing the number of parameters to estimated).

The same factor centre levels from Section 11.2 (for the RSM case) is used to calculate $f' - f$, ΔF and ΔS. Another equation is required to determine MOI recovery at W' for a feed grade based perturbation of a reference Holland-Batt spline. Here the reference Holland-Batt spline refers to the function that exactly follows Equation 3.3 (meaning no feed grade adjustment is present). Suppose we have a reference Holland-Batt spline and its extrapolation is at f' (see Figure 4.7). The new extrapolated curve will not necessarily follow Equation 3.3 precisely (the shape of the reference curve) because after feed extrapolation Equation 3.3 is technically substituted into Equations 3.4 and 3.5. Equation 3.3 is needed to find R' but first the corresponding W and R values on the reference curve must be found. The required calculation route $W' \rightarrow W \rightarrow R \rightarrow R'$ is shown in Figure 4.7.

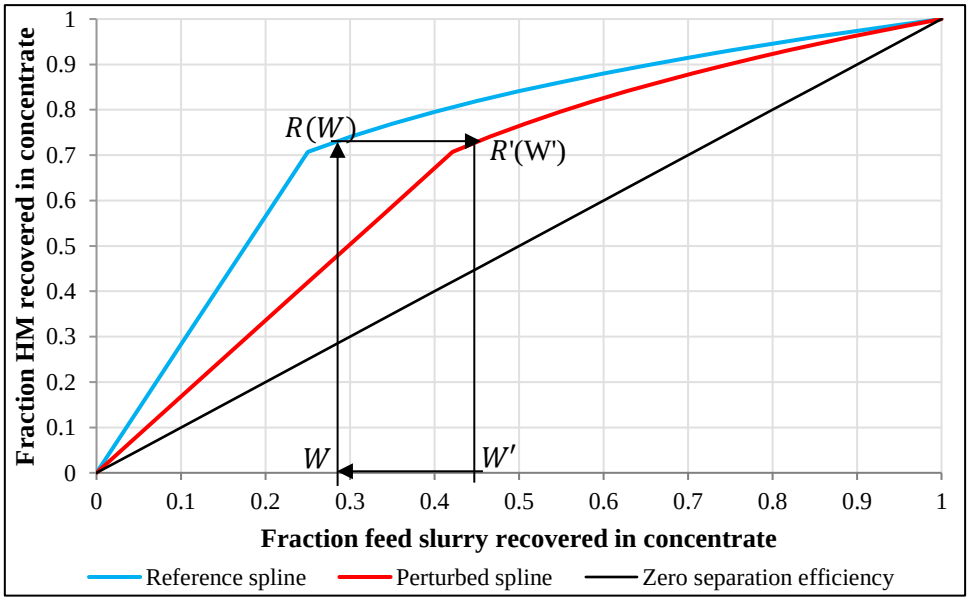

Figure 4.7: Calculation of R' at W' (the query feed slurry recovery)

Firstly, the W value (at a reference Holland-Batt spline) corresponding to a query W' must be determined. This can be achieved by formulating a minimization problem around Equation 3.5. Equation 4.9 expresses the associated optimization problem.

Stellenbosch University https://scholar.sun.ac.za

$$W^* = \underset{W}{\operatorname{argmin}} \left(W' - W - \frac{R(W)-W}{1-f} \cdot (f' - f) \right)^2 \qquad \text{(Eq. 4.9)}$$

Once the reference W is known Equation 3.3 can be interrogated to get $R(W)$ which in turn allows the use of Equation 3.4 to find $R'(W)$. Equation 4.10 shows how Equation 3.4 may be arranged to find the desired recovery value.

$$R'(W') = \frac{R(W)-W}{1-f}(1 - f') + W' \qquad \text{(Eq. 4.10)}$$

Equations 4.8, 4.7, 3.3, 3.4, 3.5, 4.9 and 4.10 are required to implement the Holland-Batt spline for changing feed conditions. Concentrate HM and solids phase recoveries were modelled with the extended Holland-Batt spline (this is required for spiral plant simulation). Constrained non-linear regression was performed in MATLAB, using constrained conjugate gradient based optimization (the fmincon implementation from MATLAB's Optimization Toolbox was used here), to solve parameters a_1 to a_4. Random initialisation was used for parameters a_2, a_3 and a_4 by sampling 3 values from a standard normal distribution (white noise model). The initial value for a_1 was arbitrarily chosen as 0.3. A simple least squares objective function, similar to Equation 4.5, was used. However, a V term was excluded (no weighting i.e. $V = 1$). Equation 4.9 is solved using MATLAB's fzero function (initial value used is W').

The lower and upper bounds for $[a_1, a_2, a_3, a_4]$ are $[0,0,0,-\infty)$ and $[1,\infty,\infty,\infty)$. Parameter a_3's interval is $[0,\infty)$ because the Holland-Batt (1990) paper concludes that higher feed flow rates should move R_3 closer to the $R = W$ line. This statement is supported by the work of Richards et al. (2000: 68) for the processing of fine minerals. Non-linear constraints for the model is based on Equation 4.7. Recovery values must remain in the interval $[0,1]$ to ensure a valid Holland-Batt spline. The constraint follows Equation 4.11.

$$W^{a_2 + a_3 \Delta F_i + a_4 \Delta S_i} \leq 1 \qquad \text{(Eq. 4.11)}$$

Where:

- ΔF_i and ΔS_i are column vectors with a length equal to the number of elements in the feature space.

Sections 4.3.1 and 4.3.2 present two spiral models: one is linear and the other non-linear. After regression is performed it is necessary to determine the best model. One method is to use the Akaike information criterion (Equation 4.12; Cavanaugh, 1997: 202). Akaike information criterion (or AIC) of different models can be compared to determine the model closest to the original data generating model. The model showing the lowest AIC is taken as the best. When a feature set is small ($n \ll (k+1) \cdot (2k+1)$) the corrected AIC (or AICc), represented by Equation 4.13, is used (Cavanaugh, 1997: 202).

Stellenbosch University https://scholar.sun.ac.za

$$AIC = -2\log\left(\frac{1}{(2\pi(J/n)^2)^{n/2}}e^{-\frac{SSE}{2\hat{\sigma}^2}}\right) + 2k \qquad \text{(Eq. 4.12)}$$

$$AICc = AIC + \frac{2k^2+2k}{n-k-1} \qquad \text{(Eq. 4.13)}$$

Where:

- k is the number of model parameters.
- The number of observations are n
- $(J/n)^2 = SSE/n. SSE = sum\ squared\ error.$

The derivation of the AIC follows for general functions but the AICc is originally proposed for linear regression. However, AICc has been justified for linear, non-linear and auto-regressive problems (Cavanaugh, 1997: 202; Hurvich & Tsai, 1989: 298).

4.4. Spiral plant simulation

After empirical models of the Multotec SC21 spiral have been prepared it is possible to model a steady-state mass balance for a spiral circuit section. The WPL spiral circuit, as presented in Section 2.2, will be modelled based on the models obtained via the methodology of Section 4.3. Information on the plant is limited with almost no measurements of process stream variables available. PSD and Cr_2O_3 concentration in the feed and product streams were available and serve as useful guidelines for typical process states.

Input variables (mostly unavailable states) to the spiral circuit include:

- Feed stream mass flow rate, solids concentration, MOI grade and feed PSD.
- Process water additions.
- Splitter settings of spirals within each spiral bank.
- Spiral circuit topology and the number of spirals per spiral bank.

Output variables (mostly unavailable states) of the spiral circuit include:

- Mass flow rate, solids concentration, MOI grade and PSD within every process stream (excluding feed).
- Concentrate interface estimates in the different spiral banks.
- Overall product grade and recovery within plant concentrate and tailings streams.

Figure 16.1, in Appendix H, gives a simplified PFD for the WPL circuit. This spiral circuit can be considered as a combination of a primary and secondary (scavenger) circuit. Primary circuit spirals include roughers, cleaners, recleaners and re-recleaners. Secondary circuit spirals include the scavengers, scavenger cleaners, scavenger recleaner and scavenger re-recleaner spirals. Pumps and feed tanks are not considered in the PFD and instead tanks are assumed to be mixing or splitting

Stellenbosch University https://scholar.sun.ac.za

points. The original PFD (see Section 2.2 and Appendix E) shows that feed tanks often have overflows that are recycled to various spiral banks; however, that is also omitted here (due to lack of information). Only major process streams (overall feed, concentrate and tailings streams) are considered for spiral circuit modelling purposes.

Figure 4.8 gives the primary spiral circuit (of the WPL plant) obtained from the more complete PFD in Figure 13.1 (Appendix E). Simulating the process in Figure 13.1 will require ignoring a cyclone that produces feed for the scavenger spiral bank and ignoring the fact that Multotec HX5 spirals are used in the scavenger circuit. The cyclone that produces the scavenger feed also produces a tailings stream, some of which is recycled at the scavenger cleaner spiral bank. Simulating the scavenger circuit is not feasible since only models for the SC21 spiral are available and PSD information is not included in the scope of Section 4.3 (since change in PSD is not included, cyclones cannot be modelled).

Only simulation of the primary circuit (as shown in Figure 4.8) of the WPL spiral plant is considered. Mass flow rates, solid fractions, and HM grades in every stream will be estimated along with operational states of the four spiral units. PSD of the process streams was not investigated experimentally and will ignored in this stage of spiral plant simulation.

Stellenbosch University https://scholar.sun.ac.za

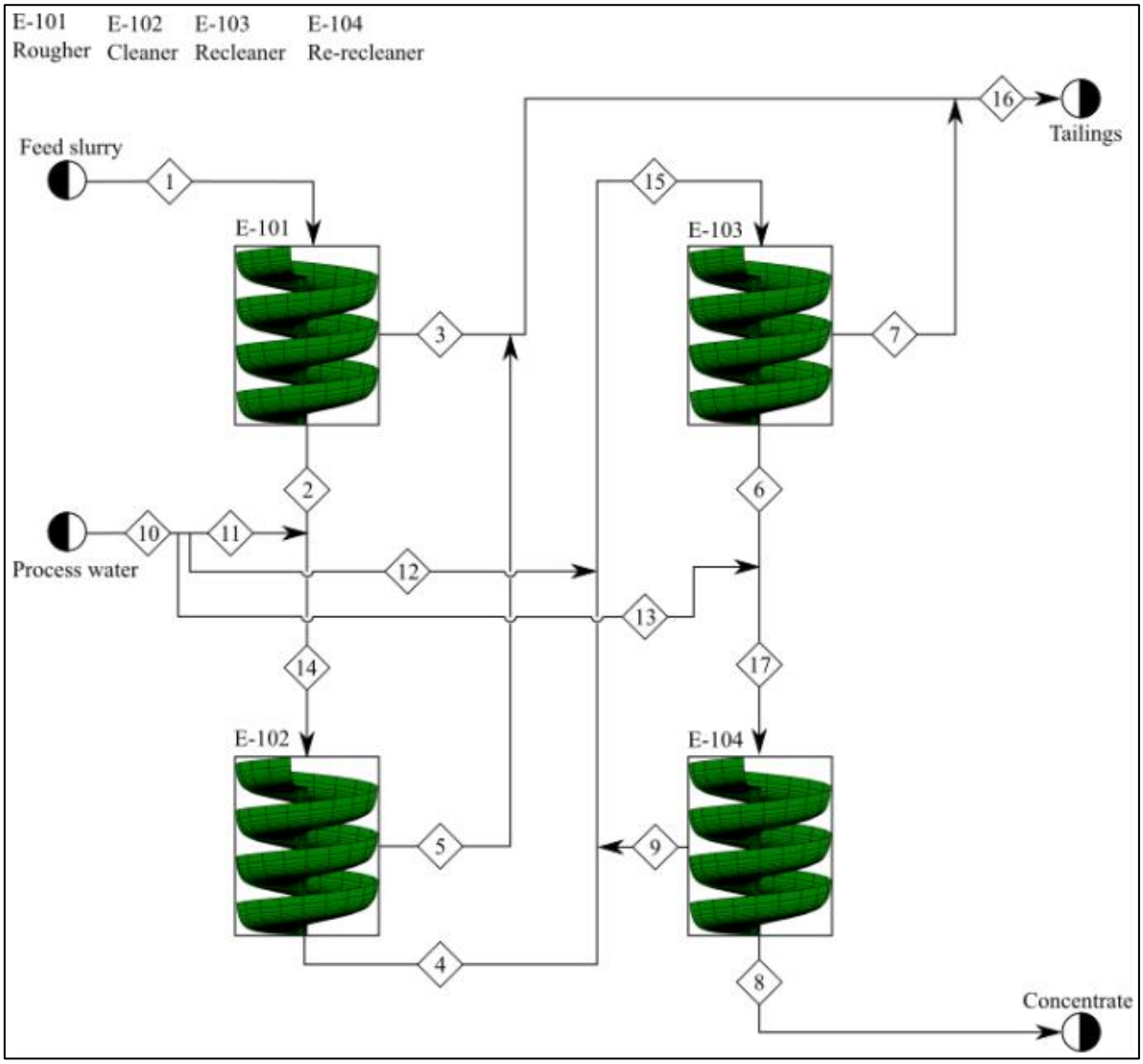

Figure 4.8: Primary circuit PFD (obtained from Figure 16.1)

Solving the primary spiral circuit process streams is approached as an optimization problem whereby squared mass and material balance errors are minimized. The parameters to be optimized include mass flow rates, solid fractions and HM grade of the streams 2, 3, 4, 5, 6, 7, 8 and 9. Combining material balances with the SC21 spiral models allows simulation of the process (by finding the single global optimum) when only feed stream properties are available.

A few assumptions are required to solve the state of the process streams in Figure 4.8. Each spiral bank contains a different number of spirals; however, the spiral models that were developed are valid for double start spirals. The number of spirals within the different spiral banks (for the primary circuit) is 72 for the rougher section, 54 for the cleaner spirals, 42 for the recleaners and 24 in the re-recleaner spiral bank. Then, the first assumption, is that feed to every spiral bank is perfectly distributed, meaning each spiral receives feed with the same solids fraction and HM grade. The second assumption is that each spiral bank is modelled as if it consists of double start spirals (e.g. the rougher bank is modelled as 36 double start spirals). Thirdly, it is assumed that process water additions at streams 11, 12 and 13 are 60 t/h (to ensure spiral feed flow rates remain close to

Stellenbosch University https://scholar.sun.ac.za

experimental design flow rates). Lastly, all spiral splitter settings will be the largest possible value (spanning 10.5 cm of the trough width) or in terms of the centered values, 1. Feed slurry recovery fractions, needed to evaluate the Holland-Batt spline, will be estimated from the RSM functions. PSD is assumed to be identical along all process streams.

The feed conditions at which the primary plant optimization problem will be evaluated at are given in Table 4.1. Mass flow rates are based on the operating conditions SC21 spirals are designed for. Solids fractions are at the minimum of the SC21 spiral's typical operating conditions. Grade values are based on experimentally observed HM content in feed samples.

Table 4.1: Feed stream conditions

Condition set	Mass flow rate (t/h)	Solids fraction	HM grade
1	316.8	0.15	0.50
2	316.8	0.15	0.65
3	385.2	0.15	0.65

Additional restrictions on the RSM-based spiral models are necessary in the code implementation so that values outside [0, 1] are not attained. Thus, the form of the RSM spiral models required in the spiral plant simulation problem is Equations 4.14 – 4.16. The mass-yield models do not require such corrections when the constraint of Equation 4.11 is met.

$$\frac{X_{1,Conc}}{X_{1,Tails}} = \begin{Bmatrix} g_1 & if\ 0 \leq g_1 \\ 0 & if\ \ g_1 < 0 \end{Bmatrix} \qquad \text{(Eq. 4.14)}$$

$$X_{3,Tails} = \begin{Bmatrix} 1 & if\ \ g_2 > 1 \\ g_2 & if\ \ 0 \leq g_2 \leq 1 \\ 0 & if\ \ g_2 < 0 \end{Bmatrix} \qquad \text{(Eq. 4.15)}$$

$$\frac{X_{1,Conc}X_{2,Conc}X_{3,Conc}}{X_{1,Feed}X_{2,Feed}X_{3,Feed}} = \begin{Bmatrix} 1 & if\ \ g_3 > 1 \\ g_3 & if\ \ 0 \leq g_3 \leq 1 \\ 0 & if\ \ g_3 < 0 \end{Bmatrix} \qquad \text{(Eq. 4.16)}$$

Where:

- $X_{1,Conc}$ and $X_{1,Tails}$ are concentrate and tailings stream mass flow rates, $X_{3,Tails}$ is the tailings HM grade and $\frac{X_{1,Conc}X_{2,Conc}X_{3,Conc}}{X_{1,Feed}X_{2,Feed}X_{3,Feed}}$ is the concentrate HM recovery.
- g_1, g_2 and g_3 are the flow-ratio, tailings HM grade and HM recovery RSM models evaluated at the respective spiral bank feed conditions.

An iterative approach was used to solve the recycle stream (stream 9). Firstly, the plant mass and species balances are solved, assuming no recycling is present. Then the balances over the recleaner

Stellenbosch University https://scholar.sun.ac.za

and re-recleaner spirals are revaluated, with stream 9 contributing to recleaner feed, to determine new plant states. This process is repeated 10 times in order to solve plant states around the final two spiral banks. Code for the plant simulation problem was prepared in MATLAB.

4.5. Interface sensor placement

4.5.1. Overview

After successful interface detection algorithms and spiral models (with plant simulations) can be established it is possible to quantify sensor performance. Two optimal sensor placement algorithms were prepared, and results are compared to determine suitability of state estimation based methods vs. potential metallurgical performance based methods. Both methods are evaluated at several different feed conditions to determine sensor placement robustness (and to evaluate any sensitivities). The required workflow is illustrated in Figure 4.9 – showing the associated sections of the methodology.

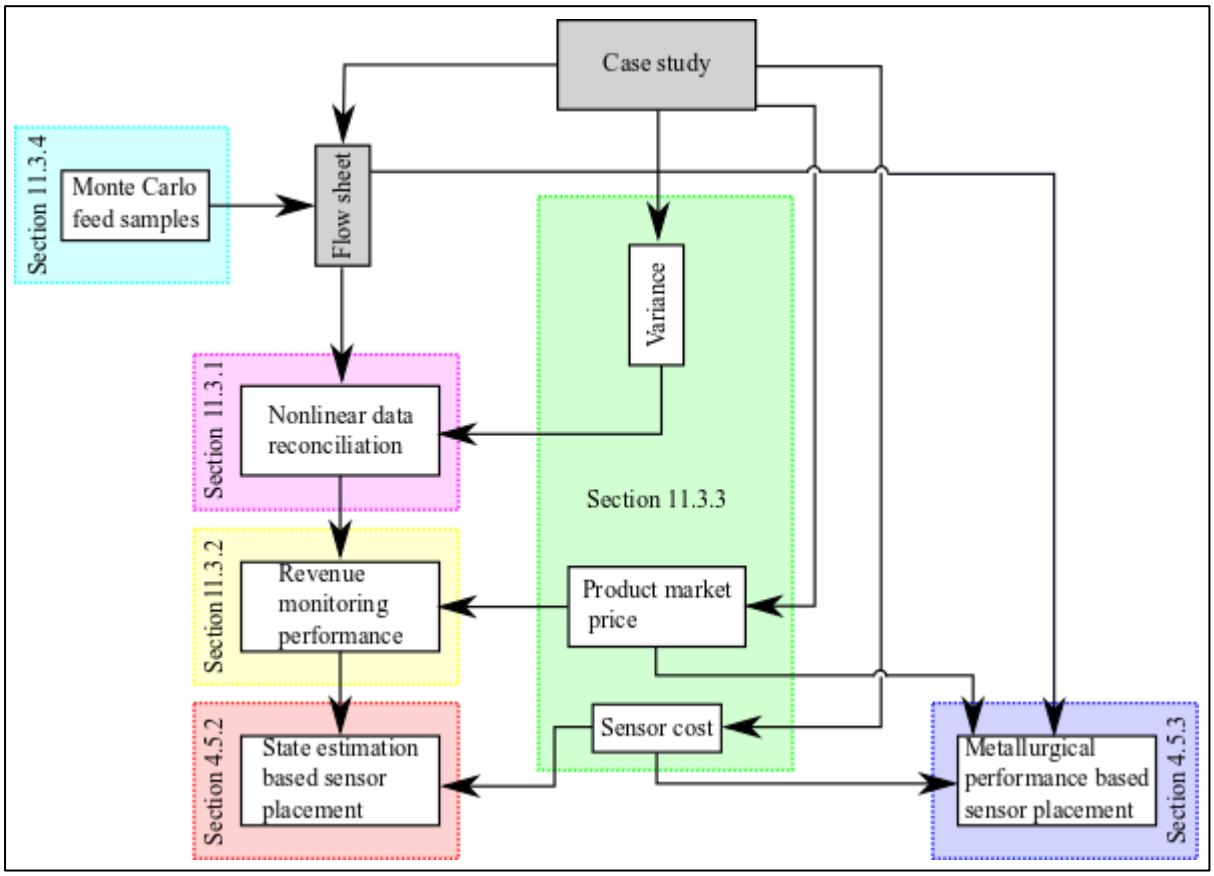

Figure 4.9: Methodology workflow diagram

An appropriate J_L objective for the state estimation approach is derived in Section 11.3.2, where performance is defined by revenue estimation, to be used in Equation 3.17. Nonlinear data reconciliation (Section 11.3.1) was used to perform primary circuit state estimation. Sensor prices, costs and concentrate HM values (for both algorithm instances) are assumed to be constant. Both optimal sensor placement algorithms are iterated over 30 Monte Carlo plant simulations to determine sensitivity of sensor placement results.

Stellenbosch University https://scholar.sun.ac.za

4.5.2. Algorithm SPI: State estimation based placement

Algorithm SPI (sensor placement algorithm I) is the first optimal sensor placement strategy and is formulated by combining the methods in Sections 11.3.1 – 11.3.4 (resulting in a mixed integer programming problem). Before optimal C can be searched it is required to solve process stream states of the WPL primary circuit for all sampled feed conditions (Section 11.3.4). This is achieved by using the methodology in Section 4.4 except that the splitter settings, used for each case, are accepted as 30 % of spiral bank feed flow rate (for each spiral bank mentioned in Section 4.4). Slitter settings are kept constant during sensor placement analysis. The solved process stream values are augmented by adding noise values based on Table 11.6 (assuming Gaussian distribution). This allows data reconciliation to solve the process mass/species balances and find the necessary state updates.

C^* are searched, at a sampled feed condition, by using a binary coded GA to search $C \in \mathcal{D}$. GAs search for optimal solutions to an objective function by stochastically generating populations of potential solutions which are perturbed by operators inspired by natural selection: selection, crossover and mutation (Deep, Singh, Kansal, and Mohan, 2009). GA populations contain a number of possible solution instances or chromosomes (which are manipulated at every iteration) that can be coded in different ways. The two most common codings use real or binary coded chromosomes.

The length of the GA's chromosomes is equal to the number of allowed sensors in C. A zero entry, in a chromosome, indicates that a sensor is removed, and 1 means a sensor is present. It is assumed that plant feed conditions, process water additions and concentrate are always monitored (this applies to flow rate, solids content and grade where applicable). Feed HM grade is measured by online XRF and concentrate HM grade is estimated by interface sensors. Table 4.2 lists the eligible sensors for C according to process stream numbers in Figure 4.8. Each C is a vector formed by concatenating the rows in Table 4.2 (with sensor presences allotted with either 0s or 1s).

Table 4.2: Plant I's process streams considered for sensor placement (as used by Algorithm SPI)

	Stream number						
Sensor	2	3	4	5	6	7	9
Mass flow rate	X	X	X	X	X	X	X
Solids fraction	X	X	X	X	X	X	X
Online XRF	-	X	-	X	-	X	X
Interface model	X	-	X	-	X	-	-

Algorithm SPI calculates monitoring performance values (according to Equation 11.34), at a feed state iteration, for each C in its population by using updated state estimates (obtained via nonlinear reconciliation). These values are combined with J_C values from the different chromosomes to search

Stellenbosch University https://scholar.sun.ac.za

for the best C (with $\alpha = 1\ hr^2$). Costs are calculated via Equation 3.15 and using the prices listed in Table 11.7. The cost of interface sensor implementation is based on the number of spirals per spiral bank. It is assumed that interface sensor implementation at a spiral bank requires that all spirals be monitored. Thus, interface sensor placement cost at the roughers will be the most expensive followed by cleaners, recleaners and re-recleaners.

MATLAB's implementation of a binary coded GA was used to find the optimal sensor configurations. The following GA specifications were used to solve the problem:

- Population: 500 chromosomes.
- Selection: stochastic uniform.
- Mutation: uniform.
- Cross-over: scattered.

The stopping criteria are:

- Generation stall limit of 100 generations.
- Objective function tolerance of 10^{-10}.

At least one chromosome, in the initial population, is set to the C that includes all sensors. This initialisation helps the GA to avoid local minima or plateaus. All other MATLAB GA stopping criteria were left at default settings. Optimization was done using a virtual machine (VM) running on a Dell PowerEdge R610 server with 12 physical CPU cores clocked at 3.324 GHz (with hyperthreading active) and 96 GB of RAM.

4.5.3. Algorithm SPII: Metallurgical performance based placement

Algorithm SPI follows standard methods in literature but suffers a serious flaw when sensor variance/price trade-offs are considered. These two performance measures can differ significantly in scale making them difficult to compare (especially when plant monitoring information is lacking). The methods of Bagajewicz (2002) & Mazzour et al. (2003) also usually focus on sensors that measure flow rates (total mass, phase or species flow) and, therefore, typical optimal sensor placement algorithms do not lend itself to different sensor placement problems (that is to say sensors not focused on flow rate measurements). To cater specifically for the optimal interface sensor configuration problem a different approach is required – one related to metallurgical plant separation performance. The methods from the previous sections (Sections 11.3.1 & 11.3.5) tries to find the C that minimizes upgrade cost and revenue monitoring variance. With Algorithm SPII (sensor placement algorithm II) it is desired to determine how different C affect the steady state optimization of the concentrate HM grade/recovery trade-off.

Thus, the second interface placement algorithm is based on finding the interface sensor configurations C that can allow operators to (potentially) adjust a spiral process to its overall optimal metallurgical

Stellenbosch University https://scholar.sun.ac.za

performance. In Algorithm SPII's case C refers to the combination of spiral banks being monitored/controlled (for instance C_1 represents the rougher spirals, C_{11} is the rougher-cleaner-recleaner spirals and C_{15} will represent all spirals; see Table 4.3).

Table 4.3: Sensor placement configurations

C	Sensor location(s)
1	Rougher
2	Cleaner
3	Recleaner
4	Re-recleaner
5	Rougher, cleaner
6	Rougher, recleaner
7	Rougher, re-recleaner
8	Cleaner, recleaner
9	Cleaner, re-recleaner
10	Recleaner, re-recleaner
11	Rougher, cleaner, recleaner
12	Rougher, cleaner, re-recleaner
13	Rougher, recleaner, re-recleaner
14	Cleaner, recleaner, re-recleaner
15	All

Optimization objectives (for each C in question) are the overall concentrate stream HM grade and recovery. Maximization of grade and recovery objectives requires adjusting concentrate HM grade/recovery values to 1 (via splitter manipulation as allowed by C). Figure 4.10 shows typical attainable recovery and grade values, for a metallurgical process, at certain feed conditions. The red dot in Figure 4.10 moves along the blue curve for different splitter settings (the blue curve shifts as feed condition or structural conditions change) and the optimal position of the red dot is the point closest to (1, 1).

Stellenbosch University https://scholar.sun.ac.za

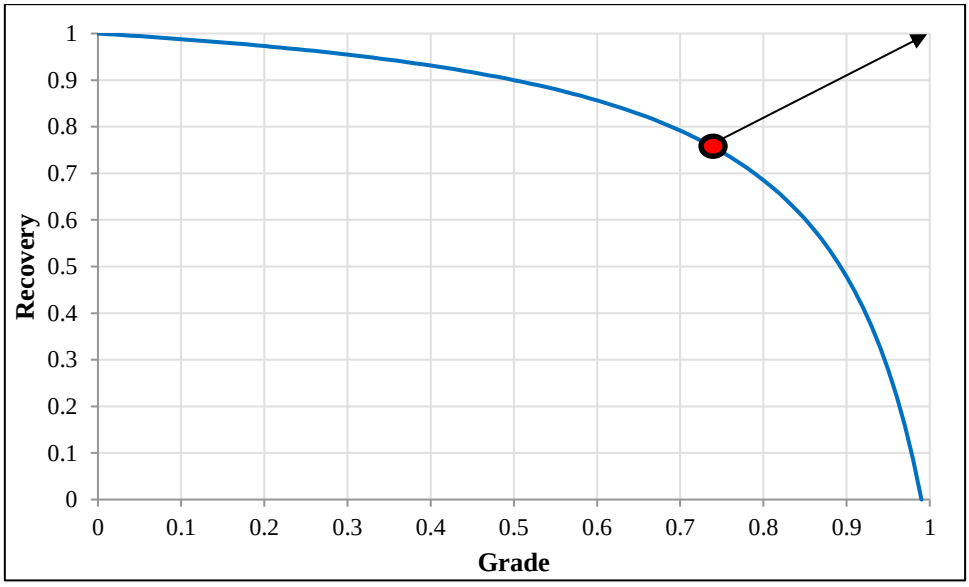

Figure 4.10: Example of a simple grade recovery curve with the black arrow showing direction of metallurgical optimization (adapted from Wills & Napier-Munn, 2005)

Using the concept of Figure 4.10 the metallurgical optimization objective then becomes Equation 4.17 – which measures the squared distance of the plant's performance from the optimal point. The plant concentrate stream's grade-recovery curve is considered by Equation 4.17.

$$J_L = (1 - \frac{X_{1,8}X_{2,8}X_{3,8}}{X_{1,1}X_{2,1}X_{3,1}})^2 + (1 - X_{3,8})^2 \qquad \text{(Eq. 4.17)}$$

Where:

- $X_{3,8}$ is the concentrate HM grade (with splitter settings as variables).
- $\frac{X_{1,8}X_{2,8}X_{3,8}}{X_{1,1}X_{2,1}X_{3,1}}$ is the concentrate HM recovery (with splitter settings as variables).

Algorithm SPII accepts as inputs plant feed conditions and an initial C (same initial splitter settings as in Section 4.5.2) and then finds the splitter settings (at the banks in C) which minimizes Equation 4.17. Algorithm SPII only adjusts splitter settings of spiral banks which are being monitored and all other spirals are left at the initial splitter position(s). Finally, minimization of Equation 4.17 is constrained by having bounds on the concentrate splitter settings. The lower bounds are 10% and the upper bounds are 40% of feed mass recovery.

When optimised splitter positions for different C cases have been obtained, it is possible to determine the potential concentrate revenue and product grade improvements (relative to initial plant conditions before optimisation of Equation 4.17). Overall optimum C's, for all feed conditions (Section 11.3.4), can be solved by minimising Equation 4.18. In this case the optimal C maximizes the HM grade, and HM mass in the concentrate stream while minimising sensor network cost.

$$C^* = \underset{C \in \mathcal{D}}{\operatorname{argmin}}(\alpha^2 \cdot P_{Cr}^2\left(\max\left(\Delta X_{1,8}^* X_{2,8}^* X_{3,8}^*\right) - \Delta X_{1,8}^* X_{2,8}^* X_{3,8}^*\right)^2 + J_C) \qquad \text{(Eq. 4.18)}$$

Stellenbosch University https://scholar.sun.ac.za

Where:

- $P_{Cr}^2 \Delta X_{1,8}^* X_{2,8}^* X_{3,8}^*$ is the improvement (or reduction) of revenue and $\max\left(P_{Cr}^2 \Delta X_{1,8}^* X_{2,8}^* X_{3,8}^*\right)$ is the maximum improvement in revenue for all feed Monte Carlo samples.
- α is a time scaling scalar (set to 1 h).
- P_{Cr} is the chromite market prices (see Appendix C Section 11.3.3).

Algorithm SPII was implemented in MATLAB and Equation 4.17 is solved using MATLAB's fmincon function (from the Optimization Toolbox). The algorithm used by fmincon was set to the sequential quadratic programming option (the default algorithm can fall prey to constraint violation). All other default optimization settings were retained. Optimization was done using a virtual machine (VM) running on a Dell PowerEdge R610 server with 12 physical CPU cores clocked at 3.324 GHz (with hyperthreading active) and 96 GB of RAM.

Stellenbosch University https://scholar.sun.ac.za

Chapter 5: Results and discussion

5.1. Overview: Core results

Results for the two interface detection algorithms (CVI & CVII) were prepared to address Objective 2 in Section 1.4. It was desired to test standard image processing algorithms against a statistical learning approach so that a suitable robust interface detection method, for industrial slurry monitoring, can be determined. Two spiral models were prepared and evaluated against experimental data (see Objective 3). Spiral plant simulation was used as a final model selection step (see Objective 3) – and was also used during optimal sensor placement (Objective 4). Finally, two optimal sensor placement algorithms were implemented and compared, for the Rowland spiral plant case, to find robust interface sensor locations – which addresses Objectives 5.

Training and testing of image processing algorithms CVI & CVII were completed on both ilmenite and chromite data sets. Algorithm MSE (J_1) and average differences between true & false positive detections (J_2) were recorded (which calculates the difference between algorithm output images and ground truth images). Both image processing algorithms can identify concentrate and middlings interfaces in all training/testing images (when optimal parameters are found) for the ilmenite/mineral sands image set. It is difficult to determine the superior algorithm based on J_1 or J_2, in this case, but the training time of the logistic regression based algorithm (algorithm CVII) is significantly lower. GA training time for Algorithm CVI can span days where Algorithm CVII's training can take a few hours (see Section 12.1 in Appendix D for details). Algorithm CVI was incapable of finding concentrate interfaces in the chromite separation image set. However, Algorithm CVII can find interfaces, in the majority of chromite images, for the training cases in Figure 5.1 (further interface detection results is detailed in Section 5.2).

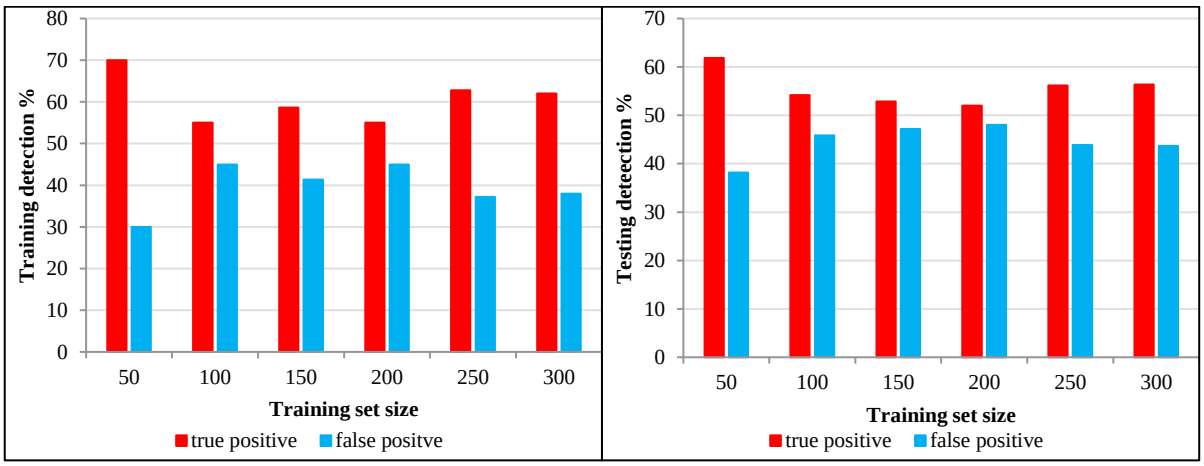

Figure 5.1: Overall true and false positive Algorithm CVII concentrate interface detections on training (left) and testing (right) images (chromite case, using 35-by-35 pixel kernel)

Stellenbosch University https://scholar.sun.ac.za

Algorithm CVII is considered the superior image processing method due to its fast training time and its ability to find interfaces in the chromite data set. The logistic regression based interface detection shows that interface tracking on industrial slurries is possible.

Spiral model preparation, model selection and WPL plant simulation followed after interface detection was established on the chromite data set. Linear regression was used to find interface sensor variance for optimal sensor placement. The extended Holland-Batt model was the preferred method for modelling spiral MOI (HM content was used as a proxy) and solids phase recoveries due to better experimental confirmation results and better plant simulation behaviour – illustrated in Figure 5.2. The RSM models provided dubious plant simulation results including: non-monotonically decreasing concentrate HM recovery (as HM grade increases), multiple points with recovery equal to 1 (see Figure 5.28) and an inability to model HM recovery when HM grade is lower than 0.2 (Section 5.5 provides the more complete plant simulation account).

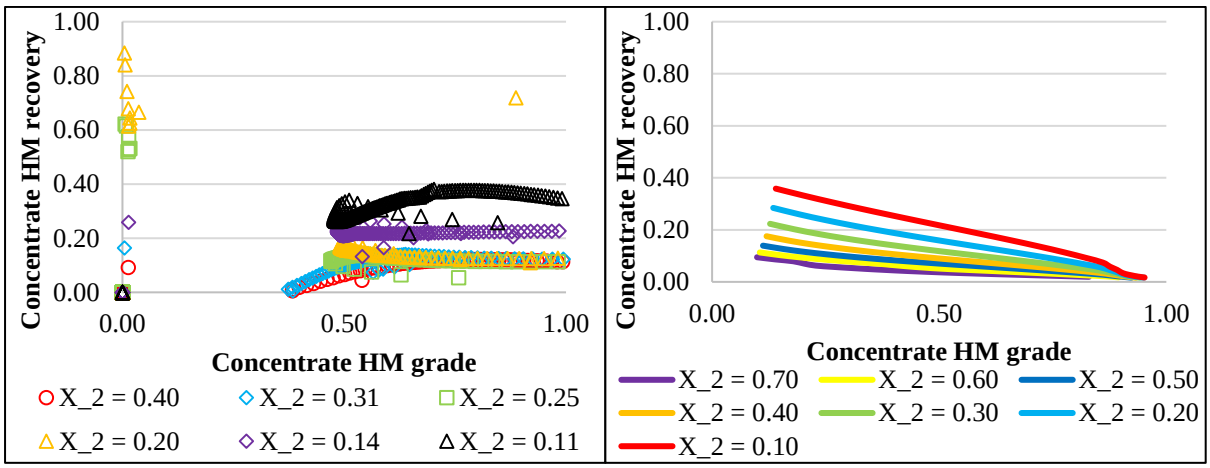

Figure 5.2: Simulated metallurgical performance contours, at different feed conditions, for WPL primary circuit concentrate stream (left: RSM model points on contours; right: extended Holland-Batt spline)

Optimal interface sensor configurations, as determined by both algorithms in Section 4.5, showed diverging solutions (see details in Section 5.6). Via state estimation it is suggested that the monitoring of re-recleaner spirals (the spirals that produce the final concentrate) is the most important. This solution gives minimum J_C (instrumentation cost) but it was also found that removal of sensors placed further from re-recleaners should occur first (when sparse sensor networks are investigated). Sensor placement via metallurgical performance suggests that the monitoring of recleaner spirals is the most important. Figure 5.3 shows the frequency of optimal sensor placements (C) found at the different Monte Carlo simulations (names of the different C's are listed in Table 4.3). The different intervals in Figure 5.3 are the sets $\mathcal{D}$ (see the legend) that Algorithm SPII is allowed to search C^*. Re-recleaner spirals were found to be the least significant for monitoring (according to SPII).

Stellenbosch University https://scholar.sun.ac.za

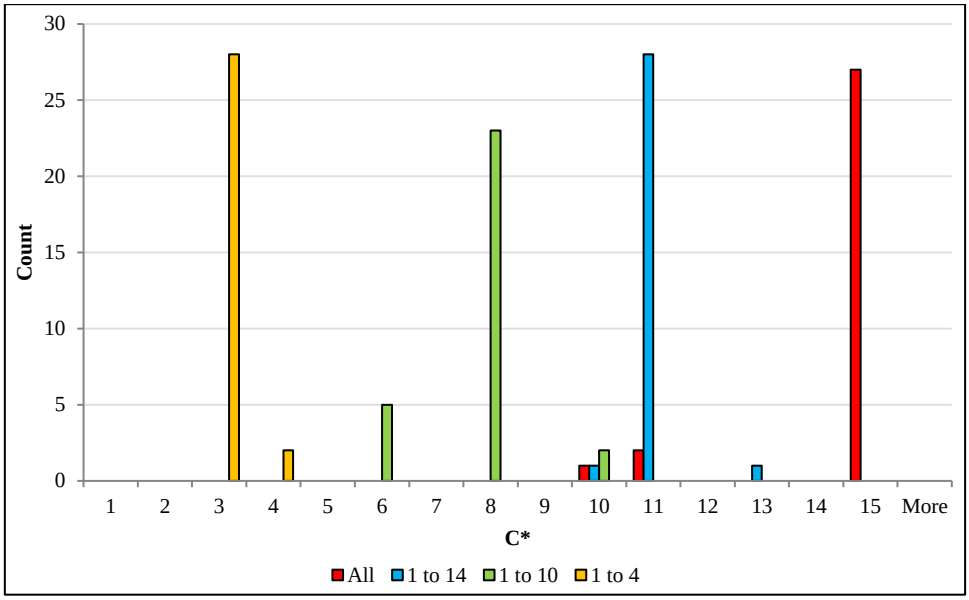

Figure 5.3: C^* solutions of Equation 4.18 with $\alpha = 24$ h (Algorithm SPII; C_3 is recleaner, C_8 is cleaner-recleaner, C_{11} is rougher-cleaner-recleaner and C_{15} includes all spiral banks)

The metallurgical performance based sensor placement algorithm is more suitable for interface sensor placement (especially when only these sensors are considered) because the sensor locations are linked to potential plant steady-state performance improvements (assuming interface sensors lead to splitter settings that maximizes Equation 4.17). Plant performance can be tied to revenue produced which is easier to compare with sensor installation cost. Algorithm SPII is also computationally less expensive. State estimation sensor placement approaches will require that mass and solids flow rate sensors be included in the analysis – which is irrelevant for this case study since such sensors are typically expensive (and only placement of interface sensors should be relevant). Algorithm SPI also only considers how sensor placements change state estimation variance and does not include improvements to plant performance.

5.2. Interface detection for chromite separation

Algorithms CVI & CVII were initially trained on the ilmenite image data set during algorithm development (see results in Section 12.1). Both algorithms were capable of isolating concentrate and middling interfaces; however, training times for Algorithm CVII were significantly lower. The ilmenite image data set proved to be a simpler segmentation problem and spiral slurries were not representative of industrial conditions (spiral slurries were artificially mixed). Algorithm evaluation was continued on the chromite data set to determine whether this result can be replicated – and if the result is not repeated the superior algorithm must be identified.

5.2.1. Algorithm CVI (GA based)

Interface detection on the chromite image set was only performed for the concentrate interface (which is the only visible one). Training was performed on image sets with 50, 100, 150, 200, 250 and 300 images and testing performed on a remaining image set of 600 images. Training times and Algorithm

Stellenbosch University https://scholar.sun.ac.za

CVI performance was recorded for each case to determine the necessity of larger training sets and thereby longer training times (typically larger training sets will lead to better testing results at the cost of longer training times). GA training options were the same as in the case of Section 12.1.1 except that populations of 50 chromosomes were used (similar to the ilmenite concentrate interface detection case) to optimise Algorithm CVI parameters. The GA converged for each training case but repeated optimisation runs are required to avoid $J_2 = 0$ minima. Figure 5.4 summarises Algorithm CVI's training results in terms of performance in the amount of edges detected and J_2 value (Equation 4.2).

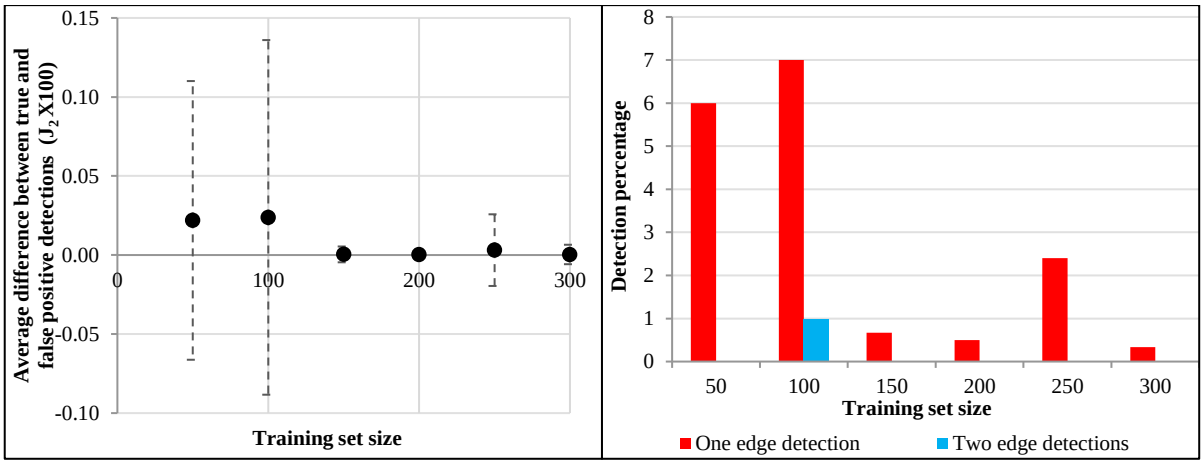

Figure 5.4: Algorithm CVI (GA-based) training results for concentrate interface detection (chromite case, error bars represent variation by $1 \times \sigma$ based on n = 50, 100, 150, 200, 250 and 300 samples)

Figure 5.5 gives examples of interface responses training of Algorithm CVI achieves (on the majority of the chromite slurry training images no detections are achieved). Successful concentrate interface detections was achieved in the left and middle frames of Figure 5.5 but not in the frame on the right. The image on the right (in Figure 5.5) is an example that indicates the difficulty of detecting interfaces for the chromite slurry case. A much less distinct interface is visible than compared to the frames in the middle and to the left (instead a more gradual change in colour exists in the slurry on the frame to the right).

Stellenbosch University https://scholar.sun.ac.za

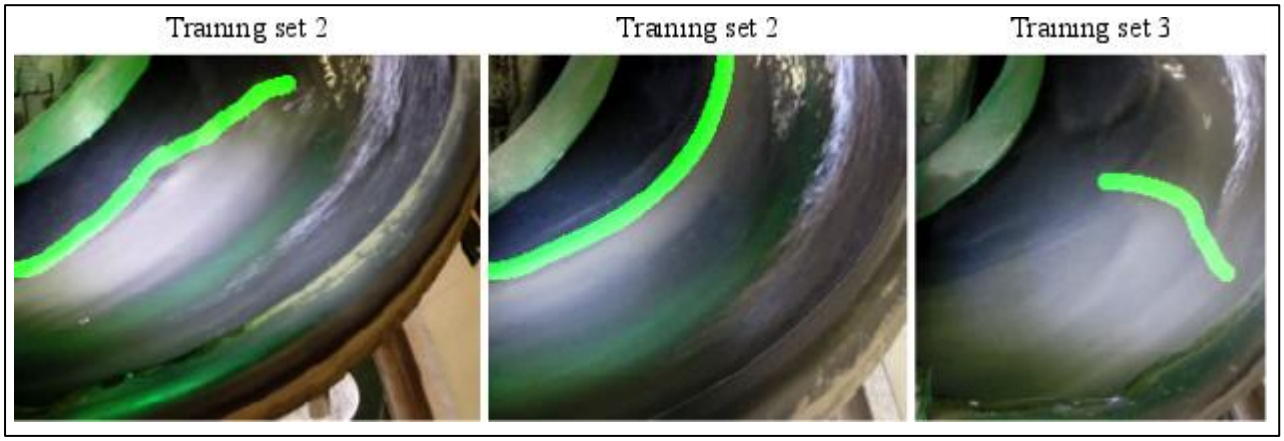

Figure 5.5: Examples of chromite concentrate interface responses that Algorithm CVI (GA-based) generates

Algorithm CVI fails to detect more than 90 % of concentrate interfaces for each training case. Training on the 50 and 100 image sets achieved the most edge detections but with the greatest uncertainty (meaning the detected edges do not represent the interfaces accurately). Training on the 150, 200 and 300 image sets provide the least detections. Figure 5.6 give the testing results summary, similar to Figure 5.4, of the trained parameters.

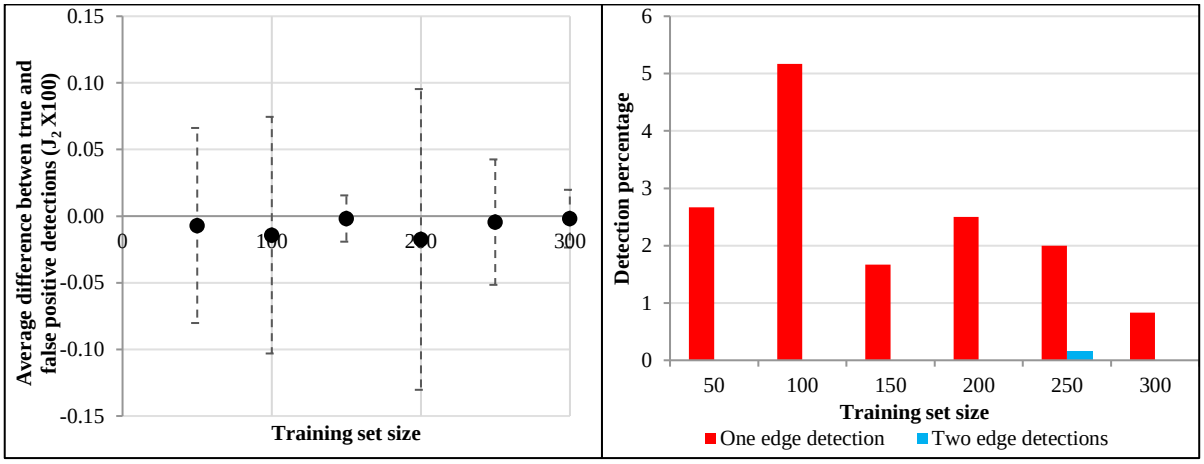

Figure 5.6: Algorithm CVI (GA-based) testing results for concentrate interface detection (chromite case, error bars represent variation by $1 \times \sigma$ *based on* $n = 600$ *samples)*

J_2 values for each testing case is lower than zero indicating majority false positive detections and the amount of edge detections is lower than 10 % for each testing case. The edge detections for the testing case also does not correspond to appropriate interface detections indicating inability of traditional edge detection to find interfaces even when optimised parameters are used. These results indicate that the GA-based Algorithm CVI was wholly unsuccessful for the chromite case; therefore further in-depth analysis of parameter sensitivity and robustness was not conducted (as was done in the ilmenite case).

Stellenbosch University https://scholar.sun.ac.za

5.2.2. Algorithm CVII (Logistic regression based)

Algorithm CVII training and testing were performed on the same image sets that was used for Section 5.2.1 (Algorithm CVI). Feature sets were manipulated in double floating precision instead of single point used in Section 5.2.1 (to achieve greater accuracy in optimal parameter attainment). Higher parameter precision also allows more definitive cuts by decision boundaries – at the cost of longer training times (single floating point precision proved to be adequate for interface detection in Section 5.2.1). Feature sets were constructed in a similar way to the ilmenite case (Section 12.1.2) except that distinct neighbourhood blocks were used instead of sliding or overlapping neighbourhoods (see Section 11.1.3). Training was also performed for different neighbourhood sizes to investigate the effect of increased number of parameters on concentrate detection. The following neighbourhood sizes were trained on each training image set:

1. 3-by-3.
2. 19-by-19.
3. 35-by-35.

Training was performed with the same optimisation algorithm used in Section 5.2.1 (conjugate gradient based) but with a limit of 2000 iterations and no regularisation (exclusion of λ). Regularisation was omitted since this would greatly increase training time when iterations (per optimisation run) is 2000, and because λ estimation is done via cross-validation (rather training on different image sets will be used to determine if overfitting occurs). The same objective function tolerance was used from Section 5.2.1. Precision, recall and the F statistic (Equation 9.13) were recorded for each training and testing case to determine concentrate detection performance. Figure 5.7 summarises training results for chromite rich concentrate interface detection. Two decision boundaries, at $h = 0.5$ and $h = 0.3$, were used to investigate change in precision, recall and F values at different thresholds. The decision boundary of 0.3 was selected to in an attempt allow more t_p and f_p detections that can coincide with pixels that represent the chromite concentrate mineral band.

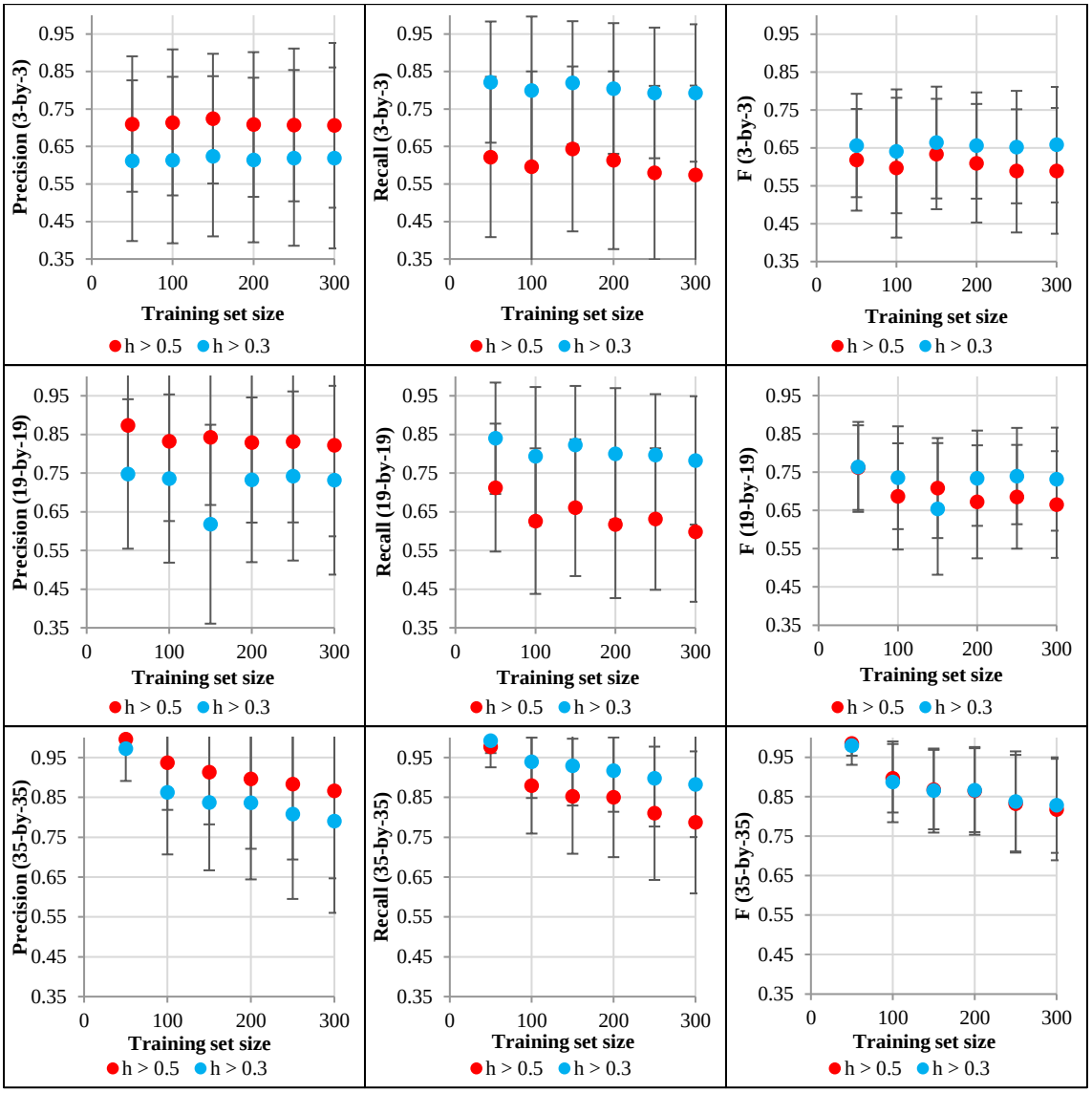

Figure 5.7: Algorithm CVII (logistic regression based) training precision, recall and F values for chromite concentrate detection (using different neighbourhood widths; error bars represent variation by $1 \times \sigma$ *based on n = 50, 100, 150, 200, 250 and 300 samples)*

Using a decision boundary of 0.5 provides higher training precision and lower recall. A decision boundary value of 0.3 generally provides the higher training F value and therefore better concentrate detection in the chromite slurry. A decision boundary of 0.5 provides higher training F values when a 35-by-35 pixel kernel is trained on image sets of 50, 100 and 150 images and the same boundary only provides better performance on the 150 image set when the 19-by-19 kernel is trained. Training the smallest kernel (3-by-3) provides the lowest training F values which does not change significantly with image set size. The largest kernel (35-by-35) gives the highest training F values and training performance reduces with increasing training image set size.

Training times are presented in Figure 5.8. Logistic regression training time range from 8.9-17.5 minutes on the smallest training set to 56.8-64.1 minutes on the largest training set. Strong linear, proportional, correlation ($R^2 \sim 0.9$) can be seen between training time and training set size. A drop in

Stellenbosch University https://scholar.sun.ac.za

optimisation time for the 3-by-3 kernel training case occur with training on the 200 image set. Training times for larger image sets then resemble training time for the 19-by-19 kernel case. This is due to convergence being achieved before the limit of 2000 iterations was reached. During training of the two larger kernels the objective function tolerance was never reached before the 2000 iteration limit.

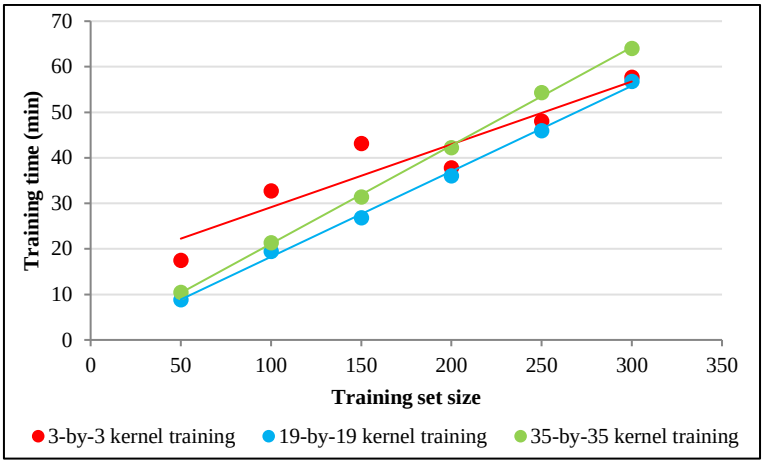

Figure 5.8: Training times for different kernel sizes (chromite case, Algorithm CVII)

Testing results are summarised in Figure 5.9 in the same format used in Figure 5.7. Similar to the training case the decision boundary of 0.3 provides higher precision, lower recall and generally higher *F* values (with the exception of the 150 image set training case using the 19-by-19 kernel). Similar to the training case, testing with a decision boundary of 0.3 provides lower precision and higher recall. The 19-by-19 and 35-by-35 kernels show improved testing performance (higher *F* values) when trained on larger image sets. Testing with the 3-by-3 kernel does not show significantly higher *F* values as the training image set size increase. Increasing the kernel width from 19 to 35 does not generally improve classification performance. Despite the 35-by-35 kernel achieving the highest *F* value the 19-by-19 kernel does outperform the largest kernel in 3 of the 6 testing cases.

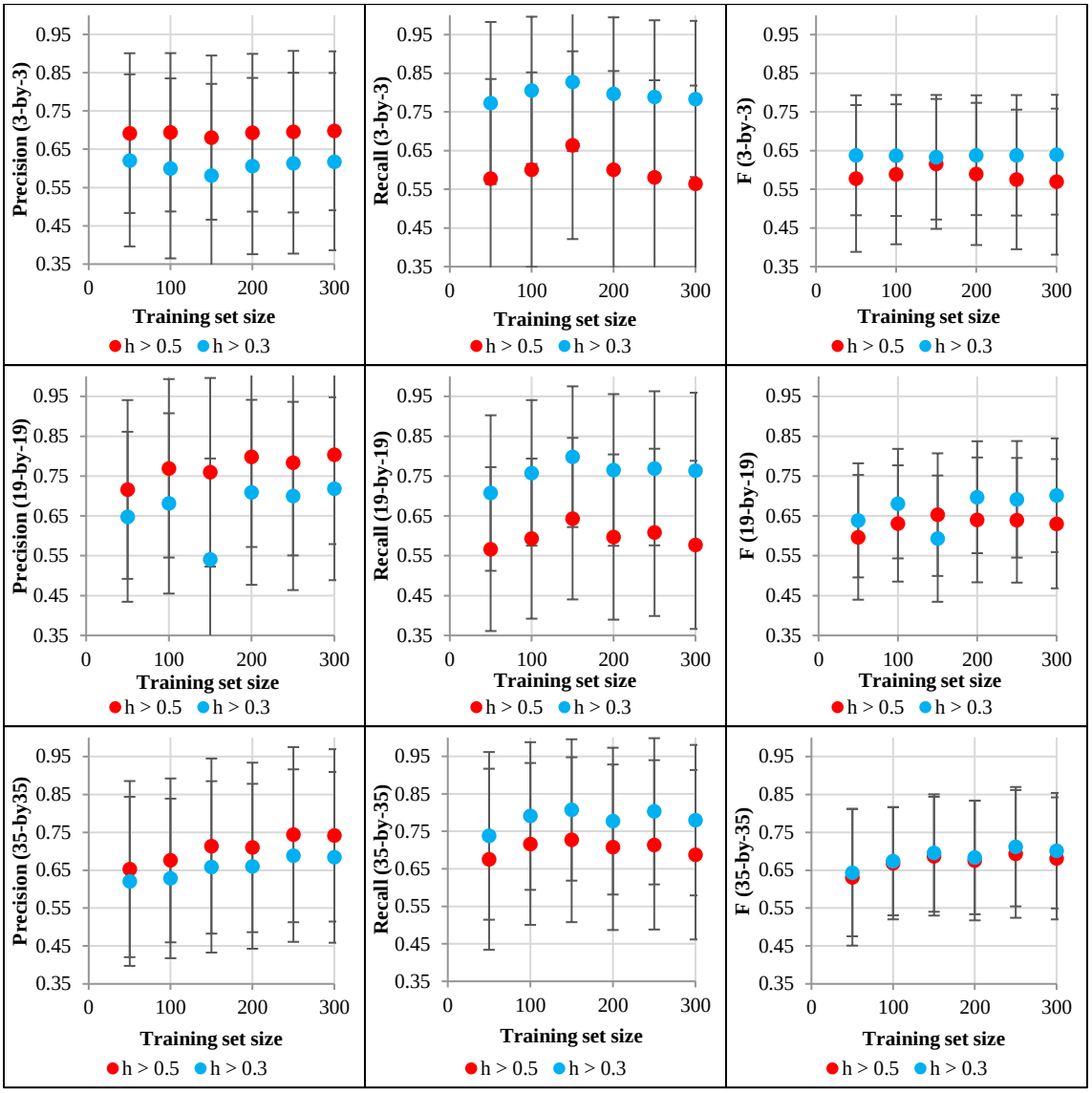

Figure 5.9: Algorithm CVII (logistic regression based) testing precision, recall and F values for chromite concentrate detection (using different neighbourhood widths; error bars represent variation by $1 \times \sigma$ based on n = 600 samples)

Optimised parameters for the largest kernel was used to estimate concentrate-tailings and gulley-concentrate mineral interfaces in the training and test images since it achieved the highest testing F value (Figure 5.9). J_2 performance values for concentrate interface detection is presented in Figure 5.10. Only three training cases and two testing cases has a J_2 value higher than 0 (representing majority true positive interface detections). Parameters obtained from training on the smallest image set performs better in terms of J_2 on its own training set and the testing set. Training on the two largest training sets results in kernels providing the 2nd and 3rd highest mean J_2 values on the testing set. Figure 5.11 present the percentage of images, in training or testing sets, that give overall true positive or false positive (detected) interface pixels.

Stellenbosch University https://scholar.sun.ac.za

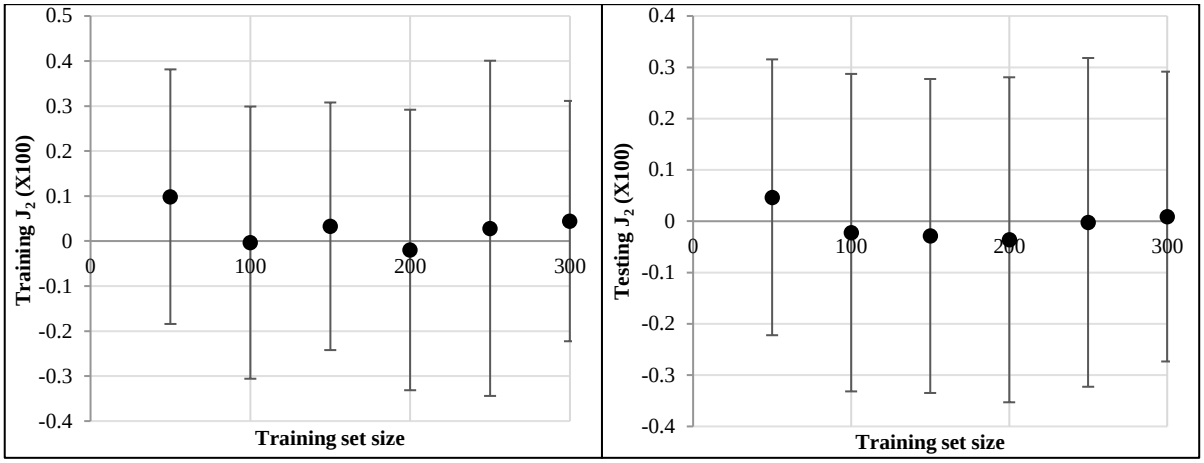

Figure 5.10: Algorithm CVII (logistic regression based) concentrate interface detection on training (left) and testing (right) images (chromite case, using 35-by-35 pixel kernel; error bars represent variation by $1 \times \sigma$ *based on n = 50, 100, 150, 200, 250 and 300 samples for training and n = 600 samples for testing)*

The same trends are present in Figure 5.10 and 5.1; however, Figure 5.1 (when compared to Figures 5.4 and 5.6) clearly shows that the logistic regression based interface detection approach (Algorithm CVII) is superior to Algorithm CVI in terms of interface detection ability (because Algorithm CVII generates responses at each chromite slurry image). All the optimised parameter sets (35-by-35 kernels) can detect mostly true positive concentrate interface pixels in over 50 % of the testing set images. Figure 5.1 also show that training a 35-by-35 kernel on the smallest training image set provides the highest true positive detection rate on testing images. This result may be spurious since it is expected that larger training sets lead to better testing performance (in Section 12.1 the smallest training set does not lead to highest performance).

Results of gulley-concentrate interface detections are processed in the same way as the concentrate-tails interface. Interface detection performance, in terms of J_2, on the training and testing image sets is presented in Figure 5.11. All mean J_2 values for gulley interface detection is positive which show better performance than the concentrate-tails interface detection case. Mean testing and training performance results are similar and remain between 0.15 and 0.2 with testing J_2 results showing greater variance.

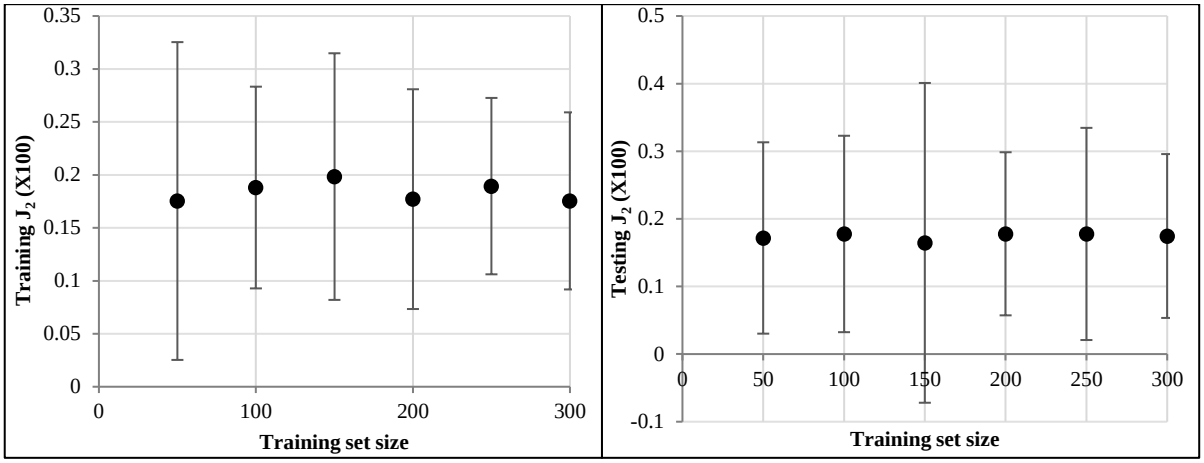

Figure 5.11: Gulley-concentrate interface detection on training (left) and testing (right) images (chromite case, using 35-by-35 pixel kernel; error bars represent variation by $1 \times \sigma$ based on n = 50, 100, 150, 200, 250 and 300 samples for training and n = 600 samples for testing)

The percentage of images with J_2 (in either training or testing image sets) greater or less than 0 is presented in Figure 5.12 (for the gulley interface detection case). True positive gulley interface detections are achieved in more than 90 % of the images in each case. Training set size does not show significant effect on the concentrate-gulley interface detection ability of Algorithm CVII.

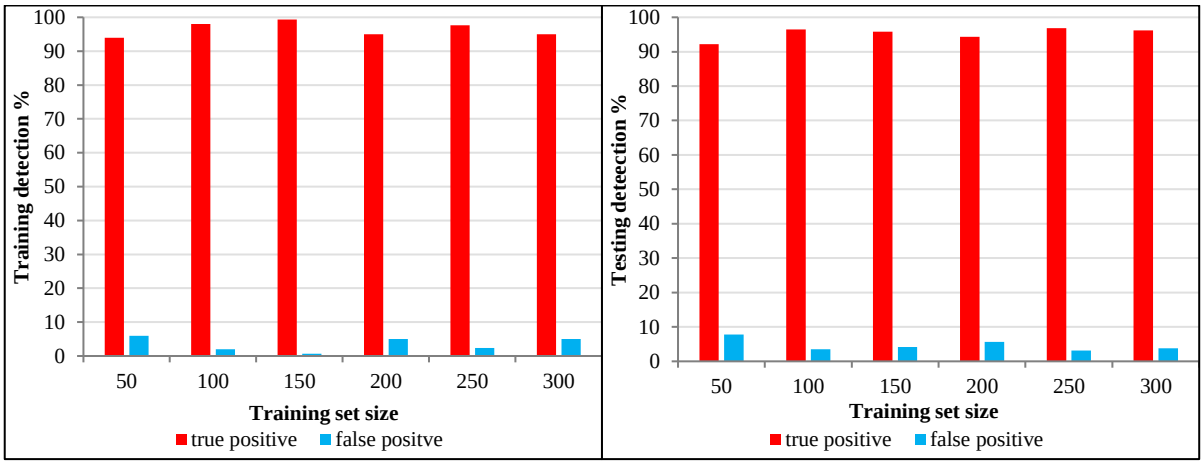

Figure 5.12: Overall true and false positive Algorithm CVII gulley-concentrate interface detections on training (left) and testing (right) images (chromite case, using 35-by-35 pixel kernel)

Algorithm CVII clearly outperforms Algorithm CVI (GA-based) for concentrate interface detection on the chromite image set. Example images of Algorithm CVII's interface detection ability are shown in Appendix I. Algorithm CVII is capable of detecting the different relevant interfaces in the majority of the chromite images. Improving logistic regression performance, however, comes at the cost of significantly increasing the number of parameters required and therefore the necessary training time. Large parameter sets can become prone to overfitting which necessitates the use of larger training image sets (larger than 300 images for Algorithm CVII training on the chromite images). However, the results presented in this section suggests training on large image sets (more than 300 images) may

Stellenbosch University https://scholar.sun.ac.za

not be necessary for the interface detection problem (this can change if environmental conditions can vary).

During the calculation of interface widths (results discussed in Section 5.3.1), using Algorithm CVII as the segmenter, it was found that valid measurements (i.e. no 0 mm widths) were obtained. Algorithm CVII produces slurry detection response for most images; however, the final interface detection only aligns with ground truth (manually labelled) images over 50% of the time. Therefore, Algorithm CVII suggest that machine learning approaches may lead to robust solutions to the spiral slurry monitoring problem.

5.3. Response surface methodology spiral models

5.3.1. Development of final tailings & interface response models

Data reconciliation of experimental data was performed with initial RSM modelling results and is provided in Appendix D Section 12.2. It was discovered that significant errors were present in runs 1, 7 and possibly run 2. Run 1 was excluded from regression analysis due to reconciliation results and complications observed during experimentation. Luckily, run 28 was a repeat of run 1 – which was performed due to run 1 error concerns – leading to the regression training set of runs 2 – 28 (still a complete Box-Behnken design). During the initial spiral response modelling (through regression analysis) it was found that including run 7 in the design matrix can lead to the grade model estimating negative grade values within the experimental design range. For the final preparation of spiral response models run 7 was removed from the design matrix and regression analysis was repeated followed by statistical parameter selection. Only the models resulting from parameter selection will be discussed here. Tailings HM grade and HM recovery RSM models are considered first because the tailings HM grade model has higher precision (than for the concentrate case).

Table 5.1 gives the correlation coefficient and F-test results of the final models. All models are statistically significant (p-values from F-tests are < 0.05) and the grade model has a $\mathcal{R}^2$ higher than 0.9 (despite being lower than the model in Section 12.3.1). The recovery and flow ratio models have increased $\mathcal{R}^2$ values suggesting greater accuracy. Adjusted $\mathcal{R}^2$ values are higher than the adjusted $\mathcal{R}^2$ values in the Section 12.3.1 suggesting that an appropriate number of parameters are selected. Partial F-test p-values are larger than 0.05 indicating that the excluded parameters (after parameter selection) cannot be accepted as non-zero values. Table 5.2 give significant variables for the spiral response models similar to the presentation in Table 12.7. Some changes in the significant variables can be observed.

Stellenbosch University https://scholar.sun.ac.za

Table 5.1: F-test and correlation coefficient results for final spiral response models

	Flow ratio model	Tailings grade model	Tailings recovery model
$\mathcal{R}^2$	0.72	0.96	0.87
$\mathcal{R}^2_{adj}$	0.66	0.95	0.81
Significance F p-value	1.43E-05	2.01E-13	4.38E-06
Partial F-test p-value	0.67	0.53	0.71

Table 5.2 shows that feed grade and splitter interaction is not significant and that the square of the feed grade is. The grade model does not include interaction between feed grade and feed flow rate. Feed grade and feed SG interaction is not significant in the final recovery model but the squared feed grade is.

Table 5.2: Significant parameters for the final flow ratio, tailings grade and tailings recovery models (x_1 – coded feed HM grade, x_2 – coded feed SG, x_3 – coded feed flow rate and x_4 – coded splitter setting)

Flow ratio model			Tailings grade model			Tailings recovery model		
Parameter	Estimate	p-value	Parameter	Estimate	p-value	Parameter	Estimate	p-value
Intercept	0.09	1.37E-10	Intercept	0.50	6.02E-25	Intercept	0.79	1.77E-18
x_1	0.02	1.87E-03	x_1	0.06	2.78E-13	x_1	-0.06	1.39E-04
x_3	-0.02	0.05	x_2	0.04	2.20E-03	x_2	0.22	1.16E-06
x_4	0.06	9.90E-06	x_4	-0.02	0.11	x_3	0.04	0.07
x_1^2	0.00	5.28E-03	x_1x_4	-0.01	0.06	x_4	-0.14	2.79E-05
			x_2^2	-0.03	0.07	x_1x_4	-0.05	0.01
						x_2x_4	0.22	7.68E-03
						x_1^2	0.01	1.22E-03
						x_2^2	-0.11	8.93E-03

Table 5.2 shows that increasing feed grade and the splitter setting increases the amount of the spiral slurry reporting to the concentrate stream. This result is acceptable as a feed with a higher grade will increase the mass flow rate of the feed (when volume is constant) and the mass of slurry reporting to concentrate (there are more heavy particles to separate). Wider splitter settings are expected to allow more material to the concentrate stream. Higher feed flow rates reduce the concentrate flow rate which is in agreement with Tripathy & Murthy's (2012) work that concluded that higher feed rates increase centrifugal forces within the spiral trough – leading to higher slurry recovery to the tailings stream.

Stellenbosch University https://scholar.sun.ac.za

The tailings grade model does not include a feed flow rate term which is a deviation from Tripathy & Murthy's (2012) results. Higher flow rates are expected to increase HM grade in the tailings stream, however, this result can be due to the omission of run 7 (which was intended to be ran at the feed flow rate level 0 and feed SG level -1). Wider splitter settings were found to reduce tailings HM grade which is a reasonable result since more HM will report to the concentrate stream with a wider splitter setting. Higher feed grade increases tailings grade since most of the feed slurry reports to the tailings stream. Feed density increases tailings HM grade but when the centered feed density exceeds 0.7 it starts to decrease. Higher feed density means more particles are introduced to the system which will result in more particles being recovered by the tailings stream. Tripathy & Murthy (2012) observed similar results and concluded that higher feed density alters the spiral slurry viscosity which increases settling time of HM particles finally increasing HM grade in the tailings stream.

Finally, Table 5.2 shows increased feed density and feed rate increase the HM recovery in tailings stream. This result is in agreement with Tripathy & Murthy (2012) who found that increasing these variables led to decreased HM recovery in the concentrate stream. Higher feed rates increases centrifugal force on the slurry forcing more particles to the tailings stream. Increasing the splitter setting reduces recovery as more particles report to the concentrate stream. Increasing feed grade decreases tailings HM recovery since the majority of heavy particles will transport to the concentrate stream due to the action of hindered settling.

Standardised residuals are given in Figure 5.13 showing no discernible heteroscedastic behaviour and, strictly speaking, no outliers. The final tails HM grade model has a possible outlier at run 29 (standardised residual value of -2.99) but is considered acceptable at this point. Once again reconciled responses and predicted values are plotted against each other in Figure 5.14 to show that the final spiral models do not predict negative responses (at least at the experimental design points).

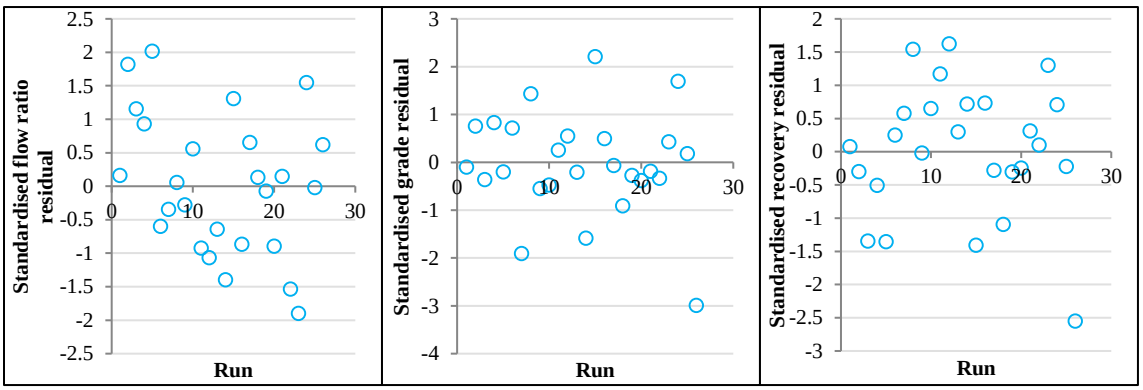

Figure 5.13: Standardised residuals for final flow ratio (left), grade (middle) and recovery (right) models

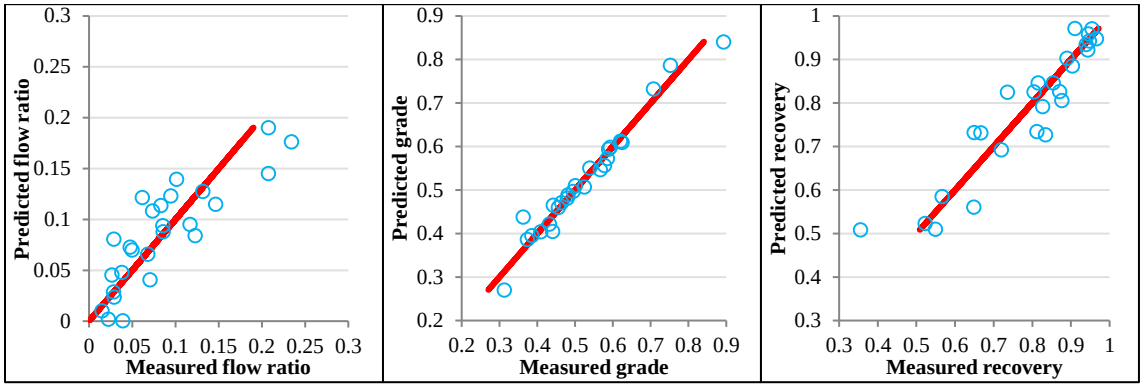

Figure 5.14: Reconciled tailings stream values vs predicted values for final spiral flow ratio (left), grade (middle) and recovery (right) models

Spiral interface models were developed following the completion of the flow, grade and recovery RSM models so that:

- Chromite interface tracking results can be compared to Vermaak et al. (2008).
- Interface measurement variance can be established for optimal sensor placement.

Interface positions were calculated (using algorithm CVII, which proved to be the most accurate interface detection approach – see Section 5.2) from the videos captured on runs 1-28 using 59 frames, spanning from the 100th to 3000th frame, from each video. Interface detections were done using a 35-by-35 filter trained on 300 images (with training testing results shown in Section 5.2). Interface measurements obtained from each frame, per video, were averaged to find a mean interface response at each run. Model fitting was performed using mean interface response determined from runs 2-28 (with run 7 removed). The design levels obtained via data reconciliation were used for regression analysis. Manually labelled images are also available for the same frames (these are the images used for labelling during the interface detector training stage) and model fitting was performed on responses obtained from these images to serve as a comparison. Parameter selection was performed on initially full quadratic models to find the final interface models.

Camera calibration reprojection errors, for each experimental test run, is presented in Appendix J (Figure 18.3). Reprojection errors are generally below 1 mm which ensures accurate transformation between image and world coordinates. Coordinate transforms are expected to be accurate assuming the measured objects lie within the same plane and remain within the general area of the calibration pattern. If the assumptions are accepted to remain true then interface measurement errors should stem from inaccurate interface segmentation and rapid change in interface position during each run.

Table 5.3 presents the descriptive statistics of models fitted to interface responses determined using Algorithm CVII and the manually labelled images. Both models are statistically significant after parameter selection. The interface model based on manually labelled images is more precise with a higher correlation coefficient value than the Algorithm CVII based one. Adjusted $\mathcal{R}^2$ values differ

Stellenbosch University https://scholar.sun.ac.za

with $\mathcal{R}^2$ values by less than 0.1 suggesting that appropriate number of parameters are included in both models. Partial F-test p-values are larger than 0.05 indicating that the excluded parameters (after parameter selection) cannot be accepted as non-zero values.

Table 5.3: $\mathcal{R}^2$ and F-test results of the interface models after parameter selection

	Algorithm CVII based model	Labels (ground truth) based model
$\mathcal{R}^2$	0.48	0.74
$\mathcal{R}^2_{adj}$	0.43	0.64
Significance F p-value	5.53E-04	2.99E-04
Partial F-test p-value	0.42	0.82

Table 5.4 contains significant parameters (determined using coefficient t-tests) for both interface models. The Algorithm CVII based model only has two variables: feed SG and feed flow rate. The manual labels based model contains nearly all allowable parameters except a squared feed SG term, a feed SG and feed flowrate interaction term.

Table 5.4: Significant variables of the interface models after parameter selection (x_1 – coded feed HM grade, x_2 – coded feed SG, x_3 – coded feed flow rate and x_4 – coded splitter setting)

Algorithm CVII			Labels (ground truth)		
Parameter	Estimate	p-value	Parameter	Estimate	p-value
Intercept	84.53	1.64E-22	Intercept	74.53	3.34E-15
x_2	15.93	2.62E-04	x_1	7.22	1.53E-03
x_3	5.69	0.07	x_2	7.25	0.11
			x_3	1.46	0.68
			x_1^2	-2.27	0.07
			x_1x_2	8.55	0.08
			x_1x_3	4.27	0.08
			x_3^2	-6.92	0.07

Similar to Vermaak et al. (2008) the interface model based on Algorithm CVII showed that feed flow rate and feed density had a significant effect on interface width (with density being the more significant variable). Feed grade is not a significant variable, which disagrees with Vermaak et al. (2008) who found it to have the most pronounced effect on concentrate interface width. The interface model prepared, using Algorithm CVII's results, is based on slurry received from industry and the presence of slimes in spiral feed can confound analysis of significant interface variables (in 2008

Stellenbosch University https://scholar.sun.ac.za

Vermaak et al. used synthetic ore combinations in spiral feed slurries). Lack of orthogonality in this study can also confound the analysis of significant factors (since feed grade was the variable showing greatest deviation from intended design levels). Another important factor that can lead to reduction in precision is the fact that only the interface in the upper spiral (of the double-start spiral concentrator) was measured (different interface positions can be present in the lower spiral). Finally, errors in segmenting the concentrate interface in the test images can introduce noise to the measured interface response further confounding the analysis of significant variables. The concentrate interface model based on the manually labelled images shows that feed grade is the most significant variable, however, no other variable shows a p-value under 0.05.

Prediction-measurement comparison results are plotted in Figure 5.15 and standardised model residuals are plotted in Figure 5.16. No outliers are present in the residual plots of Figure 5.16; however, the manual labels based model shows heteroscedastic behaviour with residual values reducing as runs increase (this; however, is to the first two runs nearing the 3rd standard deviation).

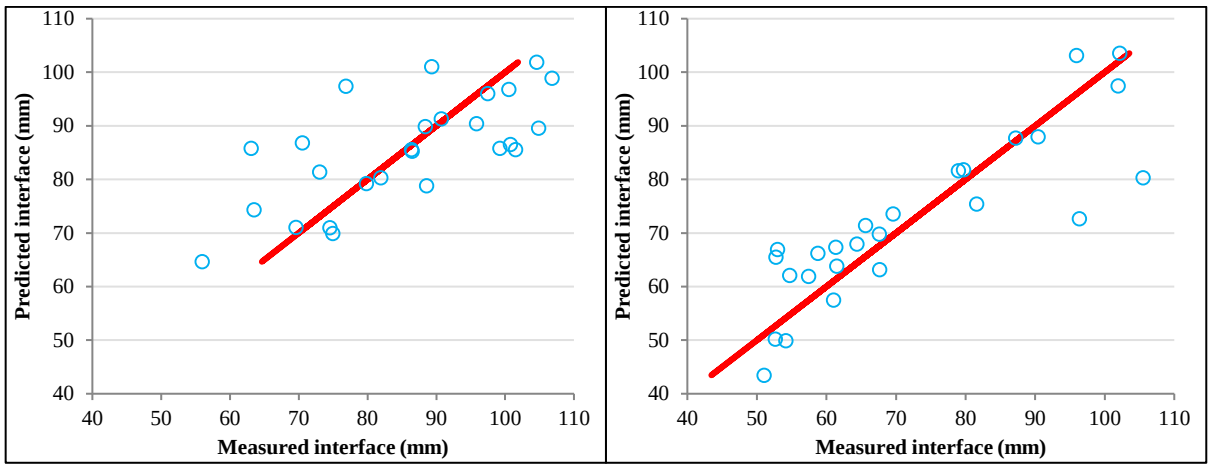

Figure 5.15: Predicted concentrate interface vs. measured interface values (left: Algorithm CVII's results, right: label image results)

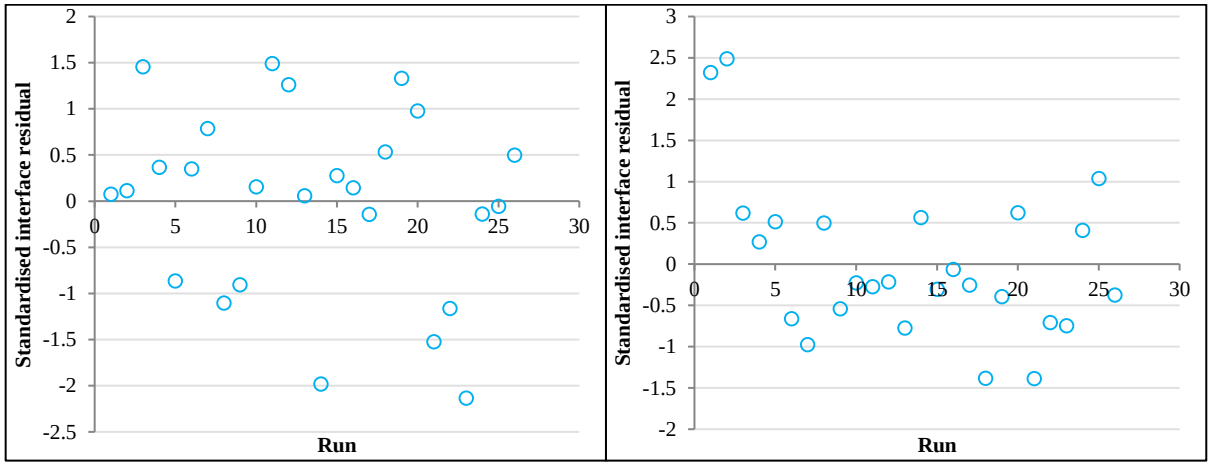

Figure 5.16: Standardised interface model residuals (left: Algorithm CVII's results, right: label image results)

The models (described by the parameters in Table 5.2 & 5.4) prepared in this section represent the final concentrate over tailings mass flow rate, tailings HM grade, tailings HM recovery and concentrate interface models. Confirmation run analysis is performed using the final models and future spiral circuit simulations will use the final spiral response models.

5.3.2. Development of spiral concentrate response models

Response surface models for concentrate HM grade and HM recovery were also prepared and serves to validate the results in Section 5.3.1. The concentrate RSM models is also prepared to serve as comparison to the extended Holland-Batt model in Section 5.4. Parameter selection, using the same methods used in Section 5.3.1, was performed to prepare reduced models. Figure 5.17 presents standardised residuals for concentrate grade and recovery models. Residuals appear homoscedastic but an outlier is present at run 16 for the concentrate HM grade model. Figure 5.18 shows reconciled values versus predicted values for the grade and recovery models.

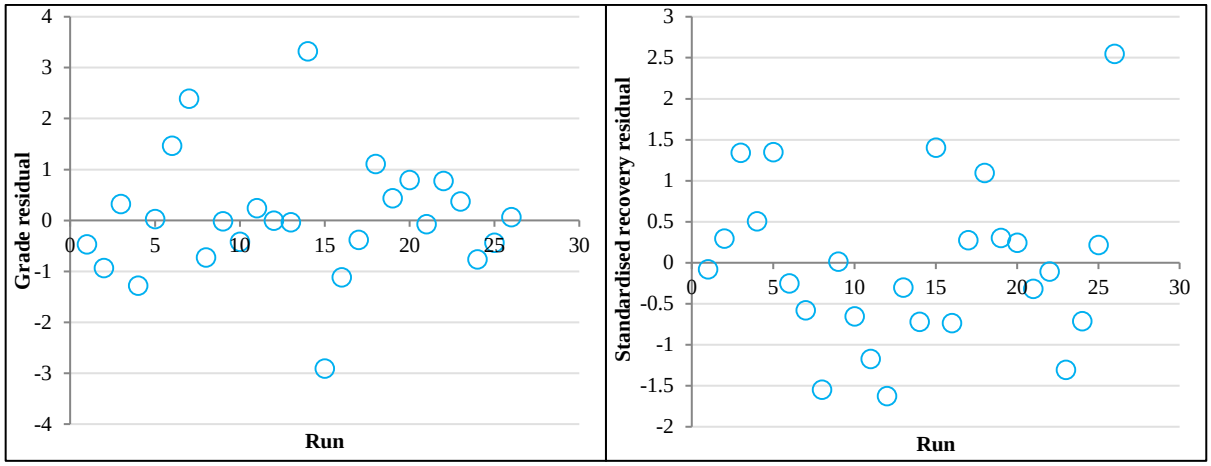

Figure 5.17: Standardised concentrate HM grade (left) and HM recovery (right) model residuals after parameter selection

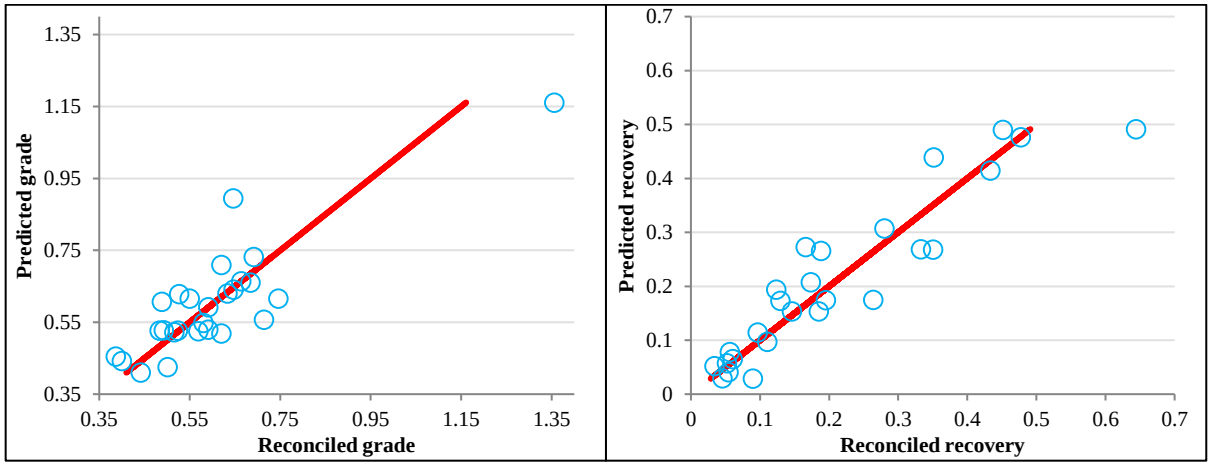

Figure 5.18: Reconciled concentrate stream response values vs. predicted concentrate HM grade (left) and HM recovery (right) responses after parameter selection

Stellenbosch University https://scholar.sun.ac.za

The left frame in Figure 5.18 shows a physically impossible grade value and prediction (values reported are over 1), suggesting that another run would have to be removed for the concentrate HM grade model fitting case. Recovery model values are within an acceptable range. HM recoveries within the concentrate stream is generally lower than 0.5; however, grade HM fractions can reach values up to 0.75.

Table 5.5 presents correlation coefficients and F-test results for the concentrate HM grade and HM recovery models. The concentrate HM recovery model's $\mathcal{R}^2$ and F-test p-values are the same as the tailings HM recovery model's. This result suggests that the statistical models for concentrate and tailings HM recovery are exactly complementary (as would be ideally expected but would not be exact if models were solely based on measurement values).

Table 5.5: $\mathcal{R}^2$ and F-test results for concentrate response models after parameter selection

	Grade model	Recovery model
$\mathcal{R}^2$	0.74	0.87
$\mathcal{R}^2_{adj}$	0.67	0.81
Significance F p-value	3.00E-05	4.38E-06
Partial F p-value	1	0.71

Partial F-test p-values were calculated for both grade and recovery models based on the model parameters in Table 5.6. Both partial F-test p-values in Table 5.5 are larger than 0.05 leading to the conclusion that none of the excluded parameters can be non-zero in value. The concentrate stream HM grade $\mathcal{R}^2$ value is lower than in the case of the tailings HM grade model (indicating a less precise model) and its $\mathcal{R}^2_{adj}$ value is lower than $\mathcal{R}^2$ indicating the inclusion of too many parameters.

Table 5.6 shows that the concentrate HM recovery model complements the tailings stream HM recovery model. The same p-values were obtained in both cases (except for the intercept). The concentrate stream HM grade model was developed using the same variables as in Table 5.2. Squared feed SG is not significant for the concentrate stream HM grade model (p-value 3 times higher than 0.05).

Stellenbosch University https://scholar.sun.ac.za

Table 5.6: Significant variables for concentrate stream response models (x_1 – coded feed HM grade, x_2 – coded feed SG, x_3 – coded feed flow rate and x_4 – coded splitter setting)

Grade model			Recovery model		
Parameter	estimate	p-value	Parameter	Estimate	p-value
intercept	0.54	1.03E-14	Intercept	0.21	3.42E-09
x_1	0.06	7.66E-05	x_1	0.06	1.39E-04
x_2	-0.05	2.18E-01	x_2	-0.22	1.16E-06
x_4	0.02	0.66	x_3	-0.04	0.07
x_1x_4	0.06	0.00	x_4	0.14	2.79E-05
x_2^2	0.07	0.17	x_1x_4	0.05	0.01
			x_2x_4	-0.22	7.68E-03
			x_1^2	-0.01	1.22E-03
			x_2^2	0.11	8.93E-03

The tailings HM grade model is more appropriate for use in mass balances since the concentrate grade model can produce unrealistic results and the presence of outliers were detected. Despite the concentrate grade model being statistically significant it is less precise - likely due to errors in concentrate stream solids and mass flow rate measurements (because the concentrate grade model has similar significant parameters and precision to the flow ratio model). Due to the use of reconciliation the same HM recovery model can be obtained regardless of the stream values used to derive the model.

5.3.3. Response models confirmation

A single confirmation run was performed at the levels shown in Table 5.7. The measured values were reconciled with the spiral setup mass balance, as done with the experimental values, and then centered with the same values (Table 12.4) used to find the coded values of the experimental design. Confirmation was not performed outside of the experimental design range. The responses that were estimated from measured values is a tailings grade and recovery of 0.40 and 0.45, a concentrate over tailings stream total flow ratio of 0.15 and concentrate interface measurement of 86.60 mm.

Table 5.7: Experimental levels for the confirmation run (run 29)

	Feed Grade	SG	Flow	Splitter
Measured mean	0.57 (-)	1.20 (-)	7.00 (m^3/h)	8.5 (cm)
Reconciled mean	0.49 (-)	1.18 (-)	6.60 (m^3/h)	-
Coded value (x)	-0.29 (-)	-0.56 (-)	-0.58 (-)	0 (-)

The confirmation point results were compared to predictions obtained from the models fitted to runs 2-28 (run 7 omitted) of the reconciled experimental values (formulated via parameter selection).

Figure 5.19 graphically compares the confirmation responses with predicted values. 95% prediction intervals are included in the plot. Grade and recovery is overestimated and the flow ratio and interface is underestimated. Only the recovery confirmation response does not fall within model 95% prediction interval. The grade model shows the best performance on the confirmation grade response with the recovery model showing the worst performance.

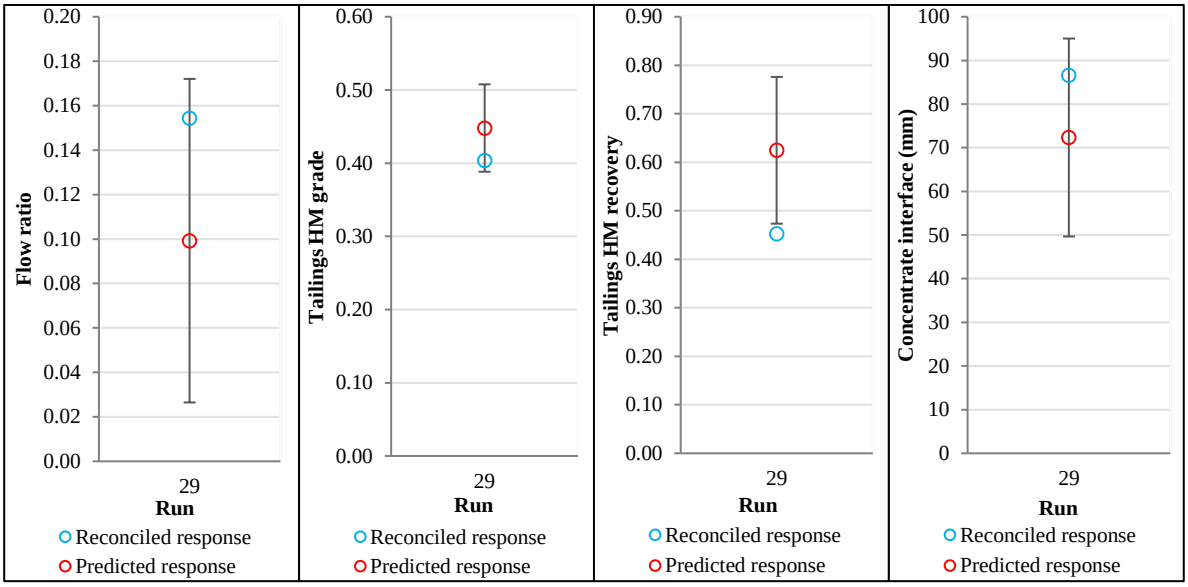

Figure 5.19: Prediction results on the confirmation run (left: flow ratio, centre left: tailings HM grade, centre right: tailings HM recovery, right: concentrate interface; error bars represent 95% prediction interval)

The points, within the experimental design space, that were the closest (by Euclidean measure) to run 29 is runs 5 & 18. Tailings HM grade and recovery at the latter points were over 0.5 and 0.8 respectively which causes the RSM models to overestimate tailings grade/recovery in the confirmation point vicinity. The feed SG of run 29 was approximately 1.2 while runs 5 & 18 had feed SGs at approximately 1.5 (feed HM grade and flow rates were similar for all 3 tests). Higher solids concentration meant that more material was transported to tailings for runs 5 & 8 (leading to higher concentrate grade and recovery).

5.4. Extended Holland-Batt spline model

5.4.1. Chromite data set

Equation 3.3 was fit to the data of runs 2-28 as described in Section 4.3.2 for the cases of feed solids and HM recovery in the concentrate. However, if each run is treated as individual tests it may be possible to overfit ($\mathcal{R}^2 = 1$) Equation 3.3 - splines may be fitted to single points. It was assumed that tests (2, 3), (9, 16), (19, 20) and (23, 25) were run at the same feed flow rates and slurry densities (as desired in the experimental design) so that only a feed correction, according to Equations 3.4 & 3.5, is required to make all feed conditions equal. The feed flow rates and slurry densities of runs 3, 16, 20 and 25 were set to the values of runs 2, 9, 19 and 23. Feed solids fractions and HM grades of runs 3,

Stellenbosch University https://scholar.sun.ac.za

16, 20 and 25 were shifted to the grades of runs 2, 9, 19 and 23. This 'correction' provides 4 cases where 2 data points are available for spline fitting.

Standardised residual plots for the two Holland-Batt spline models are given in Figure 5.20 (standard mean squared error, Gaussian variance with Bessel's correction, was used as an approximation for model variance). The residuals for the solids recovery model is similar to those of the HM recovery model (except that its residuals are generally slightly lower). Both models show potential heteroscedastic behaviour and an outlier possibly exists at run 26 (Run 28 is close to a standardised residual of 3). There are a total of 4 data points that have a standardised residual larger than 2. Concentrate solids recovery standardised residuals have a mean of 0.15 and the HM recovery model residual mean is 0.14. These mean residuals are still acceptably close to 0 (noise model variance may be inappropriate).

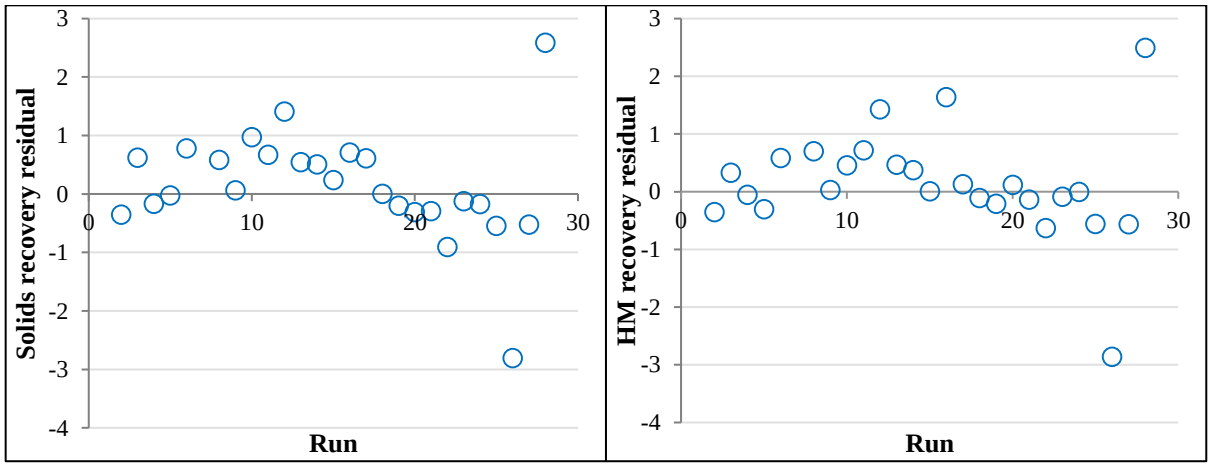

Figure 5.20: Concentrate solids (left) and HM recovery (right) standardised residuals (Holland-Batt spline case)

Figure 5.21 show plots of predicted recovery values against reconciled experimental responses. The concentrate HM recovery model shows greater deviation from the diagonal line (perfect modelling case). No physically unattainable values are obtained – as is possible with RSM models. Predicted responses show lower recovery values than that what was obtained with the reconciled responses.

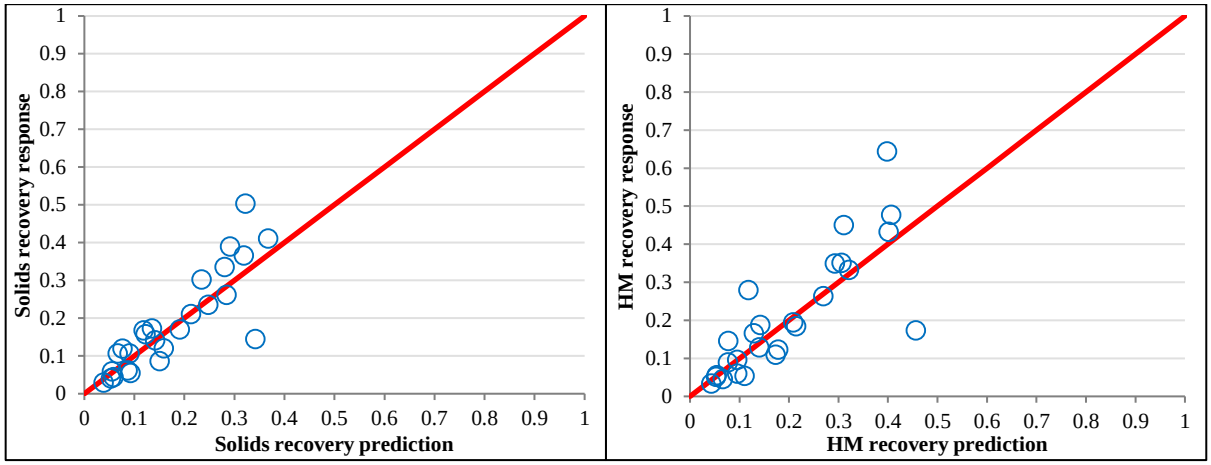

Figure 5.21: Reconciled concentrate recovery values vs. predicted concentrate solids (left) and HM recovery (right). Holland-Batt spline model case

Parameter solutions for the two Holland-Batt spline models are shown in Table 5.8. a_4 is negative meaning that higher SG values will increase separation efficiency. This is acceptable since a higher feed solids content will result in more particles, on the trough, moving to the spiral gulley (making it easier to recover more solids and HM). The flow rate parameters – a_3 – that were obtained are low; implying that flow rate does not significantly affect the recovery responses. Transition points are located at a fractional feed recovery of 0.11 in the concentrate stream. This is lower than HM grade in the feed which is contrary to Holland-Batt's (1990) description.

Table 5.8: Parameter solutions for the concentrate solids and HM recovery (Holland-Batt spline model case)

	Estimate	
Parameter	Solids recovery	HM recovery
a_1	0.11	0.12
a_2	0.62	0.57
a_3	7.00E-04	2.00E-03
a_4	-0.54	-0.77

Correlation coefficients, AIC and AICc for the solids and HM recovery models are listed in Table 5.9. $\mathcal{R}^2$ values of both models are relatively low indicating there are some significant inaccuracies. Outlier points, like run 26 (see Figure 5.20), will reduce the $\mathcal{R}^2$. Adjusted $\mathcal{R}^2$ values are not significantly smaller – indicating the number of parameters is adequate (still they do not produce great accuracy). Akaike information criteria were calculated using Equations 4.12 & 4.13.

Stellenbosch University https://scholar.sun.ac.za

Table 5.9: $\mathcal{R}^2$ and Akaike information criterion results concentrate solids and HM recovery models (Holland-batt spline model case)

	Solids recovery model	HM recovery model
$\mathcal{R}^2$	0.74	0.66
$\mathcal{R}^2_{adj}$	0.70	0.61
AIC	-57.96	-40.36
AICc	-54.96	-37.36

The AIC for the HM recovery model in Section 5.3.2 (RSM for the concentrate stream) is -55.03. For the sample size corrected version or AICc, the criterion becomes -42.09. Despite the linear regression model having 5 more parameters the log likelihood for the RSM models was still small enough to produce the superior corrected Akaike information criterion. However, AICc values only differ by about 4 suggesting nearly equivalent validity on the chromite data set.

Finally, confirmation test results (the results from run 29 – see Section 5.3.3) provide a last means to evaluate the spiral concentrate stream HM recovery models. Table 5.10 compares results from the extended Holland-Batt spline model and the RSM recovery model. The Holland-Batt spline models show an improvement of 3 % higher recovery than the RSM concentrate stream HM recovery model (prepared in Section 5.3.2). Both models underestimate the confirmation HM recovery.

Table 5.10: Confirmation point (run 29) results for concentrate stream recoveries

Solids recovery		HM recovery		
Holland-Batt spline				RSM
Response	0.45	Response	0.55	0.55
Predicted	0.35	Predicted	0.41	0.38
Difference (%)	10.36	Difference (%)	14.02	17.22

Concentrate HM recovery predictions are plotted in Figure 5.22 with prediction intervals (Monte Carlo integration of the posterior predictive distribution was used to find Holland-Batt spline prediction interval – see Appendix D). The RSM HM recovery model has a narrower prediction interval (than the Holland-Batt spline); however, the true response is outside of the prediction interval. In Figure 5.22 the Holland-Batt models shows improved accuracy with lower precision than the RSM case.

Stellenbosch University https://scholar.sun.ac.za

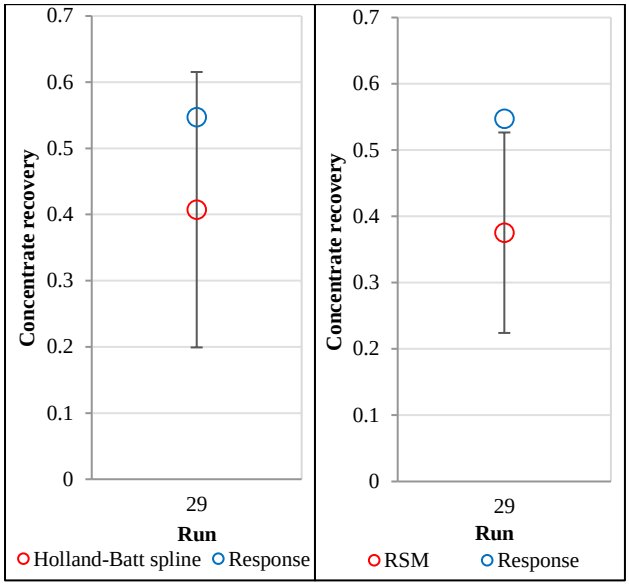

Figure 5.22: Concentrate HM recovery prediction comparison at the confirmation run for the extended Holland-Batt spline model (left) and RSM (right) (error bars represent 95% prediction interval)

It can be desirable to use the linear regression models based on the preceding statistical tests (Section 5.3.1). However, RSM performance on the confirmation run (which is an interpolation point) is lacking when compared to the Holland-batt alternative. Another important issue for the RSM case is extrapolating for wider splitter settings. This is not advised and can result in unrealistic grade/recovery values. This is not possible for the Holland-Batt spline model (which will still require further investigation on the incorporation of feed condition variation).

5.4.2. Hematite separation data set

Because the results in Section 5.4.1 are based on a new spiral, some validation of model parameters is required. It is also desirable to determine general applicability of the extended Holland-Batt model – especially to slurries with different mineral components. Thus, concentrate solids and Fe_2O_3 recovery Holland-batt spline models were prepared from the (hematite separation) data set of Sadeghi (2015). The ΔS symbol in Equation 4.7, for the modelling case in this section, represent relative solids fraction (instead of relative SG as in Section 5.4.1). Centre levels (needed to find ΔF, f & ΔG) for the hematite separation data modelling problem are based on test 7. Total feed flow rates were determined by assuming that the total mass comprises feed slurry combined with wash water additions (wash water additions are assumed to be equal to the planned experimental design levels). This assumption is required to determine total concentrate stream flow rate.

Standardised model residuals are contained in Figure 5.23 (standard mean squared error was used as an approximation for model variance). Solids recovery residuals show no apparent heteroscedastic behaviour. Fe_2O_3 recovery residuals show more potential heteroscedastic behaviour (mainly due to the values of the first 5 observations). Standardised residual means are 0.09 for the solids recovery

model and 0.03 for the Fe_2O_3 recovery model – showing a slight bias in model noise. However, the standardised residual means for the hematite data set are lower than what was obtained in Section 5.4.1. An outlier is present in the Fe_2O_3 model residuals at observation 3. This corresponds to an initial recovery point (or the concentrate recovery) in test 7.

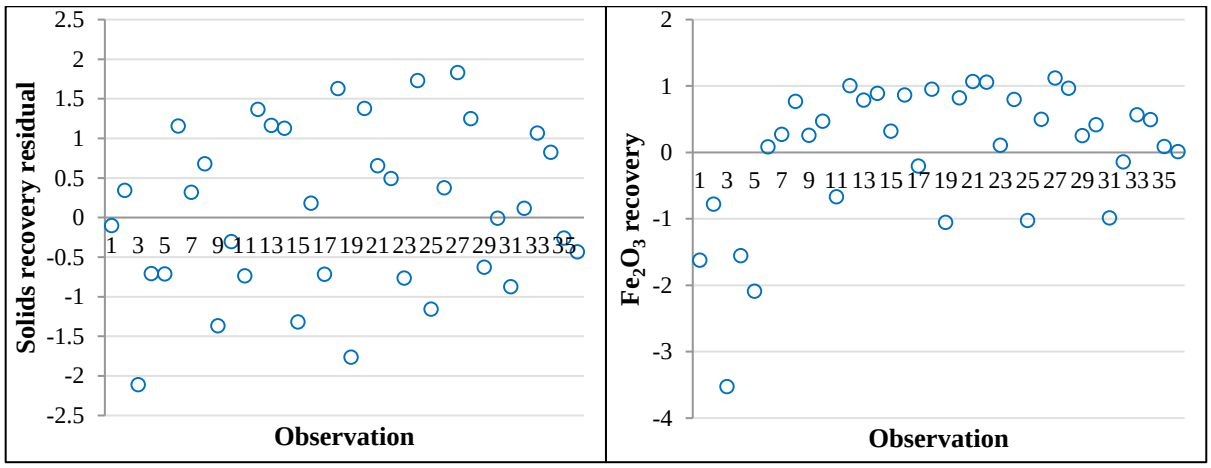

Figure 5.23: Concentrate solids (left) and Fe_2O_3 recovery (right) standardised residuals (Holland-Batt spline model case)

Figure 5.24 compares response and predicted results of test 7. The first datapoint in the left frame shows a deviation of about 0.08 which led to the potential outlier in the right frame of Figure 5.23. In Figure 5.24 the right frame shows results for the test with best model fit. Clearly the Holland-Batt model struggles to capture the 2nd recovery zone (currently modelled with a power law trend); which shows changing curvature. Recoveries are generally underestimated for the hematite data set.

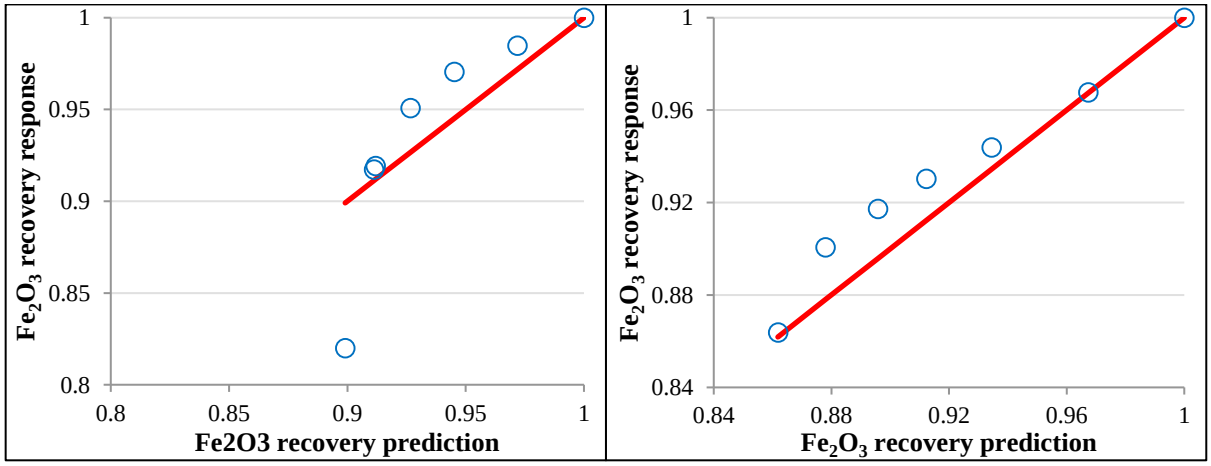

Figure 5.24: Reconciled concentrate Fe_2O_3 recovery values vs. predicted values (left: plot for test 7; right: plot for test 10). Holland-Batt spline model case

Parameter estimates and correlation coefficient results are listed in Table 5.11. $\mathcal{R}^2$ values are higher than for the chromite data set case and $\mathcal{R}^2_{adj}$ values are nearly equal to $\mathcal{R}^2$ values. Flow rate parameters have higher values than in Section 5.4.1 (this suggests flow rate should have a significant

Stellenbosch University https://scholar.sun.ac.za

effect on species recovery). The solids content parameter is negative – similar result to what is obtained in Section 5.4.1.

Table 5.11: Correlation coefficient and parameter results for the concentrate solids and Fe_2O_3 recovery (Holland-Batt spline model case)

	Solids recovery	Fe_2O_3 recovery
$\mathcal{R}^2$	0.88	0.78
$\mathcal{R}^2_{adj}$	0.87	0.76
Parameter estimates		
a1	0.33	0.07
a2	0.25	0.08
a3	0.25	0.03
a4	-3.38	-0.12

The models prepared in this section show similar results to Section 5.4.1 and the solids recovery models show best performance. MOI recovery provide the least precise models. Modelling on Sadeghi's (2015) data set show that Equation 4.7 may need tweaking to correct the curvature required for the 2nd recovery zone.

RSM models show greater precision on training data; however, the extended Holland-Batt models show promising confirmation results. Further investigation, in terms of spiral plant simulation, is required to resolve this apparent conflict.

5.5. Spiral plant simulation results

5.5.1. Response surface methodology models implementation case

The solved process stream states of the primary circuit from WPL is presented in Figure 5.26 (the case study PFD is presented in Figure 5.25 for convenience).

Stellenbosch University https://scholar.sun.ac.za

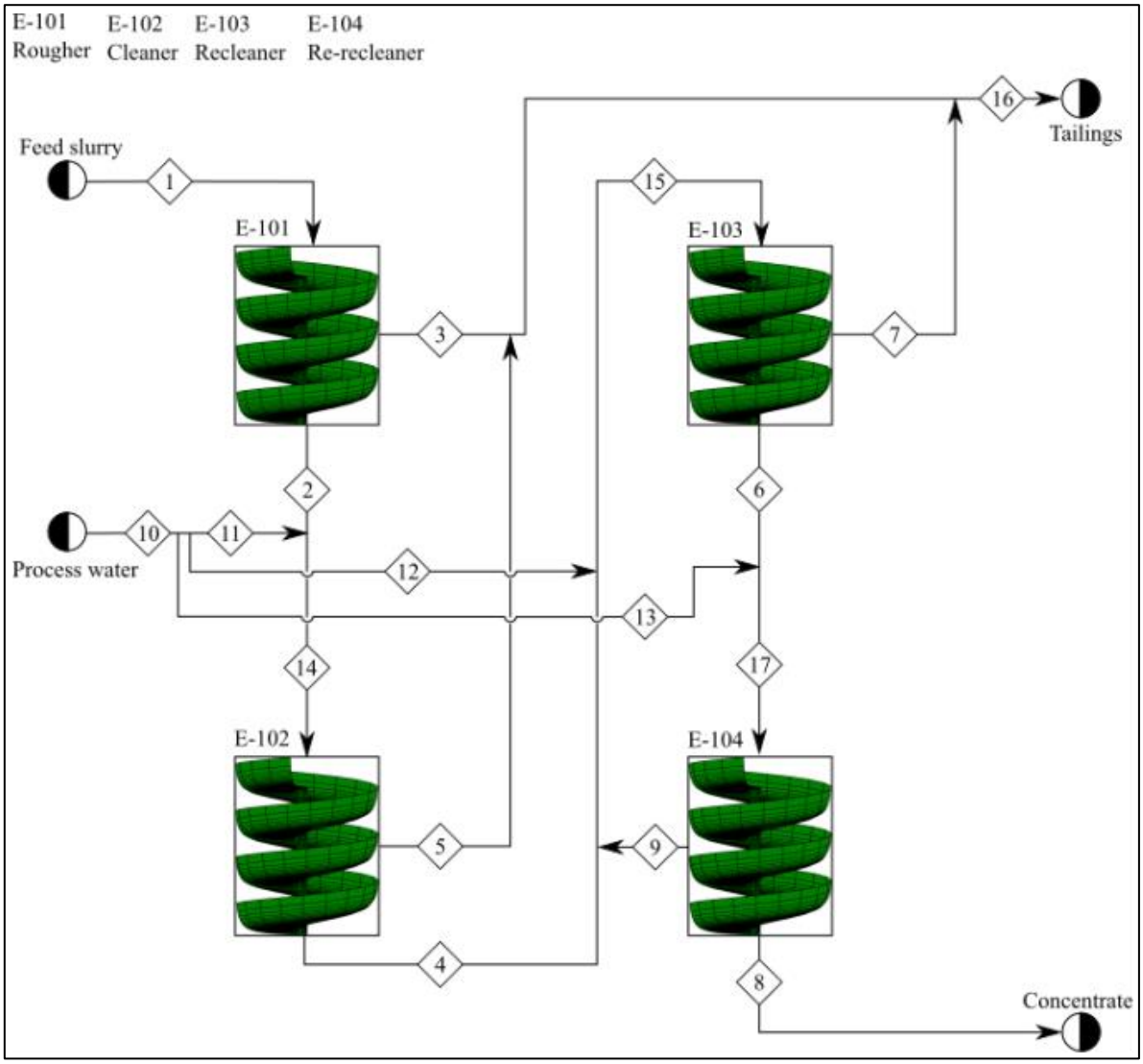

Figure 5.25: Primary circuit PFD (obtained from Figure 4.8)

The tailings RSM models from Section 5.3.1 were used to prepare the spiral simulation (due to better grade model performance than the concentrate grade model). HM grade values are acceptable but several streams (mostly tailings) show solids fraction values close to 0. The small concentrate stream flow rate results indicate that the RSM models may be evaluated outside their design or even valid range.

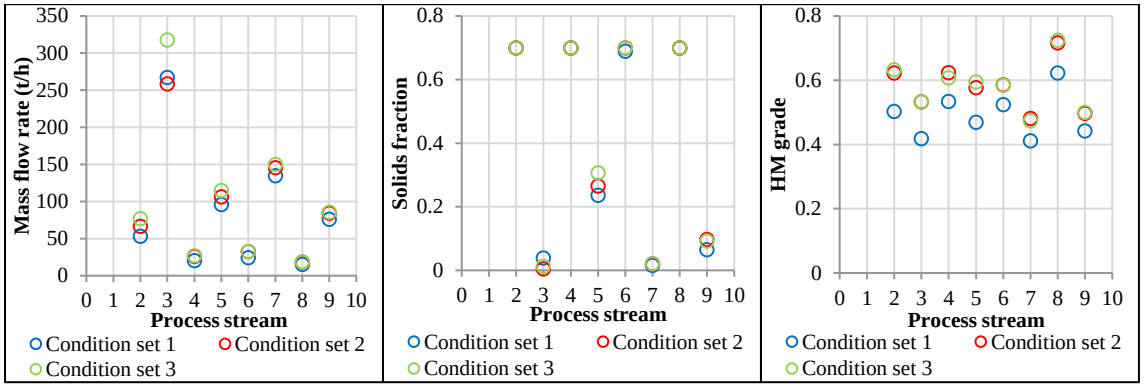

Figure 5.26: Process stream flow rate (left), solids fraction (middle) and grade (right) variables (using RSM models to simulate spirals)

Solved process stream values are tabulated in Tables 5.12, 5.13 and 5.14. In each case solids concentrations obtained for stream 3 are lower than 0.05 which already suggests poor recovery values (because all particles are going into concentrate streams). It can, at this stage, also be expected that the spiral models are evaluated well outside of their experimental range. Tables 5.12, 5.13 and 5.14 show that rougher spirals are not concentrating/upgrading heavy minerals (in stream 2) for each feed condition case.

Table 5.12: Process stream(s) results for the first feed condition set (using RSM models to simulate spirals)

	1	2	3	4	5	6	7	8	9
Mass flow (t/h): X_1	316.80	52.96	267.44	19.14	93.92	24.61	130.62	15.88	75.34
Solids fraction: X_2	0.15	0.70	0.04	0.70	0.24	0.50	0.00	0.70	0.00
HM grade: X_3	0.50	0.51	0.42	0.63	0.46	0.68	0.49	0.75	0.55

Table 5.13: Process stream(s) results for the second feed condition set (using RSM models to simulate spirals)

	1	2	3	4	5	6	7	8	9
Mass flow (t/h): X_1	316.80	66.00	258.86	24.06	104.18	25.99	141.03	19.18	81.58
Solids fraction: X_2	0.15	0.70	0.01	0.70	0.27	0.70	0.00	0.70	0.03
HM grade: X_3	0.65	0.63	0.53	0.74	0.57	0.72	0.58	0.87	0.61

Stellenbosch University https://scholar.sun.ac.za

Table 5.14: Process stream(s) results for the third feed condition set (using RSM models to simulate spirals)

	1	2	3	4	5	6	7	8	9
Mass flow (t/h): X_1	385.20	77.16	317.94	27.15	115.17	32.41	149.77	18.30	85.87
Solids fraction: X_2	0.15	0.70	0.01	0.70	0.31	0.70	0.02	0.70	0.09
HM grade: X_3	0.65	0.63	0.53	0.61	0.59	0.58	0.47	0.72	0.50

Overall mass balance errors and recoveries were calculated from the values in Tables 5.12 to 5.14 and are arranged in Table 5.15. The total flow rate error is determined by subtracting, from the feed mass flow rate (stream 1), the concentrate (stream 8) and overall tailings (streams 3, 5 and 7 combined) mass flow rates (process water additions must also be added to overall feed). Recovery values that were obtained are in an acceptable range but show that HM are not being concentrated. Instead, valuable minerals will be lost according to the simulation. Significant mass balance errors can be observed in Table 5.15. This can also contribute to the lower concentrate HM recovery (clearly the recycle stream cannot solved properly). This result is not ideal and does not reflect an effective spiral process (should the RSM models be adequate). It is clear that the RSM models are not well suited to modelling a spiral plant.

Table 5.15: Total mass flow rate error and MOI recovery in overall concentrate stream (using RSM models to simulate spirals)

Condition set	Total flow rate error (t/h)	HM recovery (%)
1	-11.06	34.98
2	-26.44	37.68
3	-35.98	24.71

It can still be useful to use RSM spiral models to simulate rougher banks – assuming feed levels stay within experimental design ranges. However, the mass balance errors clearly show that RSM models may not be suitable for further downstream spiral bank simulation. Especially when recycle streams are present (which will be the case in a typical spiral plant).

5.5.2. Extended Holland-Batt model case

Figure 5.27 shows plots similar to Figure 5.26 but for the Holland-Batt spline model case (used to solve the WPL's process stream states). The feed mass flow rate cut (or recovery) to concentrate was set to 20% for all spiral banks (based on rougher spiral's feed mass cut in Section 5.5.1). Similar flow rates were obtained in Figure 5.27, when compared to Figure 5.26. Solids fraction values do not go as low as the values in Figure 5.26 and no solids fraction value is higher than 0.35 (in Figure 5.26 values as high as 0.8 are obtained which are too high for spiral operation). HM grade values (in Figure 5.27)

Stellenbosch University https://scholar.sun.ac.za

are higher than in Figure 5.26 and every concentrate stream shows improved (more realistic) HM grade.

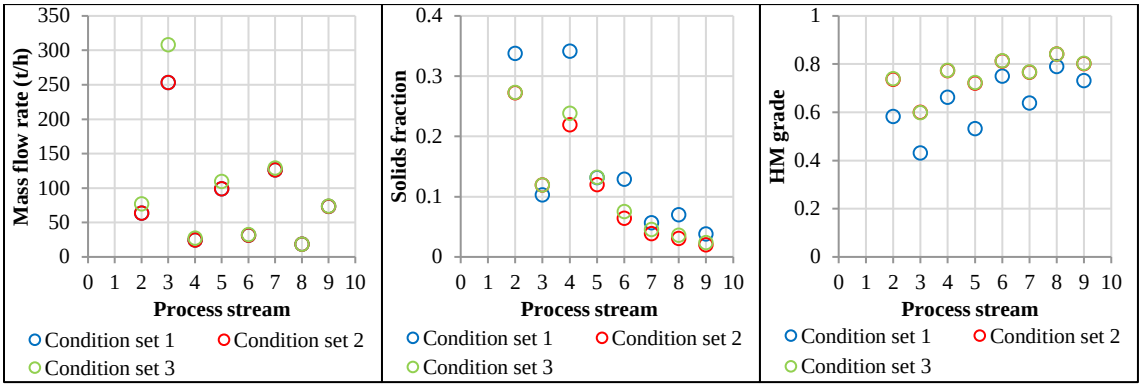

Figure 5.27: Process stream flow rate (left), solids fraction (middle) and grade (right) variables (using Holland-Batt spline mode to simulate spirals)

Table 5.16 shows the overall total mass flow rate balance error for the spiral plant and the concentrate stream (stream 8) HM recovery. Using the Holland-batt spline model improves the overall plant mass balance accounting. Recovery values are still quite low (most HM goes to tailings streams) implying that the feed conditions are far removed from optimal conditions (or that simulation of successive spiral banks become less realistic). Low recoveries can be expected, for this spiral plant, because only concentrate streams feed successive spiral banks (only a cleaner product can be achieved this way). The entire WPL circuit includes a scavenger section that treats tailings streams which will increase HM recovery.

Table 5.16: Total mass flow rate error and MOI recovery in overall concentrate stream (using Holland-Batt spline model to simulate spirals)

Condition set 1	Total flow rate error (t/h)	HM recovery (%)
1	0.0000711	4.25
2	0.0000711	1.52
3	0.0000713	1.50

The Holland-Batt spline seems to be better suited for spiral plant simulation and shows improved extrapolation behaviour. The spline based model's precision (or lack thereof) will confound the accuracy of plant variable results obtained (in Table 5.16's case it is the low recovery values) but at least unrealistic values can be avoided.

5.5.3. Simulating metallurgical performance

Sections 5.5.1 and 5.5.2 already indicate that the extended Holland-Batt model may be better suited to spiral plant simulation. However, both models show poor recovery performance at the considered feed

Stellenbosch University https://scholar.sun.ac.za

conditions. Plant simulations over 900 sampled feed conditions were performed to determine the possible concentrate HM grade and recovery variations (solids and HM grade values were uniformly drawn between 0 and 1, and flow rate values were drawn from $\mathcal{N}(360, 7.7)$). The metallurgical performance, as estimated by both spiral models, is provided in Figure 5.28 (see Section 5.1). This figure supplements Figure 5.2 which showed contours. However, in Figure 5.28's case, only single points from contours are plotted (due to the high number of feed states considered) to obtain a broad picture of changing feed condition effects.

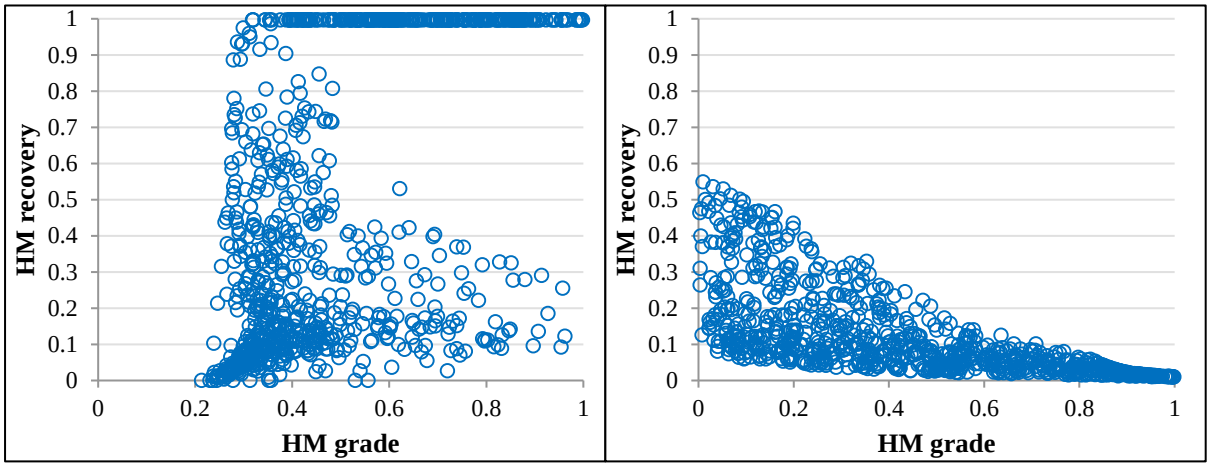

Figure 5.28: Simulated metallurgical performance, at different feed conditions, for WPL primary circuit concentrate stream (left: RSM models; right: extended Holland-Batt spline; obtained from Figure 5.2)

The left frame of Figure 5.28 clearly shows that the RSM models are not adequate for spiral plant modelling. Firstly, the RSM models achieve HM recovery of 1 at certain feed conditions which is a dubious result – especially when HM grade is higher than 0. No monotonically decreasing recovery trends are discernible in Figure 5.28's left frame – except for grade values higher than 0.3. Lastly, the RSM models do not show any data points for grade values lower than 0.2. The enhanced Holland-Batt spline based simulation shows decreasing recovery values from grade equal to 0 to 1 (which is expected from metallurgical plants). Maximum HM recovery in the right frame is 0.6 because the splitter settings were not changed – limiting the amount of spiral feed mass recovery.

5.6. Optimal sensor placement

Optimal sensor placement algorithms were developed by using the spiral plant simulations (at steady state) obtained via extended Holland-Batt model implementation. The extended Holland-Batt model is selected as the spiral concentrator simulation tool because it produced the most realistic process variables states. Thus, Algorithms SPI & SPII addresses Objectives 4 & 5 by considering the same plant and feed conditions. HM and sensor market prices are assumed to be constant and all variable errors are Gaussian. HM market prices are also taken as constant over product grade changes.

Stellenbosch University https://scholar.sun.ac.za

5.6.1. State estimation based approach

Optimal sensor locations were determined, via the minimization of Equation 3.17, for every case of sensor omission from the entire possible network (and over all 30 feed conditions in Section 11.3.4 – to investigate robustness) of the WPL's primary circuit. Figure 5.29 compares optimal sensor configuration results (J_L – monitoring loss and J_C – financial cost) for all sensor omission cases and feed conditions. The square root of J_L is used on the x-axis to rescale the original J_L values and is not intended as a measure of error or standard deviation. Reducing the number of sensors increases J_L or, in other words, reduces revenue monitoring performance. No significant reduction in revenue monitoring performance occurs when more than 3 sensors are removed (for the optimal sensor placement case). The results in Figure 5.29 is split between two frames to ensure legibility.

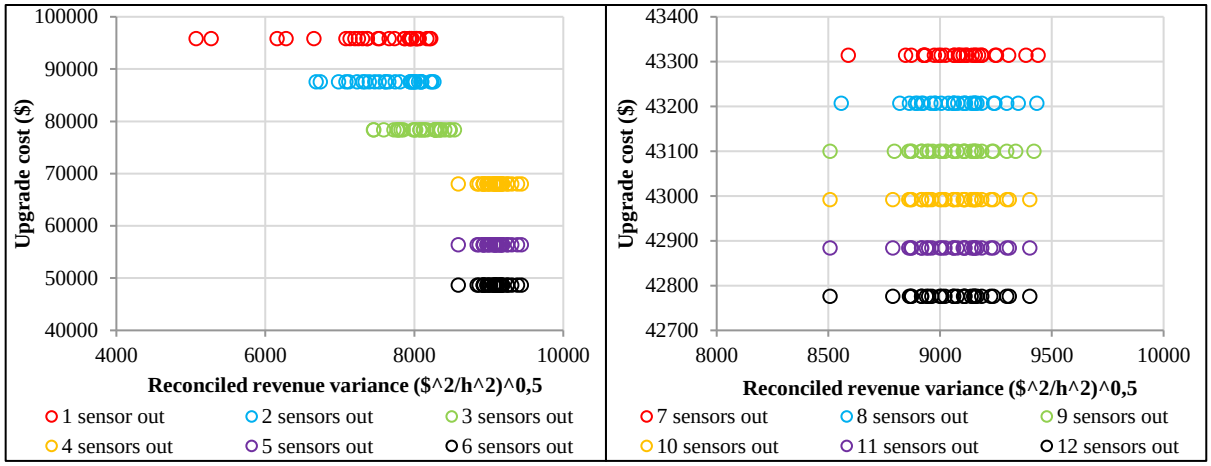

Figure 5.29: Sensor network implementation cost vs. the square root of J_L in order of reducing redundancy (left: plot for the omission of 1 – 6 sensors; right: omission of 7 – 12 sensors; Algorithm SPI)

Table 5.17 shows the optimal placement solutions for the cases of 1 – 7 sensors omitted. These are the cases that show the most robust optima of Equation 3.17. From Figure 5.29 and Table 5.17 it is clear that the first 7 sensor removals are mostly controlled by J_C. However, the sequence of sensor removal, for omission cases 1 – 4, is influenced by J_L (as sensor redundancy is reduced).

Stellenbosch University https://scholar.sun.ac.za

Table 5.17: Locations of optimally removed sensors (by Algorithm SPI) in order of reducing redundancy (1 – 7 sensor omission cases)

	Stream number			
Number of sensors omitted	Grade	Solids fraction	Flow rate	Observability
1	3 (for some cases 9)	-	-	all observable
2	3, 5	-	-	all observable
3	3, 5, 7	-	-	all observable
4	3, 5, 7, 9	-	-	all observable
5	2, 3, 5, 7, 9	-	-	not all observable
6	2, 3, 4, 5, 7, 9	-	-	not all observable
7	2, 3, 4, 5, 6, 7, 9	-	-	not all observable

The first four sensors that are optimally selected (by Algorithm SPI) for removal, as shown in Table 5.17, are the online XRF at rougher tailings (for most feed cases), cleaner tailings, recleaner tailings and re-recleaner tailings (in that order). This sequence of sensor removal arises partly from the fact that the online XRF sensors are the most expensive – leading to the greatest reduction of J_C. The order of the XRF sensor removal arises from the J_L term of Equation 3.17. If a tailings grade estimator is further away from the re-recleaner bank then its removal will lead to a lower revenue monitoring performance reduction (see Appendix D for the two spiral bank case). Hence the order from roughers to re-recleaners.

Optimal sensor locations for the 1st sensor omission case showed two optimal solutions, depending on the feed conditions. In the majority of feed cases the optimally removed sensor was the rougher's online XRF tailings sensors. In some feed cases the optimally removed sensor is the re-recleaner tailings online XRF. Figure 5.30 shows the optimal sensor removal cases versus their feed grade conditions. Re-recleaner tailings sensors are removed when plant feed HM grade is low (< 0.2 for most cases).

Stellenbosch University https://scholar.sun.ac.za

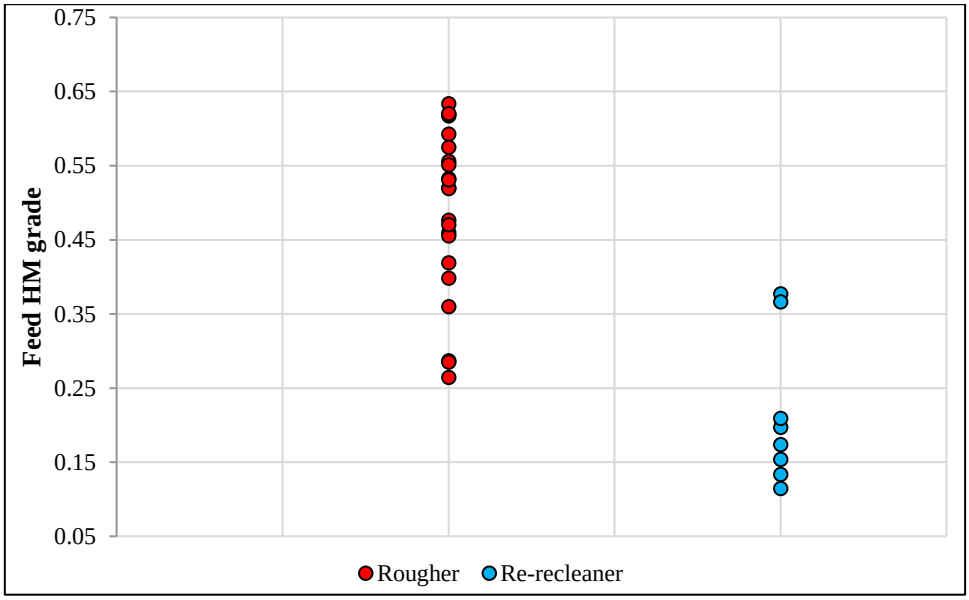

Figure 5.30: Plant feed HM grade for optimal sensor removal (1st sensor omission case; Algorithm SPI)

In the case where 2 sensors are removed, the optimal solution results in the omission of rougher and cleaner tailings online XRF. This is the solution across all feed conditions. In the cases where 3 or 4 sensors are removed the same solutions are also obtained for all feed condition cases (removal of recleaner and re-recleaner tailings sensors are added to the omissions in the 2 sensor removal case). The same solutions are also shared, for all feed conditions, over the cases where 5 – 7 sensors are omitted (only now interface sensors are removed). Further details on monitoring performance sensitivity, to varying feed conditions, are provided in Appendix D (Section 12.3.1).

When 5 sensors are removed the optimal solution includes the omitted sensors from the 4 sensor case – but now also include the rougher concentrate grade (or interface) sensors. For the sequential sensor omission cases the order of concentrate grade sensor removal is cleaner and recleaner concentrate grade sensors. Interface sensors (assuming it is necessary to monitor all spirals in a bank) are the second most expensive sensor implementation. Rougher concentrate grade sensors are removed first because it is the most expensive (the rougher spiral bank has the most spirals). The number of spirals reduce for successive spiral banks (see Section 4.4) – hence the rougher-cleaner-recleaner sequence.

In all solutions, for the 8 – 12 sensor omission cases, the grade estimators (listed in the final entry of Table 5.17) are also removed. After the omission of all allowable online grade estimators, Algorithm SPI starts to remove flow rate and solids fraction sensors. The location of sensor removal shows much more variation and suggests that multiple optima of Equation 3.17 may be found. Figure 5.29 shows the removal of these sensors have no significant effect on revenue monitoring performance.

Algorithm SPI is limited by the fact that appropriate monitoring performance formulation is difficult for metallurgical plants. This complicates the multi-objective search when considering removal of a sensor when no more redundant HM grade sensor are implemented. Removal of additional sensors do

not lead to significant J_L changes. This makes interface sensor placement difficult – especially when the placement of these sensors are the sole focus (and online flow rate monitoring is not yet desired). Changes in J_L also do not indicate how operators may be able to influence plant operation.

5.6.2. Metallurgical performance improvements

Recovery and grade values were simultaneously maximized (by changing splitter settings), for all feed conditions in Section 11.3.4 and sensor configurations, via Algorithm SPII – for the WPL plant's primary circuit. Optimal objective function values that were obtained, at new splitter settings, were subtracted from original J_L values (based on starting splitter positions) and are plotted in Figure 5.31 (against the required upgrade cost). For brevity's sake the sensor configurations (in Figure 5.31) will be referred to by the numbers in Table 4.3. Figure 5.31 does not show optimal sensor configuration solutions as in Figure 5.29 but instead shows how changing splitter settings at certain spiral banks (according to the interface sensors configurations) can hypothetically improve concentrate HM grade/recovery.

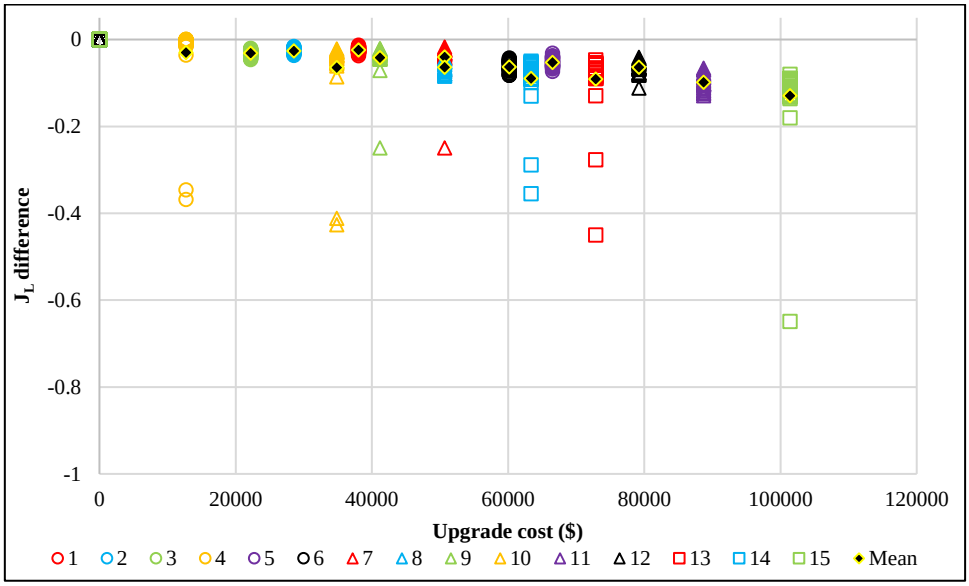

Figure 5.31: Improvement in J_L (relative to starting conditions of each optimization run) vs. sensor configuration (see Table 7 for names) cost (Algorithm SPII)

The general trend in Figure 5.31 is that more expensive configurations usually lead to better plant recovery and product grade. There are several sensor configurations that are capable of leading to significant improvements in J_L for certain feed conditions. Configuration 15 shows the data point with the greatest performance improvement (this is expected since all spirals are considered for monitoring). Configuration 13 shows the data point with the 2nd greatest performance improvement (the 12th most expensive strategy). However, configuration 10 has the points with the 3rd and 4th highest improvements – while being the 4th cheapest monitoring strategy. There exists certain feed conditions where sparse sensor configurations can achieve significant improvement in the process.

Stellenbosch University https://scholar.sun.ac.za

However, these are only particular feed state instances and it is necessary to find changes in the bulk of data points.

Figure 5.32 illustrates the improvement that different sensor configurations can hypothetically lead to – in terms of the plant revenue production rate. Original plant revenues (plant states before optimization) were subtracted from plant revenues after optimization – similar to Figure 5.31. There are clearly several cases where worse revenue rates were obtained. This is possible since J_L can still be improved when small decreases in HM recovery are offset by large HM grade improvements.

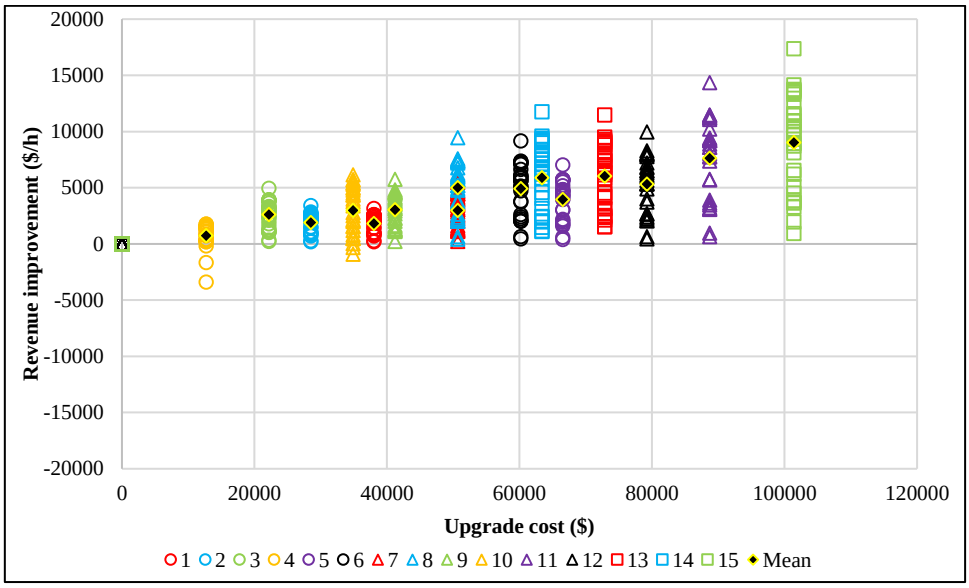

Figure 5.32: Improvement in revenue produced vs. sensor configuration (see Table 7 for names) cost (Algorithm SPII)

Monitoring all spirals lead to the best performance (highest revenue rates in this case) and the cheapest configuration results in only re-recleaner spiral monitoring (showing the worst improvement in revenue rates). Configurations 10 (recleaner & re-recleaner) and 14 (cleaner, recleaner & re-recleaner) show noticeable process improvement at much cheaper cost than configuration 15. The four configurations that achieve the best performance, in increasing order is, 11-13-14-15 (based on Figure 5.32 means). All these configurations have monitoring of the recleaner spirals in common – which serves as an early suggestion that these spirals are critical. Sensor configurations 5-6-11 do not any show points with the low negative revenue improvements as in the case of 4-10. Configurations 5-6-11 all have rougher monitoring in common. This suggests that monitoring and control at rougher spirals can be important when low revenue performance must be avoided at all different feed conditions.

Initial results of Equation 4.18 (from Algorithm SPII) leads to C_4 as the overall optimal configuration. This is the cheapest configuration and clearly shows that J_C was the main selection factor (increases in revenue are not enough to justify greater upgrade expenditure). Due to this result, it is necessary to investigate a change in the α parameter of Equation 4.18. An important assumption is that a steady

Stellenbosch University https://scholar.sun.ac.za

state must be maintained over the span of α. Solutions of Equation 3.18 (with $\alpha = 24$ h – i.e. revenue production over a day), using the values in Figure 5.32, is graphed in histogram shape in Figure 5.3. Optimal solutions were determined for the cases where 3, 2, 1 or no sensors were left out. All possible sensor implementation combinations are considered for each scenario (the different cases forces Algorithm SPII to search more frugal sensor configurations). Multiple optima are present for all different sensor placement cases in Figure 5.3. However, clear dominant optima are present for the Monte Carlo samples considered: C_3, C_8, C_{11} & C_{15}.

The spiral bank sequence of sensor removal (according to Figure 5.3 - starting from "All") is re-recleaner, rougher and then cleaner. Now, Algorithm SPII does not simply choose the cheapest option – indicating that revenue production significantly effects the optimization (when longer revenue collection time is incorporated). The omission of sensors at the re-recleaner spirals makes sense from a performance point-of-view because re-recleaner spirals are a last resort to influence concentrate grade – maximum recovery is set by rougher spirals. Omission of sensors at rougher spirals significantly reduce J_C, leading to the selection of C_8 (C_8 and C_6 have similar performance).

Figure 5.33 further illustrates the robustness of Algorithm SPII's optimal sensor placements. For the majority of feed condition samples, single clear optima exists for the three different C^* ranges. However, different sensor placement solutions are generally found at very low plant feed HM flow rates. Lower plant HM feed results in lower plant revenue (shown in Section 12.3.2) which leads to the selection of cheaper instrumentation strategies (when optimisation cannot compensate for higher upgrade cost). However, for the C^* range of configurations 1 to 10 the more expensive upgrade solution of C_6 was selected.

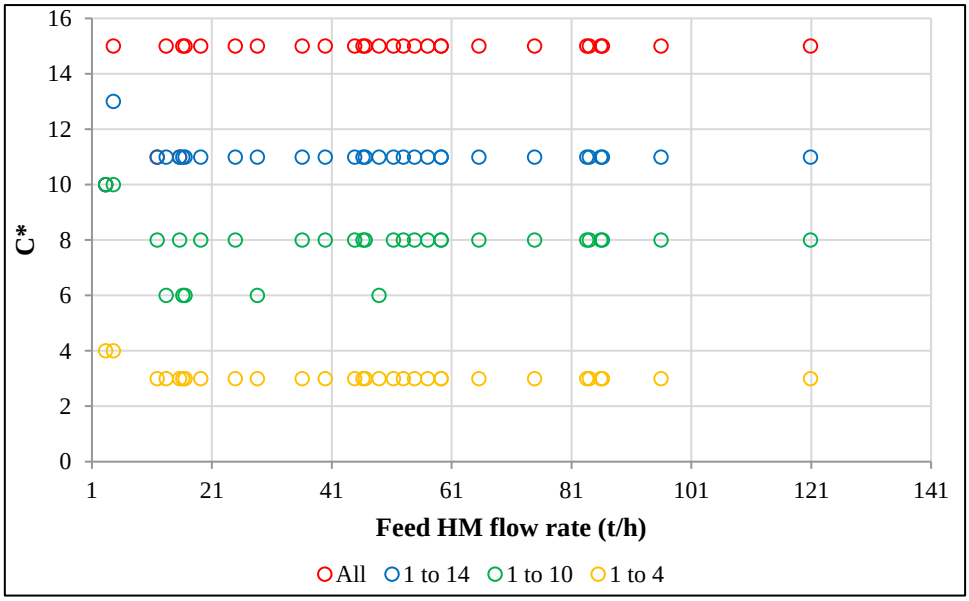

Figure 5.33: Sensor configuration (see Table 4.3 for names) solutions vs. feed HM flow rates (Algorithm SPII; $\alpha = 24$ h)

Stellenbosch University https://scholar.sun.ac.za

The overall results of this study indicate that computer vision based sensors (using logistic classifiers) can be added to a spiral plant (as simulated by the extended Holland-Batt models) to provide significant revenue benefits for a variety of feed conditions. Naturally this assumes that interface sensors can direct operators to optimize spiral MOI grade and recovery. However, the presented methodology can be used to justify further development and eventual implementation of conceptual sensors (in metallurgical plants).

Stellenbosch University https://scholar.sun.ac.za

Chapter 6: Conclusion and recommendations

6.1. Contributions and novelty

Several individual contributions to spiral monitoring, modelling and plant instrumentation design are proposed in this project. However, the main contribution is the framework that encompasses the steps from sensor development to sensor implementation. Such a framework is useful to determine future implementation of a proposed sensor. Preliminary suggestions are also provided which indicate the importance of monitoring and possible control of certain positions of units within a spiral plant. Figure 6.1 summarises the main contributions from the most important project steps.

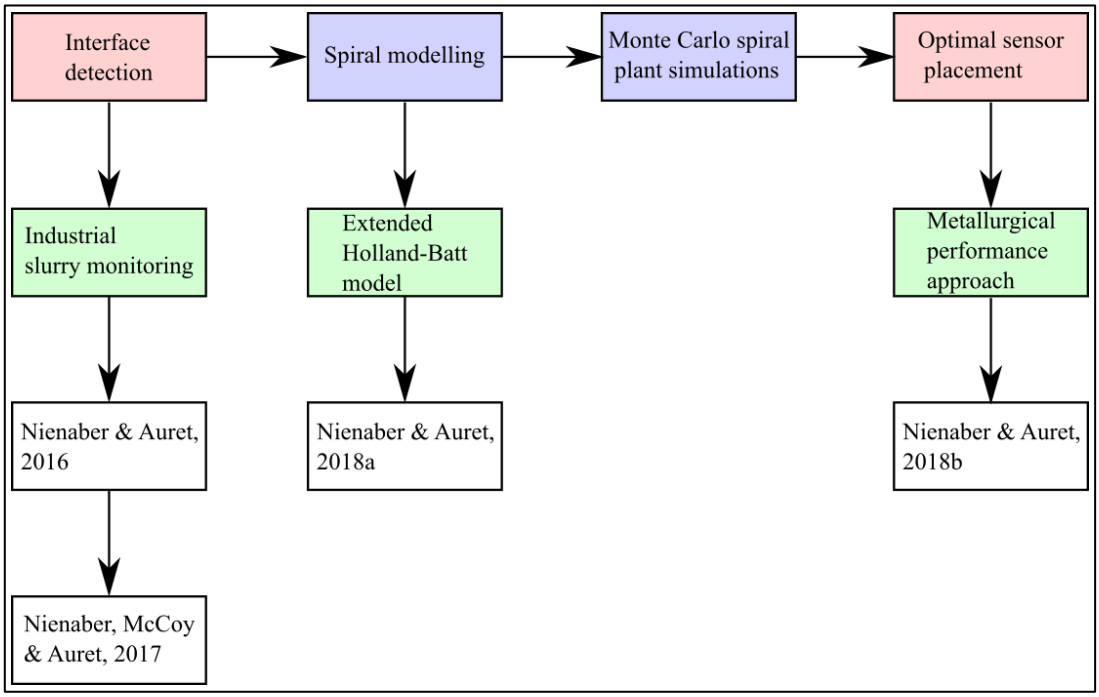

Figure 6.1: Summary of project steps and contribution(s) (green: research outputs; white: articles)

Interface detection results showed that machine learning provides an avenue for interface tracking in industrial mineral slurries (which, once solved, suggests the next step of possible future sensor implementation). Appropriate spiral models and plant simulation were required to investigate optimal sensor placement approaches. An extended version of the Holland-Batt model was proposed and compared against response surface methodology (RSM) modelling. The new Holland-Batt model was developed with spiral plant modelling kept in mind and it was found that it performed better on experimental confirmation results and also suited plant simulation better. Future spiral modelling methodologies should keep in mind plant simulation because most spiral modelling attempts, to date (see Section 3.1), stop at modelling or optimization of single spirals and do not show whether these models can lead to high fidelity plant simulations.

Finally, a metallurgical performance sensor placement approach (Algorithm SPII) was proposed and compared to the typical state estimation approach applied in literature (Algorithm SPI). Algorithm

Stellenbosch University https://scholar.sun.ac.za

SPII essentially constituted a sensitivity analysis of spiral plant optimization given different splitter control variations (varying feed conditions are not considered at length in optimal sensor placement literature). Results produced by Algorithm SPII include contributions of the different interface monitoring/splitter control configurations to plant production performance. This essentially allows classification of different spiral banks by how important their splitter settings are to the control of throughput and product grade/quality (instead of monitoring performance improvements which have little relevance at current spiral plants – see Section 1.2). Lastly, SPII compares sensor cost and revenue improvement directly (over a certain production time) leading to an overall design objective similar to the concept of return on investment. This is a new perspective on the multi-objective problem for sensor placement since previous methods relied on comparing dissimilar objectives via pareto fronts.

6.2. Interface detection

6.2.1. Conclusions

Two interface detection algorithms were formulated to solve the mineral interface (which form in spiral concentrators) detection problem. Algorithm CVI was based on existing image processing methods with parameter optimisation performed using genetic algorithms (GA). The second method, Algorithm CVII, was based on pixel classification using logistic regression. Both methods were applied to two data sets - derived from two different case studies: ilmenite sands and chromite separation. The chromite separation data set was representative of industrial spiral slurry conditions.

The ilmenite image set proved to be the simpler application of Algorithms CVI and CVII, and both methods can detect the desired interfaces. Similar mineral interface detection results were achieved using Algorithms CVI and CVII. However, Algorithm CVII proved to be the more reliable method for concentrate interface detection since Algorithm CVI can generate additional spurious edge detections. Algorithm CVII always produces a single response per interface.

Interface detection with the chromite image set was more challenging. Algorithm CVI was unable to provide a concentrate interface response in more than 90 % of the testing images (for parameters obtained from each training case). Training of Algorithm CVI for concentrate-gulley interface detection was suspended due to the poor concentrate interface detection results. Algorithm CVII can detect concentrate interfaces in more than 50 % of the images (for parameters obtained from each training case). However, Algorithm CVII cannot provide a majority of true positive concentrate interface detections in more than 65 % of the testing images (even when using the parameter set that provides the best interface detection results).

Training of Algorithm CVI is in the order of hours even when smaller chromosome populations of 50 are used. Algorithm CVII's training time is in the order of minutes and will only exceed training time of 1 h with larger training sets and greater iteration limits. Overall, it can be concluded that Algorithm

Stellenbosch University https://scholar.sun.ac.za

CVII is the superior method to detect mineral interfaces in spiral troughs. One of the major drawbacks of both algorithms is the amount of training data that must be generated manually to achieve useful interface detection results. Lastly, Algorithm CVII showed that interface detection on industrial slurries is possible and more complex machine learning methods may improve on the results found on this case study.

6.2.2. Recommendations and future work

Algorithm CVII uses logistic regression which is merely one of many statistical classifiers. Other statistical learning algorithms such as multi-layer perceptron (or neural) networks, naïve Bayesian classifiers or support vector machines could be applied to the existing image sets to determine whether the interface detection results can be improved. More labelled images should be prepared for the training of more complex classifiers – especially neural networks.

Another consideration for future study is to explore semi-supervised and unsupervised methods to segment mineral interfaces. Segmentation methods that require less user input (in this study's case less labelled images) can be developed quicker with lower chance of user labelling errors. Unsupervised segmentation methods will require more investigation into the features that must be calculated from each image to properly cluster regions of the images. Even when appropriate clustering is achieved a general methodology will have to be developed to determine which clusters belong to which part of a spiral trough or slurry.

Finally, Algorithm CVII (or improvement of the algorithms) must be applied to images obtained from industry. Industrial spirals will not always show clear mineral interfaces when spirals are not cleaned (e.g. due to lack of maintenance), feed slurries are not screened or when slimes are present. It should also be determined whether the laboratory developed Algorithms CVI or CVII's parameters can detect interfaces in industry. Another interesting problem includes testing whether optimal parameters from one spiral concentration application works for a different application (i.e. testing whether Algorithm CVII can detect ilmenite sands mineral interfaces when trained on the chromite images).

6.3. Spiral modelling & plant simulation

6.3.1. Conclusions

A 4-factor Box-Behnken experimental design was successfully performed and models were prepared based on data that were reconciled using a simple mass balance of the laboratory spiral concentrator (Multotec SC21 model). XRF analysis of all experimental solids samples were not conducted and instead a calibration curve was developed relating solids density to composition (in order to roughly estimate product stream compositions quickly). The solids phase components were grouped as light (LM) and heavy minerals (HM) and the calibration curve was developed using representative samples of the different homogenised feeds that were prepared before commencement of spiral modelling

Stellenbosch University https://scholar.sun.ac.za

experiments. Experimental spiral feed density and flow rate ranges spanned the design ranges stipulated by Multotec (Mojela, 2015).

RSM models describing concentrate interface position, concentrate-over-tailings stream mass flow rate ratio, tailings HM grade and HM recovery were prepared (all of which were statistically significant). The flow ratio and interface models were the least precise with the tailings grade model being the most precise. The final design matrices, used for model development, were not orthogonal due to blocking and the exclusion of runs with erroneous data (or where it was concluded that steady-state was not achieved). This confounds the analysis of significant factors and overall model significance. However, the models (and significant model parameters) still agreed with what has been previously observed in literature.

An extension of the Holland-Batt (1990) model was proposed, as an alternative to the RSM models, and applied to the chromite separation data set. The extended Holland-Batt spline based model shows promise as an improvement over RSM for spiral modelling (and spiral plant simulation). This can be expected since concepts like metallurgical recovery (recoveries cannot be lower than 0 or higher than 1) are built into the Holland-Batt model. Use of RSM is motivated by cheaper experimentation (in terms of time and financial cost) and the simplicity of evaluating a linear model (RSM is linear in respect to its parameters). However, the Holland-Batt based methodology require even fewer parameters but shows behaviour that is truer to spiral operation. Another issue with RSM models is that – while perhaps serving as good approximation within experimental design range – extrapolation can lead to significant deviations from a process' nature (except if a process can be expected to have general linear behaviour). Extended Holland-Batt models for solids and HM concentrate recovery were prepared (to allow spiral plant simulation); however, the precision of these models were lower than the RSM models'. RSM models also had lower AIC and $AICc$ statistics than the extended Holland-Batt model. Despite RSM's superior performance on training data, the extended Holland-Batt model showed better HM recovery predictions at the confirmation point.

The Holland-Batt model methodology was also tested on hematite separation data (from Sadeghi, 2015) to validate the extensions to Holland-batt's (1990) original model. Estimated parameters, based on the chromite and hematite data sets, show the same signs (a_4 is negative and all other parameters positive) and in both cases correlation coefficient values were lower than 0.9 (showing some lacking precision). Extended Holland-Batt modelling on both data sets showed the same trend for feed flow rate's effect on MOI recovery mentioned in Holland-Batt (1990) and Richards et. al. (2000: 68).

Steady state Monte Carlo WPL primary circuit simulations were performed to compare the different spiral models' (RSM and extended Holland-Batt) plant simulation ability over wide ranging feed conditions. It was found that the extended Holland-Batt models simulated the extended recovery-grade curves expected from metallurgical plants while the RSM models cannot provide simulations that satisfy mass balances for all sampled feed conditions. It was finally concluded that the extended

Stellenbosch University https://scholar.sun.ac.za

Holland-Batt models were the best spiral models and was subsequently used for the spiral plant simulations required for optimal interface sensor placement.

6.3.2. Recommendations and future work

Model fitting on Sadeghi's (2015) data set suggests that the 2nd recovery zone cannot be entirely modelled by a power law and that either another spline must be added, or a more general function should be used. Another important consideration is that Richards et. al. (2000: 68) states that an approximately quadratic trend exists between feed density and MOI recovery (an optimum exists at a certain SG). Regression analysis should include analysis of this trend as well.

Optimal experimental designs for extended Holland-Batt models, that also minimise experimental runs, should be investigated and prepared. Future spiral investigations will benefit greatly from frugal designs that can lead to the development of models more representative of spiral behaviour. Proper experimental designs will also reduce the level to which model parameter estimation is confounded. Future experimental work on the development of extended Holland-Batts models are also needed to validate trends in parameters found in this study.

There is still room for improvement on spiral plant simulation. In this work it was assumed all spiral starts, within the different spiral banks, receive uniform feed (from upstream banks). However, this is not necessarily true and further investigation is required to determine how feed flow to different spirals vary. This knowledge will help determine sparse interface sensor placements within spiral banks. Pilot plant scale tests will be required to experimentally determine how performance of spirals vary within a spiral bank and will be demanding in terms of cost and time. At this stage, a Monte-Carlo analysis can be used to further investigate how varying steady state spiral start feeds can affect sensor placement within banks.

6.4. Optimal sensor placement

6.4.1. Conclusions

Two interface sensor placement algorithms were tested using the simulation of the Glencore Rowland site. Algorithm SPI was based on existing methods in literature that investigates estimation variance reduction versus sensor network cost. These methods are used when it is necessary to decide where to place flow rate or species concentration sensors. However, placement of unit process sensors, like interface sensors, will require representation via some proxy if the same framework must be applied. Thus, a second framework, Algorithm SPII, was presented as an alternative means to determine interface sensor placement; relying on potential metallurgical performance improvement if certain spirals are monitored (assuming monitoring can directly lead to process optimization). A key difference between SPI and SPII was that splitter settings were held constant for SPI. Sensitivity of both Algorithms to changing feed conditions were included (by performing Monte Carlo simulations) in the analysis to determine sensor placement robustness.

Stellenbosch University https://scholar.sun.ac.za

For the case of Algorithm SPI the most important spirals to monitor, using interface sensors, in decreasing order is: re-recleaner, recleaner, cleaner and then rougher. This sequence stems from the fact that upgrade cost increases from re-recleaner to rougher and that monitoring around the re-recleaner spirals lead to lower variance in revenue estimation. From Algorithm SPII's results it is suggested that the order of spiral monitoring importance is: recleaner, cleaner, rougher and re-recleaner. Cleaner and recleaner spirals are important to monitor because they ensure higher HM recovery to the re-recleaner spirals – thus the significant impact on revenue improvement. The rougher spirals control the maximum possible revenue production but are the most expensive sensor implementation point – making roughers the third most important to monitor. Re-recleaner spirals merely improve concentrate HM grade and will not significantly increase revenue (when chromite prices are constant with respect to grade); rendering them as the least important (based on Algorithm SPII's assumptions). Interface placement results, obtained by both algorithms, were robust to changing steady state feed conditions.

It depends on the plant design or upgrade problem to decide which algorithm is better. Algorithm SPI, the state estimation approach, shows how revenue estimation may improve but data reconciliation will not necessarily show how higher or lower revenue can be achieved (as sensor configurations change). Monitoring of the variables of spiral bank streams are used as a proxy for the performance of interface monitoring but this is not currently relevant in spiral plants. The WPL spiral plant (the case study for this paper) that was considered, currently only has monitoring of overall feed and concentrate stream properties – complicating future verification of any of Algorithm SPI's findings. Also, when only the interface sensor's placement is considered, density and mass flow rate sensors become irrelevant. It will also suit plant operators better to know how changing splitter settings, at different spiral banks, affect plant performance.

Algorithm SPII is better suited to the interface sensor problem because it directly investigates how varying splitters (guided by interface monitoring) changes plant process streams. Potential revenue improvements are calculated based on the configuration of spiral monitoring and control allowing ranking configurations based on upgrade cost and revenue changes. Optimizing both objectives is simpler for SPII since both are valued in currency and revenue improvements can simply be scaled by time. Algorithm SPII is also computationally less expensive since only the different possible interface sensor configurations are iterated (instead of all possible mass flow rate and density sensors). However, Algorithm SPII does not yet include measures of metallurgical performance uncertainty.

6.4.2. Recommendations and future work

Many assumptions were required to evaluate both algorithms presented in this work. The market price of HM (the proxy for chromite) was taken as a constant. Market prices change over time and revenue also change when concentrate grade varies. Both these factors affect the value of plant concentrate and, therefore, plant revenue and possible revenue improvements (via splitter optimization). This can also affect optimal interface sensor placement. In future, sensitivity analysis of sensor placement will

Stellenbosch University https://scholar.sun.ac.za

have to include variations in revenue due to market and concentrate HM grade fluctuations. Further – detailed – investigations of sensor placement as a return on investment problem can then be performed; where optimal sensor placements are investigated over different revenue collection times.

Algorithm SPII used the assumption that initial splitter positions (for mathematical optimization purposes) are set to 30 % feed flow rate recovery for all spiral banks. This can have an impact on the sensor placement configuration and, in this case, can lead to the rougher spirals being less important to manage. The maximum allowable splitter setting, for Algorithm SPII, was 40 %; meaning rougher spirals were operated close to maximum HM recovery regardless of monitoring configuration. Including initial splitter positions in the sensitivity analysis (i.e. Monte-Carlo simulations) will help to validate optimal sensor placement behaviour (as obtained by Algorithm SPII).

Finally, a very important assumption, on the properties of the spiral banks, required that entire spiral banks are approximated as a single spiral (mass and species flow rates are divided uniformly). An advantage of Algorithm SPII is that individual spirals, inside a spiral bank, can also be considered for optimization and non-uniform flow dispersal (through a spiral bank) can also be allowed. After the recommendation in Section 6.3.2 have been addressed, then SPII can be used to find the most possible sparse sensor placement configurations per spiral or spiral start.

Lastly, it is important to note that Algorithms SPI & SPII are not necessarily mutually exclusive. Including notions of state estimation into Algorithm SPII can lead to a more comprehensive optimal sensor placement approach for metallurgical plants. An ideal optimal sensor placement framework will show how interface sensor placement can lead to improved spiral plant performance and reduction in performance uncertainty. This can be achieved by including an uncertainty in the splitter placement optimality (originating from interface measurement noise) and propagating the errors to the overall plant performance.

6.5. Published and submitted articles

Two peer-reviewed international conference articles, based on interface detection software, have already been published. The first paper (with discussion centered on Algorithm CVI) was accepted in 2016 for the International Federation of Automatic Control (IFAC) MMM conference in Vienna and the second paper (comparing results from Algorithm CVI & CVII) was accepted for the South African Council for Automation and Control (SACAC) 2017 Control Conference Africa (CCA) conference. Both articles (Nienaber & Auret, 2016; Nienaber, McCoy & Auret, 2017) are available on IFAC-PapersOnLine.

Two journal articles have been submitted to the journal *Minerals Engineering* on the following subjects:

- Spiral concentrator modelling and plant simulation using both RSM and the extended Holland-Batt model (see Nienaber & Auret, 2018a).

Stellenbosch University https://scholar.sun.ac.za

- Optimal spiral plant interface sensor placement via state estimation and metallurgical performance approaches (see Nienaber & Auret, 2018b).

Stellenbosch University https://scholar.sun.ac.za

7. References

Anthony, K.R., Van Deventer, J.S.J. & Reuter, M.A., 1991. *Steady-state simulation and optimization of gravity separation circuits by use of linear programming and expert systems*. Minerals Engineering, Vol. 4, Issues 3-4. Pages 311 – 327.

Bagajewicz, M., 2002. *A Review of Techniques for Instrumentation Design and Upgrade in Process Plants*. The Canadian Journal of Chemical Engineering. Vol. 80. Pages 3 – 16.

Bagnold, R.A., 1954. *Experiments on a gravity-free dispersion of large solid spheres in a Newtonian fluid under shear*. Proceedings of the Royal Society of London. Series A, Mathematical and Physical Sciences, Vol. 225, No. 1160. Pages 49 – 63.

Bazin, C., Sadeghi, M. & Renaud, M., 2016. *An operational model for a spiral classifier*. Minerals Engineering, Vol. 91. Pages 74 – 85.

Boucher, D., Deng, Z., Leadbeater, T. & Langlois, R., 2016. *Observation of iron ore beneficiation within a spiral concentrator by positron emission particle tracking of large (Ø = 1440 µm) and small (Ø = 58 µm) hematite and quartz tracers*. Chemical Engineering Science, Vol. 140. Pages 217 – 232.

Boucher, D., Deng, Z., Leadbeater, T., Langlois, R., Renaud, M. & Waters, K.E., 2014. *PEPT studies of heavy particle flow within a spiral concentrator*. Minerals Engineering, Vol. 62. Pages 120 – 128.

Boucher, D., Deng, Z., Leadbeater, T., Langlois, R. & Waters, K.E., 2016. *Speed analysis of quartz and hematite particles in a spiral concentrator by PEPT*. Minerals Engineering, Vol. 91. Pages 86 – 91.

Bredenhan, L., 2015. Personal communication. Rowland plant, Glencore.

Burt, R.O., 1984. *Gravity Concentration Technology*. Developments in Mineral Processing, Vol. 5. Elsevier Science Publishers, Amsterdam.

Canny, J., 1986. *A Computational approach to edge detection*. IEEE transactions of pattern recognition and machine intelligence, Vol. PAMI-8. Pages 679 – 698.

Cavanaugh, J.E., 1997. *Unifying the derivations for the Akaike and corrected Akaike information criteria*. Statistics & Probability Letters, Vol. 3. Pages 201 - 208.

Chromium Prices and Chromium Price Charts. 2017. [Online]. Available: http://www.infomine.com/investment/metal-prices/ferro-chrome/. [2017, May 28].

Clocca, G., Cusano, C. & Schettini, R., 2015. *Image orientation detection using LBP-based features and logisitic regression*. Multimedia Tools and Applications, Vol. 74. Pages 3013 – 3034.

Stellenbosch University https://scholar.sun.ac.za

Cramer, L.A., Basson, J. & Nelson, L.R., 2004. *The impact of platinum production from UG2 ore on ferrochrome production in South Africa*. The Journal of the South African Institute of Mining and Metallurgy, Vol. 104, Issue 9. Pages 517 – 527.

Dallaire, R., Laplante, A.R. & Elbrond, J., 1978. *Humphrey's spiral tolerance to feed variations*. CIM Bulletin. Pages 128 – 134.

Das, S.K., Godiwalla, K.M., Panda, L., Bhattacharya, K.K., Singh, R. & Mehrotra, S.P., 2007. *Mathematical modeling of separation characteristics of a coal-washing spiral*. International Journal of Mineral Processing, Vol. 84. Pages 118 – 132.

Davies, P.O.J, Goodman, R.H. & Deschamps, J.A., 1991. *Recent developments in spiral design, construction and application*. Minerals Engineering, Vol. 4, Issues 3-4. Pages 437 – 456.

Dawson, N.F., 2010. *Experiences in the production of metallurgical and chemical grade UG2 chromite concentrates from PGM tailings streams.* The Journal of the South African Institute of Mining and Metallurgy, Vol. 110. Pages 683 – 690.

Deb, K., 2000. *An efficient constraint handling method for genetic algorithms*. Computer Methods in Applied Mechanics and Engineering, Vol. 186. Pages 311 – 338.

Deep, K., Singh, K.P., Kansal, M.L. & Mohan, C., 2009. *A real coded genetic algorithm for solving integer and mixed integer optimization problems*. Applied Mathematics and Computation, Vol .212. Pages 505 – 518.

Deep, K. & Thakur, M., 2007. *A new mutation operator for real coded genetic algorithms*. Applied Mathematics and Computation, Vol. 193. Pages 211 – 230.

Dingran, L., Xiao-Hua, Y., Xiaomin, J., Bin, L., Quan, C. & Jianhua, Z., 2011. *Neural Network Based Edge Detection for Automated Medical Diagnosis*. Proceedings of the IEEE International Conference on Information and Automation, Shenzhen, China. Pages 343 – 348.

Dixit, P., Tiwari, R., Mukherjee, A.K. & Banerjee, P.K., 2015. *Application of response surface methodology for modelling and optimization of spiral separator for processing of iron ore slime*. Powder Technology, Vol. 275. Pages 105 – 112.

Doheim, M.A., Abdel Gawad, A.F., Mahran, G.M.A., Abu-Ali, M.H. & Rizk, A.M., 2013. *Numerical simulation of particulate-flow in spiral separators: Part I. Low solids concentration (0.3 % & 3% solids)*. Applied Mathematical Modelling, Vol. 37. Pages 198-215.

Dollár, P., Tu, S. & Belongie, S., 2006. *Supervised Learning of Edges and Object Boundaries*. IEEE Computer Society Conference on Computer Vision and Pattern Recognition, Vol. 2. Pages 1964 – 1971.

Stellenbosch University https://scholar.sun.ac.za

Dreiseitl, S. & Ohno-Machado, L., 2002. *Logistic regression and artificial network classification models: a methodology review*. Journal of Biomedical Informatics, Vol. 35. Pages 352 - 359.

Forbes, J.F. & Marlin, T.E., 1996. *Design cost: a systematic approach to technology selection for model-based real-time optimization systems*. Computers & Chemical Engineering. Vol. 20, No. 6/7. Pages 717 – 734.

Fourie, P.J., 2007. *Modelling of separation circuits using numerical analysis*. The 6th International Heavy Minerals Conference 'Back to Basics'. The Southern African Institute of Mining and Metallurgy. Pages 1 – 6.

Fu, K.S, & Mui, J.K., 1981. *A survey on image segmentation*. Pattern Recognition, Vol. 13. Pages 3 – 16.

Gold, D., 1991. *The investigation and design of a machine vision system for the detection and control of the separator in a spiral ore concentrator*. University of Cape Town. M.Sc. (Eng.) Thesis.

Gonzalez, R.C. & Woods, R.E., 2008. *Digital Image Processing.* 3rd Edition. Pearson Prentice Hall. Upper Saddle River, New Jersey.

Gonzalez, R.C., Woods, R.E. & Eddins, S.L., 2010. *Digital Image Processing using Matlab*. 2nd Edition. McGraw-Hill.

Grobler, J.D., Naudé, N. & Zietsmand, J.H., 2016. *Enhanced Holland-Batt spline for describing spiral concentrator performance*. Minerals Engineering, Vol. 92. Pages 189 – 195.

Guest, R.N. & Dunne, R.C., 1985. *An evaluation of gravity separators by use of a synthetic ore*. Journal of South African Institute of Mining and Metallurgy, Vol. 85, no. 6. Pages 187-195.

Hodouin, D., 2010. *Process observers and data reconciliation using mass and energy balance equations*. Advanced control and supervision of mineral processing plants, chapter 2. Sbárbaro, D. & Del Villar, R.. London; New York; Spirnger. Pages 15 - 82.

Hodouin, D., Kasongo, T., Kouame, E. & Everell, M.D., 1981. *BILMAT: An algorithm for material balancing mineral processing circuits, Applications to comminution, desliming and flotation circuits*. Canadian Institute of Mining Bulletin, Vol. 74, No. 833.

Holland-Batt, A.B., Balderson, G.F. & Cross, M.S., 1982. *The application and design of wet-gravity circuits in the South African minerals industry*. Journal of the South African institute of mining and metallurgy, Pages 53 – 69.

Holland-Batt, A.B., 1990. *Interpretation of spiral and sluice tests*. Transactions of the Institute of Mining and Metallurgy. Pages: C11 – C20.

Stellenbosch University https://scholar.sun.ac.za

Holland-Batt, A.B., 1995. *Some Design Considerations for Spiral Separators*. Minerals Engineering, Vol. 8, No. 11, Pages 1381 – 1395.

Holland-Batt, A.B., 1995. *The dynamics of sluice and spiral separations*. Minerals Engineering, Vol. 8, Issues 1-2, Pages 3-21.

Holland-Batt, A.B. & Holtham, P.N., 1991. *Particle and fluid motion on spiral separators*. Minerals Engineering, Vol. 4, No. 3/4, Pages 457 – 482.

Holtham, P.N., 1991. *Primary and Secondary Fluid Velocities on Spiral Concentrators*. Minerals Engineering, Vol. 5, No. 1. Pages 79 – 91.

Holtham, P.N., 1992. *Particle transport in gravity concentrators and the Bagnold effect*. Minerals Engineering, Vol. 5, No. 2. Pages 205 – 221.

Honaker, R.Q., Jain, M., Parekh, B.K. & Saracoglu, M., 2007. *Ultrafine coal cleaning using spiral concentrators*. Minerals Engineering, Vol. 20. Pages 1315 – 1319.

Hurvich, C.F. & Tsai, C., 1989. *Regression and time series model selection in small samples*. Biometrika, Vol. 76. Pages 297 – 307.

Izenman, A.J., 2008. *Modern Multivariate Statistical Techniques: Regression, Classification, and Manifold Learning*. Springer Science+Bussiness Media, LLC, 233 Spring Street, New York, USA.

Johnston, L.P., & Kramer, M.A., 1998. *Estimating State Probability Distributions from Noisy and Corrupted Data*. American Institute of Chemical Engineers, Vol. 44, No. 3. Pages 591 - 602.

Kapur, P.C. & Meloy, T.P., 1998. *Spirals Observed*. International Journal of Mineral Processing, Vol. 53. Pages 15 – 28.

King, R.P., Juckes, A.H. & Stirling, P.A., 1992. *A Quantative Model for the Prediction of Fine Coal Cleaning in a Spiral Concentrator*. Coal Preparation, Vol. 11. Pages 51 – 66.

Konishi, S., Yuille, A.L., Coughlan, J.M. & Zhu, S.C., 2003. *Statistical Edge Detection: Learning and Evaluation Edge Cues*. IEEE Transactions on Pattern Analysis and Machine Intelligence, Vol. 25, No. 1. Pages 57 – 74.

Krohne OPTIFLUX 5000F-FL flanged Electromagnetic Flow Sensor. 2017. [Online]. Available: https://www.instrumart.com/products/17683/krohne-optiflux-5000f-fl-flanged-electromagnetic-flow-sensor. [2017, May 28].

Lai, C., Chang, C., Ko, C. & Chen, C. 2003. *Optimal Sensor Placement and Maintenance Strategies for Mass-Flow Networks*. Industrial & Engineering Chemistry Research. Vol. 42. Pages 4366 – 4375.

Stellenbosch University https://scholar.sun.ac.za

Loveday, G.K., 1993. *The Modelling of Spiral Concentrators*. Department of Chemical Engineering, UCT libraries.

Luenberger, D.G., 1963. *Observing the state of a linear system*. IEEE Transactions on Military Electronics, Vol. 8, Issue 2. Pages 74 – 80.

Maini, R. & Aggarwal, H., 2010. *A Comprehensive Review of Image Enhancement Techniques*. Journal of Computing. Volume 2, Issue 3, Pages 8 – 13.

Martin, D.R., Fowlkes, C.C. & Malik, J., 2004. *Learning to Detect Natural Image Boundaries Using Local Brightness, Color, and Texture Cues*. IEEE Transactions on Pattern Analysis and Machine Intelligence, Vol. 26, No. 5. Pages 530 – 549.

Matthews, B.W., Fletcher, C.A.J., Partridge, T.C., 1998. *Computational simulation of fluid and dilute particulate flows on spiral concentrators*. Applied Mathematical Modelling, Vol. 22. Pages 965 - 979.

Matthews, B.W., Fletcher, C.A.J., Partridge, T.C., 1999. *Particle Flow Modelling on Spiral Concentrators: Benefits of Dense Media for Coal Processing*. Second International Conference on CFD on the Minerals and Process Industries. Pages 211 – 216.

Mazzour, E.H., Hodouin, D. & Makni, S., 2003. *Optimal sensor implementation in metallurgical plants – an application to a generic mineral separation plant*. International Journal of Mineral Processing, Vol. 69. Pages 185 – 203.

Medioni, G. & Kang, S.B., 2004. *Emerging Topics in Computer Vision*. Prentice Hall Professional Technical Reference. Pages 4 – 43.

Michaud, D., 2013. *Portable XRF Analyzer & Price List*. 2013. [Online]. Available: https://www.911metallurgist.com/blog/portable-xrf-analyzer-price. [2017, May 28].

Mishra, B.K. & Tripathy, A., 2010. *A preliminary study of particle separation in spiral concentrators using DEM*. International Journal of Mineral Processing. Vol. 94, Pages 192 – 195.

Mohanty, M., Zhang, B., Wang, H., Mahajan, A., Akbari, H., Bashir, Z., Ramamoorthy, S. & Hirschi, J., 2014. *Development and Demonstration of an Automation and Control System for Coal Spirals*. International Journal of Coal Preparation Utilization, Vol. 34. Pages 157 – 171.

Mohd Ali, J., Ha Hoang, N., Hussain, M.A. & Dochain, D., 2015. *Review and classification of recent observers applied in chemical process systems*. Computers and Chemical Engineering. Vol. 76. Pages 27 – 41.

Mojela, B., 2015. *Spiral data book index*. Multotec.

Stellenbosch University https://scholar.sun.ac.za

Montgomery, D.C., 2001. Fitting regression models. *Design and Analysis of Experiments*. 5th Edition. John Wiley & Sons, Inc. New York. Pages 392 – 426.

Narenda, P.M., 1981. *A Separable Median Filter for Image Noise Smoothing*. IEEE Transactions on Pattern Analysis and Machine Intelligence. Vol. PAMI-3, No. 1. Pages: 20 – 29.

Nienaber, E.C. & Auret, L., 2016. *Spiral concentrator interface monitoring through image processing: optimization for parameter selections*. IFAC-PapersOnLine. Vol 49. Pages 102 - 107.

Nienaber, E.C. & Auret, L., 2018a. *Experimental modelling and plant simulation of spiral concentrators: Comparing response surface methodology and extended Holland-Batt spline*. Minerals Engineering. Volume pending.

Nienaber, E.C. & Auret, L., 2018b. *Optimal sensor placement for spiral concentrator plants: Comparison of state estimation and metallurgical performance approaches*. Minerals Engineering. Volume pending.

Nienaber, E.C., McCoy, J.T. & Auret, L., 2017. *Spiral concentrator interface monitoring through image processing: a statistical learning approach*. IFAC-PapersOnLine. Vol. 50. Pages 53 – 58.

Pal, N.R. & Pal, S.K., 1993. *A review on image segmentation techniques*. Pattern recognition, Vol. 26, No. 9, Pages 1277 – 1294.

Peng, B., Zhang, L. & Zhang, D., 2013. *A survey of graph theoretical approaches to image segmentation*. Pattern Recognition, Vol. 46. Pages 1020 – 1038.

Petersen, A., 2016. *Correspondence*. 14 March – 30 May. Department of Process Engineering. Stellenbosch University.

Petrou, M. & Kittler, J., 1991. *Optimal Edge Detectors for Ramp Edges*. IEEE transactions on Pattern Analysis and Machine Intelligence. Vol. 13, No. 5. Pages 483 – 491.

Protiere, A. & Sapiro, G., 2007. *Interactive Image Segmentation via Adaptive Weighted Distances*. IEEE Transactions in Image Processing, Vol. 16, No. 4. Pages 1046 - 1057.

Qidwai, U. & Chen, C.H., 2010. *Digital Image Processing: An Algorithmic Approach with Matlab®*. Chapman and Hall/CRC. Pages 1 – 16.

Ren, X. & Malik, J., 2003. *Learning a Classification Model for Segmentation*. Proceedings ninth IEEE international conference on computer vision, Vol. 1. Pages 10 - 17.

Richards, R.G., MacHunter, D.M.M., Gates, P.J. & Palmer, M.K., 2000. *Gravity separation of ultra-fine (-0.1mm) minerals using spiral separators*. Minerals Engineering. Vol. 13, No. 1, Pages 65 – 77.

Stellenbosch University https://scholar.sun.ac.za

Romagnoli, J.A., & Sánchez, M.C., 2000. *Data Processing and Reconciliation for Chemical Process Operations*. Process Systems Engineering, Vol. 2. Academic Press, San Diego.

Sadeghi, M., 2015. *Study of the behaviour of iron ore particles in spiral concentrators by means of partition curves*. MSc thesis. Laval University, Quebec, QC, Canada.

Sadeghi, M., Bazin, C. & Renaud, M., 2016. *Radial distribution of iron oxide and silica particles in the reject flow of a spiral concentrator*. International Journal of Mineral Processing, Vol. 153. Pages 51 – 69.

Salvi, J., Armangué, X. & Battle, J., 2002. *A comparative review of camera calibrating methods with accuracy evaluation*. Pattern Recognition, Vol. 35. Pages 1617 – 1635.

Sánchez-Ramos, S., Doménech-Carbó, A., Gimeno-Adelantado, J.V. & Peris-Vicente, J., 2008. *Analystical and mineralogical studies of ore and impurities from a chromite mineral using X-ray analysis, electrochemical and microscopy techniques*. Talanta, Vol. 74. Pages 1592-1597.

Steinmuller, A., 2005. *Development and application of simple process models for spiral concentrators.* Heavy Minerals. Pages 167-172.

Subasinghe, G.K.N.S & Kelly, E.G., 1991. *Model of a Coal Washing Spiral*. Coal Preparation, Vol. 9. Pages 1 – 11.

Suzuki, S. & Abe, K., 1985. *Topological Structural Analysis of Digitized Binary Images by Border Following*. Computer Vision, Graphics, and Image Processing, Vol. 30. Pages 32 – 46.

Tripathy, S.K., & Murthy, Y.K., 2012. *Modelling and optimization of spiral concentrator for the separation of ultra fine chromite.* Powder Technology, Vol. 221. Pages 387-394.

Trutna, L., Spagon, P., Del Castillo, E., Moore, T., Hartley, S. & Hurwitz, A., 2013. *NIST/SEMATECH e-handbook of Statistical Method*. NIST [online]: http://www.itl.nist.gov/div898/handbook/index.htm.

Tucker, P., 1985. *An approach to modelling industrial unit processes: application to a spiral concentrator for minerals*. Applied Mathematical Modelling, Vol. 9. Pages 375 – 379.

Vapnik, V.N., 2000. *The Nature of Statistical Learning Theory*. Second edition. Springer-Verlag New York, Inc., 175 Fifth Avenue, New York, USA.

Vermaak, M.K.G., Visser, H.J., Bosman, J.B. & Krebs, G., 2008. *A simple process control model for spiral concentrators*. The Journal of the South African Institute of Mining and Metallurgy. Vol. 108. Pages 147 – 154.

Stellenbosch University https://scholar.sun.ac.za

Von der Linden, W., Dose, V. & Von Toussaint, U., 2014: *Bayesian probability theory: Applications in the physical sciences*. Cambridge University Press, New York. Pages: 492.

Walsh, D.E. & Kelly, E.G., 1992. *An investigation of the performance of a spiral using radioactive gold tracers*. Society for Mining, Metallurgy, and Exploration, Inc. Pages 1 – 6.

Wills, B.A. & Napier-Munn, T. 2005. Gravitation concentration, *Wills' Mineral Processing Technology*. Elsevier. Pages 236 - 238.

Stellenbosch University https://scholar.sun.ac.za

8. Nomenclature

8.1. Image processing, genetic algorithms & logistic regression

Symbol/abbreviation	Description	SI unit
α	Logistic regression parameters	-
α_F	F-measure scaling value	-
$\bar{\beta}$	Objective function parameter vector	-
∇	Discrete/continuous gradient operator	-
∇^2	Discrete Laplacian operator	-
λ	Regularisation parameter	-
σ	Standard deviation	-
σ_G	Gaussian convolution kernel standard deviation	-
A	Hall calibration matrix	Pixels/mm
ANN	Artificial neural network	-
b	Blue channel scaling parameter	-
B	Blue channel	-
B_c	Calibration simplifying parameter	-
C	Number of image channels	-
CV	Computer vision	-
f_n	False negative detections	-
f_p	False positive detections	-
F	Precision recall F-measure	-
F_{GA}	Penalised GA objective function	-
g_c	Convolved image	-
g	Green channel scaling parameter	-
g^{GA}	Inequality constraint(s)	-
G	Green channel	-
GA	Genetic algorithm	-
GP	GoPro	-
$h/\ P(y=1\|x,\alpha)$	Logistic regression membership function	-
H_E	Histogram equalization activator	-
h^{GA}	Equality constraint(s)	-
I	Image pixel intensity	-
I_{label}	Interface or slurry ground truth image	-
I_{out}	Algorithm CVI or CVII output image	-
J_{GA}	GA objective function	-

Stellenbosch University https://scholar.sun.ac.za

Symbol/abbreviation	Description	SI unit
J_1	MSE objective function	-
J_2	Algorithm CVI objective function	-
L	LDA membership function	-
LDA	Linear discriminant analysis	-
LoG	Laplacian of Gaussian	-
m	Number of convolution filter rows/ number of feature set observations	-
M	Number of image rows	Pixels
M_N	Median filter size	Pixels
M_{out}	Algorithm CVI output image number of rows	Pixels
MSE	Mean square error	-
n	Number of convolution filter columns	Pixels
n_π	Edge direction	-
N	Number of image columns	Pixels
N_{bins}	Number of histogram equalization bins	-
N_{out}	Algorithm CVI output image number of columns	Pixels
o_1, o_2	Upper and lower connected component orientation angle	-
PR	Precision-recall	-
p_F	Precision	-
p_1, p_2	Upper and lower orientation connected component perimeter size	Pixels
$p_r(r_j)$	Image intensity probability	-
r	Red channel scaling parameter	-
R	Red channel	-
R_θ	Rotation matrix	-
r_F	Recall	-
ROC	Receiver operating characteristic	-
s	Histogram equalization output pixel intensities	-
s_c	Calibration scaling parameter	-
t	Translation vector	-
t_p	True positive detections	-
T_1	First Canny edge detector threshold	-
T_2	Second Canny edge detector threshold	-

Stellenbosch University https://scholar.sun.ac.za

Symbol/abbreviation	Description	SI unit
T_1^H	First hysteresis threshold	-
T_2^H	Second hysteresis threshold	-
u, v	Uniform random numbers	-
VM	Virtual machine	-
w	Linear image filter	-
w_G	Linear Gaussian smoothing kernel	-
x	Pixel row coordinate/ feature set	-
X	Horizontal camera coordinate	-
X_W	Horizontal world coordinate	mm
y	Pixel column coordinate/ feature label	-
Y	Vertical camera coordinate	-
Y_W	Vertical world coordinate	mm
Z	Height camera coordinate	-
Z_W	Height world coordinate	mm

8.2. Spiral modelling, simulation and sensor placement

Symbol/abbreviation	Description	SI unit
$\odot$	Hadamard product	-
∇	Continuous gradient operator	-
α	Scale parameter	-
β	Response surface coefficients	-
δ	Regression training set	-
ΔF	Relative change in feed flow rate	t/h
$\Delta \mathrm{G}$	Relative change in feed grade	-
ΔS	Relative change in feed solids content	-
λ	Lagrange multipliers	-
E	Expectation operator	-
ϵ	Process model errors	-
σ/σ^2	Standard deviation/variance	-
A	Projection/decoupling matrix	-
$AIC, AICc$	Standard and corrected Akaike information criterion	-
a	Extended Holland-Batt model parameters	-
b	Calibration parameters	-
C	Sensor network configuration	-
C^*	Optimal sensor network	-

Stellenbosch University https://scholar.sun.ac.za

Symbol/abbreviation	Description	SI unit
CCD	Central composite design	-
CFD	Computational fluid dynamics	-
D	Estimability of plant variables	-
$\mathcal{D}$	Set of all possible sensor networks	-
DEM	Discrete element method	-
DMS	Dense medium separation	-
e	Measurement error vector	-
E	Separation efficiency	-
$E-101$	Rougher spiral bank	-
$E-102$	Cleaner spiral bank	-
$E-103$	Recleaner spiral bank	-
$E-104$	Re-recleaner spiral bank	-
E_p	Permutation matrix	-
f	Feed mineral of interest fraction	-
g	Response surface model	-
GA	Genetic algorithm	-
HM	Heavy minerals	-
$h(X)$	Inequality model	-
I	Additional condition information	-
J	Least squares objective function	-
J_C	Sensor network cost function	$\$^2$ or R^2
J_L	Monitoring/metallurgical performance objective function	$\$^2$ or R^2
k	Number of model parameters	-
LM	Light minerals	-
M	Connectivity or adjacency matrix	-
MOI	Mineral of interest	-
MSE	Mean square error	-
m	Rows of process model Jacobian	-
m_U	Size of Q matrix	-
$\mathcal{N}$	Normal/ Gaussian distribution	-
n	Number of observations	-
n_U	Columns of R matrix	-
p_{solids}	Density of species within solids phase	g/cm^3
p_{slurry}	Slurry density	g/cm^3

Stellenbosch University https://scholar.sun.ac.za

Symbol/abbreviation	Description	SI unit
p_w	Water density	g/cm^3
$\mathcal{P}$	Revenue monitoring performance	\$/h
P_1, P_2	Coefficient matrices	-
P_{Cr}	Chromium price	\$/t Cr or R/t Cr
P_r	Probability measure	-
P_s	Sensor network cost vector	\$ or R
PC	Principal component	-
PFD	Process flow diagram	-
PGM	Platinum group metals	-
PSD	Particle size distribution	-
Q	QR decomposition orthogonal matrix	-
q	Measurement model	-
$\mathcal{R}^2$	Correlation coefficient	-
R	Concentrate mineral of interest recovery	-
R_A	QR decomposition upper triangular matrix	-
RD	Relative density	-
RSM	Response surface methodology	-
r_U	Rank of coefficient matrix of unmeasured states	-
SG	Specific gravity	-
SSE	Sum squared error	-
T	Spline transition point	-
$trace$	Matrix trace operator	-
$UG2$	Upper group 2	-
u	Vector of unobservable variables	-
USD	American dollar	\$
V	Variance/Covariance matrix	-
VM	Virtual machine	-
$\hat{V}$	Updated variance estimate	-
Var	Variance operator	-
W	Feed recovery	-
WPL	Western plats	-
x_1, x_2,...	Experimental factors/state vector entries	-
X	State vector	-
$\hat{X}$	Updated state vector estimate	-

Stellenbosch University https://scholar.sun.ac.za

Symbol/abbreviation	Description	SI unit
X_1	Scalar/vector of mass flow rates	t/h
X_2	Scalar/vector of solids fractions	Solids (t/h)/ total (t/h)
X_3	Scalar/vector of MOI fractions	MOI (t/h)/ solids (t/h)
X_s	Initial/ Nominal state vector	-
XRF	X-ray fluorescence	-
y/Y	Measurements vector	-
Z	Process model	-
z_U/z_M	Unmeasured and measured process model matrices	-
ZAR	South African Rand	R

Stellenbosch University https://scholar.sun.ac.za

9. Appendix A: Background

9.1. Image processing methods

9.1.1. Digital images & camera projection models

Digital images can be understood as discrete two-dimensional projections of three dimensional real world objects. Pixels are the discrete elements of digital images and are usually associated with some discrete intensity value. Matrices provide a concise method of expressing images and can be written as $I(x, y)$ for single channel (grey-scale) images where I, the intensity of a pixel, is located in the xth row and yth column (Qidwai and Chen, 2010: 2). Figure 9.1 gives an example of a simple intensity matrix and the associated image. Other important image aspects are the spatial and intensity resolution. Intensity resolutions describe the levels into which a pixel's values are quantized. Spatial resolution describes the number of pixels per some physical distance (Gonzalez and Woods, 2008:60). The image I in Figure 9.1 consists of pixels with 8-bit intensity resolution or 256 levels with a spatial resolution of 5-by-5 pixels.

$$I = \begin{bmatrix} 44 & 11 & 92 & 24 & 74. \\ 132 & 125 & 225 & 46 & 18 \\ 254 & 114 & 190 & 242 & 49 \\ 181 & 124 & 106 & 25 & 106 \\ 20 & 42 & 232 & 99 & 74 \end{bmatrix} \rightarrow$$

Figure 9.1: Example of an intensity matrix with the 8-bit image it represents

A colour image requires three colour channels or matrices (RGB intensity values) to represent a particular real world image. There exists many RGB transformations which can be useful when representing a colour image. Hue, saturation, and luminance or value (HSV) and red/blue-chromaticity (YCbCr) are useful colour spaces for the representation of colour images, especially when change in colour over a spatial region is considered (Gonzalez and Woods, 2008: 105, 282 - 290). Three intensity matrices will require three times the amount of computer memory than a single channel grey scale image, often prompting the conversion of colour space images to intensity space images (Qidwai and Chen, 2010: 2). This allows for much more efficient use of computer memory that increases the speed at which calculations can be performed on image data.

Camera projection models are used to approximate camera behaviour which produce images. Understanding projection models becomes especially important when extracting 3D information from images (Medioni and Kang, 2004: 1). Various camera models have been formulated to describe how internal camera geometry (such as the camera lens) relates to the images produced and the desired accuracy of these models also influence their characteristics such as the number of parameters to be included. The simplest of the camera models, such as the pin-hole model, are based on linear coordinate transforms which ignore lens distortion (Salvi, Aramangué and Batlle, and 2002: 1619).

Stellenbosch University https://scholar.sun.ac.za

Equation 9.1 gives the simple linear coordinate transform, for the pin-hole model, that relates world coordinates $[X_w, Y_w, Z_w]$ to pixel coordinates $[x, y]$.

$$\begin{bmatrix} X \\ Y \\ Z \end{bmatrix} = R_\theta \cdot [X_w \quad Y_w \quad Z_w \quad 1]^T + t \qquad \text{(Eq. 9.1)}$$

Where

- $R_\theta = [R_\theta]_{3\times4}$ and $t = [t]_{3\times1}$ represent rotation and translation of world coordinates.
- X, Y, Z are the camera coordinates which are equal to $[x, y, 1]$ for the pin-hole model.

The pin-hole model requires that the camera's optical centre is collinear with a point in an image and its corresponding point in 3D real world space. This is not sufficient for most or low-end cameras which will also exhibit lens distortion (Medioni and Kang, 2004: 10). A more general camera model can be obtained by adding coordinate transformations to Equation 9.1 which model how the lens and complementary metal-oxide-semiconductor (CMOS) chip in cameras affect the final image. More generalised coordinate transforms from the world ($[X_w, Y_w, Z_w]$) to image ($[\breve{u}, \breve{v}]$) coordinates usually require four steps (Salvi, Aramangué and Batlle, 2002: 1620; Medioni and Kang, 2004: 10):

1. Transform from world coordinates $[X_w, Y_w, Z_w]$ to camera coordinates $[X, Y, Z]$.
2. Perspective projection transform of camera coordinates to ideal image coordinates $[x, y]$.
3. Lens distortion $[\breve{x}, \breve{y}]$ of ideal image coordinates.
4. Final transformation of distorted image coordinates to digital (pixelated) image coordinates $[\breve{u}, \breve{v}]$.

The overall transformation of $[X_w, Y_w, Z_w]$ to $[\breve{u}, \breve{v}]$ describes a more complete camera model which is generally representative of cameras with lens distortion and decentering distortion (that causes lens distortion to be asymmetric due to misaligned lens components) and, therefore, makes low-end cameras more suitable for accurate metric measurements. Figure 9.2 visually summarises the camera projection model as world coordinates ($[X_w, Y_w, Z_w]$) are transformed to digital image coordinates ($[\breve{u}, \breve{v}]$).

Stellenbosch University https://scholar.sun.ac.za

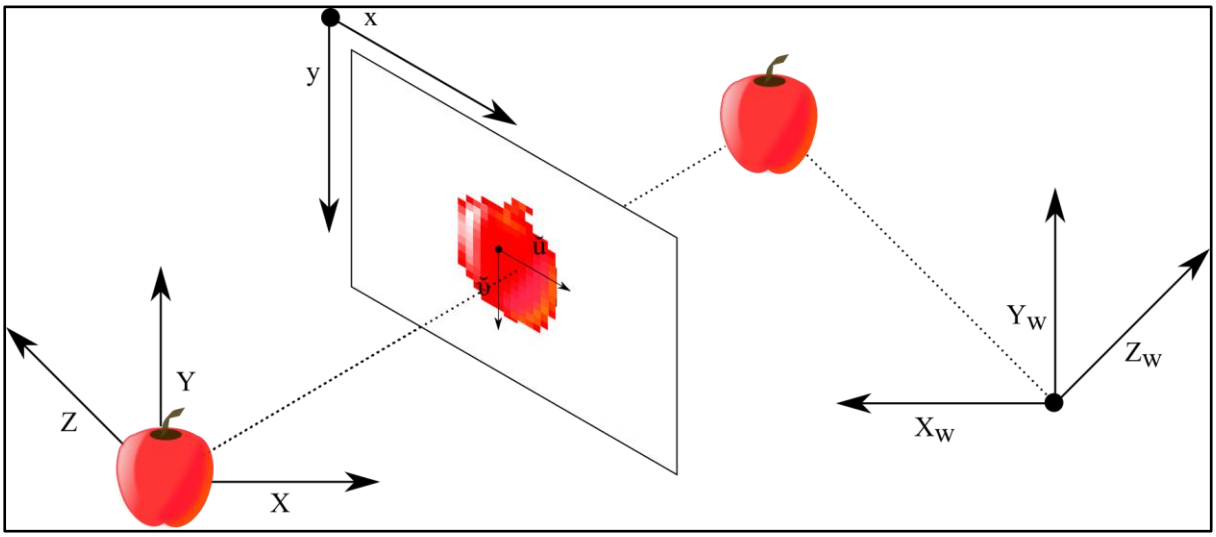

Figure 9.2: Relation between world, image and camera coordinates (Adapted from Salvi, Armangué and Batlle, 2002)

9.1.2. Contrast manipulation

Image enhancement algorithms are principally used to alter the intensity values of pixels within an image. The manner in which this is done greatly depends on the application and can require some experimentation as one must decide which features to emphasise or suppress (Maini and Aggarwal, 2010).

Contrast adjustments are typically used to enhance images and can be understood as intensity transformation operations applied over an image. These spatial domain methods involve transforming an image into a transform domain, where the processing is performed, and then performing inverse mappings to obtain an output image back in the spatial domain. This can be done locally or globally. Some common, yet simple, contrast manipulation methods include image negatives, power-law (or gamma) transformations, contrast stretching, intensity level slicing and histogram equalization (Gonzalez and Woods, 2008: 105, 108 - 120).

Histogram equalization is concerned with manipulating the histogram of an input image's pixel intensities. The original histogram is obtained by counting the frequency that intensities from 0 to 255 occur in an image and is then manipulated via equalization. Finally, an image must be produced that has a uniform histogram of intensities. Other frequency profiles can also be implemented with different frequency binning (Maini and Aggarwal, 2010; Gonzalez, Woods and Eddins, 2010: 54). Through equalization, the intensity values of the input image pixels will spread so that a wider range of values in the intensity scale is present in the equalized image. Histogram equalization is also the only "automatic" contrast adjusted method in that the contrast transformation depends only on the input image (Gonzalez and Woods, 2008: 126 & 127). The simplicity of the equalization calculations also makes histogram equalization a useful contrast manipulation tool (Gonzalez & Woods, 2008: 128). Equation 9.2 is the transformation which is used to perform histogram equalization. $T(I(x,y))$

Stellenbosch University https://scholar.sun.ac.za

is the transformation of the intensity of pixel $I(x,y)$ to the output/equalized pixel at $s(x,y)$. The transformation $T(I(x,y))$ represents a cumulative probability distribution for intensity frequencies up to the intensity $I(x,y)$. This implies that the output is a value between 0 and 1 which must be rescaled to 0 and 255 for the final output image.

$$s(x,y) = T\big(I(x,y)\big) = \sum_{j=0}^{k} p_j \qquad \text{(Eq. 9.2)}$$

Where:

- Output intensities are $s(x,y)$.
- k is equal to the intensity at $I(x,y)$.
- $p_r(r_j)$ is the probability that a pixel will have a $I(x,y) = k$ intensity.

Figure 9.3 shows an example of histogram equalization and the change in the image histograms. The original image on the left and its corresponding histogram (shown in red bars) are transformed (the new histogram shown with blue bars) leading to the output image on the right.

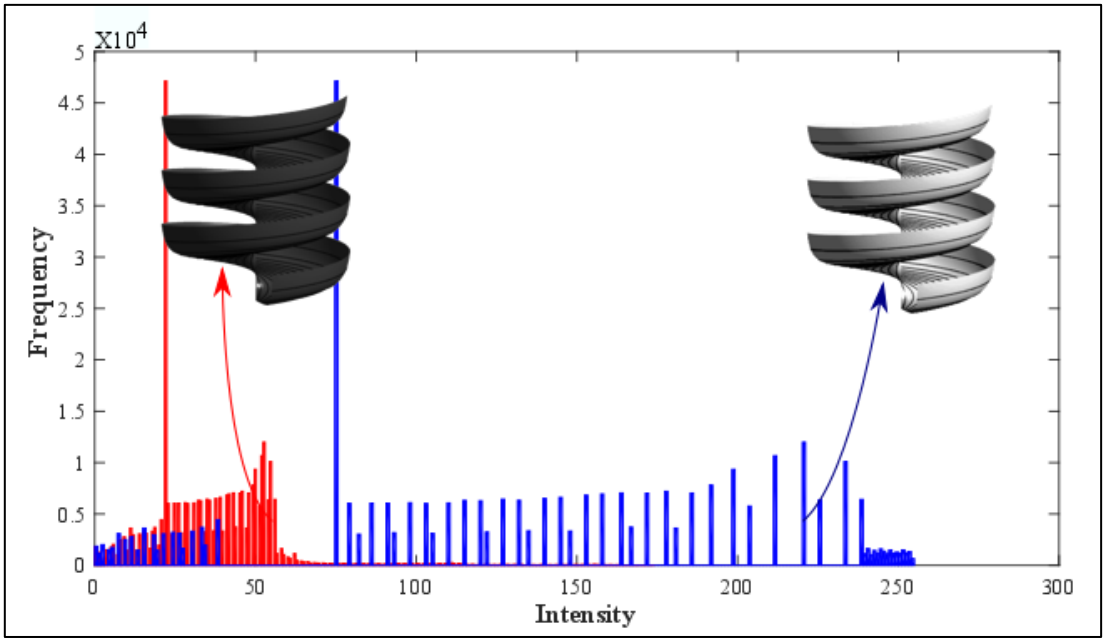

Figure 9.3: Histogram equalization example (red bars: before equalization; blue bars: after equalization)

9.1.3. Spatial filtering

Images will always be corrupted with some type of error (typically called noise) and two common types of noise models are Gaussian or salt-and-pepper noise. Low, high and bandpass filters are common methods used to treat image noise and more involved methods such as Wiener or other types of deconvolutional filters also treat image degradation (Gonzalez, Woods and Eddins, 2009: 165).

Spatial filtering of images refer to the linear or non-linear transformation of neighbourhoods in an image by use of a slide kernel (Gonzalez, Woods and Eddins, 2009: 146). Equation 9.3

Stellenbosch University https://scholar.sun.ac.za

mathematically shows how an image neighbourhood is convolved by a linear filter. It can be considered as a type of weighted averaging.

$$g_c(x,y) = \sum_{s=-m}^{s=m} \sum_{t=-n}^{t=n} w(s,t) I(x-s, y-t) \qquad \text{(Eq. 9.3)}$$

Where:

- The output image is g_c and $g_c(x,y)$ refers to a pixel location in g_c.
- w is the filtering mask of size $m \times n$.
- I is the input image of size $M \times N$.

Smoothing or averaging filters computes average values for an image pixel $I(x,y)$ based on the neighbourhood $m \times n$ surrounding that pixel. Two simple averaging filters are (Gonzalez & Woods, 2008: 153):

$$w_{box\ filter} = \frac{1}{9}\begin{bmatrix} 1 & 1 & 1 \\ 1 & 1 & 1 \\ 1 & 1 & 1 \end{bmatrix}, w = \frac{1}{16}\begin{bmatrix} 1 & 2 & 1 \\ 2 & 4 & 2 \\ 1 & 2 & 1 \end{bmatrix}$$

Another important linear filter is the Gaussian smoothing kernel which is commonly used during edge detection (Canny, 1986: 680). Equation 9.4 gives the normalized two dimensional distribution formula that calculates a kernel's value(s) (w_G) for pixel position (x,y) (Gonzalez, Woods & Eddins, 2010: 500).

$$w_G(x,y) = \frac{1}{\sigma_G\sqrt{2\pi}} e^{-(x^2+y^2)/2\sigma_G^2} \Big/ \left[\sum_{x,y} \frac{1}{\sigma_G\sqrt{2\pi}} e^{-(x^2+y^2)/2\sigma_G^2}\right] \qquad \text{(Eq. 9.4)}$$

Where:

- σ_G is the standard deviation for the Gaussian distribution.

The size of the kernel determined via Equation 9.4 is derived from the σ_G value given a certain cut off (which can defined by the user). A common method of applying Gaussian filters (with the same results compared to rectangular linear filters) is to first filter horizontally or vertically by a linear kernel and then to filter the resulting image in the remaining direction by the same linear kernel. Figure 9.4 shows an example of Gaussian image smoothing via initial horizontal filtering followed by vertical filtering.

Stellenbosch University https://scholar.sun.ac.za

Figure 9.4: Gaussian image smoothing. Filtering is performed first in the horizontal direction and then followed by filtering in the vertical direction ($\sigma_G = 4$)

Equation 9.4 can easily be extended to the non-linear case by applying a non-linear transform over the I neighborhoods. Useful non-linear smoothing filters include the median filter which is categorized as one of the order-statistic filters. Median filters use the median pixel value of a $m \times n$ neighbourhood centred on a pixel (x, y) and assigns the median intensity to the pixel at that location (Gonzalez & Woods, 2008: 156). Figure 9.5 shows the effects of different smoothing techniques.

Figure 9.5: Comparison of smoothing filters (kernel sizes used are 32-by-32 pixels)

The original image in Figure 9.5 contains additional synthetic noise to also illustrate what effect smoothing filters have on noisy images. Linear smoothing filters require larger neighbourhoods to combat severe noise; however, this results in loss of useful detail such as blurring of object edges. The

Stellenbosch University https://scholar.sun.ac.za

median filter manages to smooth image noise while preserving object edges (Narenda, 1981: 20). Due to the median filter's ability to preserve edge detail it has become one of the most useful order-statistic filters in image processing (Gonzalez & Woods, 2008: 157).

Sharpening filters act as high pass filters and, therefore, emphasize transitions in intensity between pixels of an input image I. An image showing areas of intensity changes (in I) is subtracted from the original image to obtain the enhanced image. Intensity changes are calculated by applying the discrete differentiation operators in Equations 9.5 and 9.6 or Equations 9.7 and 9.8, to an image (Gonzalez & Woods, 2008: 161) according to Equation 9.3.

$$\frac{\partial I}{\partial x} = I(x+1, y) - I(x, y) \qquad \text{(Eq. 9.5)}$$

$$\frac{\partial I}{\partial y} = I(x, y+1) - I(x, y) \qquad \text{(Eq. 9.6)}$$

$$\frac{\partial^2 I}{\partial x^2} = I(x+1, y) + I(x-1, y) - 2I(x, y) \qquad \text{(Eq. 9.7)}$$

$$\frac{\partial^2 I}{\partial y^2} = I(x, y+1) + I(x, y-1) - 2I(x, y) \qquad \text{(Eq. 9.8)}$$

Equations 9.5 and 9.8 can be applied to an image in the same way as the Gaussian filter (Figure 9.4) to find a gradient map of an image which can be subtracted from the input image ($I - \frac{\partial(\partial I/\partial x)}{\partial y}$) to find the final sharpened image.

9.1.4. Segmentation

Image segmentation refers to the partitioning of a particular image into disjoint sets of pixels based on certain properties so that meaningful objects can be discerned (Pal & Pal, 1993: 1277; Peng, Zhang & Zhang, 2013: 1020). Literature on image segmentation is vast with many techniques having been developing mostly due to the ill-posed nature of the segmentation problem. The available segmentation methods are similar to data clustering since a certain inference must be performed on features, obtained from an image, to perform classification of the image's pixels. Modern unsupervised techniques (requiring no user training input) include graph, level-set and active contour segmenters which also have user guided counter parts (Peng, Zhang & Zhang, 2013: 1020; Protiere & Sapiro, 2007: 1046).

Some of the oldest and more common segmentation methods include thresholding and edge detection (Pal & Pal, 1993: 1277; Gonzalez, Woods & Eddins, 2010: 492). The feature set required for this consists of pixel intensity values of multichannel or grayscale images. Segmentation of monochromatic images are typically based on discontinuity and similarity (Gonzalez, Woods & Eddins, 2010: 489; Fu & Mui, 1981: 3). These methods are usually simpler and computationally less expensive than graph or level-set based segmenters.

Stellenbosch University https://scholar.sun.ac.za

Simple thresholding classifies pixels with intensities that are above or below a certain threshold, thereby producing a binary image (Gonzalez, Woods & Eddins, 2010: 511). The resulting image will have pixels of value 1 where the values were higher or lower (depending on the inequality used) than the threshold and the balance will be classified as zero. Multiple thresholds can also be applied to an image producing a multiple classification of pixels. Thresholding can also be understood as a method that partitions an intensity histogram as shown in Figure 9.6 (Gonzalez, Woods & Eddins, 2010: 512).

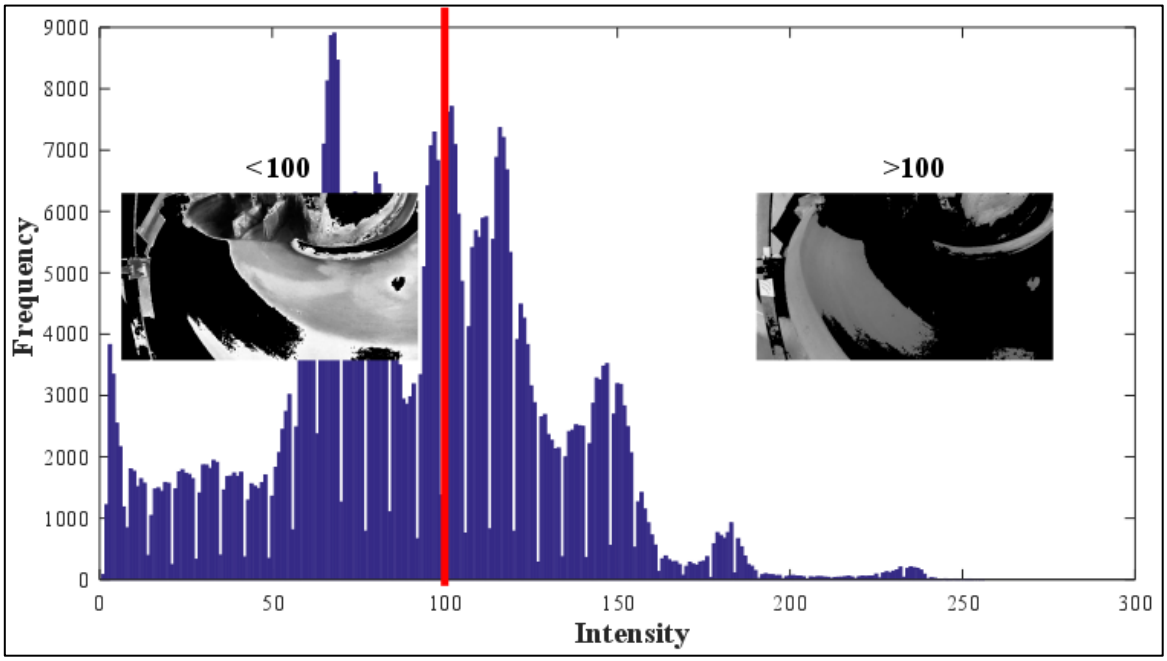

Figure 9.6: Thresholding at I(x,y) < 100 and I(x,y) > 100

Thresholding can be done on a local or global basis either manually or automated (Pal & Pal, 1993: 1279). Local or adaptive thresholding can use the discrete Laplacian ($\nabla^2 I$) of an image's intensity map while typical global methods use the intensity histogram (Pal & Pal, 1993: 1279). The Otsu algorithm is a popular optimal thresholding scheme in which a threshold is found that maximizes the between class variance of the pixels above and below the optimal threshold (Gonzalez, Woods & Eddins, 2010: 516). Since objects in an image can consist of greatly varying pixel intensities it is often useful to do segmentation via edge detection.

Edges in images can be defined as the curves that describe or represent the boundaries around objects. Edges provide information on the shape and location of objects and are used to differentiate certain objects from other objects or backgrounds in an image (Dingran, Xiao-Hua, Xiaomin, Bin, Quan, & Jianhua, 2011: 343). Object analysis can be greatly simplified when structural information is maintained and the balance is discarded (Canny, 1986: 679).

Edge detection methods can be classified as gradient or Laplacian based. Both methods approximate a derivative of the intensity values to detect the boundaries around objects. First order gradient methods use an approximation of the first derivative in an image's intensity and finds edges where the changes

Stellenbosch University https://scholar.sun.ac.za

of intensity are relatively high. Several first-order edge detectors include Sobel, Prewitt and Roberts detectors (Gonzalez, Woods & Eddins, 2010: 496). Laplacian or second order derivative edge detectors use zero crossings in second order intensity gradients to find edges (Dingran et al., 2011: 344). The Laplacian of Gaussian (LoG) edge detector is an example of a second order gradient edge detector (Pal & Pal, 1993: 1284).

Canny (1986) developed the foundations for optimal edge detection and his detector became a well-established benchmark by 1991 (Petrou and Kittler, 1991). Canny (1986: 680) developed 3 criteria for an optimised edge detector which is summarised below.

1. Good detection – corresponds to maximization of the signal-to-noise ratio (low probability of failing to mark an edge).
2. Good localization – edges detected by the algorithm should be as close as possible to the centres of the true edges.
3. Only one response to one edge – similar to poor detection performance, the detection of two edges at a single point will imply one of the edges is false (not mathematically expressed by the signal-to-noise ratio).

These criteria lead to the following four steps required to determine an edge map using Canny's method (Gonzalez, Woods & Eddins, 2010: 500):

1. Image smoothing with Gaussian filter (Equation 9.4) of specified σ.
2. Calculation of local gradient and edge direction: using Equations 9.5, 9.6, 9.9 and 9.10.

$$gradient(I_{smoothed}) = \nabla(w_G * I) \qquad \text{(Eq. 9.9)}$$

$$n_\pi = \nabla(w_G * I)/|\nabla(w_G * I)| \qquad \text{(Eq. 9.10)}$$

3. Edge thinning and hysteresis thresholding.
4. Edge linking.

The Canny edge detector achieves its criteria by finding edges in the local maxima of the normalised gradient magnitude of an image with a gradient angle in the direction of an edge (Canny, 1986; Gonzalez, Woods and Eddins, 2009: 500). Consider the image I shown in Figure 9.7 To find the object edges, the image must first be convolved with the directional gradients of a Gaussian filter (this performs a smoothing and differentiation step). The final gradient image of I is obtained by calculating the magnitude of directional derivatives. Step 2 is completed by calculating edge directions using Equation 9.10. The gradient map in Figure 9.7 is scaled by its maximum value so that absolute gradient values fall in the range of [0, 1].

Stellenbosch University https://scholar.sun.ac.za

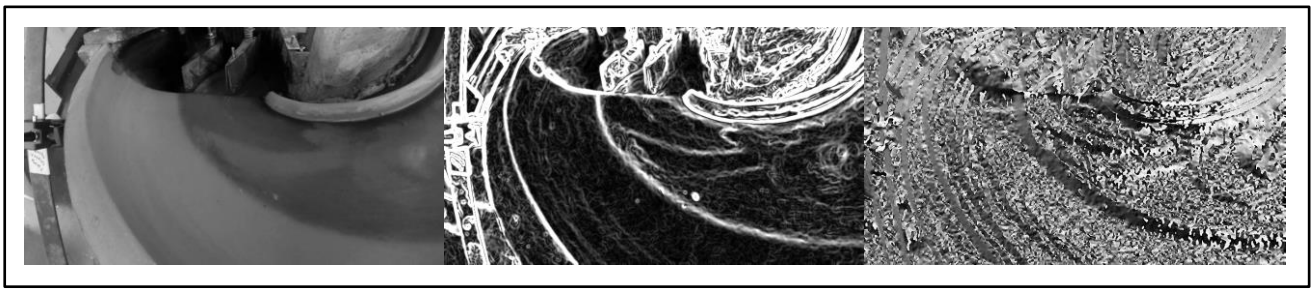

Figure 9.7: Intensity image (left), its smoothed gradient (middle, exaggerated) and gradient (or edge) direction (right) maps

Step 3, the edge thinning and hysteresis step, is performed using gradient and direction maps of the original image. Firstly, the direction map (as shown in Figure 9.7) is grouped into 4 directions (0, -45), (-45, -90], [90, 45), (45, 0) with their associated absolute gradient values $|\nabla(w_G * I)|$. A thinned edge map is generated by classifying pixels in the absolute gradient map as 1 if they are greater or equal to the interpolated local maximum gradient magnitude or as 0 otherwise. Figure 9.8 shows all the classified local maxima obtained after edge thinning on the same image presented in Figure 9.7. The middle frame in Figure 9.8 shows the thinned edge after applying a first hysteresis threshold of $T_1^H = 0.01$ to classify edge pixels as weak edges if their corresponding normalised gradient magnitude is larger than 0.01.

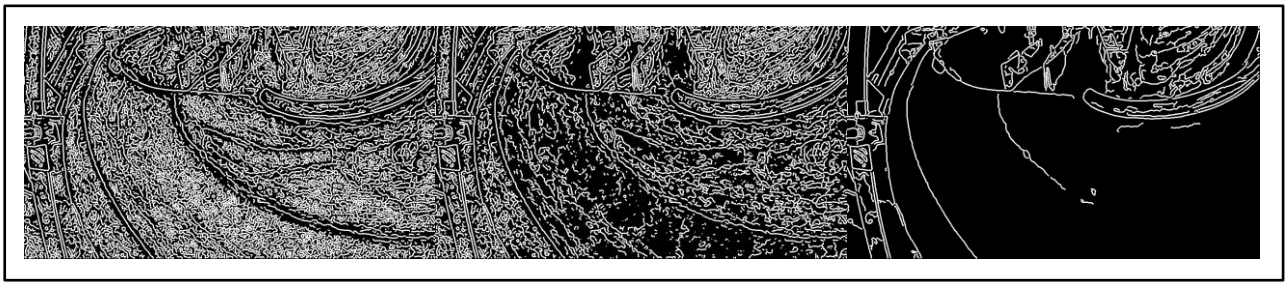

Figure 9.8: Edge thinning (left) and hysteresis thresholding (middle and right)

The second hysteresis threshold classifies edge pixels as strong edges if their corresponding normalised gradient magnitude is larger than some T_2^H (in Figure 9.7 $T_2^H = 0.1$ was used). Edge linking is finally performed by using strong edge pixels which share some connectivity with pixels classified as weak edges to produce the final edge map (shown as the right image in Figure 9.8) (Gonzalez, Woods and Eddins, 2009: 500). Section 9.1.5 focuses on the concepts of morphology and connectivity in images.

Edge detection is seen as a low-level approach to global detection of object boundaries and, in this sense, constitutes an ill-posed problem. Because edges are classically defined as abrupt changes in intensity or colour, edge detectors will not return clean object boundaries. Object boundaries are rather defined as contours that indicate where pixels are partitioned into different regions (hopefully disparate objects). Edge detectors tend to produce false positive edge responses inside textured

Stellenbosch University https://scholar.sun.ac.za

regions which a user might not consider as object boundaries but rather parts of a larger body (Martin, Fowlkes & Malik, 2004: 530; Konishi, Yuille, Coughlan & Zhu, 2003: 57).

Three attempts to achieve object boundary detection, via statistical or probabilistic methods, include Konishi et al. (2003), Martin et al. (2004) and Dollár, Tu and Belongie (2006). Each example constructed feature sets from a database of images based on gradient, colour and textural cues and used supervised machine learning methods to train statistical models for the detection of object boundaries. The database images were manually segmented with 5 to 10 ground truth (also called primal sketches) versions for each image generated by different people (Martin et al., 2004: 535).

The most useful evaluation methods for statistical edge detection are PR (precision-recall) and ROC (receiver operating characteristic) curves (Martin et al., 2004: 536). Precision (Equation 9.11) is here defined as the fraction of edge detections that represent true object boundaries and recall (Equation 9.12) as the fraction edge detections that do not miss true object boundaries (Martin et al., 2004: 536; Konishi et al., 2003: 59). Equation 9.13 gives the F-measure (with α_F usually set to 0.5) which captures the trade-off between precision and recall (Martin et al., 2004: 536). Maximizing Equation 9.13 leads to a better learning algorithm.

$$p_F = \frac{t_p}{t_p + f_p} \qquad \text{(Eq. 9.11)}$$

$$r_F = \frac{t_p}{t_p + f_n} \qquad \text{(Eq. 9.12)}$$

$$F = \frac{r_F p_F}{\alpha_F r_F + (1 - \alpha_F) p_F} \qquad \text{(Eq. 9.13)}$$

Where:

- t_p is the number of true positive detections.
- f_p is the number of false positive detections.
- False negative detections are f_n.

ROC curves are used to show the trade-off between recall and the false positive rate. PR and ROC curves should show similar trends, concerning false positive and negative detections, however, ROC curves have been found to not be appropriate for the boundary detection problem (Martin et al., 2004: 536). To calculate precision and recall for boundary detections it is necessary to find correspondences between the ground truth and automated edge detections. Simply overlaying the different edge maps, however, can misclassify (as true or false positive/negative) meaningful object boundaries since localization errors can occur in ground truth images (this can also be called user labelling errors).

Konishi (2003: 70) used morphological dilation on edge maps generated by their detector to address the localization error problem of ground truth images. A more involved method was proposed by Martin et al. (2004: 546) who used sparse bipartite assignment to determine correspondence between

Stellenbosch University https://scholar.sun.ac.za

statistical edge detection results and ground truth object boundary maps. In simple terms, the method of Martin et al. (2004:546) determines relative distances between user and automatically inferred edge pixels and classifies pixel pairs with a distance larger than some threshold as a nonhit. Graph based methods are required to make the bipartite assignment feasible since a brute force method has a complexity between $O((number\ of\ boundary\ pixels)^2)$ and $O((number\ of\ boundary\ pixels)^3)$.

9.1.5. Morphological image processing

Binary images (such as in Figure 9.8) can be considered as images of objects (referred to as connected components or sometimes blobs) with pixel intensity 1 against a background with pixel intensity set to 0. Pixels that are set to 1 can be labelled and grouped as connected components based on a certain adjacency. This is an important step for any topological structure analysis of objects in binary images (Suzuki & Abe, 1985: 32). Since edge detectors produce binary images with wanted and unwanted responses (Martin, Fowlkes & Malik, 2004: 530) additional filtering can be performed to refine results. Edges in binary images can be considered as connected components which can be filtered to remove spurious responses.

If S represents a subset of pixels within an image I then two pixels p and q in S are connected if there is a path between them in S. The connected pixels in S then also form a connected component and in general these constructs have various descriptive properties including their perimeter, orientation, area and so forth (Gonzalez, Woods and Eddins, 2009: 441). Figure 9.9 provides example images which contain objects with 4 and 8 connectivity. Different connectivities can be used over higher dimensional matrices than images.

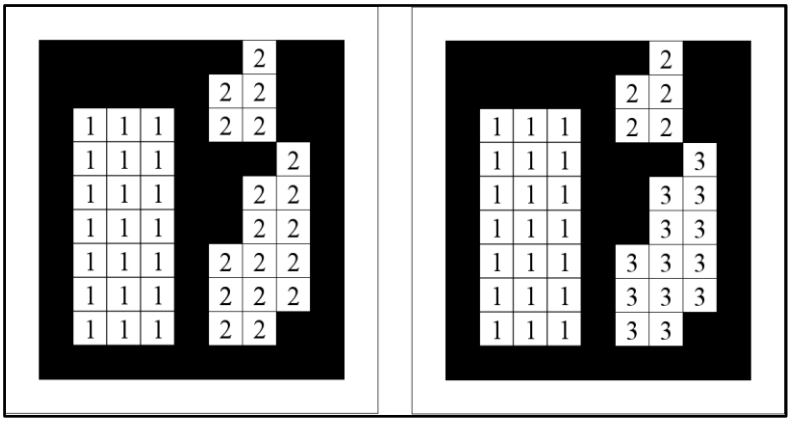

Figure 9.9: 8 (right) and 4 (left) connected components

The concept of connectivity is used during the hysteresis and edge linking steps of the Canny edge detector when strong edges are linked to weaker edges (edge pixels pixel that do not satisfy the $> T_2$ condition).

Stellenbosch University https://scholar.sun.ac.za

9.2. Experimental design

9.2.1. Design categories

Experimental designs are chosen based on certain experimental goals that must be achieved. An experimenter must decide on the goals and select suitable experiments that help produce the most useful statistical models. Four broad categories that the most common experimental objectives fall in are (Trutna, Spagon, Del Castillo, Moore, Hartley & Hurwitz, 2013: 5.3.1):

- comparative designs.
- screening designs.
- response surface methodology.
- regression modelling.

Comparative designs have a narrow scope and are focussed on investigating the effects of different levels of a factor. Screening experiments are useful when it is desired to identify the factors influencing a system/unit. Screening designs are required when an unknown system is being investigated and 3 or more factors must be characterised. RSM can be used when one wants to optimise a system response. It requires that screening has been previously performed or that major factors can be selected with a literature survey. Regression modelling just relates a system response to the factors it is dependent on (Trutna et al., 2013: 5.3.1).

9.2.2. Screening experiments

Trial tests are useful for testing the system response for all relevant factors of a system. Two level designs test the system responses at the highest (coded +1) and lowest (coded -1) allowable levels of the factors which can help the experimenter decide which factors to include in subsequent experiments (Trutna et al., 2013: 5.3.2). Table 9.1 shows the 2 level trial design for a 2 factor system.

Table 9.1: Simple 2^2screening experiment

2-level-2-factor experiment		
Trial Run	Factor 1 (x_1)	Factor 2 (x_2)
1	-1	-1
2	+1	-1
3	-1	+1
4	+1	+1
5	-	-
6	-	-
7	-	-
8	-	-

After the experimenter has executed the trials it can be decided which factors provide the least significant effect on the response and remove these from the factors in future experiments (Trutna et

Stellenbosch University https://scholar.sun.ac.za

al., 2013: 5.3.2). One noticeable problem with the screening experiments in Table 9.1 is that the results will not count an effect which only becomes pronounced when factor levels lie between extremes. If this is the case then further screening, implementing a higher number of levels, can be performed. Full factorial or RSM designs can be implemented to investigate the response effects of a greater number of factor levels.

9.2.3. Response surface methodology

An RSM experiment will provide data that can be used to formulate a model with which systems responses can be predicted. The accuracy/precision of predictions, however, will depend on the accuracy/precision of response measurements during experimentation (and the validity of assumed model structure). A quadratic response surface for a 3 factor design can be expressed with Equation 9.14 (Trutna et al., 2013: 5.3.3.6). Higher order terms can also be included but this will increase the amount of statistical inference required to justify all parameters (the risk of overfitting also increases).

$$g = \beta_0 + \beta_1 x_1 + \beta_2 x_2 + \beta_3 x_3 + \beta_4 x_1 x_2 + \cdots$$

$$\beta_5 x_1 x_3 + \beta_6 x_2 x_3 + \beta_7 x_1^2 + \beta_8 x_2^2 + \beta_9 x_3^2 \qquad \text{(Eq. 9.14)}$$

All the β_i parameters can be determined via regression from experimental data but it is likely that some parameters are not statistically significant. Regression models can be simplified by removing insignificant parameters allowing the model to suit the actual dependent response. It is also desired to have rotatable experimental designs which lead to a better prediction model. Response models from rotatable designs can provide predictions without a change in variance when the design is rotated (Trutna et al., 2013: 5.3.3.6).

There are various response surface methodologies including CCD and Box-Behnken designs which are shown in Table 9.2 (Trutna et al., 2013: 5.3.3.6). The circumscribed CCD, face centred (CCF) and Box-Behnken designs for the same number of factors are compared in Table 9.2 and it clearly shows that the Box-Behnken design requires 5 less test runs for the formulation of a 3-factor quadratic surface model.

Stellenbosch University https://scholar.sun.ac.za

Table 9.2: Three factor response surface designs

Runs	CCD (circumscribed)			CCF			Box-Behnken		
	x_1	x_2	x_3	x_1	x_2	x_3	x_1	x_2	x_3
1	-1	-1	-1	-1	-1	-1	-1	-1	0
2	-1	-1	+1	+1	-1	-1	+1	-1	0
3	-1	+1	-1	-1	+1	-1	-1	+1	0
4	-1	+1	+1	+1	+1	-1	+1	+1	0
5	1	-1	-1	-1	-1	+1	-1	0	-1
6	1	-1	+1	+1	-1	+1	+1	0	-1
7	1	+1	-1	-1	+1	+1	-1	0	+1
8	1	+1	+1	+1	+1	+1	+1	0	+1
9	-1.682	0	0	-1	0	0	0	-1	-1
10	1.682	0	0	+1	0	0	0	+1	-1
11	0	-1.682	0	0	-1	0	0	-1	+1
12	0	1.682	0	0	+1	0	0	+1	+1
13	0	0	-1.682	0	0	-1	0	0	0
14	0	0	1.682	0	0	+1	0	0	0
15	0	0	0	0	0	0	0	0	0
16	0	0	0	0	0	0	-	-	-
17	0	0	0	0	0	0	-	-	-
18	0	0	0	0	0	0	-	-	-
19	0	0	0	0	0	0	-	-	-
20	0	0	0	0	0	0	-	-	-

The desirability to perform Box-Behnken type experiments stem from the rotatable design and the reduced number of trials that is required to produce a predictive model. CCF designs require more trials but usually provide high quality predictions in the design space (for a precise and significant model). Another drawback of CCF models is that their predictive models give poor estimates for pure quadratic coefficients (Trutna et al., 2013: 5.3.3.6.3). Circumscribed CCD models are obtained from rotatable designs and produce high quality predictions within the design space. However, CCD design requires more trial runs and requires operation of a system's factors outside the levels of the factorial part of the design (Trutna et al., 2013: 5.3.3.6.3). Table 9.3 summarizes the advantages and drawbacks from the various experimental methodologies.

Table 9.3: Comparison of different 3 factor RSMs

RSM	Rotatable	Prediction quality	Design runs	Coefficient precision
Box-Behnken	Yes	Contains regions of poor predictive quality	15	High
CCD	Yes	High	20	High
CCF	No	High	20	Low

Stellenbosch University https://scholar.sun.ac.za

The final difference between CCD and Box-Behnken designs that require consideration is the variation of experimental runs by the amount of system factors. Box-Behnken designs do not require fewer trial runs than CCD designs when more than four factors are varied in an experiment (Trutna et al., 2013: 5.3.3.6.3). The difference in required runs between a CCD design and Box-Benhken design is shown in Table 9.4.

Table 9.4: CCD and Box-Behnken test run amount vs. increment in number of factors (Adapted from Trutna et al., 2013: 5.3.3.6.3)

Number of factors	Central Composite	Box-Behnken
2	13	-
3	20	15
4	30	27
5	33 (fractional factorial)	46
6	54 (fractional factorial)	54

9.2.4. Confirmation experiments

Confirmation trials are required to validate the prediction accuracy of the models obtained from the RSM designs. Even when there is restriction on the number of experimental runs that may be performed it is good practice to at least run 3 confirmation trials. If possible, one of these trials should also be run at the optimal prediction setting (if such a setting exists) even if this setting has been included in the original experimental designs (Trutna et al., 2013: 5.4.6). Optimal setting(s) of a process is typically a point of interest where high prediction accuracy is required (or at least a good estimation of uncertainty).

9.3. Data Reconciliation

9.3.1. State observers and estimation

Before the 1960's the contemporary control system designs required that all state variables (variables that contain essential information that describe the behaviour of a system) of a particular system be available for measurement. Control system design for many practical situations were limited since only a few outputs can typically be measured. The theory of state observers was introduced in the 1960's to address the problem and construct estimates of state variables from limited input and output measurements of a system (Luenberger, 1963: 74).

The Kalman filter is one of the first optimal state estimators, typically used for linear dynamic systems with variables contaminated by normally distributed noise. Research of Kalman filters is abundant in state estimation literature and was introduced in the 1960's especially for sampled (discrete) dynamic systems (Luenberger, 1963: 74; Mohd Ali, Ha Hoan, Hussain & Dochain, 2015: 28). Constrained, extended and unscented Kalman filters have been developed to extend the application of simple linear Kalman filters to more complex problems. Kalman filters and their

Stellenbosch University https://scholar.sun.ac.za

extensions are known as Bayesian estimators in that priori process knowledge is used to acquire posteriori information and that essentially maximum likelihood principles are used to minimise the difference between the values of estimated and true states of process variables (Mohd Ali, Ha Hoan, Hussain & Dochain, 2015: 28).

Similar reasoning to the Kalman filter can be used to develop state observers for steady state systems. Steady state observers are useful in chemical and especially metallurgical plants where it is desired to maintain design conditions. This will typically be an optimal steady state for stable operation and maximum product quality. The necessary observer can be derived via the maximum a posteriori method shown by Equation 9.15 (Romagnoli & Sánchez, 2000: 200). The derivation is shown in Romagnali & Sánchez (200: 201).

$$\max_{x} P_r(X|Y) = \max_{X} \frac{P_r(Y|X)P_r(X)}{P_r(Y)} \qquad \text{(Eq. 9.15)}$$

Where

- The state vector is X.
- The measurement vector is Y.
- $P_r(Y|X)$ is the likelihood distribution of Y given X. $P_r(X)$ and $P_r(Y)$ is typically known as the prior and evidence terms (Von der Linden, Dose & Von Toussaint, 2014: 28).

In Equation 9.15 X represents the plant variables' estimated states and Y represents their measurements corrupted by noise. The maximum a posteriori method seeks to maximize the probability of the estimated states given the measurements by using Bayes rule and assuming a suitable probability distribution model for $P_r(Y|X)$. When uninformative priors (such as uniform distributions) are used, Equation 9.15 will reduce to an equivalent maximum likelihood estimation problem. Typically, one will obtain a constrained weighted least squares estimation problem (from Equation 9.15) for the steady state system case. This creates the opportunity to not only acquire reliable estimates of measured variables but also to estimate unmeasured variables (given that a minimum estimability constraint is met) (Romagnoli & Sánchez, 2000: 53).

In the 1980s use of data reconciliation gained popularity in the mineral processing industry. Metallurgical plants typically have many unmeasured variables and measurements that are made usually have large errors. Development of software such as the BILMAT algorithm (Hodouin, Kasongo, Kouame & Everell, 1981) allowed reconciliation of mass balances in flotation and comminution circuits (improving the analysis and quality of data obtained during measurement campaigns). Hodouin et al. (1981) showed that metallurgical plant flow rate, composition and PSD data can be successfully reconciled (in a maximum likelihood sense).

Data reconciliation has been implemented in past spiral research that focused on iron ore concentration (Sadeghi, Bazin & Renaud, 2016: 53; Sadeghi, 2015). Sadeghi et al. (2016: 53) used the

Stellenbosch University https://scholar.sun.ac.za

BILMAT algorithm to reconcile mass flow rates of different mineral species at different particle sizes. The analysis provides the intended precise estimates but also serves as a method to determine the quality of experimental data. Sadeghi et al. (2016: 53) found that the majority of their data points were adjusted by less than 3 % of the measured value(s) and concluded that it validates the quality of the data obtained (thus further analysis could continue with more confidence).

9.3.2. Data processing, reconciliation and rectification

Confident estimates of a plant's state (including variables such as flow rates, temperatures and concentrations) are necessary before a process can be optimised, evaluated or controlled. Process models and measurements are typically used to evaluate the behaviour of a plant and can be reconciled to provide more precise estimates of plant states (Romagnoli & Sánchez, 2000: 2; Johnston & Kramer, 1998: 591). Mass and energy balances (fundamental models) can be used to formulate process models while stochastic models are used to represent how measurements are inferred and behave (Romagnoli & Sánchez, 2000: 2).

The measurement system is typically expressed as $y = q(X) + e$ with $e \sim N(0, V_e)$ and the system of process models as $z(X) = \epsilon$ with $\epsilon \sim N(0, V_\epsilon)$ (Romagnoli & Sánchez, 2000: 13). In symbolic terms a data reconciliation problem can be stated by Equation 9.16 to Equation 9.18 in the form of a weighted least squares problem (Romagnoli & Sánchez, 2000: 13).

$$\min_X J = e^T V_e^{-1} e + \epsilon^T V_\epsilon^{-1} \epsilon \qquad \text{(Eq. 9.16)}$$

With constraints:

$$z(\hat{X}) = 0 \qquad \text{(Eq. 9.17)}$$

$$h(\hat{X}) \leq 0 \qquad \text{(Eq. 9.18)}$$

Here it is tacitly understood that errors of the measurement and model are Gaussian (as previously stated). Equations 9.16 to 9.18 are not formulated for the case of gross error (also called systematic or bias error) detection but is still useful in the case of steady state operation and design of sensor networks (Romagnoli & Sánchez, 2000: 114).

Figure 9.10 shows the probability distribution of a process variable measurement and its process model value and how the variable estimate compares with them. The measurement has the largest standard deviation with the process model providing a more precise distribution around its mean. The estimate value has the smallest standard deviation and, therefore, has a much larger probability density value around the estimate mean (indicating a more likely state).

Stellenbosch University https://scholar.sun.ac.za

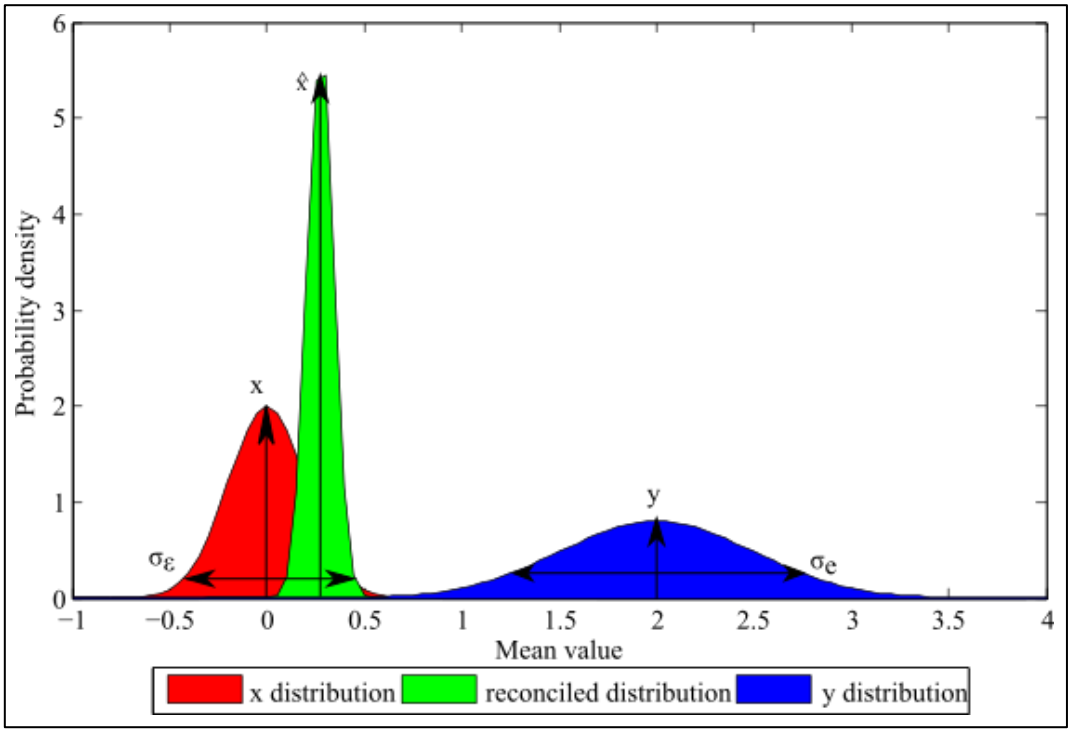

Figure 9.10: State estimation example

Looking toward simple estimation equations one can see why the estimate will be more precise:

- Variable X_1's estimate is obtained via a transform of the measurement y:

$$J = \frac{(y - X_1)^2 \sigma_e^{-2}}{2} + \frac{(X_1 - \mathrm{E}(X_1))^2 \sigma_\epsilon^{-2}}{2}$$

$$0 = \partial J / \partial X_1 = -\left(y - \hat{X}_1\right)\sigma_e^{-2} + (\hat{X}_1 - \mathrm{E}(X_1))\sigma_\epsilon^{-2}$$

$$y\sigma_e^{-2} + \mathrm{E}(X_1)\sigma_\epsilon^{-2} = \hat{X}_1(\sigma_e^{-2} + \sigma_\epsilon^{-2})$$

$$\hat{X}_1 = \frac{y\sigma_e^{-2} + \mathrm{E}(X_1)\sigma_\epsilon^{-2}}{(\sigma_e^{-2} + \sigma_\epsilon^{-2})}$$

- Variable X_1's variance can be obtained by transforming the measurement variance $\hat{\sigma}^2$:

$$Var\left(\hat{X}_1\right) = \frac{\sigma_e^{-2}}{(\sigma_e^{-2} + \sigma_\epsilon^{-2})} Var(y) \frac{\sigma_e^{-2}}{(\sigma_e^{-2} + \sigma_\epsilon^{-2})}, Var(y) = \sigma_e^2$$

$$\hat{\sigma}^2 = \frac{\sigma_e^{-2}}{(\sigma_e^{-2} + \sigma_\epsilon^{-2})^2}$$

In the simple case of Figure 9.10 the estimate variance will at least either be equal to the measurement variance or lower than it. This is one of the desirable properties of state estimation allowing us to produce more reliable data on the current state of a system. State estimation alone can produce more

Stellenbosch University https://scholar.sun.ac.za

trustworthy data but in the context of a chemical or metallurgical plant may still provide dubious results (Romagnoli & Sánchez, 2000: 4).

Reconciliation of plant data involves estimating plant state variables that are consistent with relevant conservation equations of a system (Romagnoli & Sánchez, 2000: 4). Measurements of state variables are typically corrupted by either uncorrelated errors (noise) and can also be affected by systematic or gross errors (Johnston & Kramer, 1998: 591). Thus, data reconciliation provides a means to transform observed state variables to more precise estimates that satisfies the physical constraints of the plant.

9.4. Genetic algorithms

Genetic algorithms (or GAs) are population based stochastic methods for the optimisation of problems expressed as Equation 9.19. These mathematical optimisation techniques are developed in such a way as to mimic natural selection and genetics (Deep, Singh, Kansal & Mohan, 2009: 506; Deb, 2000: 311).

$$\min_{\bar{\beta}} J_{GA}(\bar{\beta}) \qquad \text{(Eq. 9.19)}$$

Subject to:

$$g_j^{GA}(\bar{\beta}) \leq b_j^{eq}, j = 1, \cdots, \eta_1$$

$$h_j^{GA}(\bar{\beta}) = b_j^{eq}, j = \eta_1 + 1, \cdots, \eta_1 + \eta_2$$

$$\beta_i^L \leq \beta_i \leq \beta_i^U, i = 1, \cdots, \eta_3$$

Where:

- $\bar{\beta} = [\beta_1, \cdots, \beta_n]$
- β^L and β^U are upper and lower bounds for the optimization parameters.
- g^{GA} are inequality constraints.
- h^{GA} are equality constraints.
- η_1 is the number of inequality constraints, η_2 is the number of equality constraints and η_3 is the number of optimization parameters.

Typical implementation of a GA consist of 4 parts: Initialisation (or individual generation), selection, crossover and mutation. Initialisation of a GA is done by randomly generating a population of chromosomes. These chromosomes are evaluated against a certain objective and then manipulated by selection, crossover and mutation operators. An entire population is only constructed once and is then repeatedly subject to selection, crossover and mutation steps until a certain convergence criteria is met (Deep et al., 2009: 506). A chromosome represents a single instance of $\bar{\beta}$ and can be coded different ways; two popular methods include binary and real coded chromosomes. Below is an example of a

Stellenbosch University https://scholar.sun.ac.za

real coded chromosome and its binary chromosome counterpart and how these chromosomes could look in a population.

$$\bar{\beta} = [27,54,95] \leftrightarrow \bar{\beta} = [0011011,0110110,1011111]$$

$$\begin{bmatrix} 27,54,95 \\ 96,15,97 \\ 95,48,80 \\ 14,42,91 \\ \vdots \end{bmatrix} \leftrightarrow \begin{bmatrix} 0011011,0110110,1011111 \\ 1100000,0001111,1100001 \\ 1011111,0110000,1010000 \\ 0001110,0101010,1011011 \\ \vdots \end{bmatrix}$$

Binary chromosomes are suitable for integer programming problems but real coded chromosomes provide a simpler way to construct and manipulate vectors for a more diverse set of problems. Real coded chromosomes also do not require encoding and decoding steps that binary chromosomes need. Chromosome coding is essential to the efficiency of a GA and real coded GAs show faster convergence to optima than their binary versions (Deep et al., 2009: 506). Only real coded GAs will be considered in the rest of this section.

A common crossover method for real coded chromosomes is the Laplace crossover scheme which uses the Laplacian distribution to determine offspring chromosomes from progenitor chromosomes. Equations 9.20 and 9.21 give the necessary Laplace crossover formulae used for producing two offspring from two parent chromosomes (Deep et al., 2009: 507).

$$\gamma_i = \begin{cases} a - b^L \cdot \log(u_i), v_i \leq 1/2 \\ a + b^L \cdot \log(u_i), v_i > 1/2 \end{cases} \qquad \text{(Eq. 9.20)}$$

$$\bar{\tau}^1 = \bar{\beta}^1 + \gamma \circ |\bar{\beta}^1 - \bar{\beta}^2| \qquad \text{(Eq. 9.21)}$$

$$\bar{\tau}^2 = \bar{\beta}^2 + \gamma \circ |\bar{\beta}^1 - \bar{\beta}^2|$$

Where:

- Progenitor chromosomes are $\bar{\beta}^1$ and $\bar{\beta}^2$.
- Offspring chromosomes are $\bar{\tau}^1$ and $\bar{\tau}^2$.

A small crossover example is shown below to illustrate how Equations 9.20 and 9.21 can be used. The parameter a in Equation 9.20 is the location parameter and for this example is set to zero. b^L (where $b^L > 0$) is set to 0.15, u_i and v_i are uniform random numbers in [0,1] (Deep et al., 2009: 507). Smaller values for b^L is expected to produce offspring similar to the progenitors; conversely a larger b^L can lead to offspring less similar. Equations 9.20 to 9.21 are not guaranteed to produce offspring satisfying all variable lower and upper bounds. This can be ameliorated by reassigning a β_i, currently in violation of the bounds, new values randomly picked from $[\beta^L, \beta^U]$ (Deep & Thakur, 2007: 215)

$$\bar{\beta}^1 = [81,90,12], \bar{\beta}^2 = [91,63,9]$$

Stellenbosch University https://scholar.sun.ac.za

$$u = [0.2785, 0.5469, 0.9575], v = [0.9649, 0.1576, 0.9706]$$

$$\gamma = [-0.1918, 0.0905, -0.1918]$$

$$\bar{\tau}^1 \cong [79, 92, 11], \bar{\tau}^2 \cong [89, 65, 8]$$

Mutation operations are used to introduce diversity into a population during the iterations of a GA. One common mutation technique is power mutation that utilises the power distribution to produce offspring chromosomes (Deep et al., 2009: 507). Equation 9.22 gives the progeny of a chromosome via power mutation where p_m is the index of mutation, u and v are uniform random numbers in (0,1), and $\gamma = \frac{\bar{\beta}-\bar{\beta}^L}{\bar{\beta}^U-\bar{\beta}}$ (Deep et al., 2009: 507). The parameter p_m governs the amount an original chromosome is perturbed and thereby the additional randomness introduced into the population. Mutation via Equation 9.22 will always result in progeny satisfying the variable lower and upper bounds (Deep & Thakur, 2007: 214).

$$\bar{\beta} = \begin{cases} \bar{\beta} - u^{p_m} \cdot (\bar{\beta} - \bar{\beta}^L), \gamma < v \\ \bar{\beta} + u^{p_m} \cdot (\bar{\beta}^U - \bar{\beta}), \gamma \geq v \end{cases} \qquad \text{(Eq. 9.22)}$$

From the various selection techniques available, tournament selection has been shown to have better or similar performance to other selection options (Deep et al., 2009: 507). The mating pool, from which a new population is constructed, is derived via tournament selection by first selecting a mating pool size as a percentage of the total chromosome population and then filling the pool using tournaments. During each tournament k random chromosomes are picked from the original population, their fitness calculated, and the best chromosome (solution) is kept for the mating pool (Deep et al., 2009: 507).

Real coded GAs can be made to effectively handle integer constraints with a proper truncation method. Suppose a value $\beta_i \in \bar{\beta}$ must stay in $\mathbb{Z}$ (integer domain) but is in $\mathbb{R}$ (real domain) after crossover or mutation (possible according to Equations 9.20 to 9.22) then β_i can be set equal to $[\beta_i]$ or $[\beta_i] + 1$, where $[\beta_i]$ is the integer part of the number, with a probability of 0.5 (Deep et al., 2009: 507). When equality and inequality constraints are included in an optimisation problem a real coded GA's method of fitness determination must be adapted. A popular method suggested by Deb (2000: 316) uses penalty functions and makes distinctions between feasible and infeasible solutions to determine new fitness values. Equality constraints, however, must be converted to inequality constraints based on a certain tolerance (Deb, 2000: 316). Equation 9.23 summarises the constraint handling method of Deb (200: 316) which returns the normal fitness value for feasible solutions but gives infeasible solutions the worst feasible fitness along with a penalisation.

$$F_{GA}(\bar{\beta}) = \begin{cases} J_{GA}(\bar{\beta}), & if\ \bar{\beta}\ feasible \\ J_{GA}^{worst} + \sum_{j=1} |g_j^{GA}(\bar{\beta})|, & otherwise \end{cases} \qquad \text{(Eq. 9.23)}$$

Stellenbosch University https://scholar.sun.ac.za

The penalisation term is the sum of the values of the left-hand side of the violated constraints (Deb, 2000: 316). Application of Equation 9.23 will also require that tournament selection be done in such a manner that only feasible solutions proceed to the mating pool. If a tournament occurs between all infeasible solutions then the one with smaller constraint violation is preferred (Deep et al., 2009: 508). Lastly, after the calculation of fitness for a population some of the best performing solutions are kept in what is known as elite preserving. Elitism ensure that the best solutions of a population is kept and potentially gives the basis for better solutions but also keeps the population from receding into worse performing solutions (Deep & Thakur, 2007).

There are many more available options for cross-over, mutation, selection and constraint handling for real coded GAs (Deb, 2000: Deep & Thakur, 2007) but the methods given here is what the MI-LXPM (Mixed Integer Laplace Crossover Power Mutation) algorithm uses (Deep et al., 2009: 508). MI-LXPM is implemented by MATLAB when real coded GA problems are optimised. MI-LXPM makes the LXPM real coded GA (Deep & Thakur, 2007) suitable for mixed integer optimisation in a relatively simple way. Figure 9.11 gives a graphical review of the functioning of MI-LXPM.

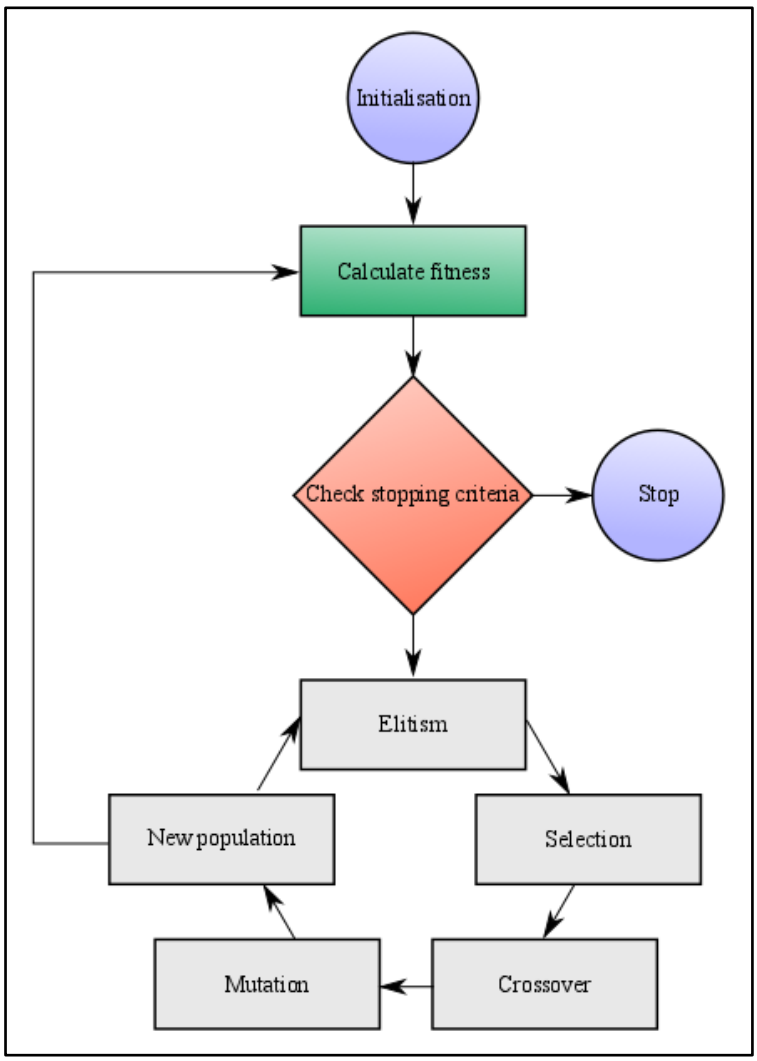

Figure 9.11: Diagram of general GA implementation

Stellenbosch University https://scholar.sun.ac.za

9.5. Logistic regression

One of the oldest and simplest statistical classifiers is known as logistic regression and is especially popular in medical science. There is also wide application of logistic regression in image processing as image classifiers and segmenters. Martin et al. (2004: 530) tested different classification algorithms to detect natural image boundaries and found logistic regression to be the algorithm of choice. Ren & Malik (2003) trained a logistic classifier to segment objects in images based on texture, brightness and contour energy cues calculated from superpixels. Clocca, Cusano & Schettini (2015: 3031) performed image orientation detection by classifying local binary pattern features with logistic classifiers.

Similar to artificial neural networks (ANNs) and decision trees, logistic regression seeks to classify data points by modelling conditional probabilities ($P(y = 1|x)$) of class membership (Dreiseitl & Ohno-Machado, 2002: 353). Logistic regression is related to the binary Bayes rule classifier and Gaussian linear discriminant analysis (LDA) except that membership probabilities are considered to follow a Bernoulli distribution. Equation 9.24 is used in LDA and assigns x to class 1 if $L(x) > 1$. f_1 and f_2 are multivariate Gaussian distributions (with the same covariance) and π_1, π_2 are the prior probabilities that a randomly selected x belongs to a class (Izenman, 2008: 242-250). The left side of Equation 9.24 is a linear function of x used to determine its membership.

$$L(x) = log\left(\frac{f_1(x)\pi_1}{f_2(x)\pi_2}\right) = log\left(\frac{P(y=1|x)}{P(y=2|x)}\right) = \alpha^T[1, x] \qquad \text{(Eq. 9.24)}$$

Where:

- α is the model parameters and x is the vector of features: $x_i = (x_{i,1}, x_{i,2}, \dots)$ for observation i.

LDA is derived by accepting that the priors do not sum to one i.e. $\pi_1 + \pi_2 < 1$. For logistic regression the conditional probabilities in Equation 9.24 are considered to be complementary leading to Equation 9.25 (Izenman, 2008: 250; Vapnik, 2000: 156).

$$L(x) = \log\left(\frac{P(y = 1|x)}{1 - P(y = 1|x)}\right) = \alpha^{\mathrm{T}}[1, \mathrm{x}] \qquad \text{(Eq. 9.25)}$$

Taking the exponential of both sides of Equation 9.25 and simplifying gives an equation of a sigmoid function (Equation 9.26) and the form of the logistic regression model typically used (Izenman, 2008: 250; Dreiseitl & Ohno-Machado, 2002: 354). Equation 9.26 has maximum of 1 and a minimum of zero and is also used to calculate activation values in ANNs. After the parameters α are estimated Equation 9.26 can be used to determine which class datapoint x belongs to. The decision boundary of a trained logistic regressor is the hyperplane $\alpha^T \cdot [1, x] = 0$ which separates points with probabilities $P(y = 1|x, \alpha) > 0.5$ or $P(y = 2|x, \alpha) < 0.5$ (Dreiseitl & Ohno-Machado, 2002: 354). When the probability is 0.5 membership can be determined by a random process (Izenman, 2008: 242).

$$P(y = 1|x, \alpha) = h = \frac{1}{1 + e^{-(\alpha^{\mathrm{T}}[1,\mathrm{x}])}} \qquad \text{(Eq. 9.26)}$$

Stellenbosch University https://scholar.sun.ac.za

Training of logistic regression parameters (α) is done via maximum likelihood estimation. The conditional likelihood for logistic regression is given by Equation 9.27 and the log-likelihood by Equation 9.28 (Izenman, 2008: 252). Here the first class membership is represented by $y = 1$ and the second by $y = 0$. Equation 9.28 is also known as the cross-entropy cost function which is typically used for binary classification problems (Dreiseitl & Ohno-Machado, 2002: 354).

$$e^{-J} = \prod\left[\left(P(y = 1|x_i, \alpha)\right)^{y_i}\left(1 - P(y = 1|x_i, \alpha)\right)^{1-y_i}\right] \qquad \text{(Eq. 9.27)}$$

$$J = -\frac{1}{m}\sum\left[y_i \cdot log\left(P(y = 1|x_i, \alpha)\right) + (1 - y_i) \cdot \log(1 - P(y = 1|x_i, \alpha))\right] \qquad \text{(Eq. 9.28)}$$

Maximizing the conditional likelihood is equivalent to the minimization of the log-likelihood which provide the values for parameters α that best describe the class membership. Optimisation can be performed using gradient descent (Gauss-Newton) type methods (Izenman, 2008: 252). The gradient of J is a vector of the same length as the vector of all model parameters α and is given by Equation 9.29.

$$\nabla J = \frac{x^T}{m}\sum\left[y_i - log\left(P(y = 1|x_i, \alpha)\right)\right] \qquad \text{(Eq. 9.29)}$$

- Where x is a matrix that contains features of the entire training set.
- m is the number of observations in the feature set x.

Overfitting can be avoided by adding regularisation terms to Equations 9.28 & 9.29 and similar variable selection methods used for linear regression (Izenman, 2008: 252). The $\alpha \cdot x$ term in Equation 9.24 is similar to a general linear model when $0 < P < 1$ which allows statistical variable selection. Logistic regression outperforms LDA when different classes have different covariances or when probability distributions other than normal Gaussian are encountered. Logistic regression is also less sensitive to outliers but requires larger training data sets than LDA to achieve similar error rates (Izenman, 2008: 256).

Classification on a simple 2D dichotomous dataset is shown in Figure 9.12. The contour levels are curved lines since quadratic hyperplanes were used in Equation 9.26 and the level labelled 0.5 indicates the decision boundary.

Stellenbosch University https://scholar.sun.ac.za

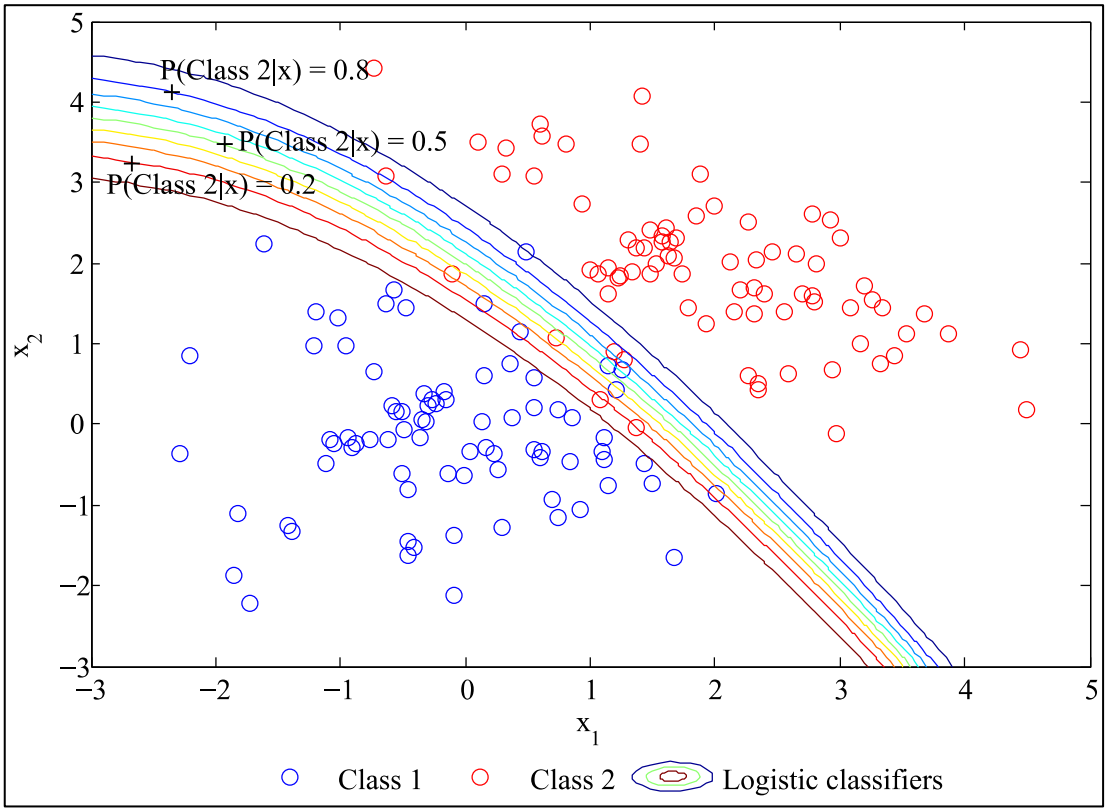

Figure 9.12: Example of logistic classification

Stellenbosch University https://scholar.sun.ac.za

10. Appendix B: Literature

10.1. Tracer tests

Tracer tests that have been performed on spirals include the work of Walsh and Kelly (1992), Boucher et al. (2014), Boucher, Deng, Leadbeater and Langlois (2016), and Boucher, Deng, Leadbeater, Langlois and Waters (2016). Walsh and Kelly (1992: 5) used gold tracers to investigate how particle shape, pulp flow, splitter settings and pulp density affect recovery. This experimental work was only an exploratory foray into tracer tests on spirals due to experimental complications and did not serve modelling purposes well.

Boucher et al. (2014 and 2016) continued with tracer tests using Positron Emitting Particle Tracking (PEPT) methods. Newer technology allowed measuring particle trajectories and velocities which can be used to validate CFD and DEM research of spiral flows. Trajectories and velocities of different minerals (usually quartz as gangue and hematite as MOI) at different particle sizes were recorded to confirm previous knowledge of spiral concentration and to, for the first time, quantitatively measure particle mechanics within a spiral trough. The work done under Boucher et al. (2014 and 2016) is still exploratory and requires refinement. Production of small tracers still poses problems and provide less accurate tracking results than larger tracer particles.

10.2. Spiral circuit configuration, measurement and sampling in laboratory tests

One of the most important considerations of spiral experimentation is whether open or closed loop configurations should be implemented. Guest & Dunne (1985: 195) suggest that open circuit tests be conducted to ensure constant feed composition to the spiral splitters. This is not always possible with a laboratory spiral with a smaller feed inventory, and limited space for extra equipment. It should also be noted that the feed inventory should have a constant composition if tests are performed to determine certain mineral recovery at a constant feed grade.

Holland-Batt et al. (1982: 59) states that closed loop laboratory tests require at least 10 kg feed to exhibit some visible degree of separation. Loveday (1993) also suggests that a closed loop circuit experiment is preferable when testing wash-waterless spirals since an open loop configuration will produce large quantities of product. Sampling in closed circulation configuration reduces the amount of slurry within the system; changing the feed composition and overall system solids content. Fresh feed material can be added but the new state of the slurry will have to be back calculated from the product compositions (Sadeghi, 2015: 31). Large feed inventories can be used to ensure changes incurred by sampling are minimal but the recommended inventory size is in the range of a few hundred litres of slurry (Loveday, 1993: 3.2).

Flow rates can be measured using a ‘bucket and stopwatch’ method but accurate flow rates should be inferred after more accurate solids densities have been obtained (Loveday, 1993: 3.12). Holtham, (Holland-Batt & Holtham, 1991: 462) used a magnetic flow meter and density gauge to determine the

Stellenbosch University https://scholar.sun.ac.za

slurry flow rate and RD. Slurry density can also be inferred using pycnometers (Sadeghi, 2015). Holtham (1991: 82) also used a 'bucket and stopwatch' method to confirm measurements from the automatic flow meters. Sampling time for flow measurements were between 15 and 30 seconds (Holtham, 1991: 82). Feed flow rates can be controlled using pump settings or simply using multiple feed pipes. When multiple feed pipes are used flow rates can be altered by simply removing pipes from the overall feed (Sadeghi, 2015: 31).

Product stream samples should be obtained simultaneously as done by Loveday (1993: 3.12) who used 10 second intervals and Holtham's (1991: 82) 15 to 30 second intervals. These sampling times were used to determine the flow rate of the slurry. Loveday (1993: 3.12) and Holtham (1991: 81) both used multiport sampling units but Loveday used 6 ports while Holtham used 8. Sadeghi (2015: 43) used automatic multiport sampling at 4 second intervals to reduce disturbance to the closed-loop system. However, this can lead to very small samples collected at certain product streams (introducing greater error to measurements). Sampling ports are usually spaced away in equal amounts with Loveday's (1993: 3.12) rig using 20 mm and Holtham (1991: 81) using 30 mm and 40 mm depending on the trough diameter.

Stellenbosch University https://scholar.sun.ac.za

11. Appendix C: Methodology

11.1. Interface detection

11.1.1. Algorithm CVI

Algorithm CVI's image processing steps, mentioned in Figure 4.5 (Chapter 4), introduces 13 parameters which is shown with their respective functions in Figure 11.1. In Algorithm CVI two Canny edge detection steps are performed and 2 different types of morphological features are filtered in the connected component filtering step. Algorithm CVI can also decide whether histogram equalization should take place.

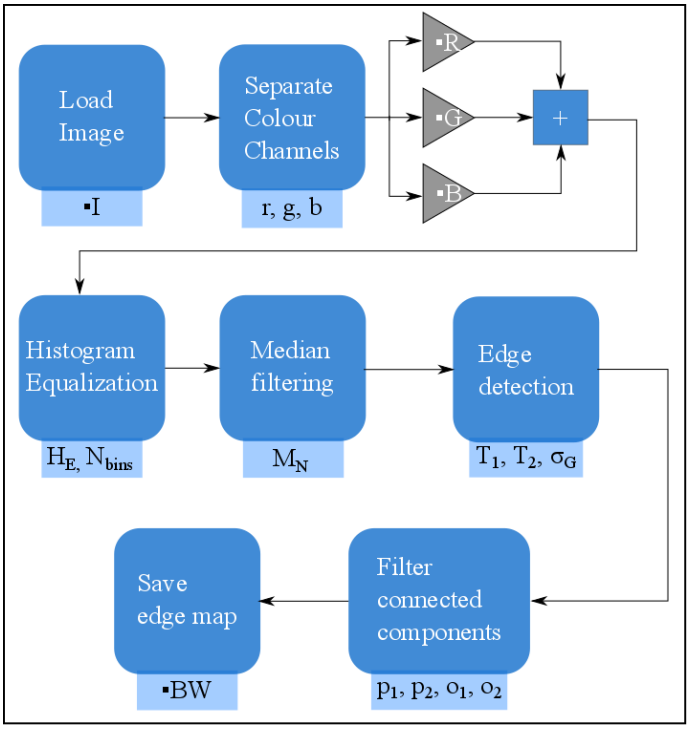

Figure 11.1: Interface detection Algorithm CVI with parameters shown

Algorithm CVI's parameters are summarized in Table 11.1. Histogram equalization is performed by Algorithm CVI when $H_E = 1$ and is excluded when $H_E = 0$. Histogram equalization can also be done to reduce the amount of intensity intervals from the original 256 levels. Median filtering is performed using a neighbourhood of M_N pixels per side to remove noise while preserving edges. Two Canny edge detection steps are done using the same Gaussian kernel but with different thresholds T_1 and T_2. Connected components in the binary edge map are filtered based on edge length (in pixels) and the angle of object major axes and the image horizontal axis.

Stellenbosch University https://scholar.sun.ac.za

Table 11.1: Algorithm CVI parameters

Parameter symbol	Parameter description
r	Red channel weight
g	Green channel weight
b	Blue channel weight
N_{bins}	Histogram equalization intensity binning levels
H_E	Histogram equalization activator
M_N	Median filter neighbourhood size
T_1, T_2	Edge detector hysteresis thresholds
σ_G	Gaussian kernel standard deviation
p_1, p_2	Connected component upper and lower perimeter size
o_1, o_2	Connected component upper and lower orientation angle

The two Canny edge detection steps serve as the first edge filtering step – succeeded by connected component filtering. This step removes spurious edges by subtracting the edge map with the most detections from the edge map with the least. A threshold value closer to 1 will result in an edge map with fewer edge detections and a smaller threshold value (for the same Gaussian kernel) produces an edge map with more edge detections. Then, for the edge detection step, the edge map with the lower threshold value is subtracted from the edge map with the higher value.

Orientation filtering of connected components compares the axes of an object to an axis of the containing image. Figure 11.2 illustrates the concept of connected component orientation. Major and minor axes of component filters are determined using equivalent ellipses (based on second moments) and their angle of rotation (of the major axis) from the image horizontal is used to determine the final orientation.

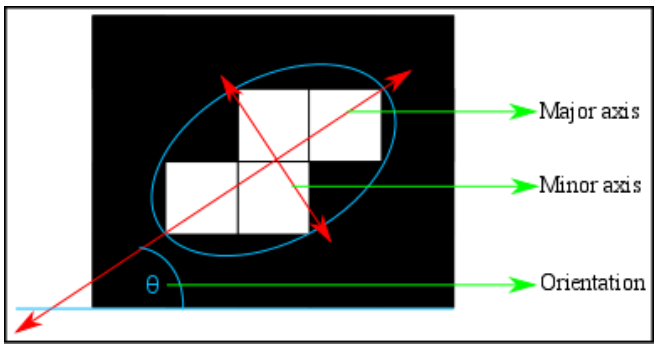

Figure 11.2: Orientation of a connected component

11.1.2. Parameter optimization for Algorithm CVI

Typical spiral plants can contain several hundred spiral concentrators and images, of mineral slurry before splitting, will vary greatly. If cameras are to be placed at all different locations in a spiral plant

Stellenbosch University https://scholar.sun.ac.za

manual parameter selection for Algorithm CVI will become taxing – selection will also be done on a qualitative basis. An optimization approach is required to find the parameters that give the best interface detection results based on images captured around a spiral plant with annotated – desired - responses.

Out of Algorithm CVI's 13 parameters 8 are real valued and 5 are positive integers. The image processing functions in Algorithm CVI have highly nonlinear and/or discrete properties considering that images with discrete values will be processed. Gradient based optimization methods are not suitable to alter the parameters of Algorithm CVI; however, GA's (as mentioned in Section 9.4) are suited to this task. The MI-LXPM GA can optimize discrete objective functions even when mixed, discrete and continuous, boundary conditions are present.

Equation 11.1 is the objective function for the supervised learning problem which seeks to find parameters $\bar{\beta} = [r, g, b, N_{bins}, H_E, M_N, T_1, T_2, \sigma_G, p_1, p_2, o_1, o_2\ ]$ which maximises J_2 (Equation 9.2). I and I_{label} symbolises the training image set of RGB images I of mineral slurry and binary images I_{label} showing a labelled interface. The score that J_2 produces is finally determined from comparing the binary image, Algorithm CVI creates, to the training image I_{label}.

$$\underset{\bar{\beta}}{\operatorname{argmax}} \sum_{I, I_{label} \in Training\ Set} \sum_{i,j} \frac{t_{p,ij}(\bar{\beta}, I, I_{label}) - f_{p,ij}(\bar{\beta}, I, I_{label})}{M \times N} \qquad \text{(Eq. 11.1)}$$

Boundary conditions needed for the optimization of Algorithm CVI is summarized with Equations 11.2 to 11.15 (grouped together in Table 11.2). Equality, inequality and discrete constraints are needed to ensure that valid parameters are selected for each iteration of the GA.

Stellenbosch University https://scholar.sun.ac.za

Table 11.2: Boundary conditions

Boundary condition	Equation number
$-2 \leq \beta_1 \leq 2$	Eq. 11.2
$-2 \leq \beta_2 \leq 2$	Eq. 11.3
$-2 \leq \beta_3 \leq 2$	Eq. 11.4
$2 \leq \beta_4 \leq 64, \beta_4 \in \mathbb{Z}$	Eq. 11.5
$\beta_5 \in [0,1]$	Eq. 11.6
$3 \leq \beta_6 \leq 31, \beta_6 \in \mathbb{Z}$	Eq. 11.7
$\beta_7 - \beta_8 < -0.01$	Eq. 11.8
$1 \leq \beta_9 \leq 21$	Eq. 11.9
$2 < \beta_{10}, \beta_{10} \in \mathbb{Z}$	Eq. 11.10
$2 < \beta_{11}, \beta_{11} \in \mathbb{Z}$	Eq. 11.11
$\beta_{10} - \beta_{11} < -0.01$	Eq. 11.12
$-\pi/2 \leq \beta_{12} \leq \pi/2$	Eq. 11.13
$-\pi/2 \leq \beta_{13} \leq \pi/2$	Eq. 11.14
$\beta_{12} - \beta_{13} < -0.01$	Eq. 11.15

The red, green and blue channel scaling parameters can attain values larger than 2 or lower than -2 which can force certain pixels to a value of 255 or 0 (since the pixels will have uint8 values). Equation 11.5 limits the maximum amount of intensity levels to 64 (arbitrarily chosen) and the minimum results in a binary image. In Equation 11.7 the largest filter size is limited to 31×31 ensuring fast execution time for median filtering. Equation 11.8 is used to ensure that T_1 is smaller than T_2 by at least a value of 0.01. Equation 11.9 restricts the size of the Gaussian kernel to ensure fast execution time. Equations 11.12 and 11.15 are used for the same purpose as Equation 11.8 except here it applies to perimeter and orientation parameters.

Supervised learning requires labelled training data to be passed to the MI-LXPM GA and Algorithm CVI requires training data in the shape of images. Figure 11.3 shows examples of training images of ilmenite slurry, in a spiral trough, and the label images with pixels of value 1 where an interface is present. Labelling is done by hand and the labelled interface is 1 pixel wide. Labelled binary images, similar to examples in Figure 10.3, are compared to Algorithm CVI's output to determine the score (according to Equation 4.2 in Chapter 4) used by the GA to find an optimized interface detector.

Stellenbosch University https://scholar.sun.ac.za

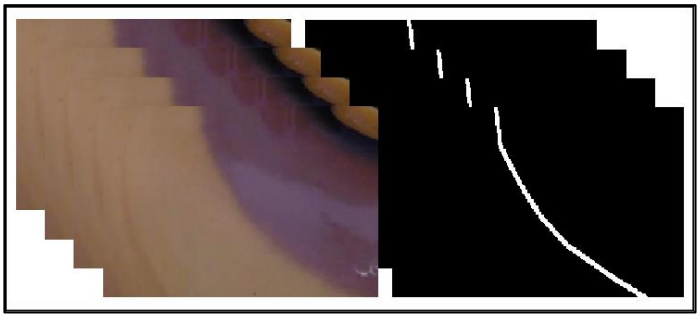

Figure 11.3: Training images (left) with labels (right)

Training of Algorithm CVI was done using MATLAB's Image Processing and Global Optimisation Toolboxes. Table 11.3 summarises how MATLAB functions were used to execute Algorithm CVI and its supervised learning.

Table 11.3: MATLAB functions used for interface detection Algorithm CVI

Algorithm CVI step	MATLAB function
Histogram equalization	histeq()
Median filtering	medfilt2()
Canny edge detection	edge()
Connected component filtering	bwpropfilt()
MI-LXPM	ga()

11.1.3. Algorithm CVII parameter optimization

The feature sets for Algorithm CVI (edge detection based) were sets of images but for Algorithm CVII, especially in the logistic classifier case, the features can be thought of as $m \times n$ regions of slurry images. Figure 11.4 shows how pixels, from training images, are unpacked to form the training feature set (in this case the ith feature vector). Red, green and blue channel neighbourhoods are unpacked into feature vectors and horizontally concatenated before sliding to the next pixel and unpacking its corresponding neighbourhood. Labelled images are simply vectorised to obtain the training label vector.

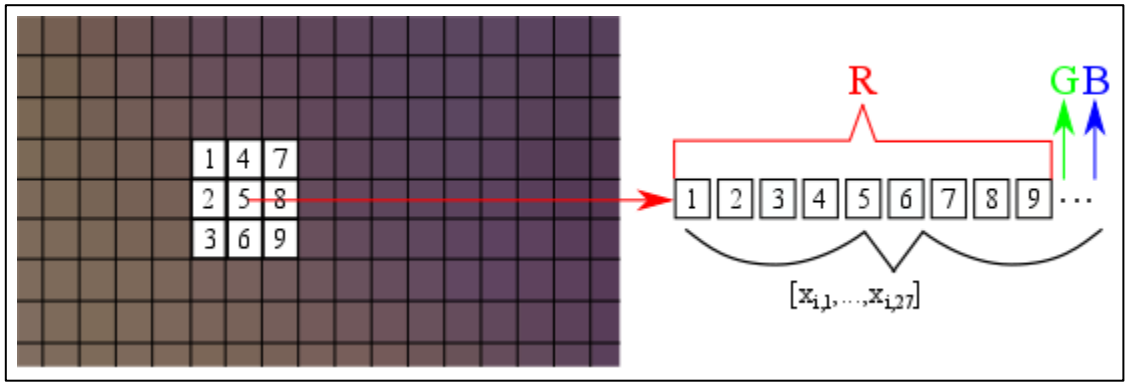

Figure 11.4: Feature extraction, from slurry images, for pixel classification (3 × 3 kernel case)

To ensure label and feature set vectors have the same amount of rows, appropriate border padding must be added to the slurry images. When $m \times n$ sliding windows are used $m - 1$ rows and $n - 1$ columns of pixel value zero are added to the slurry images. Figure 11.5 shows examples of the slurry label images used to prepare the label matrix for logistic regression training. Original label images were also converted from uint8 to binary to prepare the necessary label vector of 1s and 0s.

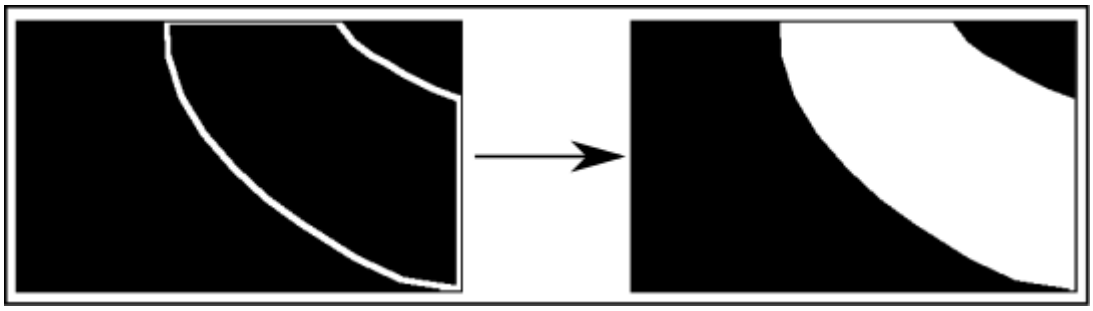

Figure 11.5: Label images for Algorithm CVII

After all training data has been prepared Equations 9.28 and 9.29 must be modified (for efficient code implementation) and then optimization of the most likely parameter values can be done. Equations 11.16 & 11.17 are similar to Equations 9.28 & 9.29 but are changed to matrix notation. Regularisation terms are also added in an attempt to address any over fitting that may be encountered with training data.

$$J = -\left(\frac{1}{m}\right)\left[y^T \cdot \log\big(P(y=1|x,\alpha)\big) + (1-y)^T \cdot \log\big(1 - P(y=1|x,\alpha)\big)\right] + \frac{\lambda}{2m}\alpha'^T\alpha \quad \text{(Eq. 11.16)}$$

$$\nabla J = \left(\frac{1}{m}\right) x^T \cdot [P(y=1|x,\alpha) - y] + \frac{\lambda}{m}\alpha' \quad \text{(Eq. 11.17)}$$

- Where the regularisation value λ omits penalizing the bias parameter
- The vector α' is equal to α except that its bias $\alpha'_0 = 0$

Cross validation (Izenman, 2008) was used to determine the appropriate λ values and whether increasing it from 1 significantly affects the trained models. Results prepared during cross validation is calculated precision and recall values combined with the F statistic (Equation 9.13) of the trained

Stellenbosch University https://scholar.sun.ac.za

logistic regression function. Maximization of the F statistic is desired and the λ value corresponding to the highest F value determines the regularisation term. Training of the logistic classifier is done using fmincg() or MATLAB's fminunc() functions. The fmincg() function uses Polak-Ribiere conjugate gradient descent with line searches implemented via approximated quadratic or cubic polynomials. MATLAB's fminunc() function, from the Optimization Toolbox, is based on the BFGS non-linear optimisation algorithm.

A trained logistic pixel classifier will usually detect blobs that, for an accurate classifier, will correspond to middling or concentrate bands of a slurry. Edges of the detected blobs must be isolated in order to assess the interface detection performance; however, trained classifiers can still give some undesired detections that must be cleaned up. The first step is to threshold (using the logistic regression decision boundary) the classifier detections and convert the result to binary. Morphological operations are then used detect the largest connected (8-connected) object of 1s, to fill the middling or concentrate detection blobs and then to trace the perimeter of the largest "cleaned" connected object.

Coordinates of the pixels, from the perimeter of the detected object, are stored and converted to polar coordinates. This allows interface segmentation from the perimeter using appropriate radius and angle terms from a common fixed point of the slurry images. Figure 4.6 (in Chapter 4) summarises the interface extraction process. Middling interfaces (as seen in Figure 4.6's example) are selected by choosing pixels in an angle range with smallest possible radius from the lower left corner of the image.

11.1.4. Hardware used to train algorithms

Optimization of Algorithm CVI was done using a virtual machine (VM) running on a Dell PowerEdge R610 server with 12 physical CPU cores clocked at 3.324 GHz (with hyperthreading active) and 96 GB of RAM. The server's computational resources are divided amongst 3 VMs and the VM that was used had the following specifications:

- One VM uses 8 CPU cores (logical) and 32 GB of RAM.

Algorithm CVII was trained using a Dell 9020 desktop computer with following properties:

- Intel i7-4790 clocked at 3.6 GHz (with 4 physical and 4 logical cores).
- 16 GB DDR3 RAM.

11.1.5. Interface measurement

When interface detection algorithms of suitable accuracy and precision have been prepared, it becomes possible to track interfaces and measure relative distances (in pixel length) between pixels of different interfaces. Certain pairs of pixels must be identified for tracking after interfaces have been extracted as shown in Figure 4.6 (from Chapter 4). Relative distances between relevant pixels can later be transformed to metric measurements using calibration matrices.

Stellenbosch University https://scholar.sun.ac.za

Figure 11.6 shows the relevant pixels that are tracked for interface measurements. The interface pixels closest to the primary splitters are used for tracking. For concentrate interface tracking the slurry-gulley and concentrate-middlings interfaces will be used. Three pixels on the concentrate-middlings interface and one pixel on the slurry-gulley interface is tracked and three relative distances are calculated.

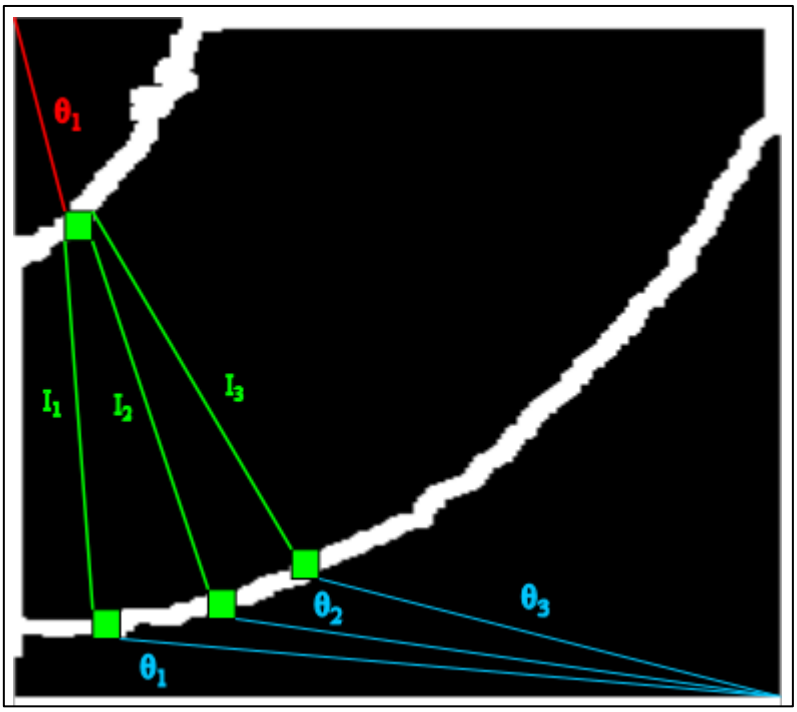

Figure 11.6: Tracking of interface pixels in binary interface map (red line extends from gulley; blue line extends from spiral trough periphery)

The positions of the pixels in Figure 11.6 are obtained at certain angle increments of the polar coordinates for pixels belonging to the different interfaces. The angle increments for the gulley-concentrate is 0.1 radians and concentrate-middling interfaces is 0.2 radians.

11.1.6. Calibration

Camera calibration is used to obtain metric measurements describing the interface widths (relative to support column or gulley) of detected interfaces. Specifically, calibration here refers to obtaining the parameters for equations that relates real world and camera coordinates. Hall calibration was used to obtain real world interface measurements by assuming a linear camera model (shown by Equation 9.1) is appropriate. Simplifying the linear camera model and ignoring z-axis terms leads to Equation 11.18:

$$\begin{bmatrix} x \\ y \\ s_c \end{bmatrix} = \begin{bmatrix} A_{11} & A_{12} & A_{14} \\ A_{21} & A_{22} & A_{24} \\ A_{31} & A_{32} & A_{34} \end{bmatrix} \begin{bmatrix} X_w \\ Y_w \\ 1 \end{bmatrix} \qquad \text{(Eq. 11.18)}$$

- Where A_{ij} are the linear calibration parameters.

Stellenbosch University https://scholar.sun.ac.za

When world and image coordinates are available, from at least 6 or more points, then A_{ij} can be calculated via least squares. Equation 11.19 is obtained after taking the transpose of Equation 11.19 and including extra calibration points in the coordinate matrices. The parameters can be solved using the Moore-Penrose inverse of the world coordinates – shown in Equation 10.20.

$$\begin{bmatrix} x_1 & y_1 & s_c \\ x_2 & y_2 & s_c \\ \vdots & \vdots & \vdots \end{bmatrix} = \begin{bmatrix} X_{w1} & Y_{w1} & 1 \\ X_{w2} & Y_{w2} & 1 \\ \vdots & \vdots & \vdots \end{bmatrix} \begin{bmatrix} A_{11} & A_{21} & A_{31} \\ A_{12} & A_{22} & A_{32} \\ A_{14} & A_{24} & A_{34} \end{bmatrix} \qquad \text{(Eq. 11.19)}$$

$$\begin{bmatrix} X_{w1} & Y_{w1} & 1 \\ X_{w2} & Y_{w2} & 1 \\ \vdots & \vdots & \vdots \end{bmatrix}^{+} \begin{bmatrix} x_1 & y_1 & 1 \\ x_2 & y_2 & 1 \\ \vdots & \vdots & \vdots \end{bmatrix} = \frac{1}{s_c} \begin{bmatrix} A_{11} & A_{21} & A_{31} \\ A_{12} & A_{22} & A_{32} \\ A_{14} & A_{24} & A_{34} \end{bmatrix} \qquad \text{(Eq. 11.20)}$$

Equations 11.18 to 11.20 contain a parameter s_c (scaling parameter) which cannot be calculated for the linear case. Instead s_c is included in the derived values of A_{ij}. Figure 11.7 shows an image with a calibration pattern, the detected calibration corners and the re-projected corners calculated using Hall calibration.

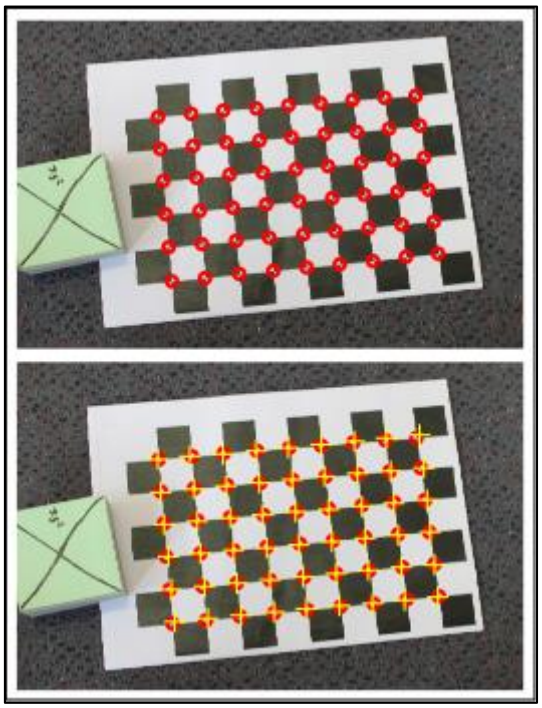

Figure 11.7: Detected checkerboard pattern corners (red circles) and re-projected corners (yellow crosses)

Calibration pattern images was captured before each spiral modelling test run (see Section 11.2) to be used for calibration and interface measurement later. A calibration pattern with checkerboard squares of size 16.5 mm (see Figure 11.11) was placed in the spiral trough for image acquisition. Hall calibration can be performed offline for each spiral modelling test after experimental work has been completed. It is assumed that the calibration pattern and spiral slurry surface are on the same plane.

Stellenbosch University https://scholar.sun.ac.za

Equations 11.21 and 11.22 (derived from Equation 11.18) are the final equations that can be used to determine world coordinates of pixels within an image. Appendix F gives the derivation of Equations 11.21 and 11.22.

$$Y_W = \frac{B_c(A_{14}-x)+A_{24}-y}{((yA_{32}-A_{22})-B_c(A_{12}-xA_{32}))} \quad \text{(Eq. 11.21)}$$

$$X_W = \frac{Y_W(A_{12}-xA_{32})+A_{14}-x}{(xA_{31}-A_{11})} \quad \text{(Eq. 11.22)}$$

Where:

- $B_c = \frac{A_{21}-yA_{31}}{xA_{31}-A_{11}}$.
- $A_{34} = 1$.

Equation 11.19 can be used to calculate X_W and Y_W but this will require estimating the inverse of the Hall calibration matrix which can take longer to execute than the implementation of Equations 11.21 and 11.22. Hard coding Equations 11.21 and 11.22 results in obtaining the analytical solutions of X_W and Y_W quickly.

11.2. Spiral experimentation: Equipment, feed preparation and experimental design

A spiral and ore, similar to what are implemented at the WPL plant, were used to prepare grade, recovery and interface models for spiral plant simulation. A double start Multotec SC 21 spiral (along with supporting frame, sump and pump) was donated by Glencore for the experimental work and Glencore also supplied four, filled, 200 L drums of different types of UG2 ore. The equipment was commissioned at Stellenbosch University to treat the UG2 ore. The four drums, which were supplied for the project, contained feed, concentrate, coarse, and fine tailings from the WPL plant (in Section 2.2).

A diagram of the commissioned equipment is shown in Figure 11.8. Ore (added using the same route as streams 7, 8 and 9) and water (added via stream 1) is introduced to the sump (E-101) and is pumped (using P-101) to the spiral via the feed tank E-102. The feed tank has a bypass that leads to the sump and can be adjusted using valve V-104. Valve V-103 controls the flow of slurry to the spiral but was left completely open during all experimental runs. Leaving V-103 unchanged means flow to the spiral is manipulated via V-104. Material can be removed from the system using valve V-102. Pump P-101 is linked to the controller I-101 which is used to set the pumping speed. Spiral splitters can be set to control the amount of concentrate, middlings and tailings slurry that can be produced.

Stellenbosch University https://scholar.sun.ac.za

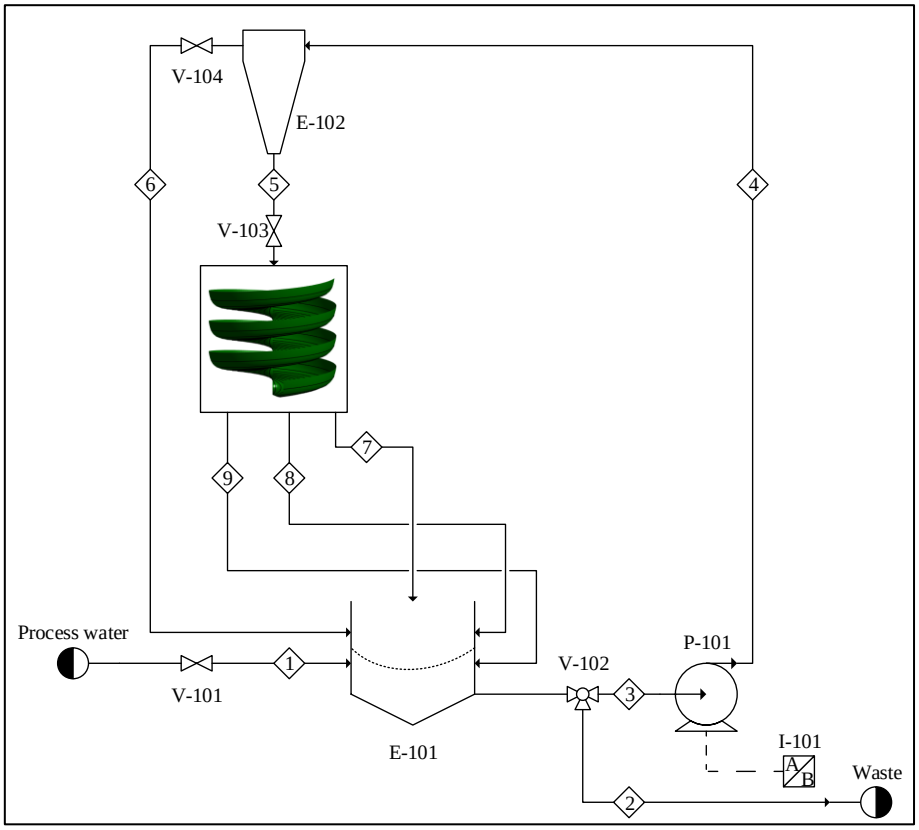

Figure 11.8: Experimental equipment diagram

The spiral equipment that was received has 3 three product streams emanating from the spiral splitter box, however, the spirals at the WPL (or Rowland site) plant only had concentrate and tailings product streams. Also, only a total concentrate and coarse tailings streams are produced by the WPL spiral plant. Stream 7 was used as the concentrate stream, during experimentation, and tailings is produced by grouping streams 8 and 9 to make the experimental equipment agree with what is observed on site (at the WPL plant).

Ore obtained from the WPL plant had to be homogenised to ensure feed for experimental runs, using ore from the same drum, stays similar. Each drum was emptied and quartered in an attempt to homogenously split up the ore in smaller 25 L drums. The chromite ore was still wet; however, which complicates the standard coning and quartering procedure. Typical coning and quartering involves piling dry material in a conical shape and division into quarters. Conical symmetry is used to assume that opposing quarters of the dry material pile is equal in composition – leading to two opposing quarters to be used for further quartering.

Wet and fine material cannot be quartered since the material tends to form clumps. Instead the following procedure was used (Petersen, 2016):

1. Ore from one of the drums is emptied into a large tundish and spread evenly.
2. After dividing the ore into sixths, four rectangles - at opposite ends - are transferred to a second tundish (see Figure 11.9). Ore in the tundishes are spread evenly and levelled.

Stellenbosch University https://scholar.sun.ac.za

3. Ore in the second tundish is then divided into sixths and the 4 opposing end corners are transferred to the first tundish. Remains are spread evenly and levelled.
4. Finally, all ore in the first tundish, after being levelled and divided into sixths, are spread evenly over the second tundish and levelled.

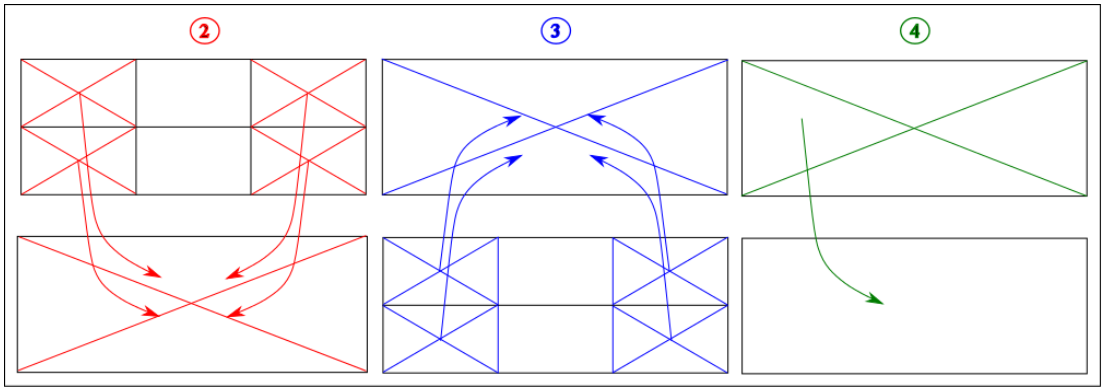

Figure 11.9: Chromite ore quartering

After the quartering process, it is assumed that the contents in the second tundish are homogenously mixed across the horizontal plane with compositional variation occurring in vertical layers. Quartering was performed on the WPL plant feed, concentrate and coarse tailings ore. After quartering for each ore type, samples were taken for XRF analysis. Representative samples were split into 100 g samples, with a riffle splitter, for milling and XRF analysis.

With the ore assumed to be homogenously mixed and the spiral equipment commissioned it was possible to perform experimental modelling of the spiral concentrator treating chromite ore. Spiral literature was used to find the most significant factors to investigate in an RSM design. From Section 3.2 (in Chapter 3) it is known that slurry flow rate, density, composition, viscosity, particle size and splitter position all effect separation efficiency. Spiral feed density and flow rates can be manipulated during experimental work by adding solids and changing pump or valve settings. The use of different feed grade, across experimental tests, will require 3 different spiral feed ore reserves for a Box-Behnken design. If change in feed particle size is included in a Box-Behnken design 9 feed ore reserves must be prepared. This requires sieving the ore in the 3 drums from Glencore 3 times each which must then be followed by mixing and compositional analysis of each feed preparation.

Changing particle size will require more involved feed preparation and a larger UG2 ore reserve (of at least double the amount received from the Rowland site). If viscosity must be changed it will have to be done artificially. Artificial manipulation of viscosity does affect mineral interfaces but is not representative of slimes since the presence of slimes can make interfaces undetectable (Vermaak et al., 2008). Including variation in viscosity and particle size in experimental test design (to feed grade, density, flow rate and splitter setting) will require 54 experimental test runs (double the amount of a 4 factor Box-Behnken design). Due to the difficulty of investigating viscosity and particles size it could not be included for the spiral modelling experiments.

Stellenbosch University https://scholar.sun.ac.za

The first 3 factors included in the experimental work is slurry flow rate, density and splitter setting as was previously done by Tripathy & Murthy (2012) and Dixit et al. (2015). Both studies concluded that main effects - flow rate, density and splitter setting - all significantly affected measured responses, and therefore, these factors are included in the overall experimental design. In this study feed grade is also varied to prepare suitable models for spiral plant modelling (since roughers, scavengers etc. treat slurries of different grades). Feed grade can be varied since different ores were received from the WPL plant. Feed grade can also have a significant effect on mineral interface position, according to Vermaak et al. (2008), making its inclusion necessary for interface modelling.

A 4 factor Box-Behnken design was used to design the experimental runs for the spiral models, based on the chosen factors and time constraints. 25 design runs are combined with two centre run replicates totalling 27 experimental runs. The Box-Behnken design leads to a minimum number of experimental runs (compared to CCD) that can still produce a statistically relevant model. Factors vary from a high (+1) to a centre (0) or a low (-1) setting (see Table 11.4) across different experimental runs.

Table 11.4: Design levels (details on level fixing during experimentation is provided in Appendix G)

	Feed Grade (% HM)	SG	Flow rate (m^3/h)	Splitter position (cm)
High (+1)	72	1.5	10	10.5
Centre (0)	53	1.3	8	8.5
Low (-1)	33	1.1	6	6.5

The levels in Table 11.4 were selected based on the material available and the design specifications of the Multotec SC21 spiral. Feed grade (based on HM) levels were left to be determined after analysis of the "homogenised" WPL feed, concentrate and coarse tailings samples. The original design runs were blocked according to feed grade and randomized to provide the order with which experiments could be correctly done (Tables 15.1 and 15.2 in Appendix G). Blocking was done due to time limitations otherwise only a single run would be possible in a day (due to cleaning of the rig to prevent sample contamination). Orthogonal blocking was not performed which can lead to confounding of factor effects and could necessitate analysis of variance to determine if blocking significantly affects spiral modelling.

Several responses from the spiral must be measured to ensure that any resulting empirical models will be valid for a spiral circuit simulation. Product stream flow rates, densities and compositions were measured to determine the spiral behaviour. Compositions are determined by sampling feed and product streams. Sampling of product streams is typically done simultaneously over a 10 to 30 second interval but in this study sampling is done individually per product stream – 3 repetitions were performed for each product stream measurement. Feed and product stream responses were measured

Stellenbosch University https://scholar.sun.ac.za

three times during each run resulting in the collection of 243 samples. Volume, mass and the time required to collect the volume were recorded for wet samples (direct from a spiral stream). All samples were dried to determine solids mass of each spiral stream.

The final response from the spiral that must be captured is the behaviour of mineral interfaces in the spiral trough. This was achieved by attaching 2 cameras to the spiral setup and collecting at least 5 minutes of video of the slurry entering the splitter box. A GoPro Hero 3+ Black edition (GP) and Milesight Mini Bullet (MS) camera were used for image acquisition at the same resolution but using different video compression regimes – resulting in different quality of images. The MS camera captured 10 frames per second while the GP captured 25 frames per second. Video was captured at significantly different angles as shown in Figure 11.10. Only video from the GP camera was used to train interface detection algorithms and to determine concentrate interface width measurements. Only the concentrate interface and its distance from spiral gulley is measured.

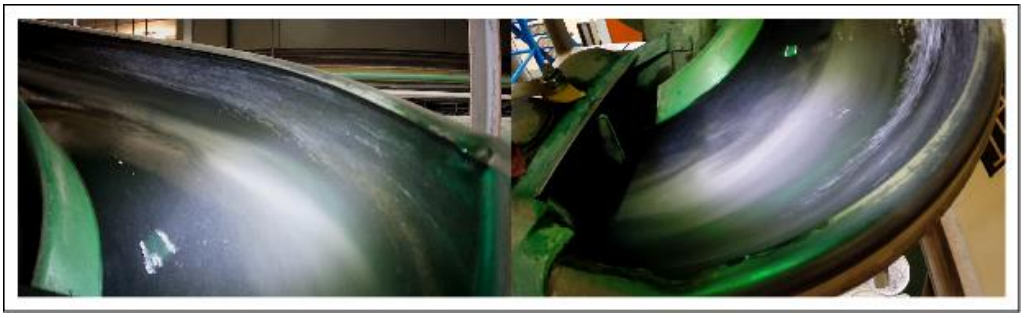

Figure 11.10: Examples of slurry images that were captured (left: Milesight camera, right: GoPro camera)

Calibration of the cameras is the first step for the start-up of the experimental equipment. Several images of a calibration pattern (that can fit in the spiral trough) are acquired, by each camera, before switching on the pump. These images are used to find the coordinate transforms that can be used to find real world coordinates from pixel coordinates. Figure 11.11 shows examples of the calibration images. Detailed experimental procedure is provided in Appendix G.

Figure 11.11: Examples of calibration images (left: Milesight camera, right: GoPro camera)

After all experimental data were gathered different response surface models are prepared according to reconciled data.

Stellenbosch University https://scholar.sun.ac.za

11.3. Interface sensor placement

11.3.1. Nonlinear data reconciliation

Data reconciliation (see Section 9.3) of different combinations of measured and unmeasured variables (flow rates, solids fractions and grades of process streams in the Rowland plant primary circuit) will be used in the optimal sensor placement algorithm. This data reconciliation step is also useful to an optimal interface placement algorithm because it quantifies how redundancy in a sensor network may improve variable estimation (leading to possibility of updating and improving estimation precision).

The weighted least squares objective function (Equation 9.16) from Section 9.3 and the process model and measurement models (Equations 3.9 & 3.10 from Chapter 3) must be modified to suit the interface sensor placement problem. Equation 11.23 gives the measurement vector and Equation 11.24 gives the non-linear equations for the spiral plant mass balance (the process model in this case).

$$Y = X + e; e \sim \mathcal{N}(0, V_e) \qquad \text{(Eq. 11.23)}$$

$$z(X) = 0 \qquad \text{(Eq. 11.24)}$$

Where:

- It is assumed the different entries of Y are independent. Therefore, off-diagonal entries of V_e are zero.

Equation 11.23 can be substituted into Equation 3.11 (from Chapter 3) to form the objective function in Equation 11.25. More precise estimates $\hat{X}$ can be obtained by minimising Equation 11.25 using Lagrange multipliers when constraints are linear (see Equation 3.12).

$$J = (Y - X)^T V_e^{-1} (Y - X) \qquad \text{(Eq. 11.25)}$$

Equation 11.24 must be linearized about a point X_s in order to derive an analytical solution to Equation 11.25. The linearized process model, approximating $z(X)$ around X_s, can be expressed using Equation 11.26. $\nabla z(X_s)$ represents the Jacobian of $z(X)$ evaluated at X_s and can be expressed by Equation 11.27.

$$z(X_s) + \nabla z(X_s) \cdot (X - X_s) = 0 \qquad \text{(Eq. 11.26)}$$

$$\nabla z(X_s) = \begin{bmatrix} M & 0 & 0 \\ M \odot \begin{bmatrix} X_2^T \\ X_2^T \\ X_2^T \\ X_2^T \end{bmatrix} & M \odot \begin{bmatrix} X_1^T \\ X_1^T \\ X_1^T \\ X_1^T \end{bmatrix} & 0 \\ M \odot \begin{bmatrix} X_2^T \odot X_3^T \\ X_2^T \odot X_3^T \\ X_2^T \odot X_3^T \\ X_2^T \odot X_3^T \end{bmatrix} & M \odot \begin{bmatrix} X_1^T \odot X_3^T \\ X_1^T \odot X_3^T \\ X_1^T \odot X_3^T \\ X_1^T \odot X_3^T \end{bmatrix} & M \odot \begin{bmatrix} X_1^T \odot X_2^T \\ X_1^T \odot X_2^T \\ X_1^T \odot X_2^T \\ X_1^T \odot X_2^T \end{bmatrix} \end{bmatrix} \cdot \begin{bmatrix} X_1 \\ X_1 \odot X_2 \\ X_1 \odot X_2 \odot X_3 \end{bmatrix} \qquad \text{(Eq. 11.27)}$$

Stellenbosch University https://scholar.sun.ac.za

Where:

- X_1 is the vector of process stream flow rates.
- X_2 is the vector of process stream solids fractions.
- X_3 is the vector of process stream HM grade.
- The $\odot$ operator represents the element-wise product.

The shape and entries of the connectivity matrix M (in Equation 11.27), for the primary circuit, is provided in Table 11.5. Note that the spiral bank designations and process streams number from Figure 4.8 (presented in Section 4.4) is used to setup M.

Table 11.5: Primary circuit connectivity matrix

	Process stream											
Spiral bank	1	2	3	4	5	6	7	8	9	11	12	13
E-101	1	-1	-1	0	0	0	0	0	0	0	0	0
E-102	0	1	0	-1	-1	0	0	0	0	1	0	0
E-103	0	0	0	1	0	-1	-1	0	1	0	1	0
E-104	0	0	0	0	0	1	0	-1	-1	0	0	1

Equations 11.23 to 11.27 are valid for a system where the variables of all process streams are measured. When different sensor placements are investigated and the number of redundant measurements should be reduced it becomes necessary to decouple the unmeasured variables X_U from the measured variables X_M in the overall variable vector X. Decoupling of unmeasured variables requires manipulation of Equation 11.26 by first rewriting $\nabla z(X_s)X$ as $\nabla z_U(X_s)X_U + \nabla z_M(X_s)X_M$ and then finding the matrix A that when multiplied by $\nabla z_U(X_s)$ gives $A\nabla z_U(X_s) = 0$ (where $\nabla z_U(X_s)$ has size $m_U \times n_U$ with $m_U \geq n_U$). The required matrix A is obtained by performing QR_A decomposition, shown by Equation 11.28, on the matrix $\nabla z_U(X_s)$ (Romagnoli, & Sánchez, 2000: 53).

$$\nabla z_U(X_s)E_p = QR_A \qquad \text{(Eq. 11.28)}$$

Where:

- Q is an orthogonal matrix so that $Q^T = Q^{-1}$ with size $m_U \times m_U$.
- R_A is usually an upper triangular matrix with size $m_U \times n_U$.
- E_p is a permutation matrix.

A can be found by inspecting the matrices Q and R_A which equals $[Q_1 \quad Q_2][\begin{matrix} R_{A,1} & R_{A,2} \\ 0 & 0 \end{matrix}]$ when unobservable variables are present in a system. Q_1 is a matrix of size $m_U \times r_U$ (where $r_U = rank(\nabla z_U(X_s))$), Q_2 is a matrix with size $m_U \times (n - r_U)$ (where n is the number of columns in

Stellenbosch University https://scholar.sun.ac.za

$\nabla z(X_s)$) and $R_{A,1}$ is strictly an upper triangular matrix. $R_{A,2}$ corresponds to the unobservable variables in a system. The matrix Q_2^T is the desired matrix A and decouples the measured from the unmeasured variables in Equation 11.26 (Romagnoli, & Sánchez, 2000: 56).

The data reconciliation optimisation problem (using linearized constraints) for different sensor placement strategies can then be stated by the following:

$$\min_X J = (Y - X)^T V_e^{-1} (Y - X)$$

s.t.

$$Q_2^T \nabla z_M(X_s) X_M = Q_2^T (\nabla z(X_s) X_s - z(X_s))$$

The solution to Equation 11.25 will have the same form as Equation 3.13. but will only provide new estimates for the measured variables X_M. Expressions for P_1 and P_2 is given by Equations 11.29 and 11.30. Unmeasured variables X_U can be estimated using Equation 11.31. New variance estimates cannot be obtained for the unmeasured variables.

$$P_1 = I - V_e\left(A\nabla z_M(X_s)\right)^T \left(A\nabla z_M(X_s) V_e \left(A\nabla z_M(X_s)\right)^T\right)^{-1} (A\nabla z_M(X_s)) \qquad \text{(Eq. 11.29)}$$

$$P_2 = V_e\left(A\nabla z_M(X_s)\right)^T \left(A\nabla z_M(X_s) V_e \left(A\nabla z_M(X_s)\right)^T\right)^{-1} A(\nabla z(X_s) X_s - z(X_s)) \qquad \text{(Eq. 11.30)}$$

$$X_U = R_{A,1}^{-1} Q_1^T (\nabla z(X_s) X_s - z(X_s) - \nabla z_M(X_s) X_M) + R_{A,1}^{-1} R_{A,2} u_{n_U - r_U} \qquad \text{(Eq. 11.31)}$$

Where:

- u_{n-r_U} is the vector of unobservable variables.

Equation 11.31 is valid when observable and unobservable variables are present in the considered system. The values of unobservable variables can be set to zero when no information is available or equal to the nominal values. New variance estimates can be obtained for the measured variables by substituting P_1, from Equation 11.29, into Equation 3.14. Because the linearized process model (Equation 11.26) is used as constraints when optimizing Equation 11.25 a global optimum will not be reached. An iterative approach is required to find the optimum $\hat{X}$ by repeating optimization of Equation 11.25 by substituting previous step $\hat{X}$ values into X_s for every following optimization step. Variance estimates can be obtained after convergence of the successive linearization steps. Convergence is achieved when differences in successive $\hat{X}$ values or differences in successive $z(\hat{X})^T z(\hat{X})$ values reach some tolerance.

11.3.2. Sensor placement monitoring performance

One goal of optimal sensor placement is the rather trivial requirement that the instrumentation cost J_C be minimised. Cost reduction must be paired with some monitoring performance measure in order to

Stellenbosch University https://scholar.sun.ac.za

distinguish performance of different sensor configurations (with the same number of sensors). In literature (Bagajewicz, 2002: 6) sensor network performance is usually given by some measure of estimability. Such performance measures are well suited for minimum estimation network design for plants, where the least number of sensors are found that allows estimation of every plant variable. However, when minimum estimability is not relevant, and more focus on a single type of sensor is required, the network performance functions must be altered.

As mentioned in Section 3.5 a revenue based plant performance is well suited to optimal sensor placement for metallurgical plants. If appropriate plant performance functions are available, a monitoring performance objective can be derived using the variance operator. Equation 11.32 gives a performance function that compares measured and estimated value of MOI in plant concentrate (by using the 8th entries of vectors X_1, $\hat{X}_1$, X_2, $\hat{X}_2$, X_3 & $\hat{X}_3$).

$$\mathcal{P} = P_{Cr}(X_{s,1,8}X_{s,2,8}X_{s,3,8} - \hat{X}_{1,8}\hat{X}_{2,8}\hat{X}_{3,8}) \qquad \text{(Eq. 11.32)}$$

Where:

- P_{Cr} is the value (in \$/t) of MOI.

Applying the variance operator to Equation 11.32 results in (assuming $Cov\left(X_{s,1,8}X_{s,2,8}X_{s,3,8}, \hat{X}_{1,8}\hat{X}_{2,8}\hat{X}_{3,8}\right) = 0$):

$$Var(\mathcal{P}) = P_{Cr}^2 Var\left(X_{s,1,8}X_{s,2,8}X_{s,3,8} - \hat{X}_{1,8}\hat{X}_{2,8}\hat{X}_{3,8}\right)$$

$$Var(\mathcal{P}) = P_{Cr}^2 \left(Var\left(X_{s,1,8}X_{s,2,8}X_{s,3,8}\right) + Var\left(\hat{X}_{1,8}\hat{X}_{2,8}\hat{X}_{3,8}\right)\right)$$

The variance of the performance is effectively the difference between measurement variance and estimation variance of MOI value in the concentrate stream. Optimal sensor configurations should result in lower $Var\left(\hat{X}_{1,8}\hat{X}_{2,8}\hat{X}_{3,8}\right)$ which will lead to minimization of $Var(\mathcal{P})$. A reasonable monitoring objective is then Equation 11.33.

$$J_L = P_{Cr}^2 Var(\hat{X}_{1,8}\hat{X}_{2,8}\hat{X}_{3,8}) \qquad \text{(Eq. 11.33)}$$

An optimal sensor configuration should minimize instrumentation cost and Equation 11.33 simultaneously. From the properties of the variance operator it is known that $Var\left(\hat{X}_{1,8}\hat{X}_{2,8}\hat{X}_{3,8}\right) = \mathrm{E}\left(\left(\hat{X}_{1,8}\hat{X}_{2,8}\hat{X}_{3,8}\right)^2\right) - E\left(\hat{X}_{1,8}\hat{X}_{2,8}\hat{X}_{3,8}\right)^2$; however the $\mathrm{E}\left(\left(\hat{X}_{1,8}\hat{X}_{2,8}\hat{X}_{3,8}\right)^2\right)$ term is nonlinear and more complex to estimate. To calculate J_L it is necessary to linearize the $\hat{X}_{1,8}\hat{X}_{2,8}\hat{X}_{3,8}$ term (to avoid Monte Carlo or other sampling approximations of Equation 11.33):

$$\hat{X}_{1,8}\hat{X}_{2,8}\hat{X}_{3,8} \sim \hat{X}_{1,8,0}\hat{X}_{2,8,0}\hat{X}_{3,8,0} + \nabla\left(\hat{X}_{1,8}\hat{X}_{2,8}\hat{X}_{3,8}\right)_0 \cdot \left([\hat{X}_{1,8}, \hat{X}_{2,8}, \hat{X}_{3,8}] - [\hat{X}_{1,8,0}, \hat{X}_{2,8,0}, \hat{X}_{3,8,0}]\right)^T$$

Where:

Stellenbosch University https://scholar.sun.ac.za

- $[\hat{X}_{1,8,0}, \hat{X}_{2,8,0}, \hat{X}_{3,8,0}]$ is the point around which $\hat{X}_{1,8}\hat{X}_{2,8}\hat{X}_{3,8}$ is linearized.
- $\nabla(\quad)_0$ represents the gradient at the linearization point.

The simplified version of Equation 11.33 then becomes Equation 11.34 if the linearization point is [0,0,0]:

$$J_L = P_{Cr}^2 \nabla\left(\hat{X}_{1,8}\hat{X}_{2,8}\hat{X}_{3,8}\right) Var\left([\hat{X}_{1,8}, \hat{X}_{2,8}, \hat{X}_{3,8}]\right) \nabla\left(\hat{X}_{1,8}\hat{X}_{2,8}\hat{X}_{3,8}\right)^T \quad \text{(Eq. 11.34)}$$

J_L now matches the monitoring objective's shape as mentioned by Mazzour et al. (2003). Essentially, Equation 11.34, provides a means to determine the uncertainty in plant product quality. Higher certainty in the product quality can lead to better estimation of the amount of revenue (and time) needed to justify plant upgrades (through return of investment – per example). J_L in Equation 11.34 is only an approximation and for highly non-linear performance functions J_L can become inaccurate (especially for $\hat{X}$ values far from 0).

11.3.3. Sensor variances, cost and product value

Sensor variances, required for data reconciliation, are shown in Table 11.6 and are equivalent to the process variable variances that will be used as weights during data reconciliation. Mass flow rate and solids fraction variances are estimated from experimental values as averages of the reconciled experimental variances (See Table 18.2 in Appendix J).

Table 11.6: Initial process stream variable variances

Sensor type	Sensor variance
Mass flow rate $(t/h)^2$	0.37
Solids fraction	0.000994
Grade (online XRF)	0.001
Grade (interface model)	0.02

Online X-ray fluorescence (or XRF) analysers will be approximated as handheld XRF analysers for this study. Prices of industrial online XRF can be expected to be significantly higher. Online XRF variance for grade estimates were obtained for an Olympus Delta pro handheld XRF analyser (Michaud, 2013). Interface measurements can be used as an alternative method to estimate HM grades. For the current sensor placement analysis, the interface sensors are assumed to act as spiral concentrate stream soft sensors. Vermaak et al. (2008) suggest that interface sensors can be used to analyse feed conditions, however, in the South African spiral plant, concentrate streams are the feed streams to each spiral bank (except for the rougher spirals). Variance values are based on mean square error (MSE) values obtained from the regression analysis (relating splitter setting and interface position to concentrate grade values) shown in Appendix K.

Stellenbosch University https://scholar.sun.ac.za

Prices for flow rate, density gauges and online XRF analysers are given in Table 11.7 (in US Dollars or South African Rand). It is assumed that density gauges can serve as process stream solids fraction soft sensors. Flow rate and density gauges prices are assumed to be the same and are based on the OPTIFLUX-5000 magnetic flow rate meter by Krohne (Krohne OPTIFLUX 5000F-FL flanged Electromagnetic Flow Sensor, 2017). Final interface sensor implementation cost is determined by assuming that interface sensors must be applied to every spiral in a spiral bank - suggesting that the cost equals the number of spirals (mentioned in Section 4.4) times the interface sensor camera cost.

Table 11.7: Sensor price estimates

	USD (× 1000)	ZAR (× 1000)
Online interface sensor	0.53	7.00
Online XRF	20.00	265.20
Density gauge	3.00	39.78
Flow meter	6.00	79.56

Table 11.8 gives the chromium price per ton for the 17th of March 2017 (Ferro-chrome price, 2017). The revenue produced by the primary circuit is determined using the amount of HM in the plant concentrate stream. HM price is assumed to be equal to P_{Cr} which will be higher than the actual cost of the HM (since minerals containing Cr and other unwanted elements) but this will give reasonable initial estimates of plant revenue.

Table 11.8: Chromite market price estimates per ton of chromium/chromite

	$ (× 1000)	R (× 1000)
Chromium (or P_{Cr})	2.29	30.37
40-42 % UG2 chromite (in 2014)	0.18	2.39

The possible revenue present in the HM is affected by the mass of Cr_2O_3 (in the concentrate stream) and the grade of Cr_2O_3. In practice P_{Cr} can change based on the grade of the concentrate product. However, it is assumed, at this stage, that the price stays constant (over time and for different product grades).

11.3.4. Monte Carlo simulations

Typically in literature, the data reconciliation methods, described in Section 3.5, are applied to a single instance of plant input and (solved) output conditions. Reconciled process variables can be substituted into Equation 3.17 to determine the cost of a sensor configuration. An appropriate optimisation algorithm can be used to search the optimal sensor configuration that minimises Equation 3.17 (for different number of sensors implemented). The problem with this setup is that the

Stellenbosch University https://scholar.sun.ac.za

optimal sensor configuration is only valid for the original plant conditions and no information is obtained on the robustness of the solution. If sensor configurations can be sensitive to plant feed conditions, it will be useful to understand how optimal sensor placement would be affected.

Monte Carlo simulations of the WPL's primary circuit will be used to prepare many plant initial states for data reconciliation. Performing sensor network optimisation on each set of plant conditions should provide a method that indicates factors affecting optimal sensor placement. Different feed flow rate conditions will be sampled from a Gaussian distribution of mean equal to zero and variance equal to 1. Feed solids content and HM grade values are sampled from uniform distributions to produce numbers in the range (0, 1). Feed flow rate sample values are scaled by 60 t/h and translated by 360.0 t/h. Figure 11.12 shows 2 plots of the sampled feed conditions that will be used. Only sample points with solids fraction values in (0.05, 0.5) and HM grade values in (0.1, 0.7) were accepted (these values cover the design space of the spiral concentrators used in the WPL primary circuit – see Section 2.2).

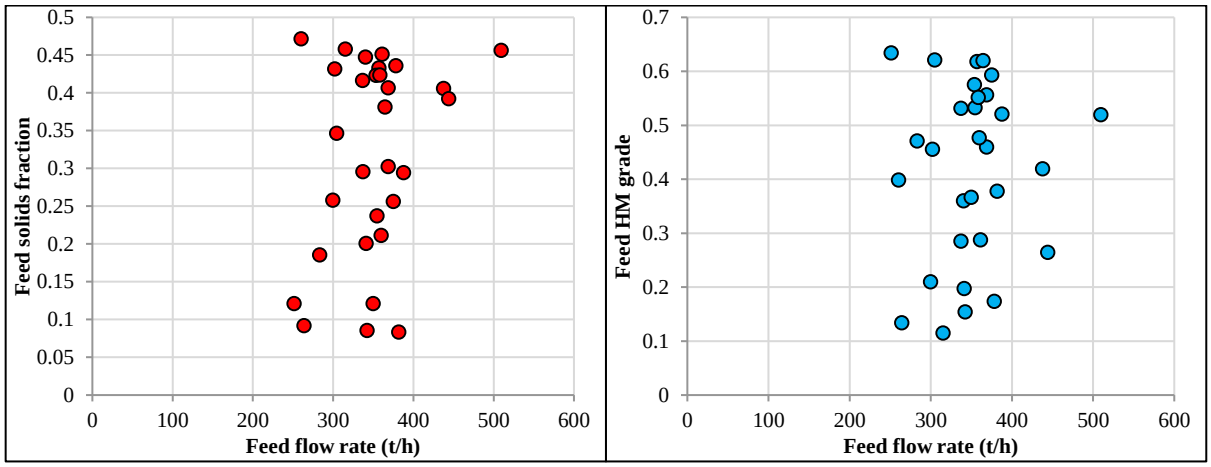

Figure 11.12: 30 sampled feed conditions for Plant I (left: feed flow rate vs. feed solids content; right: feed flow rate vs. feed HM grade)

Thirty sampling points are selected for Monte Carlo analysis. Mass balance and fraction sign checks were implemented to ensure that only valid feed points are selected. The range of the feed conditions were also selected since primary circuit simulations cannot provide valid process stream values (in terms of overall mass balances) when feed solids fraction and feed HM grade are both larger than 0.8 - the rest of the feed condition space can be reliably sampled (as in Figure 11.12).

Stellenbosch University https://scholar.sun.ac.za

12. Appendix D: Results

12.1. Interface detection for ilmenite separation

12.1.1. Algorithm CVI (GA based)

Training and testing were performed on an image set of 1300 images of ilmenite separating on a spiral trough. Image sets of sizes 50, 100, 150, 200 and 300 were randomly drawn for parameter optimization and testing was done on the remaining 500 images (not including any of the training image batches) with the parameters obtained. Training image sets do not share images, in other words the image in the training and testing sets were all captured at different times. The original images had a resolution of 1920-by-1080 and were cropped to 397-by-240, which is an area only covering the spiral trough, to reduce training time. Training was only done once per image set and computation time, generation count, training cost and the optimal parameters were saved. Results are divided between the algorithm's ability to detect middling and concentrate interfaces. Tracking middling and concentrate interfaces will provide information useful to splitter position setting.

GA optimization was performed using a population size of 500 chromosomes and the following convergence criteria:

1. Generation stall limit of 100 generations.
2. Objective function tolerance of 10^{-10}.
3. Constraint tolerances of 10^{-6}.

Convergence was achieved for every training case when the generation stall limit was reached. The GA was capable of matching the edge detection result with each labelled interface in the training runs (i.e. 100% detection of middling interfaces). Figure 12.1 summarises the average J_1 and J_2 values calculated for each training case to show robustness of the training performance with respect to training set size. J_1 gives a rough indication of how labels and interface detections overlap and J_2 indicates whether majority true positive detections were attained per pixel. Tabulated results, concerning the statistics of J_1 and J_2, is presented in Appendix I.

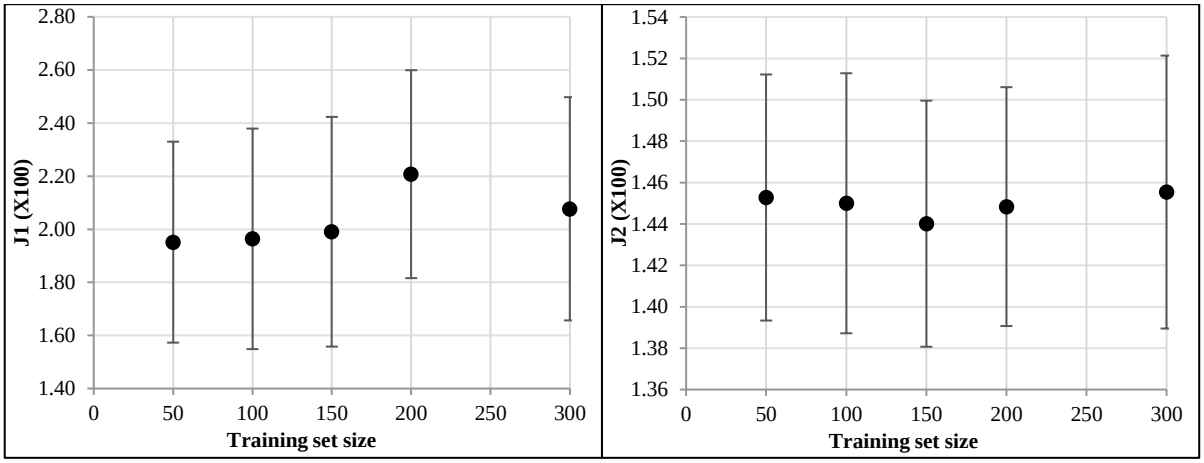

Figure 12.1: Performance function results during training of Algorithm CVI (GA based) on ilmenite image sets of different sizes (middling case; error bars represent variation by $1 \times \sigma$ *based on n = 50, 100, 150, 200 and 300 samples)*

A single edge detection (corresponding to a single interface detection response) was obtained for each image at each training case (no additional spurious interface detections were present). All mean J_1 and J_2 values are positive indicating that the majority of interface detections are true positive. Similar values were obtained for J_1 and J_2 (Equations 4.1 & 4.2) for each training case with mean J_2 between 1.44 and 1.46, and mean J_1 between 1.95 and 2.22. Similar variances across training images were found for each case suggesting similar training quality. This result indicates robustness of training performance to training set size. Training on the 200 and 300 image set had significantly higher J_1 values and training on the 150 image set had the lowest J_2 value.

Training time and generation count for training on each image set is reported in Table 12.1. Typical training time that can be expected will extend over 70 hours and can run to over 120 hours. Larger image sizes are likely to have a longer duration than the maximum value in Table 12.1. This result is undesirable and training times must be decreased to improve the rate at which interface detection algorithms can be prepared especially if hyperparameters must be optimized (by way of repeated training runs) in the future.

Table 12.1: GA training time (ilmenite, middlings case)

Training set (number of images)	Generation count	Training time (h)
50	396	72.74
100	466	124.44
150	396	72.74
200	466	124.44
300	177	65.34

Stellenbosch University https://scholar.sun.ac.za

Training to detect concentrate interfaces is essentially the same as for the middling case, except that a smaller chromosome population is used. 50 chromosomes are used instead of 500 in an attempt to significantly reduce optimization time of the GA. The same convergence criteria were used and the same training image sets. Figure 12.2 shows the mean J_1 and J_2 values obtained after training with successful convergence (tabulated results are presented in Appendix I). Training on image sets of size 50 and 100 yield similar results with training on sets 150, 200 and 300 showed significant deviation from the other training runs.

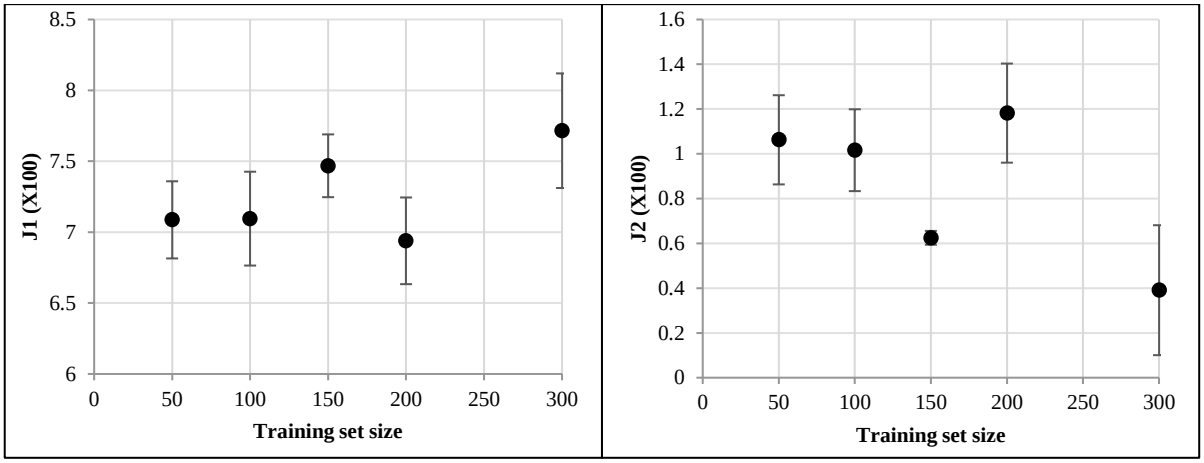

Figure 12.2: Training on image sets of different sizes (ilmenite concentrate case; error bars represent variation by $1 \times \sigma$ *based on n = 50, 100, 150, 200 and 300 samples)*

The variation in training performance, for concentrate interface detection, can be explained – in part- by the amount of edges detected by the trained algorithm. Figure 12.3 shows the differences in interface detection performance between each training case. Only training on the 150 image set resulted in a parameter set capable of delivering interface detection performance similar to the middling interface detection case.

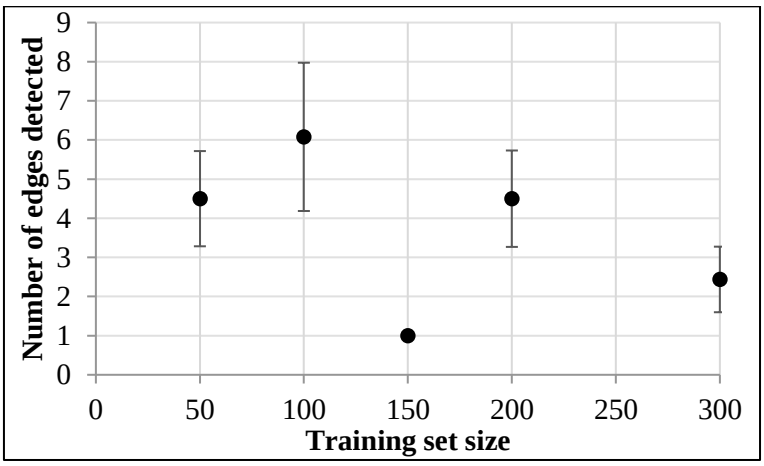

Figure 12.3: Resulting edge detections for ilmenite concentrate interface detection (error bars represent variation by $1 \times \sigma$ *based on n = 50, 100, 150, 200 and 300 samples)*

Stellenbosch University https://scholar.sun.ac.za

All other training instances (shown in Figure 12.3) have average number of detections higher than 2 with standard deviations larger than 0.8 edge detections. Figure 12.3 shows that additional, and even spurious, edge detections are allowed by the GA based approach as long as the additional edge detections are made in close proximity to the interface label (which is an undesired property of an interface detector). Training time (Table 12.2) for the concentrate case is considerably shorter due to the use of fewer chromosomes in the GA population. Convergence can be achieved in less than 6 hours (instead of less than 80 h) with similar numbers in generation counts. On larger image sets training times reaching over 14 h can still be expected – with longer generation counts.

Table 12.2: GA training time (ilmenite, concentrate case)

Training set (number of images)	Generation count	Training time (h)
50	308	1.32
100	228	1.98
150	340	4.77
200	275	5.25
300	519	14.46

Different sets of optimal parameters were obtained for each training case of Algorithm CVI. The value determined for H_E was 1 in all parameter sets (allowing the use of histogram equalization). Figure 12.4 gives the visual summary for parameter values obtained in each training run (in the ilmenite middling case) to determine the allowable parameter values that result in optimal interface detections. Figure 12.4 also investigates whether training set size affects the values of the optimal parameters. If parameters remain invariant over training set size then smaller training sets are appropriate for the training of an interface detector.

Scaling values for the green and blue channels (g and b) were smaller than for the red channel (r) for each training case. Median filter sizes are 3 or 4 for each optimization case and 49 or 55 histogram bins are selected except for the 300 image training run that selected 2 histogram bins. For edge detection the Gaussian kernel standard deviation σ_G selected was 6.4 or 5.6 except for the final case where 2.2 was selected. T_2 higher than 0.9 was selected for each case and T_1 is smaller than 0.51 for each case. Perimeter and orientation parameters all attain 1 of two different values except for the 300 image set training case.

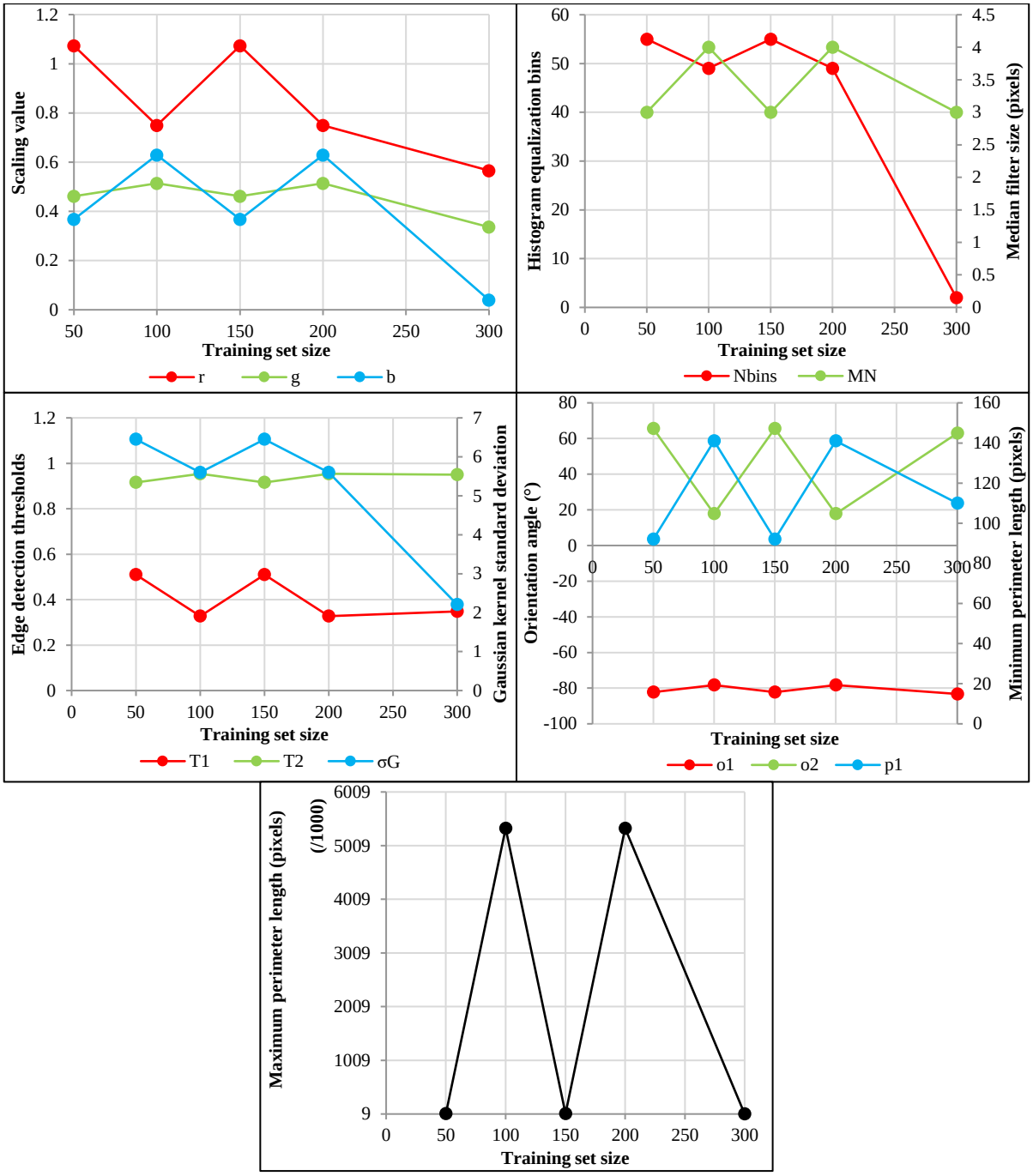

Figure 12.4: Variations in trained parameters for the GA-based Algorithm CVI (ilmenite, middling case)

From Figure 12.4 it appears that optimal interface detection on training image sets larger than 300 will require lower r, g and b values, less histogram equalization bins and smaller Gaussian smoothing kernels.

Training Algorithm CVI for concentrate detection also produced sets with different levels for parameters in each case. All optimised parameters are visualised in Figure 12.5 in a similar way to Figure 12.4. Significant differences between the optimal middling and concentrate detection parameters can be seen in each of the frames in Figures 12.4 & 12.5. The 100, 150 and 200 image set

training cases selected negative values for either g or b. Concentrate interface detection also uses less intensity histogram bins (N_{bins}) and larger median filtering neighbourhoods (M_N). Values p_2 are also much lower for concentrate interface detection.

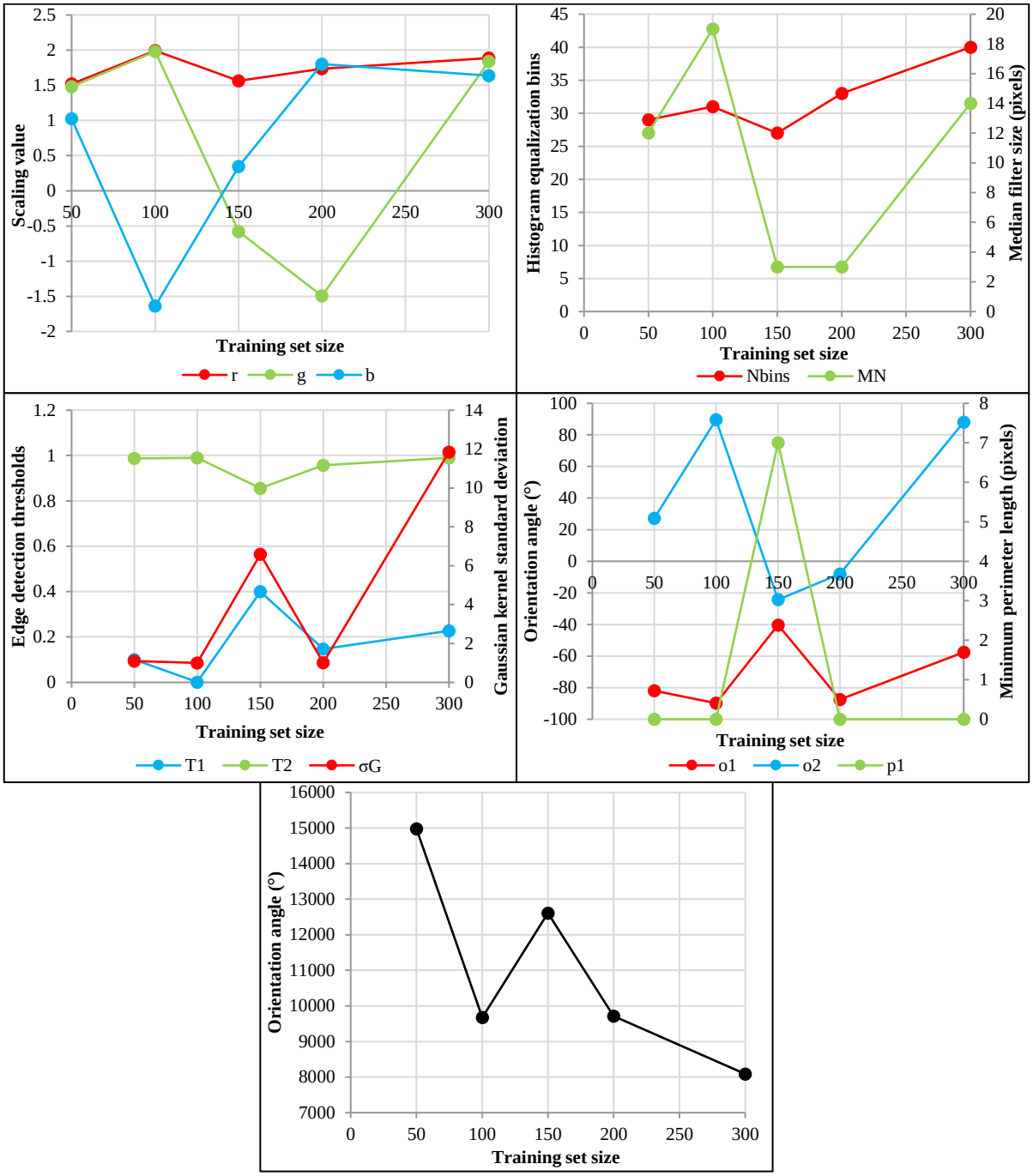

Figure 12.5: Variations in trained parameters for the GA-based Algorithm CVI (ilmenite, concentrate case)

No clear trends can be concluded from Figure 12.5. Repeated training instances, of Algorithm CVI, are required to make any potential trends in Figures 12.4 and 12.5 clear.

Testing was performed using parameters from each training run to determine concentrate and middling interface detection on "new" images. Values for J_1 and J_2 were also recorded for middling

Stellenbosch University https://scholar.sun.ac.za

and concentrate interface detection cases to determine mean and standard deviation values for each performance function. Figures 12.6 & 12.7 summarise the performance of the optimised parameters for Algorithm CVI (tabulated results are presented in Appendix I). Testing for middling interface detection yielded higher J_1 and lower J_2 mean values. Variance of J_2 values (over every training image) was higher for testing than training; however, testing variances for J_1 is similar to the training case.

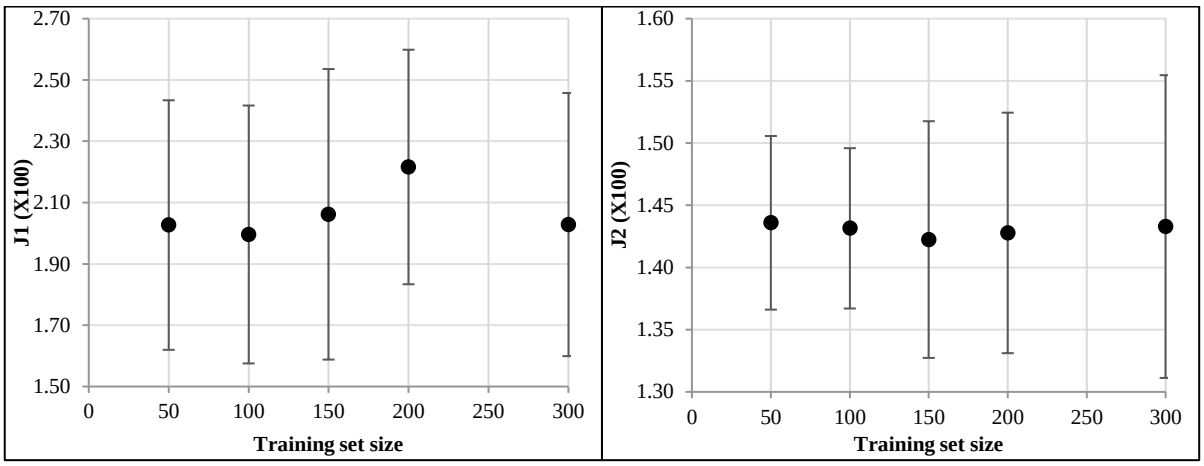

Figure 12.6: Performance function results during testing of Algorithm CVI (GA-based) with optimal parameter sets (ilmenite, middling case; error bars represent variation by $1 \times \sigma$ *based on n = 500 samples)*

It is expected that trained algorithms (especially in the case of statistical classifiers) will not perform as well on testing sets as on training sets. The lower values of J_2 is due to spurious detections and poor localization. However, testing performance appears invariant to training set size in Figure 12.6. This suggests that training on smaller image sets is appropriate for the ilmenite middling interface detection case.

Edges detected by the optimised middling interface detectors are summarised in Table 12.3. The clear majority of detections were single interface detections with training on the 100 image set delivering parameters with the best performance. Testing parameters obtained from training on the 150 image set had 7 instances of multiple interface detections and parameters from the 300 image set training case had instances where no detections are made.

Stellenbosch University https://scholar.sun.ac.za

Table 12.3: Number of middling interface detections (ilmenite case, GA-based Algorithm CVI testing)

Training set size (number of images)	None	One	Two
50	0	499	1
100	0	500	0
150	0	493	7
200	0	498	2
300	2	497	1

Performance from testing parameters for concentrate interface detection is generally more varied and lower compared with the middling case. Parameters obtained from the 150 image set training instance outperformed the other training runs (as expected from the training results since it was the only training case that delivers single concentrate interface detections for every testing image). The 100 image set training case delivered the worst testing results due to having the lowest mean J_2 due to only partial interface detections.

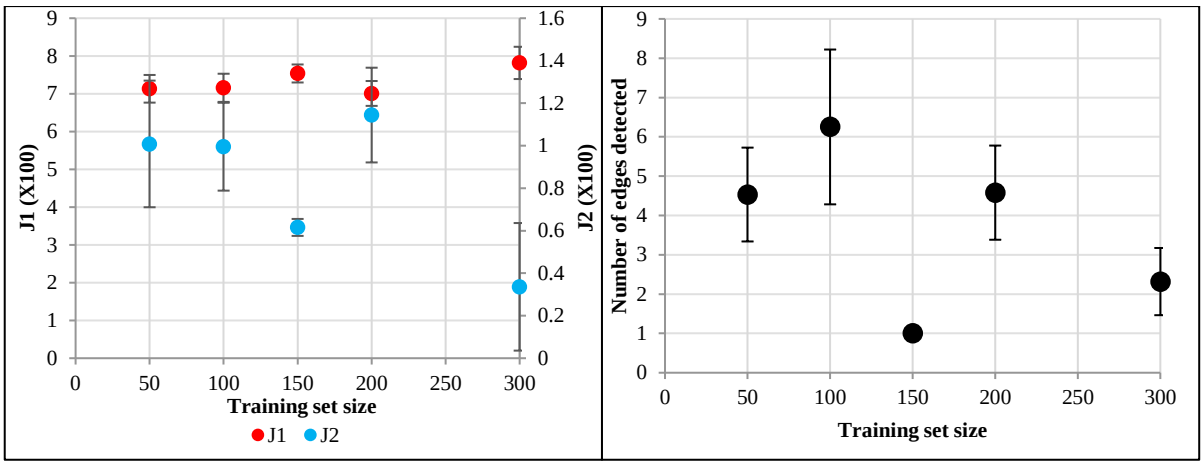

Figure 12.7: Performance function results during testing of Algorithm CVI (GA-based) with optimal parameter sets (ilmenite, concentrate case; error bars represent variation by $1 \times \sigma$ based on n = 500 samples)

Sensitivity analysis of middling interface detection was performed by varying parameters, from the 100 image set training case, by 10% (the 500 image testing set was used to find J_2 values). Parameters most sensitive to change were r (red channel scaling parameter), p_1 (lower connected component perimeter threshold) and H_E (Histogram equalization activator) and the results are graphically shown in Figure 12.8. For middling interface detection (in the case of ilmenite separation) histogram equalization is essential and significantly influences the detection performance. Reducing the value in p_1 and increasing the value of r increases uncertainty in middling interface detection.

Figure 12.8: Sensitive parameters for ilmenite middling interface detection (error bars represent variation by $1 \times \sigma$ based on n = 500 samples)

Figure 12.9 shows example ilmenite images and how middling interface detection changes when the significant parameters (Figure 12.8) varies. Change in the p_1 can allow spurious additional edge detections and change in H_E can lead to completely unsuccessful interface detections.

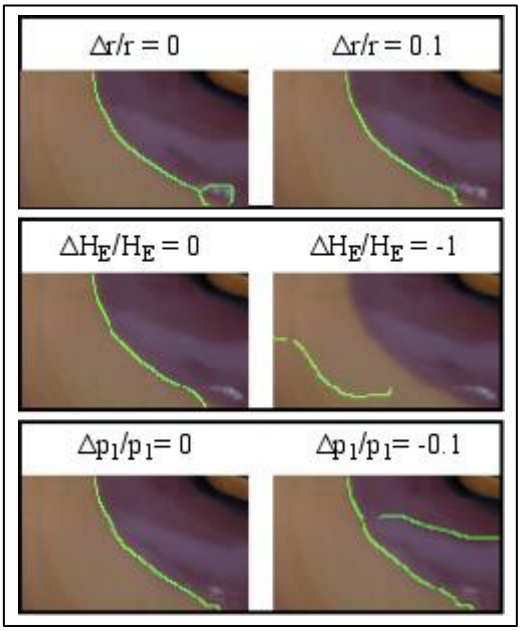

Figure 12.9: Change in ilmenite middling interface detection during sensitivity analysis

Similar sensitivity analysis was done to determine the most sensitive image processing variables for concentrate interface detection. Parameters obtained from training on the 150 image set were tested on the 500 image set as parameters were varied, one by one, by 10% or -10%. In the case of histogram equalization the variable was just switched to 0 and integer parameters were rounded. If a rounded integer parameter did not produce a different integer the integer was subtracted by one or added to one. The most sensitive parameters were H_E, σ_G (Gaussian smoothing kernel standard deviation), T_2 (Canny edge detector threshold) and o_1 (lower connected component orientation threshold) which is more variables than in the middling interface case. Results are visually compared in Figure 12.10.

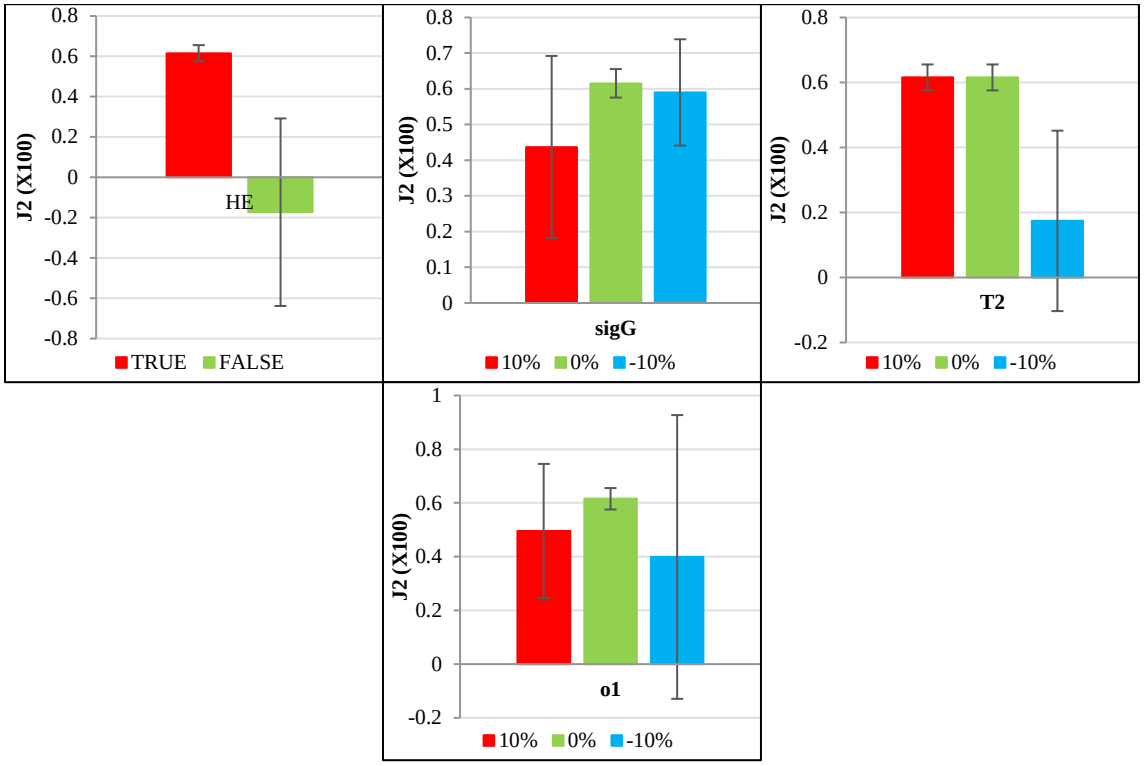

Figure 12.10: Sensitive parameters for ilmenite concentrate interface detection (error bars represent variation by $1 \times \sigma$ *based on n = 500 samples)*

Change in H_E showed the most pronounced effect on Algorithm CVI's performance. T_2 is only sensitive to a decrease from the optimal value; however, this results in it being the second most sensitive parameter. σ_G and o_1 reduces performance when increased or decreased and variance in interface detections are significantly effected in each case. Figure 12.11 visually compares the differences when sensitive parameters are varied. Changes in σ_G, T_2 and o_1 can lead to the case where no interface detection is made. Changing H_E can lead to spurious edge detections or even false concentrate interface detections (similar to the ilmenite middlings interface detection case).

Stellenbosch University https://scholar.sun.ac.za

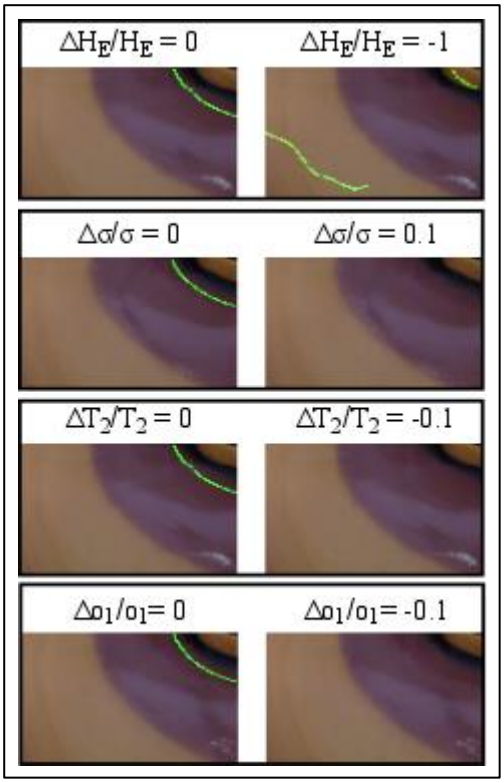

Figure 12.11: Change in ilmenite concentrate interface detection during sensitivity analysis

The GA-based interface detection algorithm (Algorithm CVI) was applied to the ilmenite concentrate and middling interface detection problems. Convergence was achieved for every training case and both interfaces can be identified by Algorithm CVI (after optimisation). Middling interface detection is more robust than concentrate interface detection and less spurious edge detections are produced for the middling interface detection case. Training time of Algorithm CVI can be significantly reduced with the use of smaller chromosome populations (Table 12.2) but still takes several hours for training sets larger than 300 images.

12.1.2. Algorithm CVII (Logistic regression based)

Algorithm CVII was trained and tested using the same image sets as in the case of Algorithm CVI. The same descriptive statistics were recorded; however, additional emphasis is placed on recall and precision of the trained logistic classifiers. Logistic regression was also performed with regularisation (Equations 11.16 & 11.17) and the optimal regularisation parameter λ was determined using 10-fold cross-validation (the range of λ was $[0, 10] \in \mathbb{Z}$). No mixed or quadratic terms were included in the feature set to allow optimisation of linear parameters. Optimisation was stopped when either of the following conditions were met:

- A maximum of 100 iterations were reached.
- Objective function tolerance of 10^{-7} is reached.

Features and labels were converted to single floating point precision (to reduce memory demands) before being passed to the conjugate gradient based optimisation algorithm. Convergence was

Stellenbosch University https://scholar.sun.ac.za

achieved for each training case and optimised parameters, training time along with optimal λ were recorded. The optimal λ was selected based on the F statistic calculated for each cross-validation iteration (this also selects the optimal parameters to be saved for later interface detection).

The optimal λ was 0 for each training case – meaning λ = 0 delivers the maximum F-statistic value (see Appendix I for graphs of the cross-validation results). Precision and recall, of each training case, were determined using the standard decision boundary of 0.5 and also a higher decision boundary of 0.99 (practically this implies a reduction in false positive detection rate). Figure 12.12 summarises the ilmenite middling slurry detection performance for each training case. The standard decision boundary ($P(y = 1|x, \alpha) > 0.5$) provides improved recall performance that is also less sensitive to particular training image sets used compared to a higher decision boundary; however, the converse is true for precision performance. This result is an indication that less false positive slurry detections are made with a higher decision boundary (which increase precision if the number of true positives remain constant). A higher decision boundary gave an overall superior F-statistic performance that is much more stable across over training on different image sets.

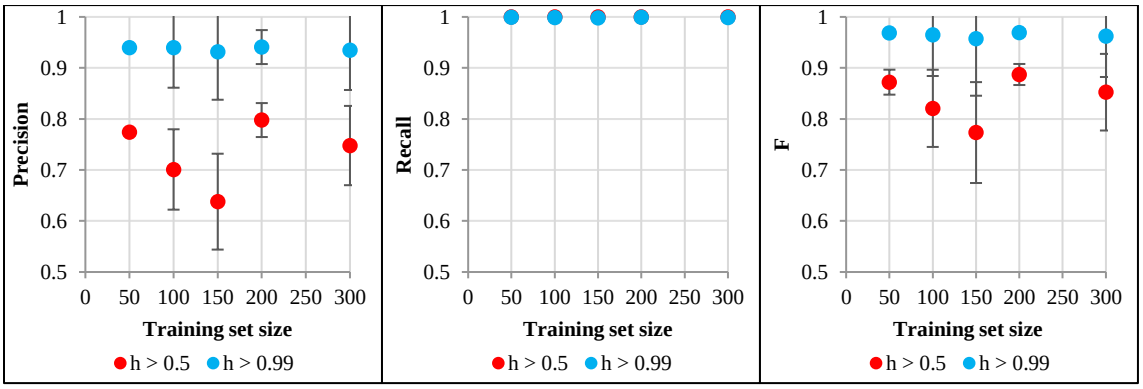

Figure 12.12: Precision, recall and F-statistc for logistic classifier training, ilmenite middling case (error bars represent variation by $1 \times \sigma$ based on n = 50, 100, 150, 200 and 300 samples)

Optimised parameters obtained from each training run are presented in Figure 12.13. Parameters obtained between training runs show similar values (expected from logistic regression convergence to global optimum) but no trend can be observed on how a particular image set changes parameter values compared to parameters obtained from a different training set. The most similar parameter, between all training instances, is the bias term which has a mean of -8.57 with a standard deviation of 0.55. All other parameters showed more variation between training cases.

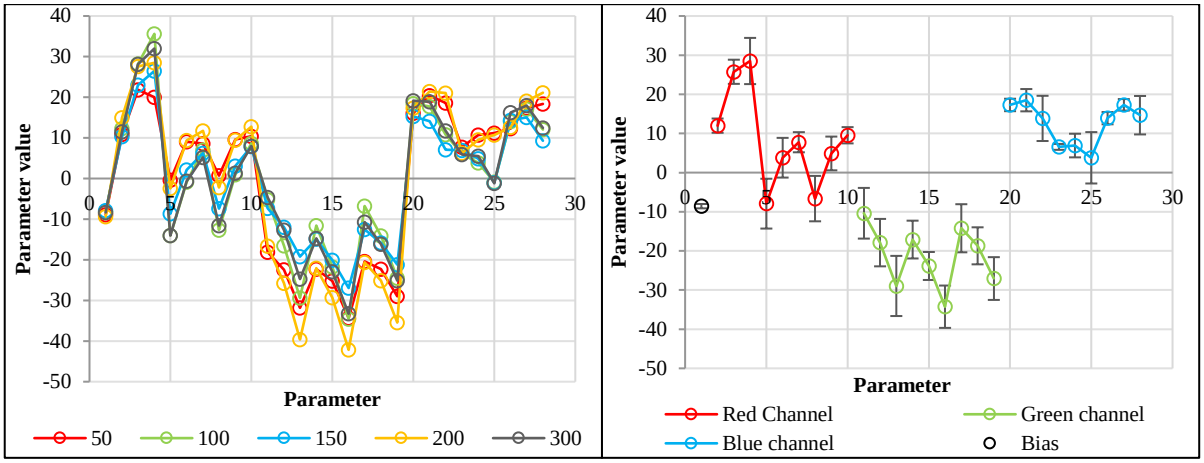

Figure 12.13: Left: optimal parameters from logistic regression for each training set, right: averaged optimal parameters (ilmenite case, error bars represent variation by $1 \times \sigma$ *based on n = 5 replicates)*

The optimal logistic regression parameters can be visualized as three convolution channels when the bias term is excluded (there is only one bias term per parameter set - not per channel). Figure 12.14 presents the visualization of the kernels and the channels they should be convolved with. The red channel kernel resembles a diagonal edge detector, the green channel kernel is similar to a horizontal edge detector and the blue channel kernel acts as a vertical edge detector.

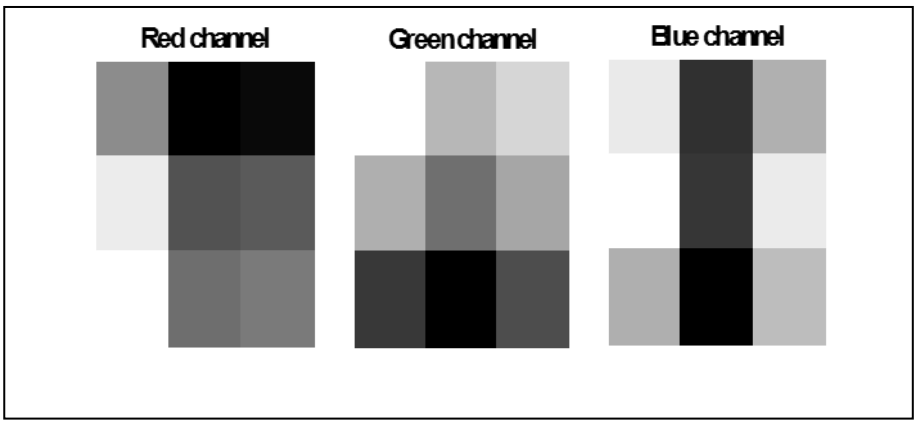

Figure 12.14: Convolution kernels for red, green and blue channels (obtained from mean parameter values plotted in Figure 12.13)

Training times for logistic regression ranged between 1 minute and 7 minutes per optimization run (there were 110 optimization runs for each training case to find optimal λ). A linear increase in training time can be seen when the amount of training images is increased from 50 to 200. Training on the 300 image training set is less than 10 seconds longer than the 200 image set training instances. Since the maximum amount of iterations is limited to 100 this means that fewer iterations were necessary and the objective tolerance limit is reached earlier. Training time is graphically presented in Figure 12.15.

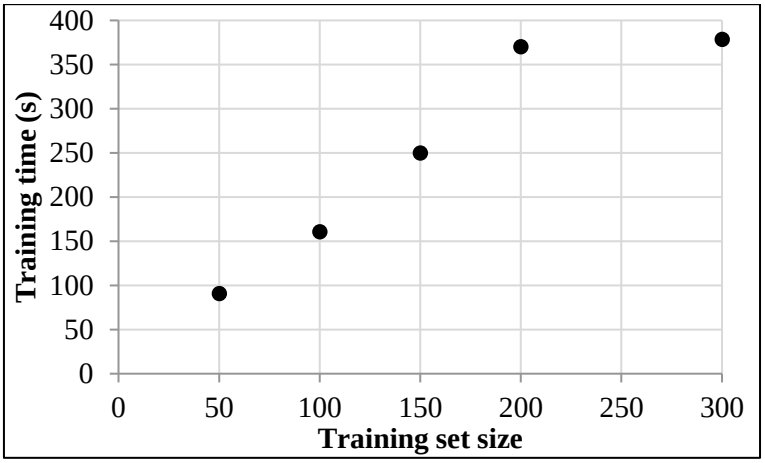

Figure 12.15: Logistic regression training times for ilmenite slurry detection case

Slurry detection performance of the trained logistic classifiers were tested on the same 500 image set used to test Algorithm CVI. Recall, precision and F-statistics were recorded similar (for each training case's testing performance) to the training step and results are shown in Figure 12.16. Slightly decreased performance can be observed in precision, recall and the F-values for testing; however, testing with the 100 and 150 image training sets' parameters showed improved performance in terms of precision. This also influenced the F values which also increased for the 100 and 150 image training case. Testing using the higher decision boundary of 0.99 also showed improved performance over use of the standard decision boundary.

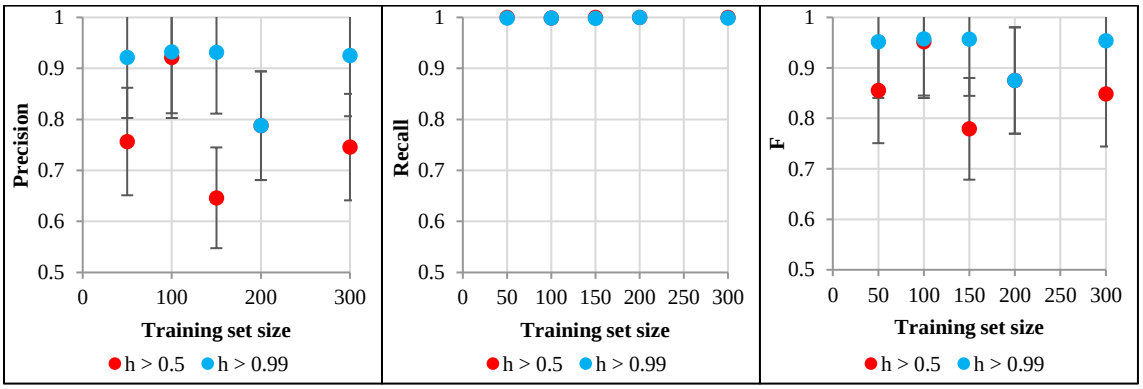

Figure 12.16: Precision, recall and F-statistc for logistic classifier testing (ilmenite case, error bars represent variation by $1 \times \sigma$ based on n = 50, 100, 150, 200 and 300 samples)

Middling and concentrate interfaces were detected using the methods outlined in Section 11.1.5 and was evaluated on training and testing sets. The decision boundary used to detect middling slurry is $h = 0.99$ - which produces the segmentation needed to extract middling and concentrate interfaces. J_1 and J_2 middling interface detection values were recorded for testing (2nd frame) and training (1st frame) and is shown in Figure 12.17 (tabulated results are presented in Appendix I). Results for mean J_2 values are similar on the training and testing sets; however, variance increases when middling

interfaces are detected on the testing images. J_1 results across training and testing images do not show significant differences except that mean J_1 values slightly decrease over testing images.

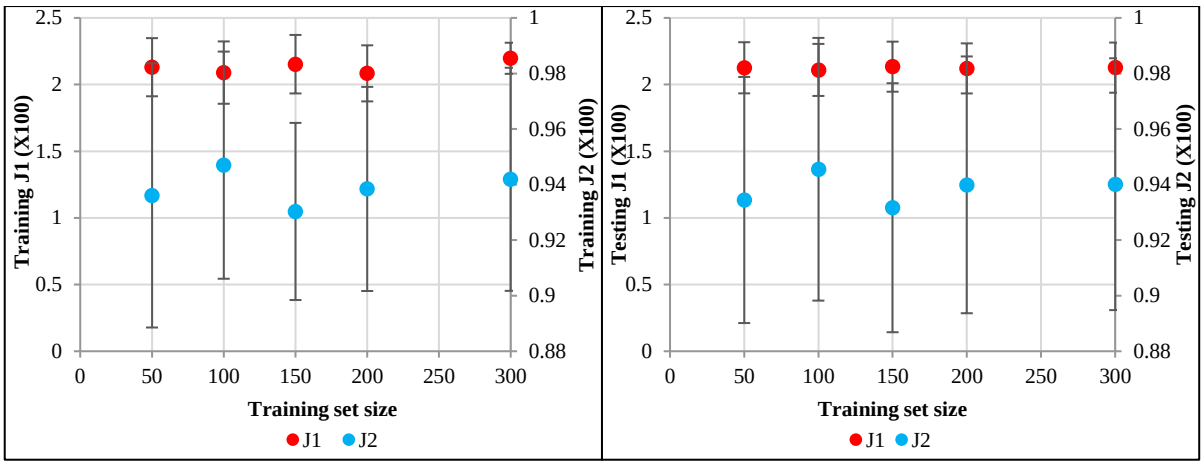

Figure 12.17: Ilmenite middling interface detection results on training (left) and testing (right) sets (Algorithm CVII, error bars represent variation by $1 \times \sigma$ *based on n = 50, 100, 150, 200 and 300 samples for training and n = 500 samples for testing)*

J_1 and J_2 values for concentrate interface detection also remained similar across testing and training images. J_1 variance across testing images is significantly increased and J_2 variance slightly increased over the testing images. Results are visually reported in Figure 12.18 (1st frame is for training and the 2nd for testing – tabulated results reported in Appendix I).

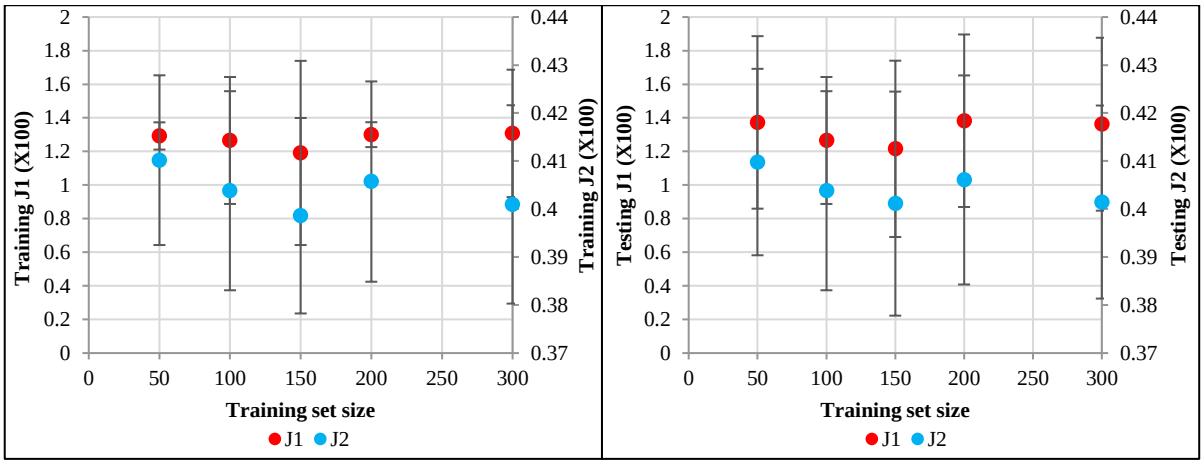

Figure 12.18: Ilmenite concentrate interface detection results on training (left) and testing (right) sets (Algorithm CVII, error bars represent variation by $1 \times \sigma$ *based on n = 50, 100, 150, 200 and 300 samples for training and n = 500 samples for testing)*

Figure 12.19 gives example images of the ilmenite slurry and interface detections that Algorithm CVII can perform after training. In the middle frame of Figure 12.19 there is a spot that was not classified as middlings slurry, however, Algorithm CVII can produce accurate and precise interface detections when most of the correctly classified pixels are located on and next to the interfaces.

Stellenbosch University https://scholar.sun.ac.za

Figure 12.19: Ilmenite slurry (middle), middling interface and concentrate interface (right) detection using Algorithm CVII ($\alpha = 0.99$)

The logistic regression based Algorithm CVII was applied to the ilmenite middling and slurry problem. Optimised parameters were obtained for each training case and middling and concentrate interfaces can be detected in each testing case (with only one interface response produced per image). Algorithm CVII produces lower mean J_2 values than Algorithm CVI but has lower variance. Algorithm CVI was capable of producing higher J_2 values because it allows more than 1 interface response. Training time for Algorithm CVII is significantly lower than for Algorithm CVI and also only required one training instance to produce the slurry detection needed to track middling and concentrate interfaces.

12.2. Experimental results and spiral modelling

12.2.1. Analysis of experimental design levels

Experimental work was concluded with a total of 29 runs being executed. The 28th run was a repeat of run 1 because preliminary analysis showed significant deviation from planned experimental levels. Run 29 will serve as a confirmation run. All experimental factors show some deviation from the standard orthogonal design levels except for splitter settings which were assumed to be perfectly attained at each run. Figure 12.20 gives the residuals for the centered experimental levels (for the first three factors) to investigate any potential blocking effects (ideal experimental levels should yield zero values for residuals). Factors were centered using the original experimental levels aimed for at all experimental runs (see Table 11.4). The measured experimental values are reconciled and plotted (also centered using the original planned levels) with the measured values in Figure 12.20. Appendix F contains data of the measured (and reconciled) experimental levels and system responses. All mass and species balances were off by less than 10^{-14} t/h after 5 data reconciliation iterations.

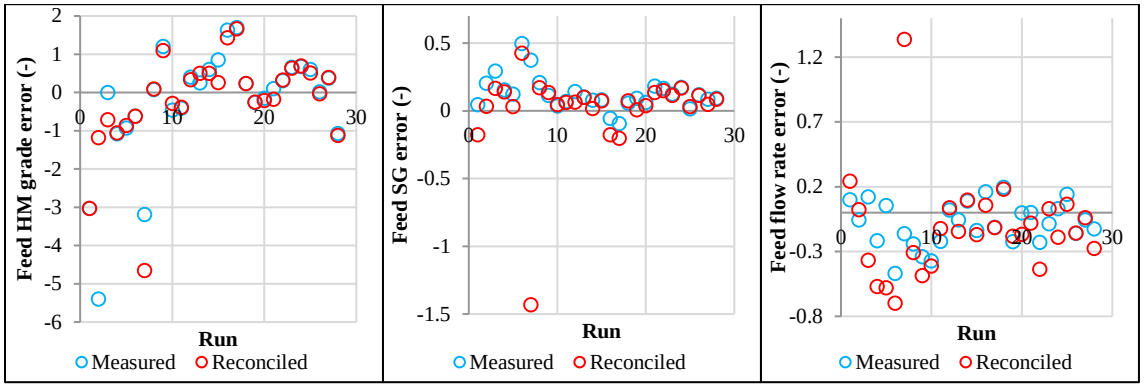

Figure 12.20: Scaled deviation of measured and reconciled design levels (left: feed HM grade, middle: feed SG, right: feed volumetric flow rate)

Figure 12.20 shows that runs 1, 2, 6 and 7 have the largest deviation from the planned experimental levels and will introduce significant error for response surface modelling. Feed grade shows the greatest deviation from desired experimental levels (majority of points between 2 and -2) with feed SG and feed flow rate showing lower deviations from desired levels (0.2 and -0.2). Reconciliation shifts feed SG and grade means closer to the desired experimental design levels; however, this intended result is not entirely achieved for feed flow rate deviations. Run 7 shows the largest residual for feed SG and feed flow rate levels and the second largest for feed grade levels.

Figures 12.21 and 12.22 also visualise deviation from the 4 factor Box-Behnken design using principal component analysis (PCA) of the desired, measured and reconciled design matrix (Izenman, 2008). PCA of the measured design matrix shows that runs 1, 2 and 7 show the greatest deviation from the design matrix. The ideal Box-Behnken design matrix was transformed using the principal component coefficients from the measured design matrix to allow visualization of 25 of the 27 design points (three points of the design matrix represent the same conditions and cannot be showed individually).

Stellenbosch University https://scholar.sun.ac.za

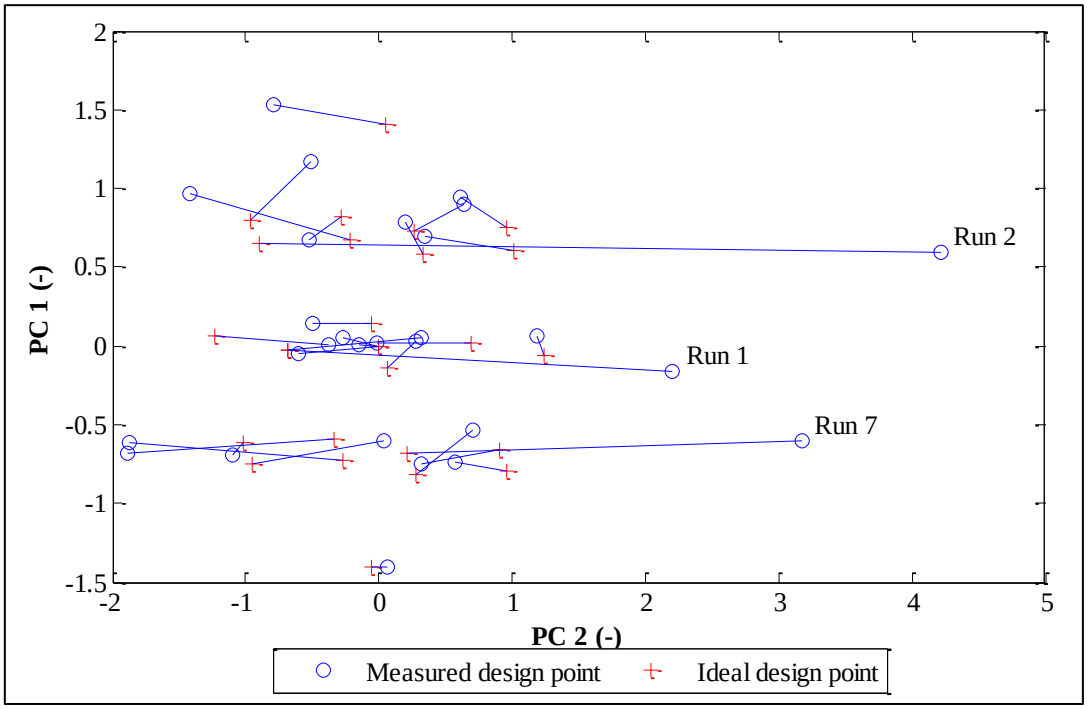

Figure 12.21: Measured experimental levels and design levels (first two principal components from 4; 58.5 % variance captured by PC 1, 16.7 % variance captured by PC 2)

The PCA projection in Figure 12.22 shows that reconciled design points lie closer to the intended design levels except for runs 1 and 7 (in agreement with the measurement based case). It is expected that these two runs (1 and 7) can complicate the modelling of spiral responses and it can become possible that these points must be omitted for RSM. Run 1 can be replaced with 28 for design purposes but omitting run 7 will result in loss of orthogonality in the experimental design matrix.

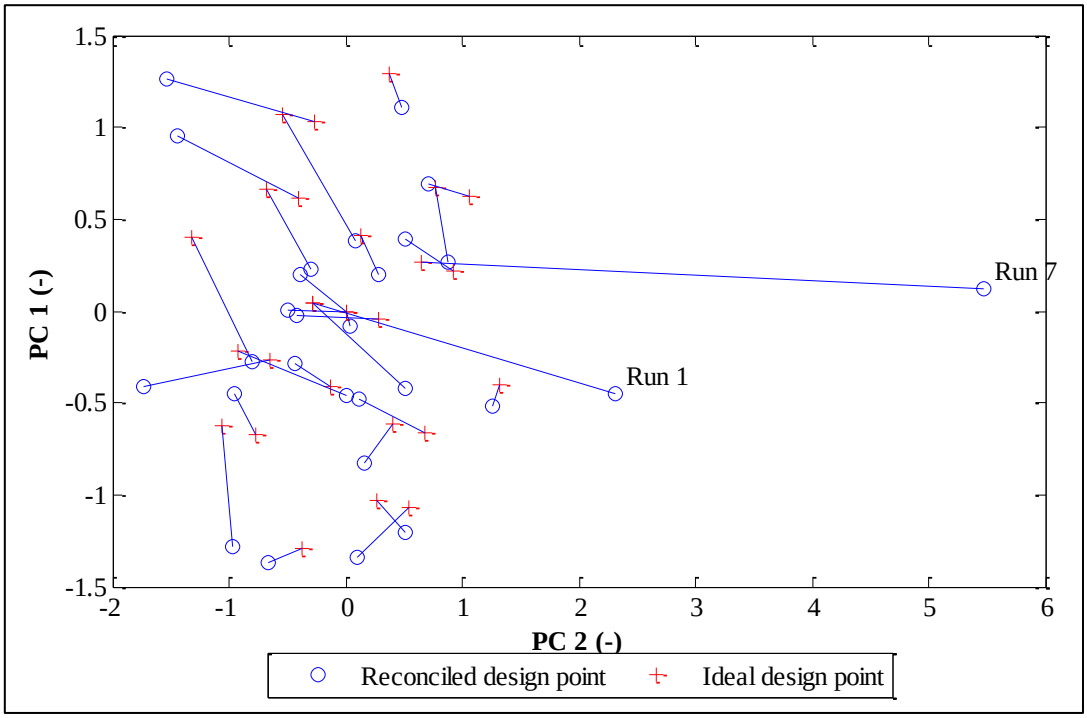

Figure 12.22: Reconciled experimental levels and design levels (first two principal components from 4; 62.8 % variance captured by PC 1, 16.6 % variance captured by PC 2)

The first three spiral responses that will be modelled via RSM are the tailings HM grade, tailings HM recovery and the ratio of total concentrate mass flow rate over tailings mass flowrate. Figure 12.23 gives the responses that were measured during the experimental runs. Grade and recoveries lower than 0 is recorded in the measured values at runs 2, 6, 7 and 12 and at runs 5, 18, 19 and 27 the values are higher than 1. No negative concentrate-tails flow ratio values are recorded; however, there is large uncertainty at runs 3, 6, 7, 22 and 28. HM grade and recovery measurements at run 6 are lower than -9 and have the largest uncertainty. Because grade and recovery values below 0 and above 1 are dubious, reconciliation of experimental data can become essential to obtain response estimate that are physically possible.

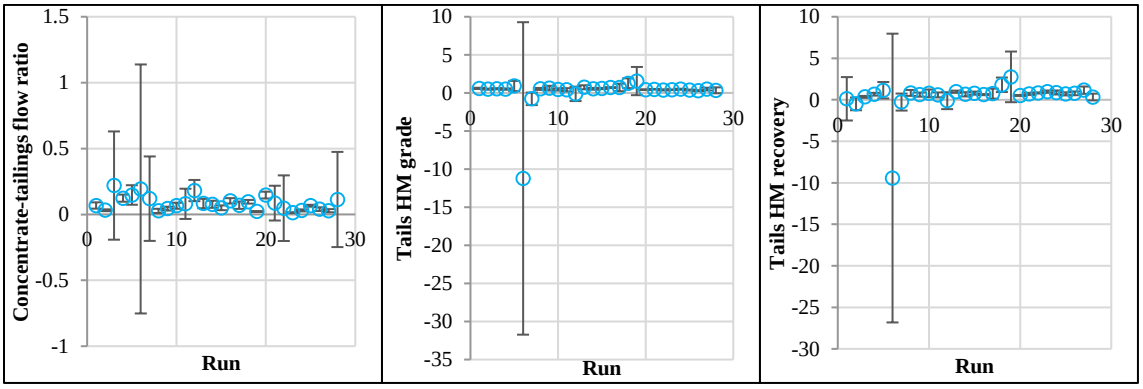

Figure 12.23: Measured spiral tailings responses (left: flow ratio, middle: tailings HM grade, right: tailings HM recovery; error bars represent 1 × σ based on n = 3 replicates)

Figure 12.24 shows the reconciled values of the same responses in Figure 12.23. Reconciled grade and recovery values fall in the acceptable range of 0-1 except for the grade at run 6 (which is below 0) and recovery at run 1 (which is above 1). Flow ratio values are still above 0 but the uncertainty is increased except at runs 4 and 5. Uncertainty in reconciled grade values are reduced for each experimental run.

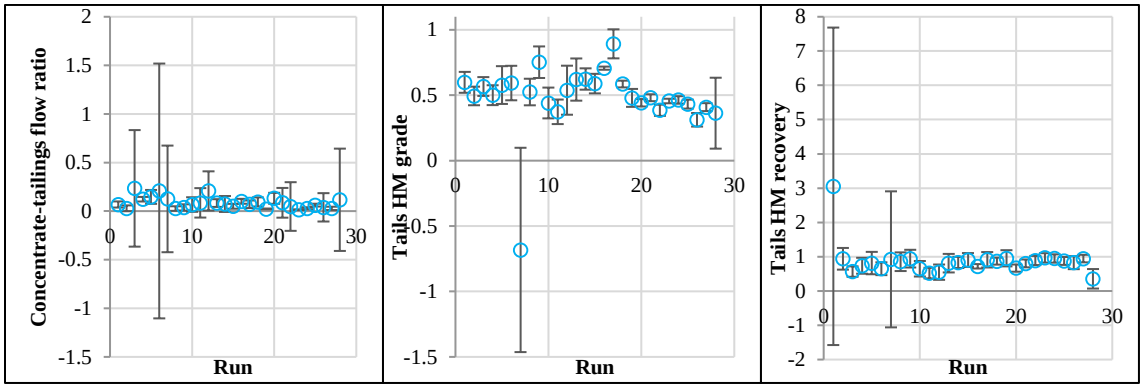

Figure 12.24: Reconciled spiral tailings responses (left: flow ratio, middle: tailings HM grade, right: tailings HM recovery; error bars represent $1 \times \sigma$ *based on n = 3 replicates)*

Only reconciled values were considered for model fitting since measured grades and recoveries can attain physically impossible values. The design for each modelling case will only consider runs 2-28 (due to the deviations run 1 shows from the ideal run 1 levels). Modelling is also performed using "new" experimental levels based on the reconciled feed HM grade, feed SG and feed volumetric flow rate. New levels are obtained using least squares to find the levels that best serve to centre the reconciled experimental design. These levels are also better estimates of the levels the experiments were carried out at. Table 12.4 presents the levels used to centre reconciled experimental design values for model fitting.

Table 12.4: Estimated experimental design levels for model development (runs 2-28)

Feed	Low (-1)	Centre (0)	High (+1)
Grade (fraction)	0.44	0.51	0.57
SG	1.09	1.30	1.52
Flow rate (m^3/h)	5.78	7.73	9.68

The new feed SG levels span a wider range than the original's while feed flow rate levels are lower. New feed HM grade levels span a narrower range than the planned HM grade levels. The following sections (and Chapter 5) use the values in Figures 12.20, 12.24 and Table 12.4 for RSM.

12.2.2. Response surface methodology for spiral models (based on tailings stream responses)

Full quadratic models were fit to the same values used in Section 12.2.1 except that descriptive statistics are based only on response errors (errors in factor levels is not included in the analysis).

Stellenbosch University https://scholar.sun.ac.za

Table 12.5 gives the correlation coefficients and F-test results for the flow, HM grade and HM recovery models. Grade and recovery models are statistically significant and more precise than the flow ratio model. The flow ratio model is nearly significant with a significance F p-value that is approximately 0.06.

Table 12.5: F-test and correlation coefficient results for quadratic tailings models based on reconciled values

	Flow ratio model	Tailings grade model	Tailings recovery Model
$\mathcal{R}^2$	0.75	0.99	0.85
$\mathcal{R}^2_{adj}$	0.45	0.99	0.68
Significance F p-value	5.74E-02	2.08E-11	4.07E-03

Adjusted $\mathcal{R}^2$ for the grade model is close to the $\mathcal{R}^2$ value suggesting that most of the model parameters can be retained. Flow ratio and recovery model $\mathcal{R}^2_{adj}$ are lower than their $\mathcal{R}^2$ values suggesting parameter selection will be necessary. Standardised residuals of the full quadratic models are presented in Figure 12.25. There are no outliers visible in any of the models and model residuals show homoscedastic behaviour except for the recovery model that shows an almost oscillatory pattern.

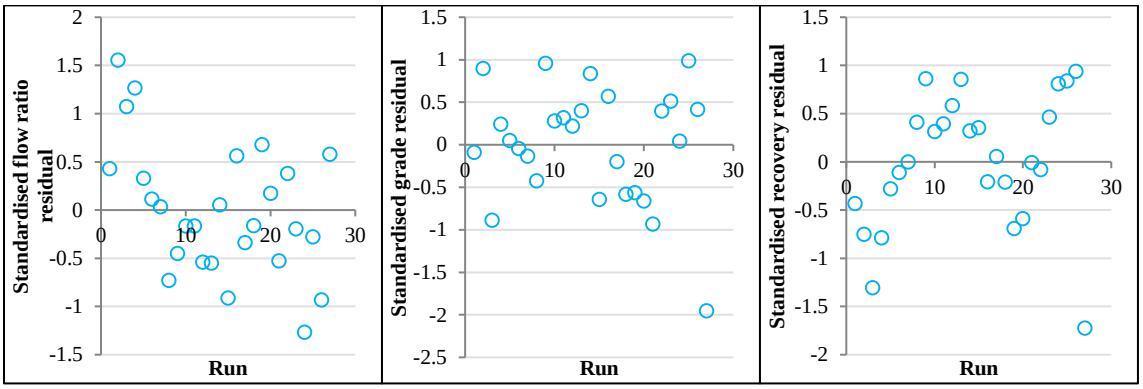

Figure 12.25: Standardised residuals for flow ratio (left), tailings HM grade (middle) and tailings HM recovery (right) full quadratic models

Significant variables of the flow ratio model are only the feed HM grade and splitter setting. The HM grade model significant variables include feed grade, feed SG, splitter setting and feed grade interaction and the feed SG squared. Recovery model significant variables are feed grade, feed SG, splitter setting and the feed SG squared.

Parameter selection was performed to remove statistically insignificant terms from the flow, grade and recovery models. F-test and correlation coefficient results are presented in Table 12.6 showing

Stellenbosch University https://scholar.sun.ac.za

improvement in adjusted $\mathcal{R}^2$ values and significance F-tests. All models are significant after parameter selection with the trade-off that precision is lost in the flow ratio and recovery models.

Table 12.6: F-test and correlation coefficient results after parameter selection

	Flow ratio model	Tailings grade model	Tailings recovery model
$\mathcal{R}^2$	0.65	0.99	0.81
$\mathcal{R}^2_{adj}$	0.59	0.99	0.73
Significance F p-value	7.97E-05	2.21E-18	3.50E-05

Table 12.7 gives the values and t-test p-values for the retained parameters of the flow, grade and recovery models after parameter selection. The flow ratio model is only affected by feed grade, flow rate and splitter setting variables where the remaining models include linear effects from all experimental factors. All parameters for the flow and recovery models can be considered as significant except for the grade model case where a linear feed flow rate variable is not significant but its interaction with feed grade is.

Table 12.7: Significant parameters for the flow ratio, tailings HM grade and tailings HM recovery models after parameter selection (x_1 – coded feed HM grade, x_2 – coded feed SG, x_3 – coded feed flow rate and x_4 – coded splitter setting)

Flow			Tailings grade			Tailings recovery		
Parameter	Estimate	p-value	Parameter	Estimate	p-value	Parameter	Estimate	p-value
Intercept	0.08	8.04E-10	Intercept	0.50	2.67E-24	Intercept	0.81	1.49E-18
x_1	0.01	0.03	x_1	0.06	2.09E-12	x_1	-0.04	2.13E-03
x_3	-0.03	0.02	x_2	0.04	9.06E-04	x_2	0.23	5.88E-06
x_4	0.06	4.15E-05	x_3	0.00	0.74	x_3	0.05	0.03
x_1x_4	-0.01	0.02	x_4	-0.02	0.04	x_4	-0.14	7.10E-05
			x_1x_3	0.01	0.03	x_1x_2	0.03	0.01
			x_1x_4	-0.01	0.06	x_1x_4	-0.04	0.07
			x_2^2	-0.04	0.01	x_2x_4	0.24	0.02
						x_2^2	-0.13	0.02

Figure 12.26 presents the standardised residuals of the response models after parameter selection. No outliers are present and no pattern (heteroscedastic) in the residuals exist. Figure 12.27 shows graphs of the predicted response values versus the reconciled response values the models were based on.

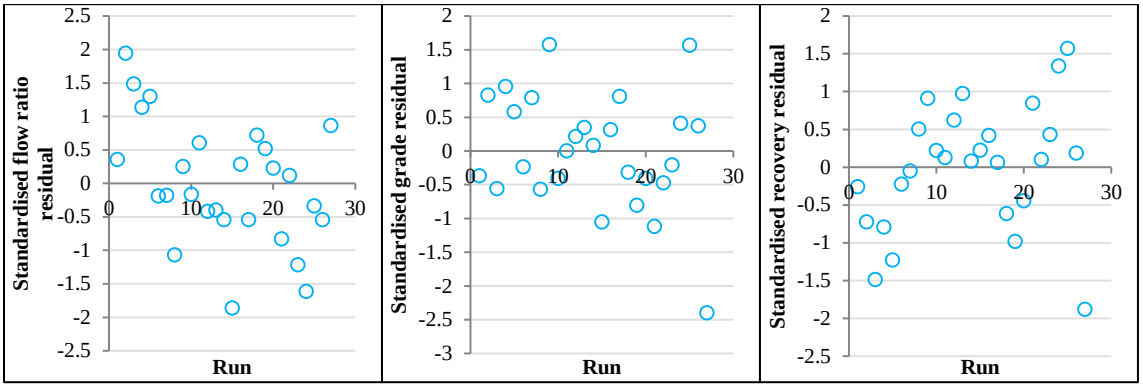

Figure 12.26: Standardised residuals for flow ratio (left), tailings HM grade (middle) and tailings HM recovery (right) models after parameter selection

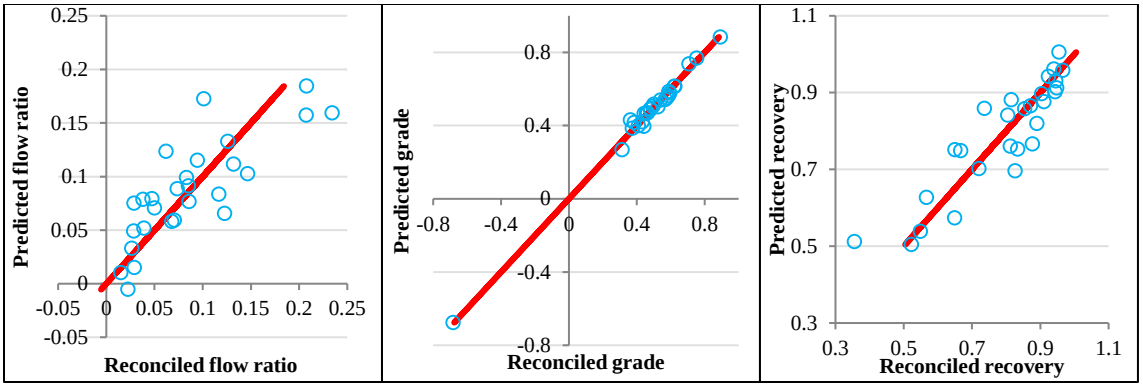

Figure 12.27: Reconciled tailings stream response values vs predicted values (left: flow ratio, middle: tailings HM grade, right: tailings HM recovery)

The statistical spiral response models are nearly complete except that the tailings grade model can potentially output negative grade values. A negative reconciled grade response was found at run 7 and the fitted model can predict this point well; however, this is an unwanted response that must be removed from the model before the statistical response models can be useful.

Removal of run 7 for regression analysis will further confound the desired orthogonality and rotatability of the spiral models. Correlation between estimated model parameters complicates the conclusions that can be drawn from hypothesis testing; especially testing on the significance of parameters. Removal of a design point also affects rotatability and can make model variance difficult to interpret. F-tests on regression models will become the most important tool in further model development.

12.2.3. Extended Holland-Batt model prediction interval estimation

The prediction interval, for the extended Holland-Batt model, was determined by finding the distribution of the possible predicted recovery R_{pred} values for the confirmation run (at the conditions in Table 5.7). This can be achieved by estimating the posterior predictive distribution – which is the result of marginalizing the prediction likelihood with the regression model posterior (Von der Linden,

Dose & Von Toussaint, 2014: 492). Performing the integration in Equation 12.1 gives the required distribution (remembering the assumption that model errors are Gaussian).

$$P_r\left(R_{pred}\middle|\delta, I\right) = C\int_{c_1\subseteq\mathbb{R}^4} \sigma^{n-1} e^{-\frac{\left(R_{pred}-R\left(X_{pred},W_{pred}\right)\right)^2}{2\sigma^2}} \ldots$$

$$e^{-\frac{\sum_\delta\left(R_i-R(X_i,W_i)\right)^2}{2\sigma^2}} da_1 da_2 da_3 da_3 d\sigma \qquad \text{(Eq. 12.1)}$$

Where:

- c_1 are integration bounds.
- C is the normalization constant.
- δ is the data set the probability functions are conditioned on (chromite data set was used).

A numerical solution of Equation 12.1 was achieved using Monte Carlo integration (50000 samples at 200 evenly spaced R_{pred} points). The cumulative distribution of $P_r\left(R_{pred}\middle|D, I\right)$ was used to find the width of the 95% prediction interval (i.e. the points on cumulative $P_r\left(R_{pred}\middle|D, I\right)$ that was closest to 0.025 and 0.975).

12.3. Optimal sensor placement

12.3.1. Effect of plant feed conditions on Algorithm SPI

Changing feed flow rate effect on reconciled plant revenue variance (from optimally selected sensor network) is shown in Figure 12.28. The largest differences, between data points from sensor networks with successively lower redundancies, along the x-axis occur for the first 4 sensor omission cases. Data points in Figure 12.28 become more linearly correlated for cases where more than 4 sensors are removed from sensor networks. In general, higher flow rates results in greater uncertainty in possible revenue produced.

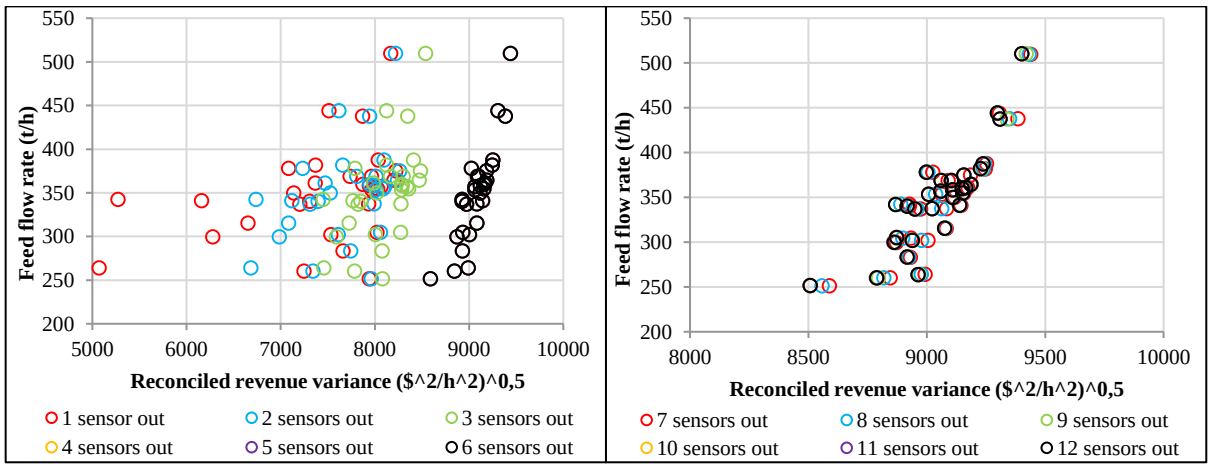

Figure 12.28: Feed flow rate vs. the square root of J_L (left: plot for the omission of 1 – 6 sensors; right: omission of 7 – 12 sensors; Algorithm SPI)

Stellenbosch University https://scholar.sun.ac.za

Feed solids fraction and reconciled revenue variance comparisons are plotted in Figure 12.29. The strong correlations in Figure 12.28 are not so prevalent in the top frames of Figure 12.29. Only for the single sensor omission case, can it be said that lower uncertainty in revenue produced can be observed with lower feed solids fraction. Feed HM grade shows linear proportionality with revenue variance (and with greater correlation than in Figure 12.28). The strong correlation and direct proportionality diminishes when more than 4 sensors are omitted from the sensor network (due to the lack in grade estimation redundancy).

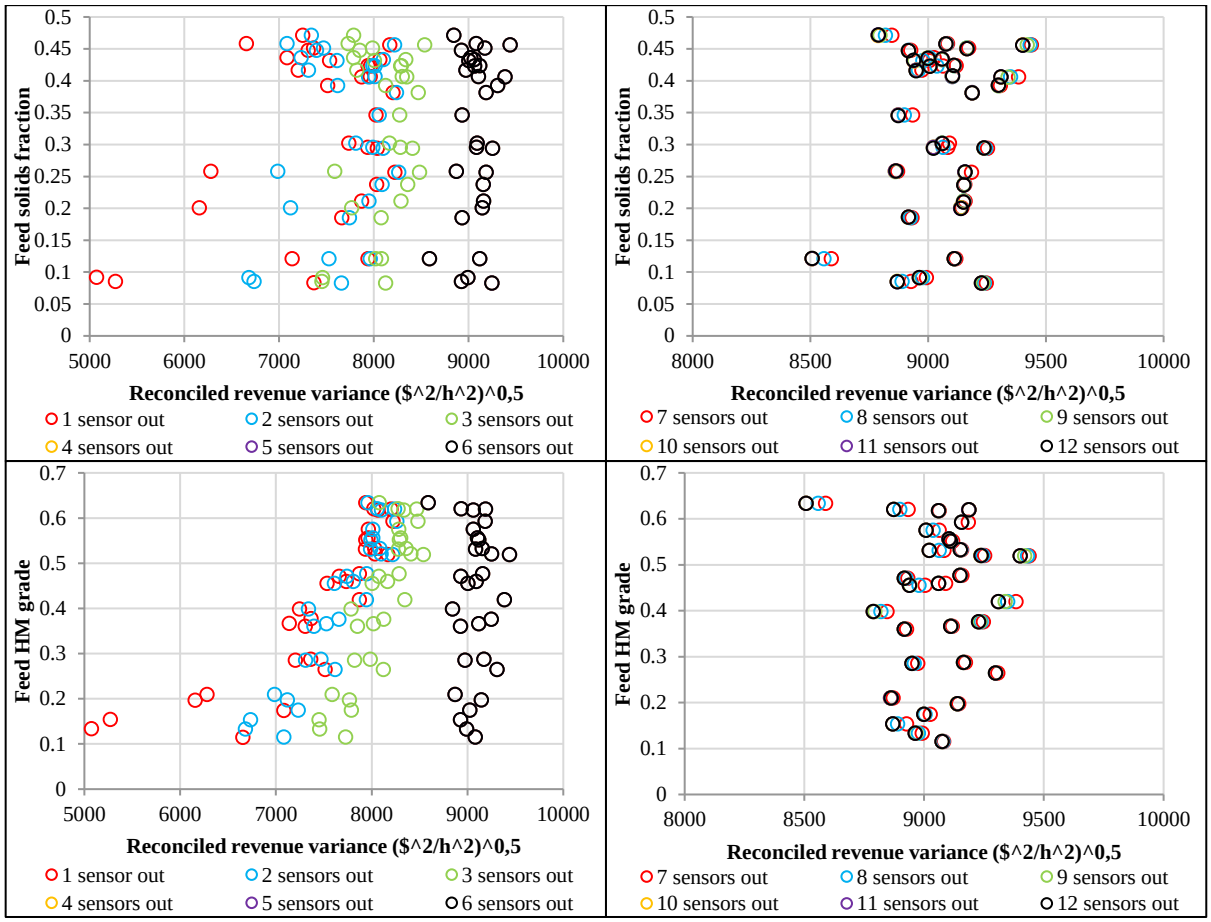

Figure 12.29: Feed solids fraction (top) and HM grade (bottom) vs. the square root of J_L (left: plot for the omission of 1 – 6 sensors; right: omission of 7 – 12 sensors; Algorithm SPI)

Finally, Figure 12.30 compares reconciled plant revenue, as generated by the concentrate stream, with the revenue monitoring performance for all feed conditions and sensor omission cases. The general trend, particularly for the 1 – 3 sensor omission cases, is that reconciled revenue and variance values are directly proportional. However, this trend diminishes when 4 or more sensors are omitted (because no more redundant grade sensors are left).

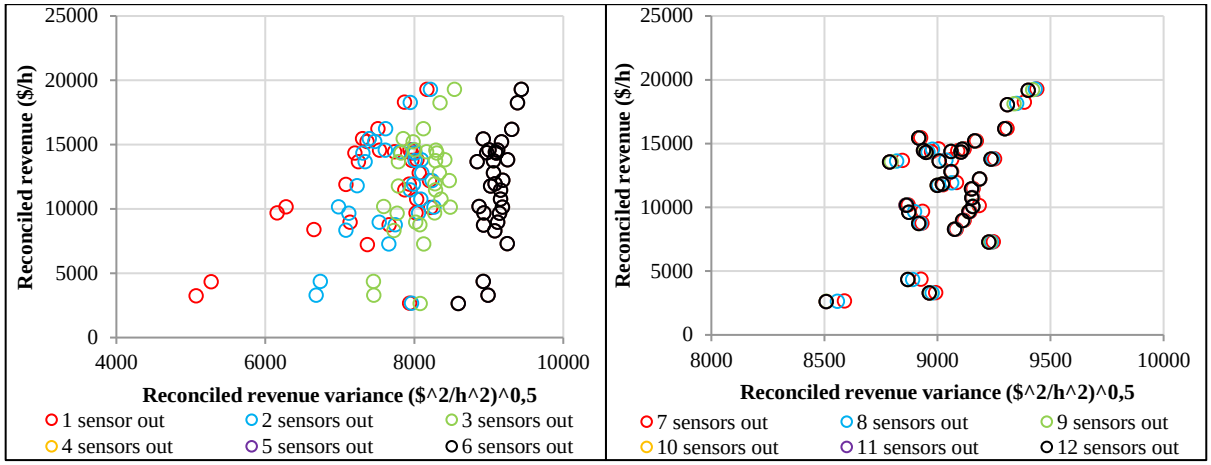

Figure 12.30: Reconciled revenue vs. the square root of J_L (left: plot for the omission of 1 – 6 sensors; right: omission of 7 – 12 sensors; Algorithm SPI)

12.3.2. Effect of plant feed conditions on Algorithm SPII

Sensitivity of WPL primary circuit revenue improvements at different feed conditions is illustrated in Figure 12.31. Revenue improvements (as determined by Algorithm SPII) are generally higher at the highest plant feed flow rates. The remaining data points do not show strong linear correlations.

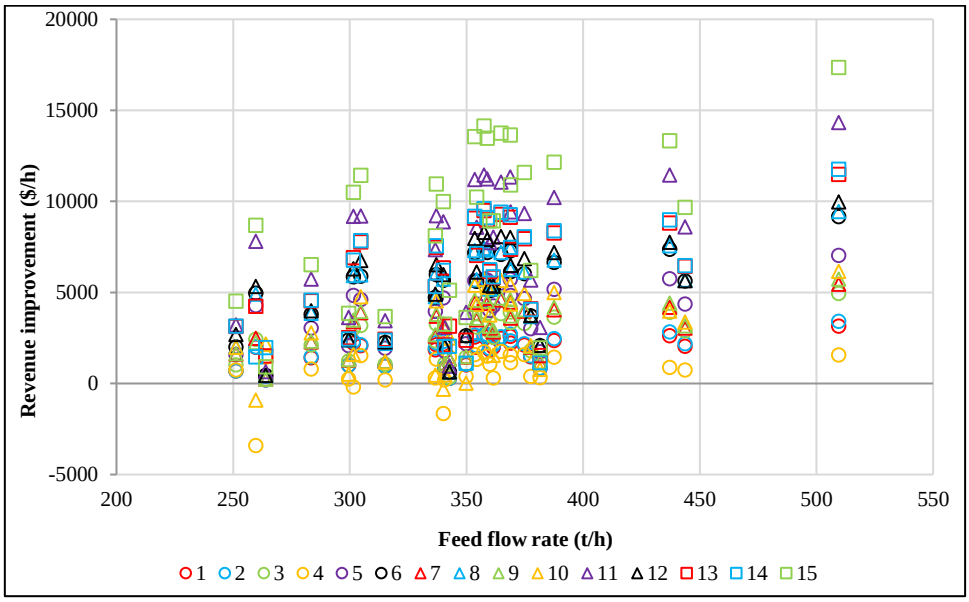

Figure 12.31: Improvement in revenue produced vs. feed flow rate at different sensor configurations (see Table 4.3 for configuration names; Algorithm SPII)

Figure 12.32 shows revenue improvement sensitivity to feed solids fraction. The highest revenue improvements are observed for feed solids fractions between 0.4 and 0.46. When the feed solids fraction is lower than 0.3 it can be observed that WPL revenue improvements show significant decrease. Revenue decreases again when feed solids fraction values are higher than 0.46. However, sensor configurations 4 and 10 are the clear exceptions – showing decreases from feed solids fraction values higher than 0.4.

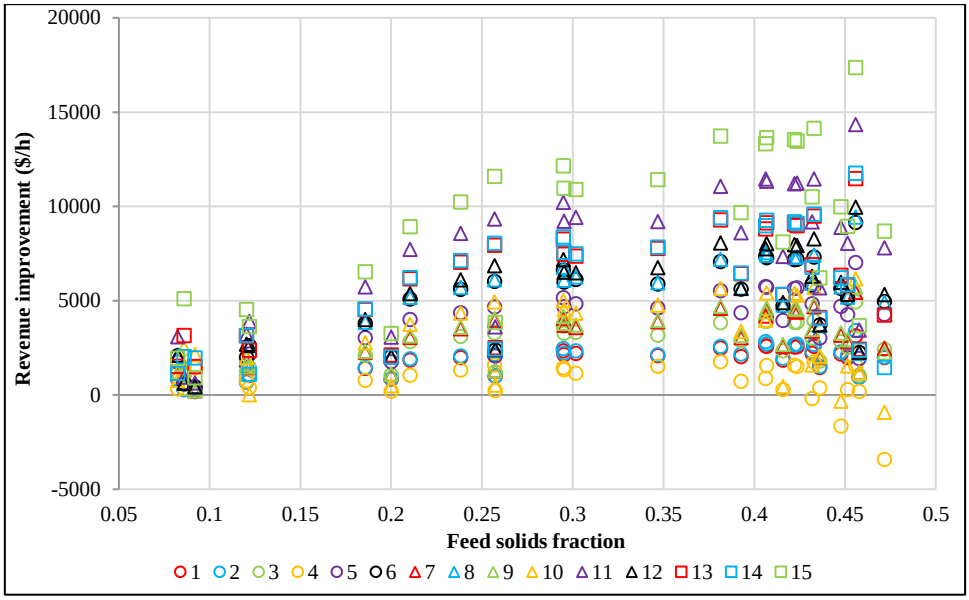

Figure 12.32: Improvement in revenue produced vs. feed solids fraction at different sensor configurations (see Table 4.3 for configuration names; Algorithm SPII)

WPL revenue improvement sensitivity to feed HM grade is presented in Figure 12.33. Higher revenue improvements are coupled with higher feed HM grades. Revenue decreases occur mostly between grades of 0.3 and 0.5 for configurations 4 and 10. When feed HM grade is higher 0.62 the revenue increases seem to decrease.

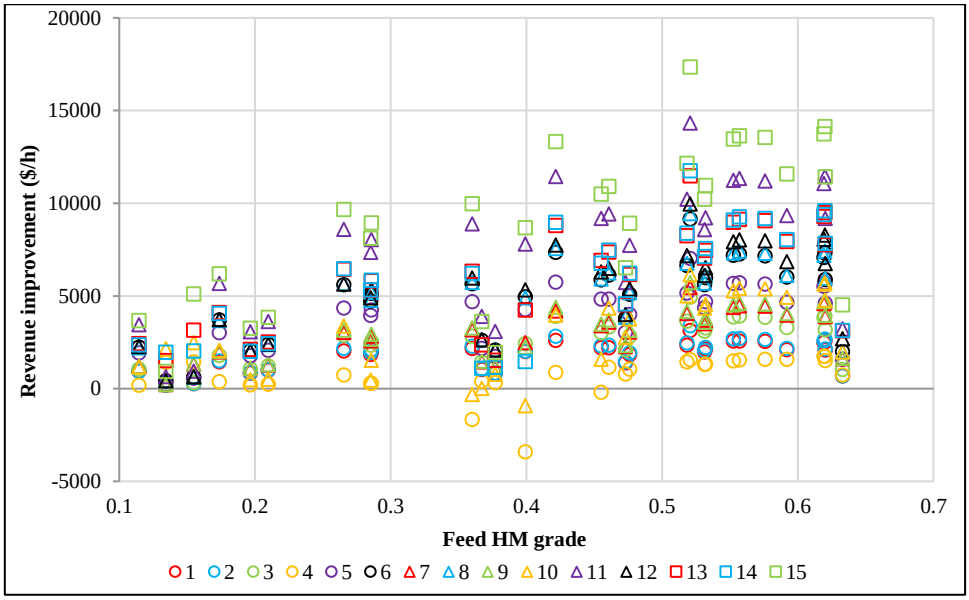

Figure 12.33: Improvement in revenue produced vs. feed HM grade at different sensor configurations (see Table 4.3 for configuration names; Algorithm SPII)

Overall, it is clear (in Figures 12.31 – 12.33) that sensor configurations 11 and 15 are the most robust implementations when feed conditions change.

Stellenbosch University https://scholar.sun.ac.za

12.3.3. Concentrate flow rate variance for two spiral bank case

This section partially explains the sequence of interface sensor placement found in Section 5.6.1. Mass flows about the rougher and cleaner spiral banks from the flowsheet in Section 4.4 is considered (separate nomenclature is used for this section). The following connectivity matrix can be obtained:

$$M = \begin{bmatrix} 1 & -1 & -1 & 0 & 0 \\ 0 & 1 & 0 & -1 & -1 \end{bmatrix}$$

With variance matrix (assuming independent measurements):

$$V = \begin{bmatrix} v_1 & 0 & 0 & 0 & 0 \\ 0 & v_2 & 0 & 0 & 0 \\ 0 & 0 & v_3 & 0 & 0 \\ 0 & 0 & 0 & v_4 & 0 \\ 0 & 0 & 0 & 0 & v_5 \end{bmatrix}$$

Using matrix P_1 and P_2, from Equation 3.13, to find solution:

$$P = I - VM^T(M\,VM^T)^{-1}M$$

Then the matrix entries of P_1 can be found by simplifying:

$$VM^T = \begin{bmatrix} v_1 & 0 & 0 & 0 & 0 \\ 0 & v_2 & 0 & 0 & 0 \\ 0 & 0 & v_3 & 0 & 0 \\ 0 & 0 & 0 & v_4 & 0 \\ 0 & 0 & 0 & 0 & v_5 \end{bmatrix} \begin{bmatrix} 1 & 0 \\ -1 & 1 \\ -1 & 0 \\ 0 & -1 \\ 0 & -1 \end{bmatrix} = \begin{bmatrix} v_1 & 0 \\ -v_2 & v_2 \\ -v_3 & 0 \\ 0 & -v_4 \\ 0 & -v_5 \end{bmatrix}$$

$$MVM^T = \begin{bmatrix} 1 & -1 & -1 & 0 & 0 \\ 0 & 1 & 0 & -1 & -1 \end{bmatrix} \begin{bmatrix} v_1 & 0 \\ -v_2 & v_2 \\ -v_3 & 0 \\ 0 & -v_4 \\ 0 & -v_5 \end{bmatrix} = \begin{bmatrix} v_1 + v_2 + v_3 & -v_2 \\ -v_2 & v_2 + v_4 + v_5 \end{bmatrix}$$

Matrix inverse entries of $(M\,VM^T)^{-1}$ is set A, B, C & D for further simplification:

$$(MVM^T)^{-1}M = \begin{bmatrix} D & C \\ B & A \end{bmatrix} \begin{bmatrix} 1 & -1 & -1 & 0 & 0 \\ 0 & 1 & 0 & -1 & -1 \end{bmatrix} = \begin{bmatrix} D & -D + C & -D & -C & -C \\ B & -B + A & -B & -A & -A \end{bmatrix}$$

$$VM^T(MVM^T)^{-1}M = \begin{bmatrix} 1 & 0 \\ -1 & 1 \\ -1 & 0 \\ 0 & -1 \\ 0 & -1 \end{bmatrix} \begin{bmatrix} D & -D + C & -D & -C & -C \\ B & -B + A & -B & -A & -A \end{bmatrix}$$

$$= \begin{bmatrix} D & 0 & 0 & 0 & 0 \\ 0 & D - C - B + A & 0 & 0 & 0 \\ 0 & 0 & D & 0 & 0 \\ 0 & 0 & 0 & A & 0 \\ 0 & 0 & 0 & 0 & A \end{bmatrix}$$

Finally, matrix P is expressible as:

Stellenbosch University https://scholar.sun.ac.za

$$P = \begin{bmatrix} 1 - Dv_1 & 0 & 0 & 0 & 0 \\ 0 & 1 - (D - B - C + A)v_2 & 0 & 0 & 0 \\ 0 & 0 & 1 - Dv_3 & 0 & 0 \\ 0 & 0 & 0 & 1 - Av_4 & 0 \\ 0 & 0 & 0 & 0 & 1 - Av_5 \end{bmatrix}$$

Where A is:

$$A = \frac{v_1 + v_2 + v_3}{(v_1 + v_2 + v_3)(v_2 + v_4 + v_5) - v_2^2}$$

Updated variance of final concentrate becomes:

$$\hat{v}_5 = v_5(1 - Av_5)^2$$

No rougher tailings monitoring (v_3) will lead to lower $\hat{v}_5$ than removing cleaner tailings sensor (v_4) – when all v's are equal. However, J_L is influenced by flow rate, solids fraction and grade estimates. This can lead to lower J_L even when redundancy is lost at final concentrate.

Stellenbosch University https://scholar.sun.ac.za

13. Appendix E

13.1. Rowland plant description

Chromite in the flotation tails received from a nearby PGM concentration plant is upgraded/concentrated at the Rowland site via the following route:

- Process water and flotation tails are mixed in a feed tank with level control (set to adjust the process water feed valve according to the mixing tank level).
- Rougher spiral cyclones receive feed from the plant feed tank via a VSD pump and produces an overflow of fine tails.
- Rougher cyclone underflow reports to the rougher header tank (which also contains level control to adjust process water addition) which finally feeds the rougher spirals.
- Process water is added to the rougher concentrate which then reports to the cleaner spirals.
- Cleaner spiral concentrate is mixed with process water and then pumped to the recleaner spirals' overhead tank. Recleaner overhead tank overflow is recycled to the recleaner feed.
- Recleaner concentrate and additional process water is fed to the re-recleaner spirals which produces final concentrate and a tailings stream which is mixed with recleaner spiral feed.
- Rougher, cleaner and recleaner tailings is with mixed process water and pumped to the scavenger cyclones which produces overflow reporting to the fine tails.
- Scavenger cyclone underflow reports to the scavenger spiral header tank which also contains level control.
- Scavenger spiral tails form part of the final coarse tails stream and scavenger concentrate flows to the scavenger cleaner header tank (with level control that adds scavenger cyclone overflow).
- Scavenger cleaner tails is added to the final coarse tails stream. Scavenger cleaner concentrate is mixed with scavenger cyclone overflow and scavenger recleaner recycled feed (in a tank with level control) and pumped to the scavenger recleaner spirals.
- Scavenger recleaner tails are mixed with scavenger spiral feed and the scavenger recleaner concentrate receives process water addition which flows to scavenger re-recleaner spirals.
- Scavenger re-recleaner tails report to rougher spiral feed and the concentrate reports to the final concentrate product.

13.2. Rowland plant PFD

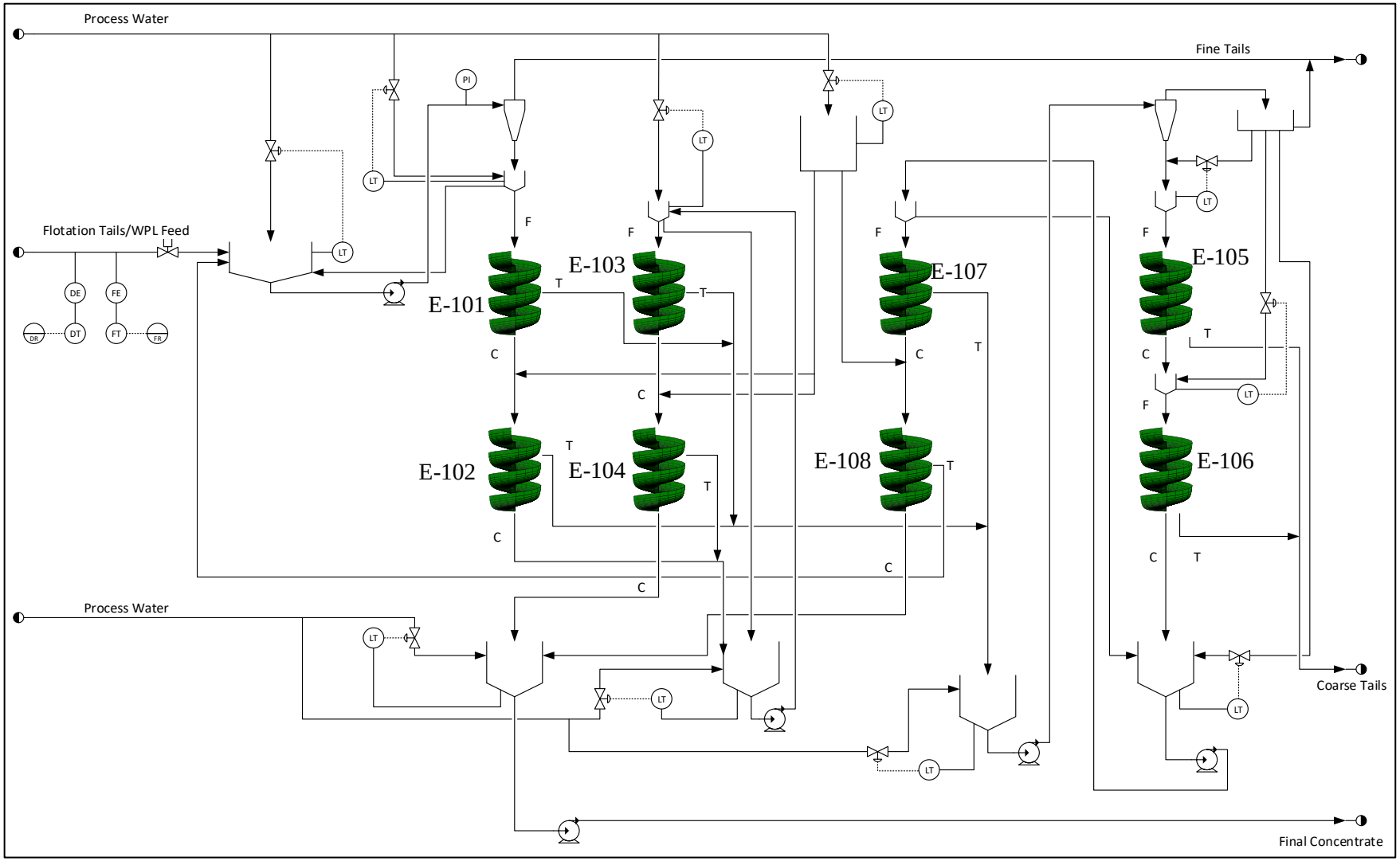

Figure 13.1: Simplified PFD (stream and equipment tags omitted)

Stellenbosch University https://scholar.sun.ac.za

14. Appendix F

Derivation of equations used to transform from image coordinates $[x, y]$ to world coordinates $[X_W, Y_W]$ when calibration matrix A has been calculated is given here. First solve for X_W:

$$x = \frac{A_{11}X_W + A_{12}Y_W + A_{13}Z_W + A_{14}}{A_{31}X_W + A_{32}Y_W + A_{33}Z_W + A_{34}}$$

$$y = \frac{A_{21}X_W + A_{22}Y_W + A_{23}Z_W + A_{24}}{A_{31}X_W + A_{32}Y_W + A_{33}Z_W + A_{34}}$$

$$xA_{31}X_W + xA_{32}Y_W + xA_{33}Z_W + xA_{34} = A_{11}X_W + A_{12}Y_W + A_{13}Z_W + A_{14}$$

$$X_W(xA_{31} - A_{11}) = A_{12}Y_W + A_{13}Z_W + A_{14} - xA_{32}Y_W - xA_{33}Z_W - xA_{34}$$

$$X_W = \frac{Y_W(A_{12} - xA_{32}) + A_{13}Z_W + A_{14} - xA_{33}Z_W - xA_{34}}{(xA_{31} - A_{11})}$$

Solve for Y_W:

$$yA_{31}X_W + yA_{32}Y_W + yA_{33}Z_W + yA_{34} = A_{21}X_W + A_{22}Y_W + A_{23}Z_W + A_{24}$$

$$Y_W(yA_{32} - A_{22}) + yA_{33}Z_W + yA_{34} = (A_{21} - yA_{31})X_W + A_{23}Z_W + A_{24}$$

$$Y_W(yA_{32} - A_{22}) + yA_{33}Z_W + yA_{34} = \frac{Y_W(A_{12} - xA_{32}) + A_{13}Z_W + A_{14} - xA_{33}Z_W - xA_{34}}{(xA_{31} - A_{11})}(A_{21} - yA_{31}) + A_{23}Z_W + A_{24}$$

$$Y_W\left((yA_{32} - A_{22}) - \frac{(A_{12} - xA_{32})}{(xA_{31} - A_{11})}(A_{21} - yA_{31})\right) + yA_{33}Z_W + yA_{34} = \frac{A_{13}Z_W + A_{14} - xA_{33}Z_W - xA_{34}}{(xA_{31} - A_{11})}(A_{21} - yA_{31}) + A_{23}Z_W + A_{24}$$

Simplify by setting $Z_W = 0$ and $A_{34} = 1$:

$$Y_W\left((yA_{32} - A_{22}) - \frac{(A_{12} - xA_{32})}{(xA_{31} - A_{11})}(A_{21} - yA_{31})\right) + y = \frac{A_{14} - x}{(xA_{31} - A_{11})}(A_{21} - yA_{31}) + A_{24}$$

The final solutions for X_W and Y_W in terms of x and y are:

$$Y_W = \frac{B(A_{14} - x) + A_{24} - y}{\left((yA_{32} - A_{22}) - B(A_{12} - xA_{32})\right)}$$

$$X_W = \frac{Y_W(A_{12} - xA_{32}) + A_{14} - x}{(xA_{31} - A_{11})}$$

Stellenbosch University https://scholar.sun.ac.za

Where:

$$B = \frac{A_{21} - yA_{31}}{xA_{31} - A_{11}}$$

Stellenbosch University https://scholar.sun.ac.za

15. Appendix G

15.1. Experimental test run order

Table 15.1: Original 4 factor Box-Behnken design and blocked 4 factor Box-Behnken design

4 facktor Box-Behnken (centered)				
Run	Grade	SG	Flowrate	Splitter
1	-1	-1	0	0
2	-1	1	0	0
3	1	-1	0	0
4	1	1	0	0
5	0	0	-1	-1
6	0	0	-1	1
7	0	0	1	-1
8	0	0	1	1
9	-1	0	0	-1
10	-1	0	0	1
11	1	0	0	-1
12	1	0	0	1
13	0	-1	-1	0
14	0	-1	1	0
15	0	1	-1	0
16	0	1	1	0
17	-1	0	-1	0
18	-1	0	1	0
19	1	0	-1	0
20	1	0	1	0
21	0	-1	0	-1
22	0	-1	0	1
23	0	1	0	-1
24	0	1	0	1
25	0	0	0	0
26	0	0	0	0
27	0	0	0	0

Blocked (centered)				
Run	Grade	SG	Flowrate	Splitter
1	1	-1	0	0
2	1	1	0	0
3	1	0	0	-1
4	1	0	0	1
5	1	0	-1	0
6	1	0	1	0
7	0	0	-1	-1
8	0	0	-1	1
9	0	0	1	-1
10	0	0	1	1
11	0	-1	-1	0
12	0	-1	1	0
13	0	1	-1	0
14	0	1	1	0
15	0	-1	0	-1
16	0	-1	0	1
17	0	1	0	-1
18	0	1	0	1
19	0	0	0	0
20	0	0	0	0
21	0	0	0	0
22	-1	-1	0	0
23	-1	1	0	0
24	-1	0	0	-1
25	-1	0	0	1
26	-1	0	-1	0
27	-1	0	1	0

Stellenbosch University https://scholar.sun.ac.za

Table 15.2: Blocked 4 factor Box-Behnken design with within block randomization

Blocked and Randomized				
Run	Grade	SG	Flowrate	Splitter
1	1	-1	0	0
2	1	0	0	-1
3	1	0	0	1
4	1	0	1	0
5	1	1	0	0
6	1	0	-1	0
7	0	-1	0	1
8	0	-1	0	-1
9	0	1	0	-1
10	0	-1	1	0
11	0	-1	-1	0
12	0	0	-1	1
13	0	0	0	0
14	0	0	0	0
15	0	0	-1	-1
16	0	1	0	1
17	0	1	1	0
18	0	1	-1	0
19	0	0	1	-1
20	0	0	1	1
21	0	0	0	0
22	-1	0	-1	0
23	-1	0	0	-1
24	-1	1	0	0
25	-1	0	0	1
26	-1	-1	0	0
27	-1	0	1	0

15.2. Detailed experimental procedure

Spiral equipment start-up steps:

1. While valve V-102 is closed open valve V-101 and add approximately 100 L of water.
2. Fix cameras above the spiral trough at the entrance of the splitter box.
3. Ensure the entire trough is within camera(s) field of view.
4. Place calibration pattern in the trough and capture approximately 20 s of video before removing the pattern.
5. Ensure that valves V-103 and V-104 are completely open, and start pump P-101 at 650 rpm.

Stellenbosch University https://scholar.sun.ac.za

6. Take timed measurements of the combined product streams to determine average feed volumetric flow rate.
7. Volumetric flow rate can be increased by adding water (opening V-101), slightly closing V-104 or increasing pump speed.
8. Volumetric flow rate can be decreased by removing water (opening V-102), by opening V-104 or reducing pump speed.
9. Adjust volumetric flow rate until the test run flow rate is achieved.
10. Add feed ore (with grade corresponding to what the specific run is coded) in increments of 5 L until required feed SG is achieved.
11. Measure feed SG by weighing combined product stream samples.
12. After feed volumetric flow rate and SG is achieved wait 15 minutes for steady-state.

Spiral experiment test run procedure:

1. Set splitter setting to the setting required by the specific experimental run.
2. Measure feed flow rate and SG to confirm steady-state. If the flow rate changed then alter pump speed or valve V-104. If SG has reduced then repeat step 10 of the start-up. If feed SG is over the required level then continue to shutdown and repeat start-up (excluding steps 3, 4 and 5)
3. If all fed conditions are met then the cameras can be set to record images of the slurry entering the splitter box. Timed feed, concentrate and tails slurry samples are collected and weighed.
4. When all samples have been collected the cameras can be switched off.
5. All samples are filtered (using a filter press and 8 µm filters) to keep slurry solids and then solids are placed in an oven to dry.
6. After a test run is successfully completed the shutdown steps can commence.

Spiral equipment shutdown steps:

1. Remove cameras from the spiral equipment.
2. Collect slurry (for later use) into empty buckets and open valve V-101 to ensure that air does not reach the pump.
3. When the water in the system is clear valve V-101 can be closed.
4. Switch off pump P-101.
5. Drain process water, via process line 2, by opening valve V-102.

Stellenbosch University https://scholar.sun.ac.za

16. Appendix H

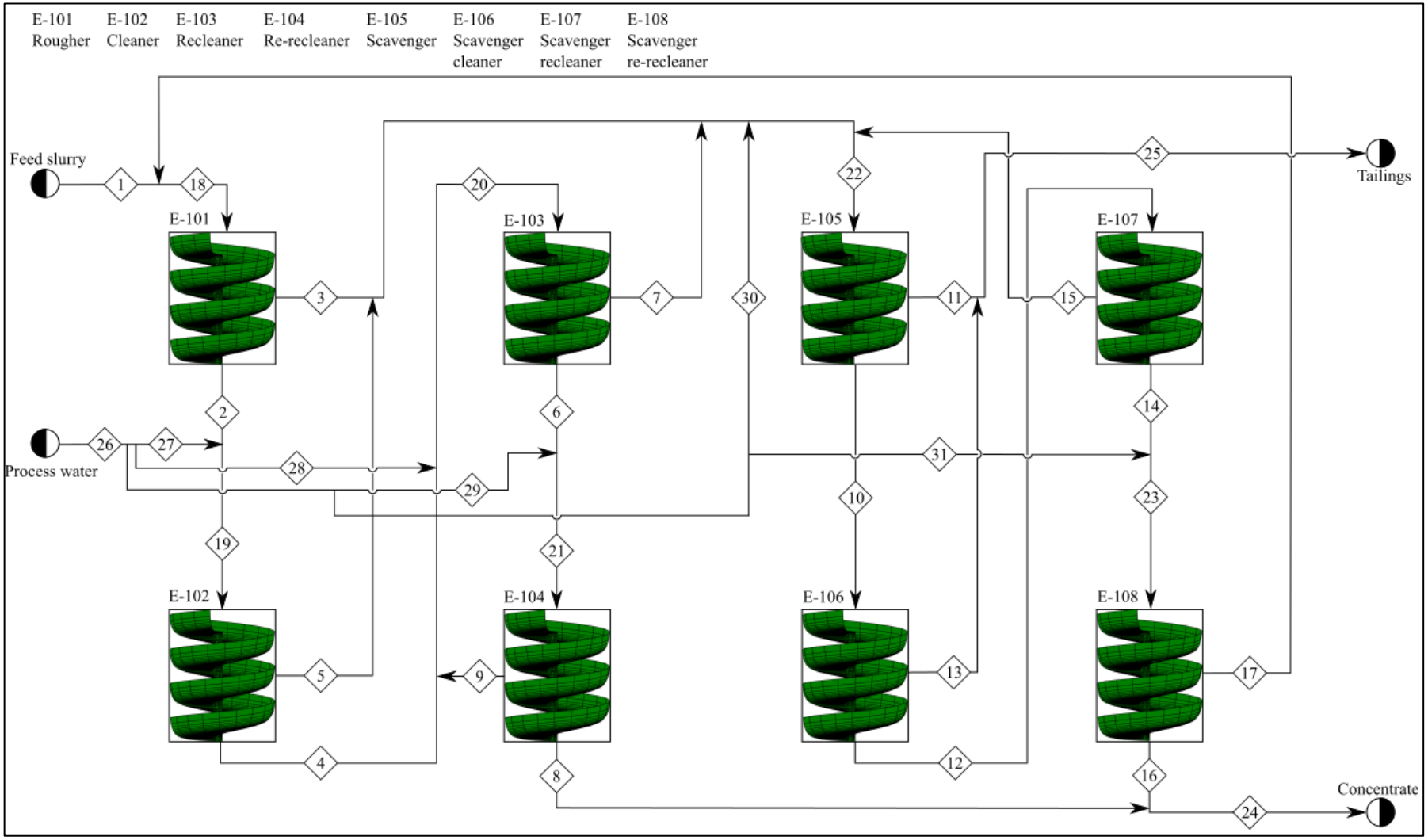

Figure 16.1: Simplified PFD of primary and secondary spiral circuits

Stellenbosch University https://scholar.sun.ac.za

17. Appendix I

17.1. Ilmenite interface detection results

17.1.1. Algorithm CVI (GA-based)

Table 17.1: σ and mean results for J_1 and J_2 results for the ilmenite middling detection training case (GA-based Algorithm CVI)

	J_1 ($\times$ 100)		J_2 ($\times$ 100)	
Training image set size	Mean	$1 \times \sigma$	Mean	$1 \times \sigma$
50	1.95	0.38	1.45	0.06
100	1.96	0.42	1.45	0.06
150	1.99	0.43	1.44	0.06
200	2.21	0.39	1.45	0.06
300	2.08	0.42	1.46	0.07

Table 17.2: σ and mean results for J_1 and J_2 results for the ilmenite middling detection testing case (GA-based Algorithm CVI)

	J_1 ($\times$ 100)		J_2 ($\times$ 100)	
Training image set size	Mean	$1 \times \sigma$	Mean	$1 \times \sigma$
50	2.03	0.41	1.44	0.07
100	2.00	0.42	1.43	0.06
150	2.06	0.47	1.42	0.10
200	2.22	0.38	1.43	0.10
300	2.03	0.43	1.43	0.12

Table 17.3: σ and mean results for J_1 and J_2 results for the ilmenite concentrate detection training case (GA-based Algorithm CVI)

	J_1 ($\times$ 100)		J_2 ($\times$ 100)	
Training image set size	Mean	$1 \times \sigma$	Mean	$1 \times \sigma$
50	7.09	0.27	1.06	0.20
100	7.10	0.33	1.02	0.18
150	7.47	0.22	0.62	0.03
200	6.94	0.31	1.18	0.22
300	7.72	0.40	0.39	0.29

Stellenbosch University https://scholar.sun.ac.za

Table 17.4: σ and mean results for J_1 and J_2 results for the ilmenite concentrate detection testing case (GA-based Algorithm CVI)

	J_1 ($\times$ 100)		J_2 ($\times$ 100)	
Training image set size	Mean	$1 \times \sigma$	Mean	$1 \times \sigma$
50	7.13	0.37	1.01	0.30
100	7.16	0.37	1.00	0.21
150	7.54	0.24	0.62	0.04
200	7.01	0.33	1.14	0.22
300	7.82	0.43	0.34	0.30

17.1.2. Algorithm CVII (logistic regression based) cross-validation

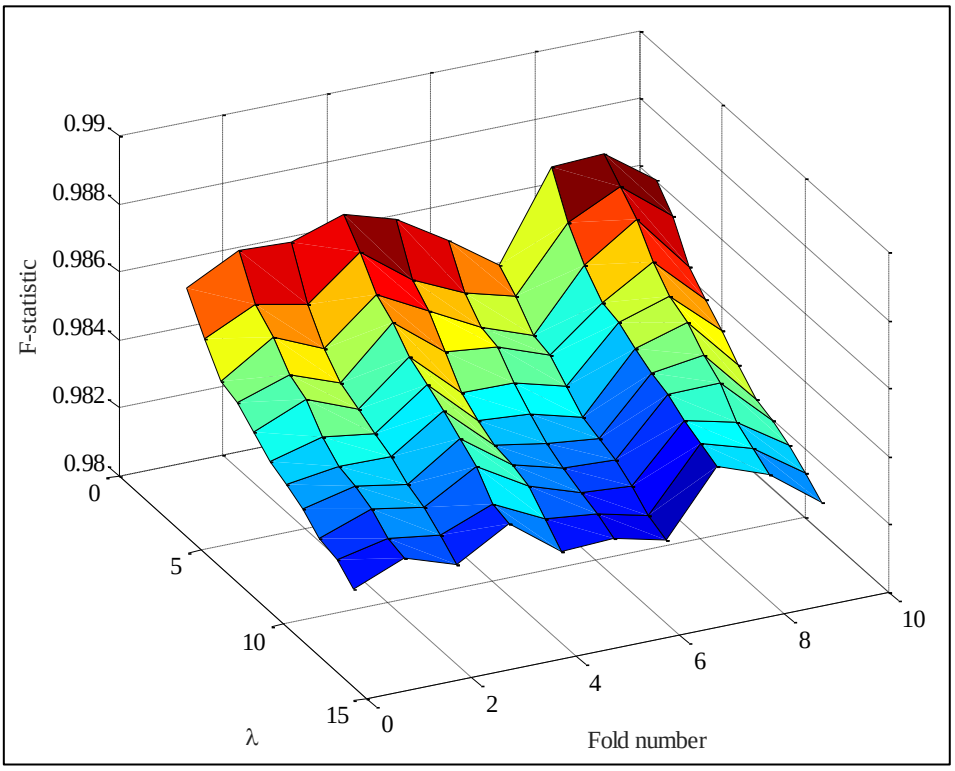

Figure 17.1: Cross-validation results for logistic regression training (ilmenite case with training 50 images; regularization parameter – λ – values are given on the y-axis)

Stellenbosch University https://scholar.sun.ac.za

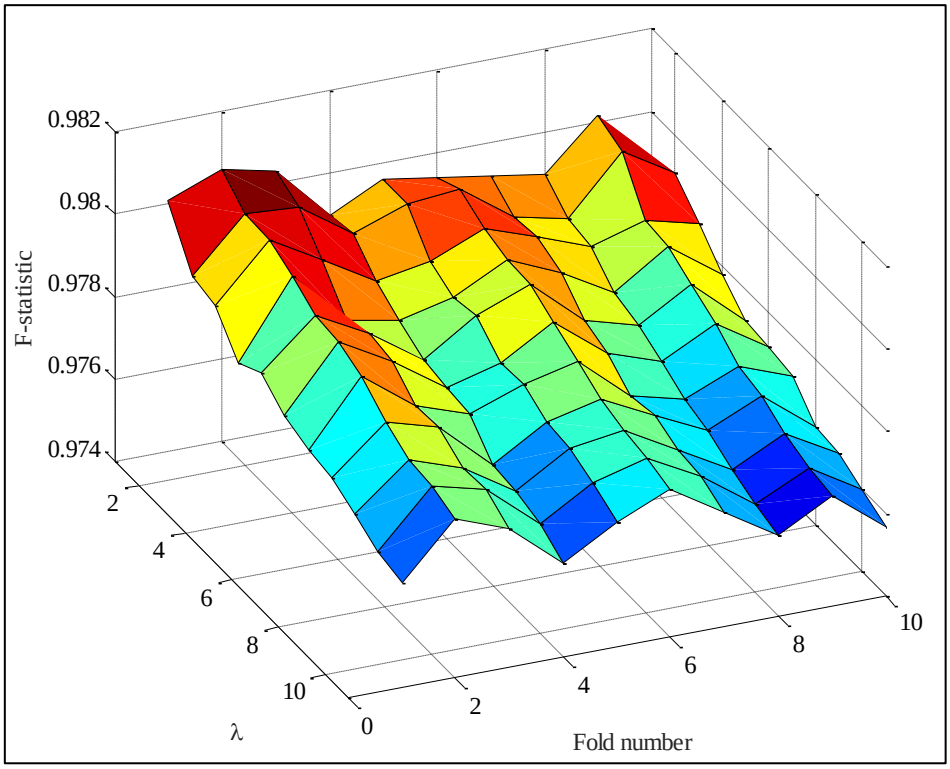

Figure 17.2: Cross-validation results for logistic regression training (ilmenite case with training 100 images; regularization parameter – λ – values are given on the y-axis)

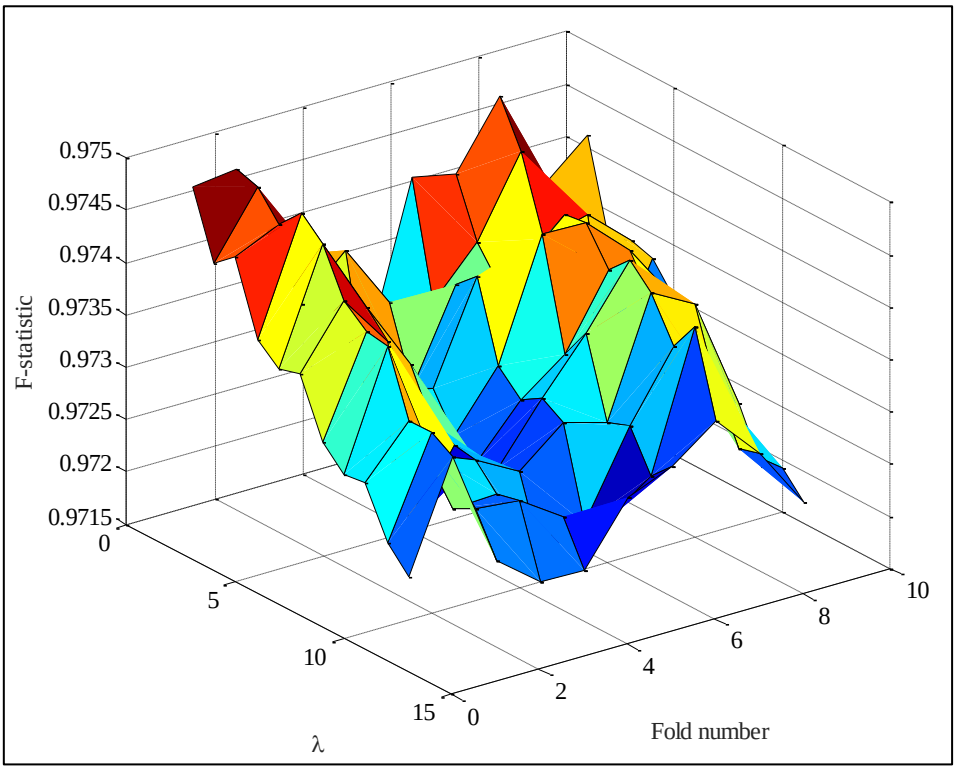

Figure 17.3: Cross-validation results for logistic regression training (ilmenite case with training 150 images; regularization parameter – λ – values are given on the y-axis)

Stellenbosch University https://scholar.sun.ac.za

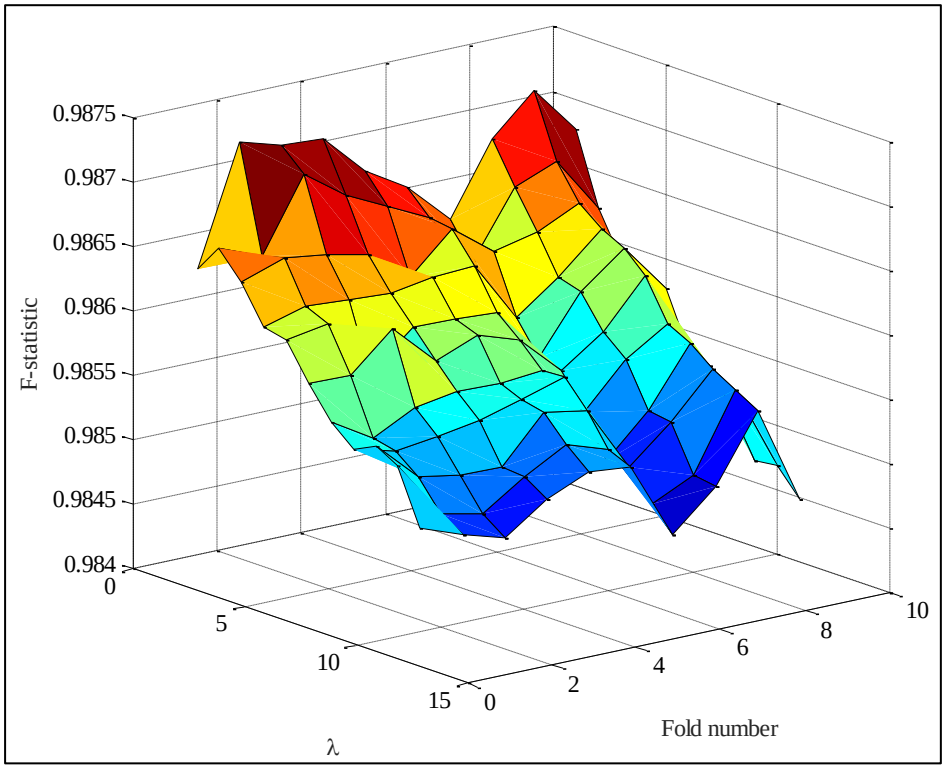

Figure 17.4: Cross-validation results for logistic regression training (ilmenite case with training 200 images; regularization parameter – λ – values are given on the y-axis)

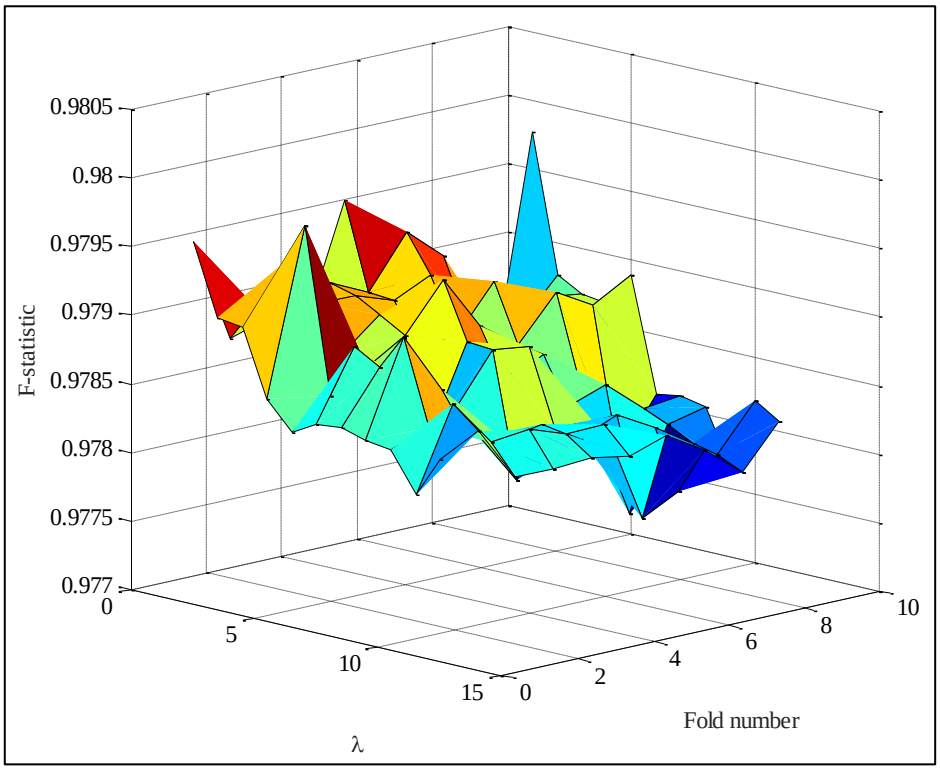

Figure 17.5: Cross-validation results for logistic regression training (ilmenite case with training 300 images; regularization parameter – λ – values are given on the y-axis)

Stellenbosch University https://scholar.sun.ac.za

17.1.3. Algorithm CVII (logistic regression based) interface detection

Table 17.5: σ and mean results for J_1 and J_2 results for the ilmenite middling detection training case (logistic regression based Algorithm CVII)

	J_1 ($\times$ 100)		J_2 ($\times$ 100)	
Training image set size	Mean	$1 \times \sigma$	Mean	$1 \times \sigma$
50	2.13	0.22	0.94	0.05
100	2.09	0.23	0.95	0.04
150	2.15	0.22	0.93	0.03
200	2.08	0.21	0.94	0.04
300	2.20	0.12	0.94	0.04

Table 17.6: σ and mean results for J_1 and J_2 results for the ilmenite middling detection testing case (logistic regression based Algorithm CVII)

	J_1 ($\times$ 100)		J_2 ($\times$ 100)	
Training image set size	Mean	$1 \times \sigma$	Mean	$1 \times \sigma$
50	2.13	0.19	0.93	0.04
100	2.11	0.20	0.95	0.05
150	2.13	0.19	0.93	0.04
200	2.12	0.19	0.94	0.05
300	2.13	0.19	0.94	0.05

Table 17.7: σ and mean results for J_1 and J_2 results for the ilmenite concentrate detection training case (logistic regression based Algorithm CVII)

	J_1 ($\times$ 100)		J_2 ($\times$ 100)	
Training image set size	Mean	$1 \times \sigma$	Mean	$1 \times \sigma$
50	1.29	0.08	0.41	0.02
100	1.27	0.38	0.40	0.02
150	1.19	0.55	0.40	0.02
200	1.30	0.07	0.41	0.02
300	1.31	0.38	0.40	0.02

Stellenbosch University https://scholar.sun.ac.za

Table 17.8: σ and mean results for J_1 and J_2 results for the ilmenite concentrate detection testing case (logistic regression based Algorithm CVII)

	J_1 ($\times$ 100)		J_2 ($\times$ 100)	
Training image set size	Mean	$1 \times \sigma$	Mean	$1 \times \sigma$
50	1.37	0.51	0.41	0.02
100	1.27	0.38	0.40	0.02
150	1.22	0.52	0.40	0.02
200	1.38	0.51	0.41	0.02
300	1.36	0.51	0.40	0.02

17.2. Chromite interface detection results

17.2.1. Algorithm CVII (logistic regression based) interface detection

Table 17.9: σ and mean results for J_1 and J_2 results for the chromite concentrate detection training case (logistic regression based Algorithm CVII using 35-by-35 filter)

	J_1 ($\times$ 100)		J_2 ($\times$ 100)	
Training image set size	Mean	$1 \times \sigma$	Mean	$1 \times \sigma$
50	1.13	0.24	0.10	0.28
100	1.19	0.33	0.00	0.30
150	1.20	0.28	0.03	0.28
200	1.22	0.33	-0.02	0.31
300	1.33	0.39	0.03	0.37

Table 17.10: σ and mean results for J_1 and J_2 results for the chromite concentrate detection testing case (logistic regression based Algorithm CVII using 35-by-35 filter)

	J_1 ($\times$ 100)		J_2 ($\times$ 100)	
Training image set size	Mean	$1 \times \sigma$	Mean	$1 \times \sigma$
50	1.11	0.31	0.05	0.27
100	1.17	0.33	-0.02	0.31
150	1.16	0.31	-0.03	0.31
200	1.35	0.33	-0.04	0.32
300	1.32	0.31	0.00	0.32

Stellenbosch University https://scholar.sun.ac.za

Table 17.11: σ and mean results for J_1 and J_2 results for the chromite gulley-concentrate detection training case (logistic regression based Algorithm CVII using 35-by-35 filter)

	J_1 ($\times$ 100)		J_2 ($\times$ 100)	
Training image set size	Mean	$1 \times \sigma$	Mean	$1 \times \sigma$
50	0.55	0.12	0.18	0.15
100	0.52	0.09	0.19	0.10
150	0.58	0.21	0.20	0.12
200	0.56	0.24	0.18	0.10
300	0.51	0.11	0.19	0.08

Table 17.12: σ and mean results for J_1 and J_2 results for the chromite gulley-concentrate detection testing case (logistic regression based Algorithm CVII using 35-by-35 filter)

	J_1 ($\times$ 100)		J_2 ($\times$ 100)	
Training image set size	Mean	$1 \times \sigma$	Mean	$1 \times \sigma$
50	0.52	0.12	0.17	0.14
100	0.51	0.14	0.18	0.15
150	0.55	0.23	0.16	0.24
200	0.54	0.18	0.18	0.12
300	0.51	0.15	0.18	0.16

Stellenbosch University https://scholar.sun.ac.za

17.2.2. Algorithm CVII interface detection examples from experimental runs

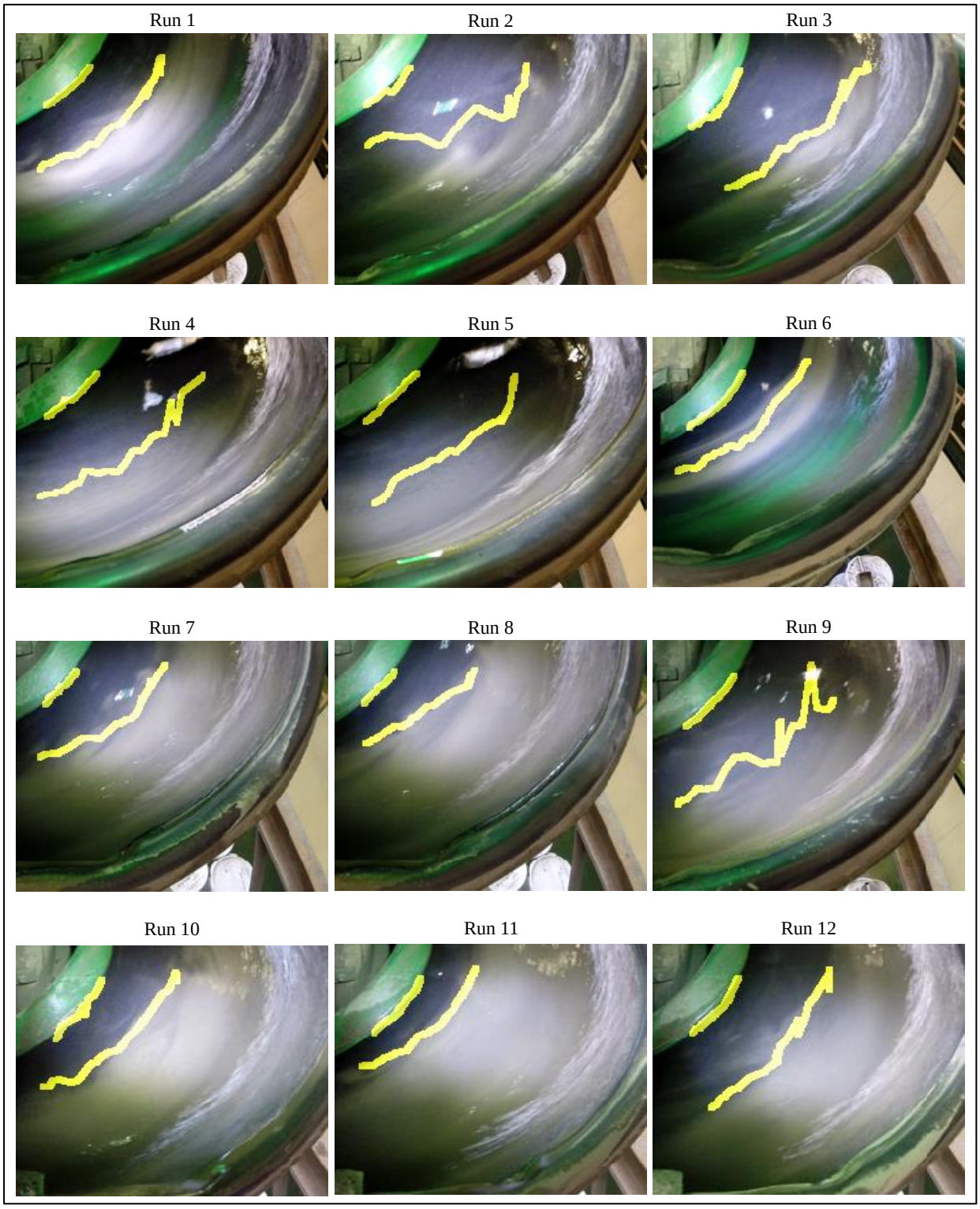

Figure 17.6: Chromite slurry interface detection, using Algorithm CVII, in example images from experimental runs 1 to 12 (using 35-by-35 filter trained on 300 images; $h > 0.3$; interfaces are dilated by 5 pixels)

Stellenbosch University https://scholar.sun.ac.za

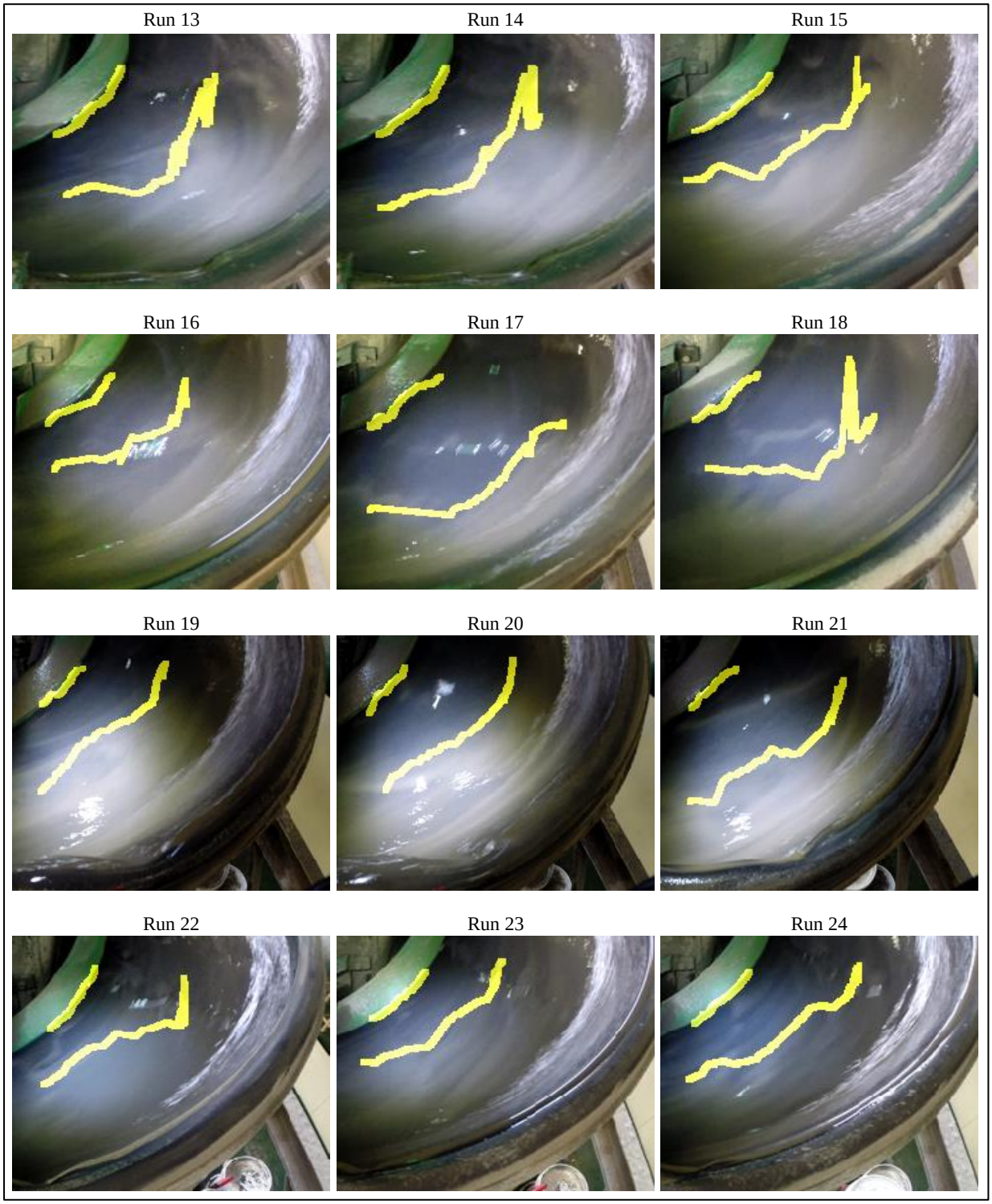

Figure 17.7: Chromite slurry interface detection, using Algorithm CVII, in example images from experimental runs 13 to 24 (using 35-by-35 filter trained on 300 images; $h > 0.3$; interfaces are dilated by 5 pixels)

Stellenbosch University https://scholar.sun.ac.za

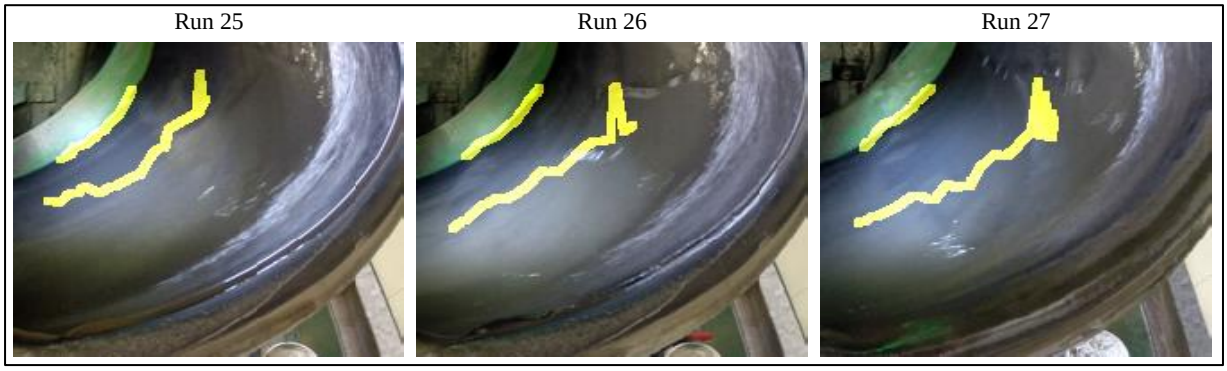

Figure 17.8: Chromite slurry interface detection, using Algorithm CVII, in example images from experimental runs 25 to 27 (using 35-by-35 filter trained on 300 images; $h > 0.3$; interfaces are dilated by 5 pixels)

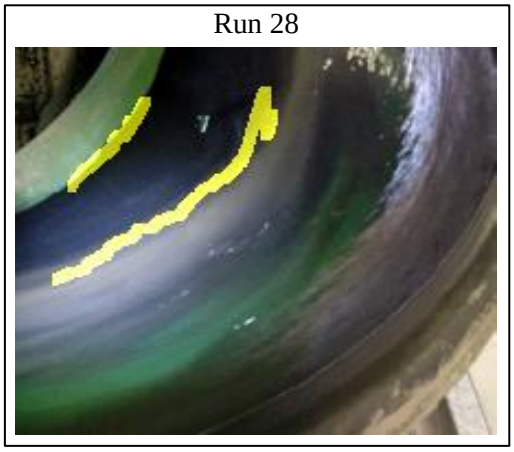

Figure 17.9: Chromite slurry interface detection, using Algorithm CVII, in an example image from experimental run 28 (using 35-by-35 filter trained on 300 images; $h > 0.3$; interfaces are dilated by 5 pixels)

17.3. Interface detection pseudocode

17.3.1. Algorithm CVI training (GA based)

Function IntGA()

1. % Initialization
2. Load slurry images = I;
3. Load interface labels = L;
4. % Use Matlab ‘s Parallel Processing Toolbox
5. Initialize parallel pool: gcp;
6. Set GA options = opt;
   6.1. Population = 50 chromosomes;
   6.2. Objective function tolerance = 10^{-10};
   6.3. Iteration stall limit = 100 iterations;
7. % Equality constraints

8. A = zeros(13,13);
9. b = zeros(13,1);
10. $A_{9,7} = 1$; $A_{9,9} = -1$; $A_{10,10} = 1$; $A_{10,11} = -1$; $A_{11,12} = 1$; $A_{11,13} = -1$;
11. $b_9 = -0.01$; $b_{10} = -1$; $b_{11} = -1$;
12. % Optimization using Matlab's ga() function from Global Optimization toolbox
13. % integer constraints and parameter boundaries are passed here
14. Lower_boundary_constraints = [-2, -2, -2, 0, 2, 3, 0, 1, 0, 0, 0, -90, -90];
15. Upper_boundary_constraints = [2, 2, 2, 1, 64, 31, 0.99, 21, 0.99, inf, inf, 90, 90];
16. Integer_constraints = [4, 5, 6, 10, 11]; % indices of variables that can only be integers
17. Save optimal parameters: β = ga(J_2(I,L,β), A, b, [], [], Lower_boundary_constraints^T, Upper_boundary_constraints^T, [], Integer_constraints, opt);
18. Close parallel pool: gcp;

End

Function J_2(I,L,β)

1. Pre-allocate j_2
2. For all I in Training set
   2.1. Separate I Channels: R = I(:, :, 1); G = I(:, :, 2); B = I(:, :, 3);
   2.2. Convert from RGB to grayscale: $K_1 = R\beta_1 + G\beta_2 + B\beta_3$;
   2.3. Historgram equalization: K_2 = histeq(K_1, β_5)β_4 + K_1(1 - β_4);
   2.4. Median filtering: K_3 = medfilt2(K_2, β_6);
   2.5. Edge detection: K_4 = edge(K_3, 'canny', β_7, β_9) - edge(K_3, 'canny', β_8, β_9); % Matlab's edge detector
   2.6. Filter connected components: K_5 = bwpropfilt(K_4, 'orientation', β_{10}, β_{11}, 'orientation', β_{12}, β_{13});
   2.7. Get j_2 = mean2(LK_5) – mean2((1 - L)K_5);
3. End
4. Save objective function: J_2 = sum(j_2);

End

17.3.2. Algorithm CVII training (logistic regression based)

Function LogReg()

1. % Initialization
2. Load slurry images = I;
3. Load interface label = L;
4. Pre-allocate Feature and label sets: Feat; labels;
5. Initialize logistic classifier parameters: $\beta_{initial}$;
6. % Unpack features and labels

Stellenbosch University https://scholar.sun.ac.za

7. For all I and L

   7.1. I_{unpack} = im2col(I, [3,3], 'sliding');

   7.2. Vertically concatenate Feat: Feat = $\begin{bmatrix} Feat \\ I_{unpack} \end{bmatrix}$;

   7.3. Vectorize L and vertically concatenate: labels = $\begin{bmatrix} labels \\ L(:) \end{bmatrix}$;

8. End

9. % Randomization

10. Randomize Feat and labels matrices;

11. % Optimize with no regularization and cross validation

12. Set conjugate gradient descent options = opt;

13. % fmincg can be found online for free

19. Save optimal parameters: β = fmincg(Cost(Feat, labels, β), $\beta_{initial}$, opt);

End

Function Cost(Feat, labels, β)

14. % Calculate log-likelihood

15. Get number of rows in Feat: m;

16. Calculate sigmoid of Feat β: h = Sigmoid(Feat β);

17. Find log-likelihood: $J = \left(\frac{-1}{m}\right)[\, labels^T \cdot \log(h) + (1 - labels)^T \cdot log(1-h)]$;

18. % Gradient

19. Gradient of log-likelihood: $G = \left(\frac{1}{m}\right)(Feat \cdot \beta)^T \cdot [labels - h]$;

End

Function Sigmoid(X)

20. % Calculate log-likelihood

21. Sigmoid = $\frac{1}{1+\exp(-X)}$;

End

Stellenbosch University https://scholar.sun.ac.za

18. Appendix J

18.1. Feed grade and solids density calibration curve

Quick composition analysis of representative samples from the quartered ore (received from the WPL plant) was performed, via XRF, to determine feed grade levels for experimental design. Densities of the minerals in the representative samples were also determined to establish how composition affects feed density. Figure 18.1 summarises the analysis of the 200 L ore samples obtained from Glencore. The major components are Cr_2O_3, Fe_2O_3, Al_2O_3, MgO and SiO_2 which represent more than 93 % of the ore mass for each respective WPL sample.

A linear function was fitted to the data in Figure 18.1 to find a function relating HM composition of a UG2 sample and its sample density. R^2 of the function is higher than 0.7 (shown in second frame of Figure 18.1) and the probability that the variance is not accounted by the model is 5.06×10^{-5} (significance F-test). The intercept and HM composition variable are both significant parameters to the model (Student based t-statistics provide p-values lower than 0.05). Despite the lack of precision the density-HM model is preferred due to its simplicity and the lack of additional points on the HM-axis.

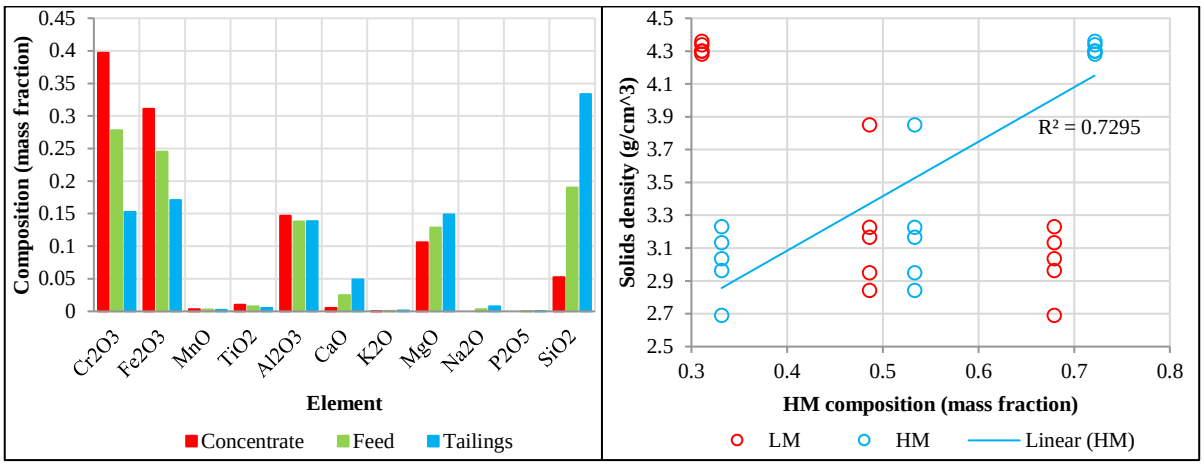

Figure 18.1: XRF (left) and density analysis (right) of WPL ore samples after quartering

The HM/LM coordinates on the second frame of Figure 18.1 were determined by grouping Cr_2O_3, Fe_2O_3, MnO and TiO_2 (the heaviest elements) as HM and the balance as LM. Combining the respective compositions gives HM and LM composition of an XRF analysed sample. Solids density was determined by weighing dry ore samples then adding them to a known volume (and mass) of water to produce a mixture with measurable volume and mass. For the curve in frame 2 of Figure 18.1 the density measurements were repeated 5 times. The HM and LM composition determined from Figure 18.1 was used to determine the feed grade level for the spiral experimental design. Using Figure 18.1's data, Equation 4.4 (from Section 4.3) becomes:

$$p_{solids} = 1.76 + 3.32 \cdot X_3$$

Stellenbosch University https://scholar.sun.ac.za

Equation 4.4 provides a fast method to roughly determine composition of ore samples (assuming that PSD and mineral types remain constant between samples) and was used to produce the results in Section 5.3. Composition analysis, in spiral literature, is usually reported according to XRF results (along with PSD analysis). However, past spiral experiments did not have the high number of experimental runs (and collected samples) of this study – which significantly increases sample analysis time and financial cost.

Stellenbosch University https://scholar.sun.ac.za

18.2. Measured and reconciled experimental design levels

Table 18.1: Measured and reconciled experimental design level means

Measured				Reconciled			
	Feed				Feed		
Run	Grade (mass fraction)	SG	Volumetric flow rate (m^3/h)	Run	Grade (mass fraction)	SG	Volumetric flow rate (m^3/h)
1	0.13	1.11	8.20	1	0.12	1.06	8.49
2	-0.35	1.34	7.89	2	0.49	1.31	8.05
3	0.73	1.36	8.25	3	0.59	1.33	7.27
4	0.51	1.33	9.57	4	0.52	1.33	8.86
5	0.54	1.52	8.11	5	0.56	1.51	6.84
6	0.61	1.40	5.06	6	0.61	1.39	4.61
7	-0.11	1.17	7.67	7	-0.40	0.81	10.67
8	0.55	1.14	7.52	8	0.55	1.13	7.38
9	0.77	1.52	7.32	9	0.75	1.53	7.03
10	0.44	1.11	9.26	10	0.47	1.11	9.18
11	0.45	1.11	5.56	11	0.45	1.11	5.76
12	0.61	1.33	6.04	12	0.60	1.31	6.08
13	0.58	1.32	7.89	13	0.63	1.32	7.71
14	0.65	1.32	8.18	14	0.63	1.30	8.19
15	0.70	1.32	5.73	15	0.58	1.32	5.66
16	0.86	1.49	8.33	16	0.82	1.46	8.12
17	0.87	1.48	9.78	17	0.86	1.46	9.77
18	0.58	1.51	6.39	18	0.58	1.51	6.36
19	0.48	1.32	9.55	19	0.48	1.30	9.64
20	0.50	1.31	10.00	20	0.49	1.31	9.67
21	0.55	1.34	8.00	21	0.50	1.33	7.84
22	0.39	1.33	5.55	22	0.40	1.33	5.13
23	0.46	1.32	7.83	23	0.46	1.32	8.06
24	0.47	1.53	8.06	24	0.47	1.53	7.62
25	0.45	1.30	8.29	25	0.43	1.31	8.13
26	0.33	1.12	7.68	26	0.32	1.12	7.68
27	0.41	1.32	9.89	27	0.41	1.31	9.93
28	0.52	1.12	7.75	28	0.51	1.12	7.45
29	0.57	1.20	7.00	29	0.49	1.18	6.60

Stellenbosch University https://scholar.sun.ac.za

Table 18.2: Measured and reconciled experimental design level variances

Measured			
	Feed		
Run	Grade (mass fraction)	SG	Volumetric flow rate (m^3/h)
1	0.04	0.00	0.41
2	2.96	0.00	0.04
3	0.03	0.00	0.38
4	0.01	0.00	1.04
5	0.01	0.00	2.34
6	0.01	0.00	0.46
7	1.07	0.01	2.22
8	0.02	0.00	0.78
9	0.01	0.00	0.36
10	0.02	0.00	0.22
11	0.00	0.00	0.29
12	0.01	0.00	0.07
13	0.02	0.00	0.30
14	0.00	0.00	0.27
15	0.04	0.00	0.17
16	0.00	0.00	0.10
17	0.01	0.00	0.87
18	0.00	0.00	0.05
19	0.00	0.00	0.89
20	0.00	0.00	0.22
21	0.01	0.00	0.61
22	0.00	0.00	0.02
23	0.00	0.00	0.30
24	0.00	0.00	0.23
25	0.00	0.00	0.12
26	0.00	0.00	0.00
27	0.00	0.00	0.18
28	0.03	0.00	0.05

Reconciled			
	Feed		
Run	Grade (mass fraction)	SG	Volumetric flow rate (m^3/h)
1	0.04	0.00	0.05
2	0.02	0.00	0.01
3	0.01	0.00	0.02
4	0.00	0.00	0.23
5	0.01	0.03	0.05
6	0.01	0.00	0.01
7	0.52	2.03	4418.64
8	0.01	0.00	0.03
9	0.01	0.01	0.04
10	0.01	0.00	0.02
11	0.00	0.00	0.01
12	0.01	0.00	0.01
13	0.02	0.00	0.01
14	0.00	0.00	0.01
15	0.01	0.00	0.01
16	0.00	0.00	0.00
17	0.01	0.01	0.07
18	0.00	0.00	0.01
19	0.00	0.00	0.07
20	0.00	0.00	0.04
21	0.00	0.00	0.01
22	0.00	0.00	0.00
23	0.00	0.00	0.04
24	0.00	0.00	0.02
25	0.00	0.00	0.02
26	0.00	0.00	0.00
27	0.00	0.00	0.01
28	0.02	0.00	0.00

Stellenbosch University https://scholar.sun.ac.za

Table 18.3: Deviations of centered measured and centered reconciled feed conditions from the experimental design levels (centering performed with originally planned experimental levels)

Measured			
	Feed		
Run	Grade (mass fraction)	SG	Volumetric flow rate (m^3/h)
1	-3.02	0.05	0.10
2	-5.39	0.20	-0.06
3	0.00	0.29	0.12
4	-1.08	0.15	-0.22
5	-0.93	0.12	0.06
6	-0.62	0.50	-0.47
7	-3.19	0.37	-0.16
8	0.08	0.21	-0.24
9	1.21	0.12	-0.34
10	-0.45	0.04	-0.37
11	-0.41	0.07	-0.22
12	0.40	0.14	0.02
13	0.26	0.10	-0.06
14	0.60	0.08	0.09
15	0.86	0.08	-0.14
16	1.64	-0.06	0.16
17	1.70	-0.09	-0.11
18	0.23	0.06	0.20
19	-0.25	0.09	-0.22
20	-0.15	0.06	0.00
21	0.11	0.18	0.00
22	0.31	0.17	-0.23
23	0.67	0.12	-0.08
24	0.68	0.17	0.03
25	0.61	0.01	0.14
26	0.02	0.12	-0.16
27	0.38	0.09	-0.06
28	-1.07	0.09	-0.12

Reconciled			
	Feed		
Run	Grade (mass fraction)	SG	Volumetric flow rate (m^3/h)
1	-3.03	-0.18	0.24
2	-1.18	0.03	0.02
3	-0.71	0.17	-0.37
4	-1.05	0.14	-0.57
5	-0.86	0.03	-0.58
6	-0.62	0.43	-0.70
7	-4.65	-1.43	1.34
8	0.09	0.17	-0.31
9	1.10	0.14	-0.48
10	-0.28	0.05	-0.41
11	-0.39	0.06	-0.12
12	0.34	0.06	0.04
13	0.51	0.10	-0.15
14	0.50	0.02	0.10
15	0.26	0.08	-0.17
16	1.43	-0.18	0.06
17	1.67	-0.20	-0.11
18	0.24	0.07	0.18
19	-0.25	0.01	-0.18
20	-0.20	0.04	-0.17
21	-0.17	0.14	-0.08
22	0.33	0.15	-0.43
23	0.64	0.11	0.03
24	0.70	0.17	-0.19
25	0.52	0.03	0.07
26	-0.03	0.12	-0.16
27	0.39	0.05	-0.04
28	-1.12	0.09	-0.28

Stellenbosch University https://scholar.sun.ac.za

Table 18.4: Measured and reconciled tailings response means

Measured			
Run	Flow ratio	Tails HM grade	Tails HM recovery
1	0.07	0.60	0.12
2	0.03	0.50	-0.49
3	0.22	0.55	0.35
4	0.12	0.50	0.67
5	0.15	0.91	1.15
6	0.19	-11.22	-9.43
7	0.12	-0.78	-0.27
8	0.03	0.53	0.83
9	0.04	0.63	0.62
10	0.07	0.46	0.78
11	0.08	0.41	0.59
12	0.18	-0.12	-0.11
13	0.08	0.74	0.97
14	0.08	0.54	0.66
15	0.05	0.57	0.80
16	0.10	0.71	0.63
17	0.07	0.72	0.74
18	0.10	1.27	1.81
19	0.02	1.56	2.76
20	0.15	0.43	0.52
21	0.09	0.48	0.71
22	0.05	0.40	0.82
23	0.01	0.42	0.98
24	0.03	0.48	0.88
25	0.07	0.38	0.71
26	0.04	0.30	0.78
27	0.03	0.50	1.16
28	0.11	0.34	0.33

Reconciled			
Run	Flow ratio	Tails HM grade	Tails HM recovery
1	0.07	0.60	3.05
2	0.03	0.49	0.94
3	0.23	0.57	0.57
4	0.12	0.50	0.74
5	0.15	0.58	0.82
6	0.21	0.59	0.65
7	0.13	-0.68	0.92
8	0.03	0.52	0.85
9	0.04	0.75	0.94
10	0.07	0.44	0.65
11	0.09	0.37	0.52
12	0.21	0.54	0.55
13	0.08	0.62	0.81
14	0.07	0.62	0.83
15	0.05	0.59	0.90
16	0.10	0.71	0.72
17	0.07	0.89	0.91
18	0.09	0.59	0.87
19	0.02	0.48	0.95
20	0.13	0.44	0.67
21	0.09	0.48	0.80
22	0.05	0.39	0.89
23	0.01	0.46	0.97
24	0.03	0.46	0.95
25	0.06	0.43	0.88
26	0.04	0.31	0.83
27	0.03	0.41	0.95
28	0.12	0.36	0.36

Stellenbosch University https://scholar.sun.ac.za

Table 18.5: Measured and reconciled tailings response variances

Measured			
Run	Flow ratio	Tails HM grade	Tails HM recovery
1	0.00	0.01	6.84
2	0.00	0.01	0.59
3	0.17	0.01	0.01
4	0.00	0.01	0.03
5	0.01	0.45	0.98
6	0.89	420.58	302.36
7	0.10	0.67	1.05
8	0.00	0.02	0.13
9	0.00	0.09	0.06
10	0.00	0.02	0.21
11	0.01	0.05	0.09
12	0.01	0.89	1.04
13	0.00	0.07	0.02
14	0.00	0.01	0.07
15	0.00	0.01	0.04
16	0.00	0.00	0.00
17	0.00	0.25	0.37
18	0.00	0.42	0.76
19	0.00	3.43	9.31
20	0.00	0.00	0.00
21	0.02	0.00	0.02
22	0.06	0.01	0.01
23	0.00	0.00	0.02
24	0.00	0.00	0.06
25	0.00	0.00	0.04
26	0.00	0.00	0.05
27	0.00	0.03	0.19
28	0.13	0.15	0.17

Reconciled			
Run	Flow ratio	Tails HM grade	Tails HM recovery
1	0.00	0.01	21.44
2	0.00	0.01	0.10
3	0.36	0.01	0.02
4	0.00	0.01	0.05
5	0.01	0.02	0.11
6	1.72	0.02	0.03
7	0.30	0.61	3.94
8	0.00	0.01	0.07
9	0.00	0.01	0.07
10	0.01	0.01	0.05
11	0.02	0.01	0.02
12	0.04	0.04	0.05
13	0.00	0.03	0.07
14	0.01	0.01	0.03
15	0.00	0.01	0.04
16	0.00	0.00	0.00
17	0.00	0.01	0.05
18	0.00	0.00	0.01
19	0.00	0.00	0.06
20	0.00	0.00	0.01
21	0.02	0.00	0.01
22	0.06	0.00	0.02
23	0.00	0.00	0.02
24	0.00	0.00	0.01
25	0.00	0.00	0.01
26	0.02	0.00	0.04
27	0.00	0.00	0.01
28	0.28	0.07	0.08

Stellenbosch University https://scholar.sun.ac.za

Table 18.6: Mean interface measurements per experimental run based on the results of Algorithm CVII and manually labelled images

Interface measurement (mm)		
Test run	Algorithm CVII	Manual labelling
1	78.23	61.77
2	86.37	96.34
3	86.47	105.50
4	104.88	81.56
5	100.53	90.41
6	73.05	60.98
7	77.33	56.05
8	74.51	61.32
9	106.81	95.91
10	63.50	67.63
11	55.96	57.40
12	81.93	67.57
13	101.53	78.92
14	99.22	79.70
15	79.83	58.74
16	76.86	101.93
17	104.59	102.12
18	97.47	87.17
19	88.40	61.45
20	95.82	52.73
21	100.75	69.55
22	88.56	54.14
23	70.54	52.95
24	89.34	65.60
25	63.06	54.67
26	69.60	52.64
27	90.72	51.04
28	74.93	64.34

18.3. Camera calibration errors

Figures 18.2 and 18.3 give reprojection errors for camera calibration of each experimental test run case. Errors in Figure 18.2 were calculated by transforming the ideal calibration pattern world coordinates to image coordinates (using the training Hall calibration matrix) via Equation 10.18. Euclidean distances between the detected calibration coordinates and the reprojected image coordinates are calculated and averaged (per experimental run) to find the final calibration error.

Stellenbosch University https://scholar.sun.ac.za

Figure 18.3's errors are determined by comparing the ideal calibration pattern world coordinates to the coordinates obtained via Equations 10.21 and 10.22.

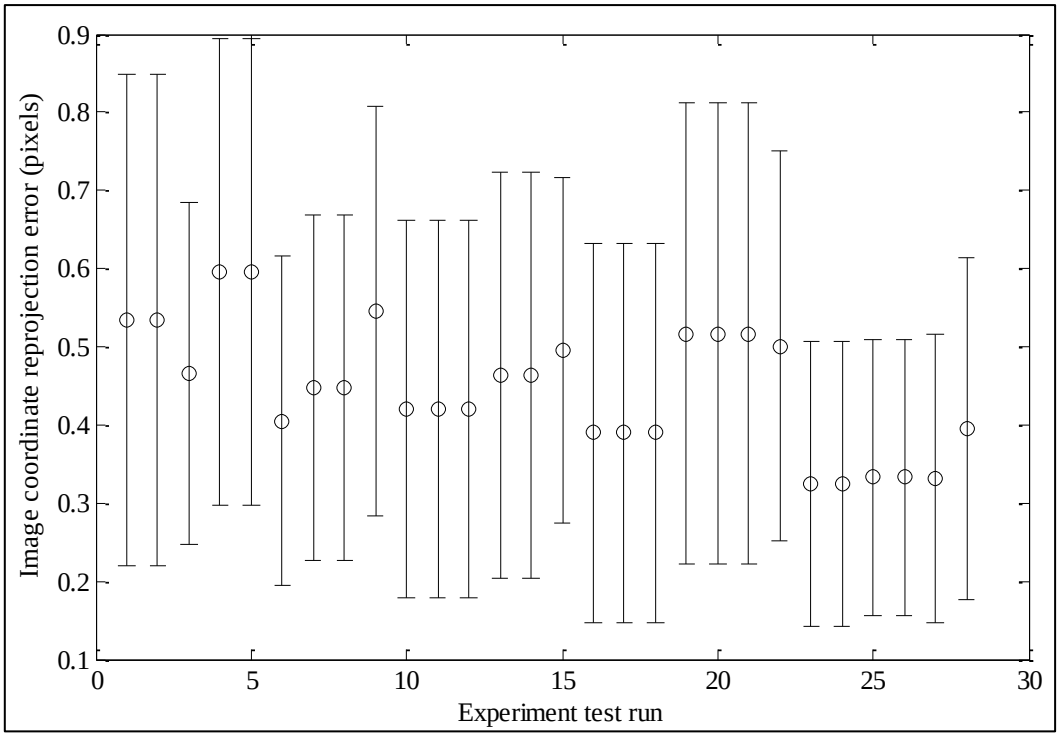

Figure 18.2: Image coordinate reprojection errors for each experimental run (error bars represent $1 \times \sigma$, based on n = 54 replicates)

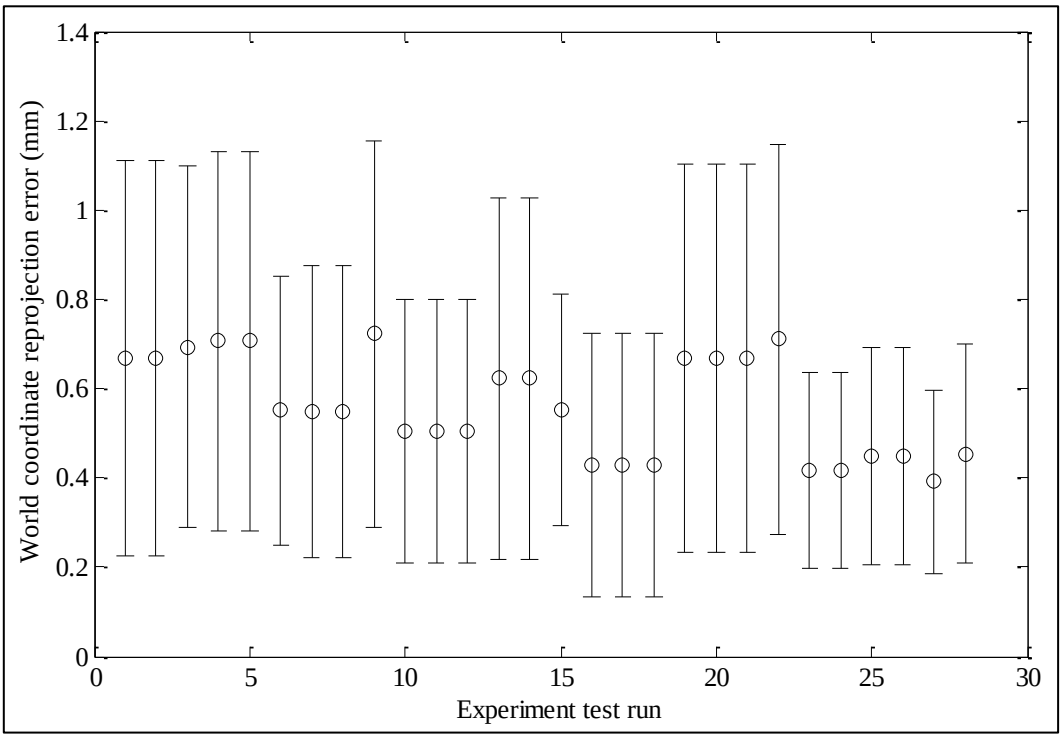

Figure 18.3: World coordinate reprojection errors for each experimental run (error bars represent $1 \times \sigma$, based on n = 54 replicates)

Stellenbosch University https://scholar.sun.ac.za

19. Appendix K

19.1. Concentrate grade soft sensor variance

This section presents the calculation of variance of the hypothetical composition soft sensors (based on concentrate interface measurements) shown in Table 11.6 (Section 11.3.3). A regression model was prepared, relating spiral concentrate stream HM grade to concentrate interface measurements, to determine a standard deviation for spiral concentrate stream grade inference. The following regression model was considered:

$$g_4 = X_{3,conc} = \beta_0 + \beta_1 x_1 + \beta_2 x_2 + \beta_3 x_1 x_2 + \beta_4 x_1^2 \qquad \text{(Eq. 19.1)}$$

Where:

- g_4 follows the nomenclature in Section 4.4.

In Equation 19.1 the left-hand side represents concentrate HM grade, x_1 is the concentrate interface measurement and x_2 is the splitter setting. Regression analysis was performed (similar to what is described in Section 4.3) and the values for $\bar{\beta}$ are listed in Table 19.1.

Table 19.1: Parameter and t-test results for Equation 19.1

β_i	Parameter Value	p-value
0	-0.09	0.90
1	0.02	0.47
2	-0.25	0.18
3	4.40E-03	0.08
4	-7.36E-05	0.59

Only parameter β_3 is considered statistically significant since, despite being slightly greater than 0.05, it has the lowest p-value. Parameters β_1 and β_2 are also considered significant due to the inclusion of the higher order parameter β_3. β_4 and β_0 are not statistically significant. A squared splitter setting parameter was not included in Equation 19.1 since it was found to not have a significant impact on concentrate grade in Section 5.3.

$\mathcal{R}^2$ for Equation 19.1 after regression is 0.37 and the F-test p-value is 0.04. The concentrate interface-grade model is statistically significant; however, it is severely lacking in terms of precision. SSE for this regression model is 0.51 and the degrees of freedom are 21 resulting in $MSE = 0.0244$ (which is the concentrate grade sensor variance). The low correlation coefficient can be caused due to the exclusion of spiral feed parameters that directly affect concentrate stream grade and inaccuracies in the segmentation, coordinate transformation and the final concentrate interface measurement

Stellenbosch University https://scholar.sun.ac.za

calculation. Spiral feed variables are excluded in Equation 19.1 because it was desired to obtain an empirical equation that can estimate spiral concentrate grade in a way that does not require measurement of spiral feed properties (in essence to prepare a calibration curve for the soft sensor).

19.2. Data reconciliation and sensor network implementation cost MATLAB code

```
function JL_JC = SensorLocations(ind)
% load incidence matrix
load('IncidenceMat.mat')
M = m;M(m==2) = -1;M(m==3) = -1;M2 = M(:,1:end-3);


% load process stream variables
load('info.mat')
load('par.mat')

x = par;
x0 = [316.8,x(1:8),60,60,60,0.15,x(9:16),0.5,x(17:end)];
% variance vector
V0 = [Vars(1)*ones(1,12),Vars(2)*ones(1,9),Vars(3),Vars(3),...
    Vars(3),Vars(3),Vars(3),Vars(3),Vars(3),Vars(3),Vars(3)];
% sensor cost vector
P0 = [SensorCost(4)*ones(12,1);SensorCost(3)*ones(9,1);...
    SensorCost(2);SensorCost(2);SensorCost(2);...
    SensorCost(2);SensorCost(2);...
    SensorCost(2);SensorCost(2);...
    SensorCost(2);SensorCost(2)];

j5 = ind;x = x0;
% make diagonal variance matrix
V = diag(V0(ind));
flag = 1;
for i = 1:10
    % calculate mass balances
    F = [M,zeros(size(M2)),zeros(size(M2));...
        zeros(size(M)),M2.*repmat(x(1:9),[4,1]),zeros(size(M2));...
        zeros(size(M)),zeros(size(M2)),M2.*repmat(x(1:9).*x(13:21),[4,1])];
    % find gradient of mass balances at nominal conditions
    F_div = [M,zeros(size(M2)),zeros(size(M2));...
        M.*repmat([x(13:21),0,0,0],[4,1]),M2.*repmat(x(1:9),[4,1]),...
        zeros(size(M2));...
   M.*repmat([x(13:21),0,0,0],[4,1]).*repmat([x(22:end),0,0,0],[4,1]),...
        M2.*repmat(x(1:9),[4,1]).*repmat(x(22:end),[4,1]),...
        M2.*repmat(x(1:9),[4,1]).*repmat(x(13:21),[4,1])];
    % Separate measured and unmeasured variables
    varies = 1:30;varies(ind) = [];
    Ax = F_div(:,ind);
    Au = F_div(:,varies);
    % Perform QR decomposition
    [Q,R,E] = qr(Au);m_u = rank(Au);j7 = [size(Q,2),m_u];
    P = Q(:,m_u+1:end)'; % this is the projection matrix
    R1 = R(1:m_u,1:m_u);R2 = R(1:m_u,m_u+1:end);
    Q1 = Q(:,1:m_u);
    y = x(ind);y = y';% vector of measured variables
    u = x(varies);u = u';% vector of unmeasured variables

    b = Ax*y + Au*u - F*x';
```

Stellenbosch University https://scholar.sun.ac.za

```
    y1 = y - V*(P*Ax)'*inv((P*Ax)*V*(P*Ax)')*(P*Ax*y - P*b);% reconciled
estimates
    y = y1;

    % estimate observable unmeasured variables
    u2 = E'*u;
    if numel(varies) == 1
        u1 = (inv(R1)*Q1')*(b - Ax*y);
    else
        u1 = (inv(R1)*Q1')*(b - Ax*y) + ...
            (inv(R1)*R2)*u2(size((inv(R1)*Q1')*(b - Ax*y),1)+1:end);
    end
    x = zeros(size(x));

    x(varies) = E*u2;
    x(ind) = y;
end
if flag
    % reconcile sensor variances
    Vest = (eye(numel(y))-V*(P*Ax)'*inv((P*Ax)*V*(P*Ax)')*P*Ax)*...
        V*(eye(numel(y))-V*(P*Ax)'*inv((P*Ax)*V*(P*Ax)')*P*Ax)';
    L = zeros(numel(x0));
    % find diagonal entries of performance Hessian
    L(8,8) = -Rev*x(20)*x(29);
    L(20,20) = -Rev*x(8)*x(29);
    L(29,29) = -Rev*x(8)*x(20);

    V_hat = zeros(size(V0));
    V_hat(ind) = diag(Vest);

    JL_JC = [0.5*trace(L*diag(V_hat)*L'),sum(P0(ind).^2)];% JL and JC
objectives

end

end
```